Control Relevant Modeling and Design of Scramjet-Powered Hypersonic Vehicles

by

Jeffrey James Dickeson

A Dissertation Presented in Partial Fulfillment
of the Requirements for the Degree
Doctor of Philosophy

Approved April 2012 by the
Graduate Supervisory Committee:

Armando Rodriguez, Chair
Jennie Si
Valana Wells
Konstantinos Tsakalis
Matthias Kawski

ARIZONA STATE UNIVERSITY

May 2012

ABSTRACT

This report provides an overview of scramjet-powered hypersonic vehicle modeling and control challenges. Such vehicles are characterized by unstable non-minimum phase dynamics with significant coupling and low thrust margins. Recent trends in hypersonic vehicle research are summarized. To illustrate control relevant design issues and tradeoffs, a generic nonlinear 3DOF longitudinal dynamics model capturing aero-elastic-propulsive interactions for wedge-shaped vehicle is used. Limitations of the model are discussed and numerous modifications have been made to address control relevant needs. Two different baseline configurations are examined over a two-stage to orbit ascent trajectory. The report highlights how vehicle level-flight static (trim) and dynamic properties change over the trajectory. Thermal choking constraints are imposed on control system design as a direct consequence of having a finite FER margin. The implication of this state-dependent nonlinear FER margin constraint, the right half plane (RHP) zero, and lightly damped flexible modes, on control system bandwidth (BW) and FPA tracking has been discussed. A control methodology has been proposed that addresses the above dynamics while providing some robustness to modeling uncertainty. Vehicle closure (the ability to fly a trajectory segment subject to constraints) is provided through a proposed vehicle design methodology. The design method attempts to use open loop metrics whenever possible to design the vehicle. The design method is applied to a vehicle/contral law closed loop nonlinear simulation for validation. The 3DOF longitudinal modeling results are validated against a newly released NASA 6DOF code.

ACKNOWLEDGEMENTS

Thank you Karen for your patience. Meeting you was the most important moment in my life. Thank you Dr. Rodriguez for convincing me not to give up, easily the second most important moment. Thank you Dr. Bolender for the models and the assistance you have provided. Readers are referred to Dr. Bolender for details not specified above or in the cited references.

TABLE OF CONTENTS

LIST OF TABLES

LIST OF FIGURES

Figure Page

Chapter 1

INTRODUCTION

This motivation and overview provided below was a collaborative effort between the author and Dr. Armando A. Rodriguez. The work was part of a research surveys [11–16] for a papers presented at the AIAA Conference on Guidance, Navigation and Control and AIAA International Space Planes and Hypersonic Systems and Technologies Conference. It is not the author's intention to claim sole credit for this survey, but it will be presented in it's entirety for completeness.

1.1 Motivation

With the historic 2004 scramjet-powered Mach 7 and 10 flights of the X-43A [17–20] , hypersonics research has seen a resurgence. This is attributable to the fact that air-breathing hypersonic propulsion is viewed as the next critical step toward achieving (1) reliable affordable access to space, (2) global reach vehicles. Both of these objectives have commercial as well as military implications. While rocket-based (combined cycle) propulsion systems [21] are needed to reach orbital speeds, they are much more expensive to operate because they must carry oxygen. This is particularly costly when traveling at lower altitudes through the troposphere (i.e. below 36,152 ft). Current rocket-based systems also do not exhibit the desired levels of reliability and flexibility (e.g. airplane like takeoff and landing options). For this reason, much emphasis has been placed on two-stage-to-orbit (TSTO) designs which involve a turbo-ram-scramjet combined cycle first stage and a rocket-scramjet second stage, as seen in Figure 1.1. This report focuses on modeling and control challenges associated with scramjet-powered hypersonic vehicles in order to suitably limit the scope of the presentation. Such vehicles are characterized by significant aero-thermo-elastic-propulsion interactions and uncertainty [1, 3, 5, 17–34]. This paper discusses some of the associated modeling and control challenges and tradeoffs. Specific control-relevant analysis and results will be presented based on the nonlinear model discussed within [1–9, 35–38].

1.2 Overview of Hypersonics Research

The 2004 scramjet-powered X-43A flights ushered in the era of air-breathing hypersonic flight. Hypersonic vehicles that have received considerable attention include the National Aerospace Plane (NASP, X-30) [39–42], X-33 [27, 43, 44], X-34 [45, 46], X-43 [17, 19, 20, 47], X-51 [48], Falcon (Force Application from CONUS) [43, 49–51] and Blackswift[52]. A summary of hypersonics research programs prior to the X-43A flights is provided within [53]. Some of this, and more recent,

Figure 1.1: NASA Two Stage To Orbit, Artist Rendition (courtesy of NASA Ames Research Center)

work is now described.

- *General Research on Scramjet Propulsion.* NASA has pursued scramjet propulsion research for over 40 years [53, 54]. During the mid 1960's, NASA built and tested a hydrogen-fueled and cooled scramjet engine that verified scramjet efficiency, structural integrity, and first generation design tools. During the early 1970's, NASA designed and demonstrated a fixed-geometry, airframe-integrated scramjet "flow path" (capable of propelling a hypersonic vehicle from Mach 4 to 7) in wind tunnel tests.

- *NASP.* The NASP X-30 (1984-1996, $\$3B^{+}$) was a single-stage-to-orbit (SSTO) shovel-shaped (waverider) hydrogen fueled vehicle development effort involving DOD and NASA. At its peak, over 500 engineers and scientists were involved in the project [53, 55]. Despite the fact that no flights took place, much aero-thermo-elastic-propulsion research was accomplished through this effort [19, 39, 53, 56–59]. The program was unquestionably too ambitious [18] given the (very challenging) manned requirement as well as the state of materials, thermal protection, propulsion, computer-aided-design technology readiness levels (TRLs) and integration readiness levels (IRLs). Within [60], relevant cutting-edge structural strength/thermal protection issues are addressed; e.g. high specific strength (strength/density) that ceramic matrix composites (CMCs) offer for air-breathing hypersonic vehicles experiencing $2000^{\circ} - 3000^{\circ}F$ temperatures.

- *SSTO Technology Demonstrators.* The X-33 and X-34 would follow NASP.

  – The X-33 (Mach 15, 250 kft) [27, 43, 44] was a Lockheed Martin Skunk Works unmanned sub-scale (triangularly shaped) lifting body (linear aerospike) rocket-engine powered technology demonstrator for their proposed VentureStar SSTO reusable launch vehicle (RLV).

  – The X-34 (Mach 8, 250 kft) [45, 46], much smaller than the X-33, was an unmanned sub-scale (shuttle shaped) Orbital Sciences (Fastrac) rocket-engine powered technology demonstrator intended to operate like the space shuttle.

- *HyShot Flight Program.* Supersonic combustion of a scramjet in flight was first demonstrated July 30, 2002 (designated HyShot II) by the University of Queensland Centre for Hypersonics (HyShot program) [61, 62]. Another flight demonstration took place on March 25, 2006 (HyShot III). During each flight, a two-stage Terrier-Orion Mk70 rocket was used to boost the payload (engine) to an apogee of 330 km. Engine measurements took place at altitudes between 23 km and 35 km when the payload carrying re-entry Orion reached Mach 7.6. Gaseous hydrogen was used to fuel the scramjet. Flight results were correlated with the University of Queensland's T4 shock tunnel. Thus far, the centre has been involved with five flights - the last on June 15, 2007 (HyCAUSE) [63].

- *Hyper-X.* In 1996, the Hyper-X Program was initiated to advance hypersonic air-breathing propulsion [54]. The goal of the program was to (1) demonstrate an advanced, airframe-integrated, air-breathing hypersonic propulsion system in flight and (2) validate the supporting tools and technologies [17–20, 47]. The Hyper-X program culminated with the (March 27, November 16) 2004 Mach 7, 10 (actually 6.83, 9.8) X-43A scramjet-powered flights [18–20]. Prior to these flights, the SR-71 Blackbird held the turbojet record of just above Mach 3.2 while missiles exploiting ramjets had reached about Mach 5 [55].

  – *Flight 1.* The first X-43A flight was attempted on June 2, 2001. After being dropped from the B-52, the X-43A stack (Orbital Sciences Pegasus rocket booster plus X-43A) lost control. A "mishap investigation team" concluded that the (Pegasus) control system design was deficient for the trajectory selected due to inaccurate models [18, 64]. The trajectory was selected on the basis of X-43A stack weight limits on the B-52. The mishap report [64] (5/8/2003) said the (Pegasus) control system could not maintain stack stability during transonic flight. Stack instability was observed as a roll oscillation. This

caused the rudder to stall. This resulted in the loss of the stack. Return to flight activities are summarized in [65].

– *Flight 2.* Results from Flight 2 (Mach 7, 95 kft, 1000 psf) are described within [22, 24, 66, 67]. The X-43A (Hyper-X research vehicle) was powered by an airframe-integrated hydrogen-fueled, dual mode scramjet. The fueled portion of the scramjet test lasted approximately 10 sec. The vehicle possessed 4 electromechanically actuated aerodynamic control surfaces: two (symmetrically moving) rudders for yaw control and two (symmetrically and differentially moving) all moving wings (AMWs) for pitch and roll control.

  Onboard flight measurements included [22] 1) three axis translation accelerations, 2) three axis rotational accelerations, 3) control surface deflections, 4) three space inertial velocities, 5) geometric altitude, 6) Euler angles (i.e. roll, pitch, and heading angles), and 7) wind estimates, 8) flush air data systems (FADS), amongst others (e.g. over 200 surface pressure measurements, over 100 thermocouples, GPS, weather balloon atmospheric measurements) [19, 68]. Body axis velocities, AOA, and sideslip angle [22] were estimated using (4) and (6).

  Control system design was based on sequential loop closure root locus methods [67]. Gains were scheduled on Mach and angle-of-attack (AOA) with dynamic pressure compensation. Gain and phase margins of 6 dB and 45° were designed into each loop for most flight conditions. Smaller margins were accepted for portions of the descent. Control system operated at 100 Hz, while guidance commands were issued at 25 Hz.

  Scramjet engine performance was within 3% of preflight predictions. During powered flight, AOA was kept at $2.5^\circ \pm 0.2^\circ$. Pre-flight aero-propulsive database development for Flight 2 (based on CFD and available ground-test data) is discussed within [69]. Relevant X-43A pre-flight descent aero data, including experimental uncertainty, is discussed within [25]. The data suggests vehicle static stability (in all three axes) along the descent trajectory. Moreover, longitudinal stability and rudder effectiveness are diminished for AOA's above 8°.

– *Flight 3.* Flight 3 (Mach 10, 110 kft, 1000 psf) results are described within [70]. Scramjet development tests exploiting the NASA/HyPulse Shock Tunnel in support of Flight 3 are described within [71]. The X-43A was a very heavy, short, very rigid (3000 lb, 12 ft, 5 ft wide, 2 ft high, 42 Hz lowest structural frequency [72]) lifting body and hence

thermo-elastic considerations were not significant.

Aerodynamic parameter identification results obtained from Flight 3 descent data at Mach 8, 7, 6, 5, 4, 3, based on multiple orthogonal phase-optimized sweep inputs applied to the control surfaces, are described within [73]. A linear aero model was used for fitting purposes. The fitting method (which led to the best results) was an equation-error frequency domain method. In short, estimated data agreed well with preflight data based on wind tunnel testing and computational fluid dynamics (CFD).

It is instructive to compare the operational envelops of several modern hypersonic vehicles. This is done in [45]. In this paper, elliptical envelops are given for the X-30, X-33, X-34, and X-43A. Approximate altitude and Mach extremes for these vehicles are as follows:

X-30: 250 kft, Mach 25;

X-33: 250 kft, Mach 15;

X-34: 250 kft, Mach 8;

X-43A: 110 kft, Mach 10.

The associated envelop scale back is, no doubt, a direct consequence of the aggressive goals of NASP - goals, in part, motivated by the politics of gaining congressional and presidential approval [18]. More fundamentally, this scale back reflects the need for carefully planned demonstrations and flight tests.

- *HiFIRE.* The Hypersonic International Flight Research Experimentation (HiFIRE) is an ongoing collaboration between NASA, AFRL, Australian Defence Science and Technology Organization (DSTO), Boeing Phantom Works, and the University of Queensland [74]. It will involve 10 flights over 5 years. HiFIRE flights will focus on the goal of understanding fundamental hypersonic phenomena.

- *X-51A Scramjet Demonstrator Waverider.* The Boeing X-51A is an expendable hydrocarbon fueled scramjet engine demonstrator waverider vehicle (26 ft long, 4000 lb.) that is being developed by AFRL, Boeing, and Pratt & Whitney [48]. The X-51 completed its first powered flight successfully on May 26th, 2010 by flying for over 200 seconds and reaching a speed of Mach 5. A second test took place on June 13th, 2011, but ended early when the scramjet engine did not transition to JP-7 fuel operation after an ethylene start. The X-51-booster stack is carried via B-52 to a drop altitude of 50,000 feet. An Army tactical missile system solid rocket booster propels the vehicle to Mach 4.5. At that point, the Pratt & Whitney Rocketdyne SJY61 scramjet takes over and accelerates the vehicle.

- *Advanced Hypersonic Weapon* On November 17th, 2011 the US Army Space and Missile Defense Command/Army Strategic Command conducted the first flight test of the Advanced Hypersonic Weapon (AWH). The AWH is unpowered conical shaped glide vehicle launched to hypersonic speeds from a a 3 stage-booster system. The prototype was launched from Hawaii and hit a target on Kwajalein Atoll over 2300 miles away in less than 30 minutes.

- *Falcon.* Aspects of the Falcon waverider project are described within [43, 49–52, 75] . The project began in 2003 with the goal of developing a series of incremental hypersonic technology vehicle (HTV) demonstrators. It involves the United States Air Force (USAF) and DARPA. Initially, ground demonstrations (HTV-1) were conducted. The first flight (HTV-2) [50] is scheduled for 2009. HTV-3X will involve a reusable launch vehicle with a hydrocarbon-fueled turbine-based combined-cycle (TBCC) propulsion system that takes off like an airplane, accelerates to Mach 6, and makes a turbojet powered landing. These demonstrations are designed to develop technologies for a future reusable hypersonic cruise vehicle (HCV) designed for prompt global reach missions.

- *Aero-Thermo-Elastic-Propulsion CFD-FE Tools.* The design of subsonic, transonic, and supersonic vehicles have benefited from extensive ground testing. Such testing is much more difficult for hypersonic vehicles. As such, the use of state-of-the-art CFD-FE-based aero-thermo-elasticity-propulsion modeling tools is particularly crucial for the development of hypersonic vehicles. While much has been done at the component level (e.g. wings, surfaces), relatively little has been done that addresses the entire vehicle (at least in the published literature). This, of course, is due to the fact that accurate CFD studies often require the nation's most advanced super computing resources. Relevant work in this area is described within the following and the associated references [43, 55, 76, 77]. A major contribution of the 2004 X-43A flights was the validation of design tools [17, 18]. It should be noted that CFD is often applied in conjunction with or after applying classic engineering methods (e.g. panel methods) as described within [23, 29, 78]. Widely used programs that support such methods include (amongst many others) HABP (Hypersonic Arbitrary Body Program), APAS (Aerodynamic Preliminary Analysis System), and CBAERO (Configuration Based Aerodynamics prediction code) [23, 29, 42, 78]. Given the above, it is useful to know what was used for the X-43A. The primary CFD tool used for preflight performance analysis of the X-43A is GASP [69] - a multiblock, structured grid, upwind-based, Navier-Stokes flow solver which addresses (1) mixtures of thermally perfect gases via polynomial thermodynamic curve fits, (2) frozen,

equilibrium, or finite-rate chemistry, (3) turbulent flow via Baldwin-Lomax algebraic turbulence model with Goldberg back flow correction. The SRGULL (developed by NASA's Zane Pinckney) and SHIP (supersonic hydrogen injection program) codes were used to predict scramjet performance for the X-43A [19, 68, 69]. SRGULL uses a 2D axis-symmetric Euler flow solver (SEAGULL). This was used [69] to address the forebody, inlet, and external nozzle regions of the X-43A lower surface flowpath. SRGULL also includes a 1D chemical equilibrium analysis code (SCRAM) which was used to approximate the combustor flow field. X-43A CFD flow field solutions may be visualized in [19]. Extensive databases exist for designing engines which exhibit good performance in the range Mach 4-7 [19].

1.3 Controls-Relevant Hypersonic Vehicle Modeling

The following describes control-relevant hypersonic vehicle models addressing aero-thermo-elastic-propulsion effects.

- In support of NASP research, the work within [42] describes a 6DOF model for a 300,00 lb, 200 ft, horizontal-takeoff winged-cone SSTO hypersonic vehicle. The model was generated using a (1) subsonic/supersonic panel code (APAS [78]), (2) hypersonic local surface inclination code (HABP [78]), (3) 2D forebody, inlet, nozzle code, and a (4) 1D combustor code. This model/vehicle has been used to guide the work of many controls researchers [79–86]. A significant short coming of the above model is that it cannot be used for control-relevant vehicle configuration design studies (at least not without repeating all of the work that went into generating the model); e.g. examining stability and coupling as vehicle geometry is varied. Efforts to address this are described below.

- Within [87] the authors describe the development of one of the first control-relevant first principles 3-DOF models for a generic hypersonic vehicle. Aerodynamic forces and moments are approximated using classical 2D Newtonian impact theory [23] . A simple static scramjet model is used. The flow is assumed to be quasi-one-dimensional and quasi-steady. Scramjet components include an isentropic diffuser, a combustor modeled via Rayleigh flow (1D compressible flow with heat addition) [88], and an isentropic internal nozzle. The aft portion of the fuselage serves as the upper half of an external nozzle. The associated free-stream shear layer forms the lower half of the external nozzle. This layer is formed by the equilibration of the static pressure of the exhaust plume and that of the free-stream flow. A simplifying aft

nozzle-plume-shear layer assumption is made that smoothly transitions the aft body/nozzle pressure from an exit pressure value p_e to the downstream free-stream value p_∞. Implicit in the assumption is the idea that Mach and AOA perturbations do not change the location of the shear layer and that aft pressure changes are determined solely by exit pressure changes and elastic motion [87, pg. 1315]. Controls include an elevator, increase in total temperature across the combustor, and diffuser area ratio. A single body bending mode was included based on a NASTRAN derived mode shape and frequency for a vehicle with a similar geometry. This model is a big step toward permitting control-relevant vehicle configuration design studies.

- The following significant body of work (2005-20010) [3],[],[2],[36],[1],[89] examines aero-thermo-elastic-propulsion modeling and control issues using a first principles nonlinear 3-DOF longitudinal dynamical model which exploits inviscid compressible oblique shock-expansion theory to determine aerodynamic forces and moments, a 1D Rayleigh flow scramjet propulsion model with a variable geometry inlet, and an Euler-Bernoulli beam based flexible model. The model developed in this work will be used as the basis for the presentation - one which describes important control system design issues; e.g. importance of FER margin as it relates to the control of scramjet powered vehicles.

- Within [90] the authors describe the development of a nonlinear 3-DOF longitudinal model using oblique shock-expansion theory and a Rayleigh scramjet (as above) for the winged-cone vehicle described within [42]. Euler-based (inviscid) computational fluid dynamics (CFD) is used to validate the model. A related line of work has been pursued in [91]. Within [79], wind-tunnel-CFD based nonlinear and linear longitudinal and lateral models are obtained for the above winged-cone vehicle.

- X-43A related 6-DOF Monte-Carlo robustness work is described within [17]. Results obtained from conducting closed loop simulations in the presence of uncertainty are presented (as permitted). Limited comparisons between flight data and simulation data are made in an effort to highlight modeling shortfalls.

- A 6-DOF modeling tool developed by VSI Aerospace is described within [92],[93], [94]. The modeling tool is designed to obtain nonlinear and/or linear 6-DOF models with varying degrees of fidelity using approximate engineering methods. The modeling tool aims too develop models with fully coupled longitudinal-lateral dynamics to improve fidelity by capturing the effects of coupled dynamics.

- Within [95] a three-dimensional, six-degree-of-freedom hypersonic vehicle model is being developed. The aerodynamic loads are calculated by using or combining two-dimensional shock/expansion theory and the Taylor-Maccoll equations for conical flow. Comparisons with computational results show good agreement of resultant force and moment for the top and bottom vehicle surfaces and for most trials for the side surfaces.

The above demonstrates the need for (mathematically tractable) parameterized control system design models that can be used for configuration design studies as well as higher fidelity control system evaluation models.

Chapter 2

CONTRIBUTIONS

The focus of this dissertation will be to layout a preliminary design process for a flexible, air-breathing hypersonic class of vehicle that improves upon current best practices. The main driver for improvement will be the inclusion of control-relevant metrics; e.g. metrics that quantify the system's performance in a "closed loop" sense. In order to accommodate the design process, a multidisciplinary optimization (MDO) framework has been developed for hypersonic vehicles that exhibit aero-servo-elastic-propulsive (ASTEP) interactions. An overview of the framework can be seen in Figure 2.1. More details of the framework are discussed in Chapter 8.

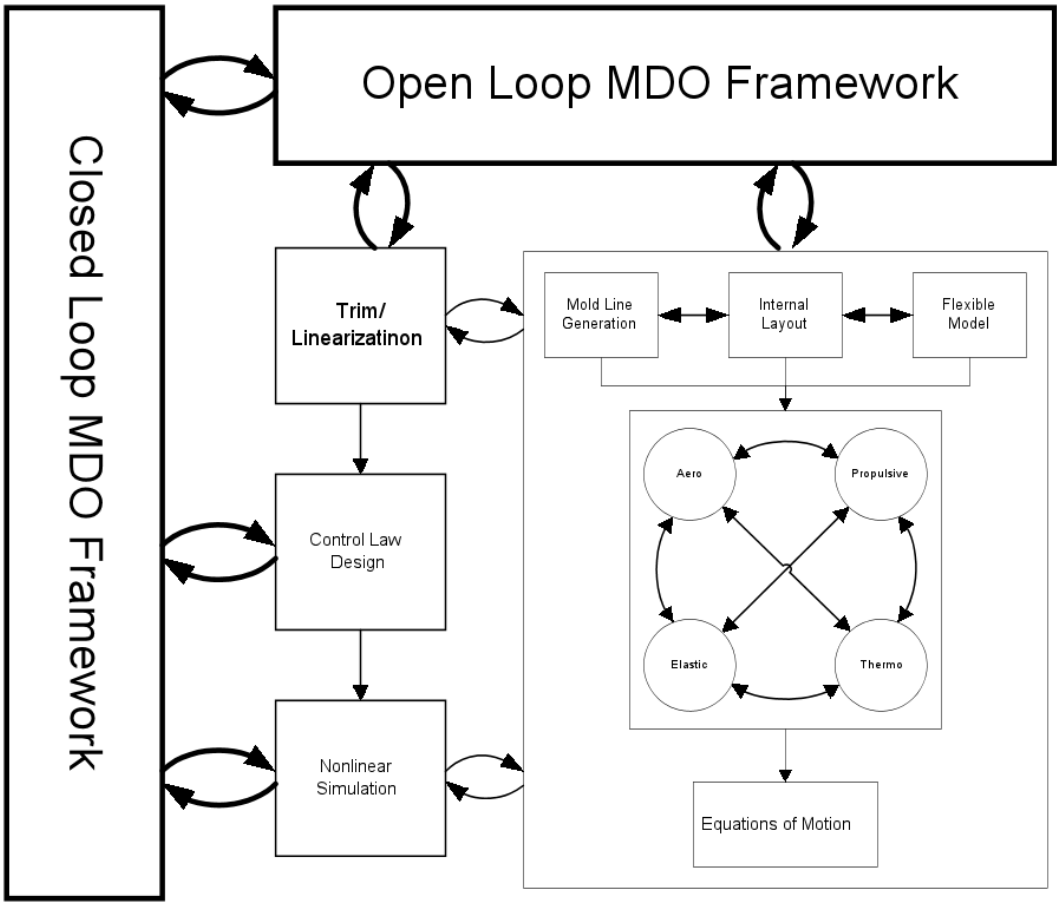

Figure 2.1: Closed Loop MDO Framework

A preliminary design process aims to come up candidate vehicle design(s) that comes close to satisfying some set of requirements. Some generalized requirements may include attaining orbital speed at a given altitude (space shuttle), maximizing range (gliders, transport aircraft), maximiz-

ing combat radius (fighter aircraft) maximizing speed and or maneuverability (missiles), and many more. The measure of closeness is typically determined by the changes that must be made to the design when using higher fidelity modeling tools. Therefore, the best preliminary vehicle designs will require minimal modification as modeling fidelity increases. Improving the preliminary design process mean less iteration between different disciplines, less rework, and ultimately reduced cost. This is especially true for highly integrated systems such as air-breathing hypersonic vehicles, where high fidelity analysis can be extremely expensive and time consuming.

A brief overview of relevant past and ongoing hypersonic research was given above. The modeling and control challenges associated with air-breathing hypersonic vehicles will be summarized. Some of these challenges (e.g. interactions and uncertainty) have only been partially described within the controls literature. An effort has been made to provide a more comprehensive (albeit incomplete) description. A simplified nonlinear model for the longitudinal dynamics of a scramjet-powered hypersonic vehicle [2, 3, 36, 38] is considered. Limitations of the modeling method are discussed and modifications are made to the model to address some the most control-relevant limitations. The 3DOF longitudinal modeling results are verified against a newly released NASA 6DOF code. Limitations of the 3DOF modeling methodology addressed, particularly for the engine inlet and plume modeling methodologies. It is shown that the 3DOF modeling methodology is valid for spillage and shock on lip conditions, but not valid for cases where the shock is swallowed by the inlet. Issues related to both 3 and 6DOF modeling choices are examined. It is shown that certain modeling methodologies choices can result in a model that is not amenable to design optimization.

Two vehicle configurations are analyzed at different operating points throughout the air-breathing corridor. It is shown how static and dynamic properties of the model change as a function of the flight condition; i.e. altitude, Mach, dynamic pressure at level flight, as well as the vehicle design choices. Static (trim) characteristic to be examined include trim requirements as well as fuel (FER) margins; i.e. additional fuel required for thermal choking to occur or for or stoichiometric fuel-to-air ratio to be reached. Dynamic characteristics to be examined include pole/zero migrations, flexible dynamics, and achievable closed loop robustness.

Control system design tradeoffs are then examined. Fundamental questions examined include: How can performance and/or robustness be maximized while keeping the design methodology simple, and therefore suitable for use within an design optimization loop? It is shown how the vehicle instability, non-minimum phase zeros, flexibility, and FER margin limit achievable perfor-

mance. A control methodology has been proposed that addresses the above dynamics while providing some robustness to modeling uncertainty for both 3 and 6 DOF vehicles. Further robustness is provided through the proposed vehicle design methodology.

Finally, the dissertation illustrates fundamental tradeoffs that vehicle and control system designers should jointly consider during the early stages of vehicle conceptualization/design. While vehicle designers may want to use a higher fidelity model to conduct more accurate vehicle trade studies, this report shows that a (first principles) 3DOF nonlinear engineering model that can be used to simulate trajectories - such as that used in this work - may be very useful during the early stages of vehicle conceptualization and design. Due to the ASTEP interactions, a vehicle that does not properly account for control-relevant phenomena can be almost impossible to control. The design method is applied over a trajectory similar to what might be used for a two-stage to orbit (TSTO) booster vehicle.

Chapter 3

MODELING AND CONTROL ISSUES/CHALLENGES

Lifting Body and Waverider Phenomena/Dynamics. Much attention has been given in the literature to integrated-airframe air-breathing propulsion [21] lifting body designs; e.g. X-30 [39–41], X-33 [27, 43, 44], X-34 [45, 46], X-43 [17, 19, 20, 47], X-51 [48]. Waverider designs [23, 96–99] - a special subclass of lifting body designs - have received particular attention; e.g. X-30, X-51 [48], Falcon [49–52, 75, 100] . Relevant phenomena/dynamics are now discussed.

Why Waveriders? Generally, lift-to-drag (L/D) decreases with increasing Mach and is particularly poor for hypersonic vehicles (flat plate: $(L/D)_{max} = 6.5$; Boeing 707: $(L/D)_{max} = 20$ cruising near Mach 1) [23, page 251]. Conventional hypersonic vehicles typically have a detached shock wave along the leading edge and a reduced $(L/D)_{max}$. This is particularly true for blunt lifting body designs. In contrast, waveriders are hypersonic vehicles that (if properly designed and controlled) have an attached shock wave along the leading (somewhat sharp) edge [23, pp. 251-252] and "*appear to ride the bow shock wave*." Moreover, the high pressure flowfield underneath the vehicle remains somewhat contained with little leakage over the top in contrast to conventional hypersonic vehicles. As such, waveriders can exhibit larger L/D ratios, a larger lift for a given angle-of-attack (AOA), and can be flown at lower AOAs. A maximum L/D is desirable to maximize range [23]. It follows, therefore, that *waveriders are ideal for global reach cruise applications*. A major design advantage associated with waveriders is that their associated flow fields are generally (relatively speaking) easy to compute [23]. This can be particularly useful during the initial design phase where it is critical to explore the vehicle parameter design space in order to address the inherent multidisciplinary optimization [89, 100].

Aero-Thermo. Drag can be reduced by making the body more slender (increased fineness) [101]. While this can reduce drag, it increases structural heating [23]; e.g. nose (stagnation point) heating, is inversely proportional to the nose radius. For this reason, *most hypersonic vehicles possess blunt noses*; e.g. Space Shuttle [23, page 200]. The needle-nosed coned-wing studied in [82, 85] and other studies may generate excessive heat for the first stage of a TSTO solution. Despite this, the authors strongly recommend that the reader examine the work described within [82, 85]. The point here is that fundamentally, hypersonic vehicle design is heat-driven, not drag-driven. This is because within the hypersonic regime *heating varies cubicly with speed, while drag varies quadratically* [23,

pp. 347-348].

Scramjet Propulsion. The *entire underbelly of a waverider is part of the scramjet propulsion system*. Waveriders rely on bow shock and forebody design to provide significant *compression lift*, while the aftbody acts as the upper half of an expansion nozzle. Hypersonic vehicles generally possess long forebody compression surfaces to make the effective free-stream capture area as large as possible relative to the engine inlet area [21, pp. 40-41]. Generally, multiple compression ramps are used to achieve the desired conditions at the inlet. The X-43A, for example, used three compression ramps.

In contrast to rockets, air-breathing propulsion systems need not carry an oxidizer. This significantly reduces take-off-gross-weight (TOGW) [102]. Roughly, for a given payload weight $W_{payload}$, $\frac{W_{rocket}}{W_{payload}} \approx 25$ while $\frac{W_{airplane}}{W_{payload}} \approx 6.5$ [21, page 16]. Moreover, air-breathing systems offer increased safety, flexibility, robustness, and reduced operating costs [54, 103]. Scramjet propulsion specifically offers the potential for significantly increased specific impulse I_{sp} in comparison to rocket propulsion - hence lower cost-per-pound-to-orbit [65] (I_{sp} for hydrogen is much greater than that for hydrocarbon fuels). Scramjet operation is roughly Mach 5-16 [21], while air-breathing propulsion operation is roughly below 200kft [21, page 44]. In contrast to regular jets which have a compressor, scramjets (which rely on forebody compression) have no moving parts. When fuelled with hydrogen, they can (in theory) operate over a large range of Mach numbers (Mach 5-24) [104]. Scramjets are typically optimized at a selected design Mach number (e.g. Mach 7) to satisfy a shock-on-lip condition. At off-design speeds, a cowl door can be used to minimize air mass flow spillage. Cowl doors are generally scheduled open-loop [104]. For a very flexible vehicle, however, feedback may be required in order to reduce sensitivity to modeling errors.

Trajectories. Likely vehicle trajectories will lie within the so-called air-breathing corridor corresponding to dynamic pressures in the range $\overline{q} \in [500, 2000]$ psf - lower bound dictated by lifting area limit, upper bound dictated by structural limits. At Mach 16, the lower $\overline{q} = 500$ bound will require flight below 150kft [21, page 39]. Generally speaking, scramjet-powered vehicles will fly at the highest allowable (structure permitting) dynamic pressure in order to maximize free-stream mass airflow per unit area to the engine. It should be noted, however, that accelerating vehicles would have to increase dynamic pressure in order to maintain mass flow per unit area to the engine

[21, page 41]. For this reason, one may wish to fly the vehicle being considered at $\doteq 1500 - 1750$ psf (see Figure 3.1) so that it has room to increase dynamic pressure by moving toward larger Mach numbers while avoiding thermal choking at the lower Mach numbers (e.g. Mach 5). Within [21, page 39], the air-breathing corridor is about 30 kft wide vertically (see Figure 3.1). Assuming that the vehicle is flying along the center of the corridor, a simple calculation shows that if the flight path angle (FPA) deviates by about 2.86° ($\gamma \geq \sin^{-1}\left(\frac{\Delta h/\Delta t}{v}\right) \approx \sin^{-1}\left(\frac{15000/30}{10(1000)}\right)$) for 30 sec at Mach 10, then the vehicle will leave the corridor. (This simple calculation, of course, doesn't capture the potential impact of dynamics.) This unacceptable scenario illustrates the need for FPA control - particularly in the presence of uncertain flexible modes.

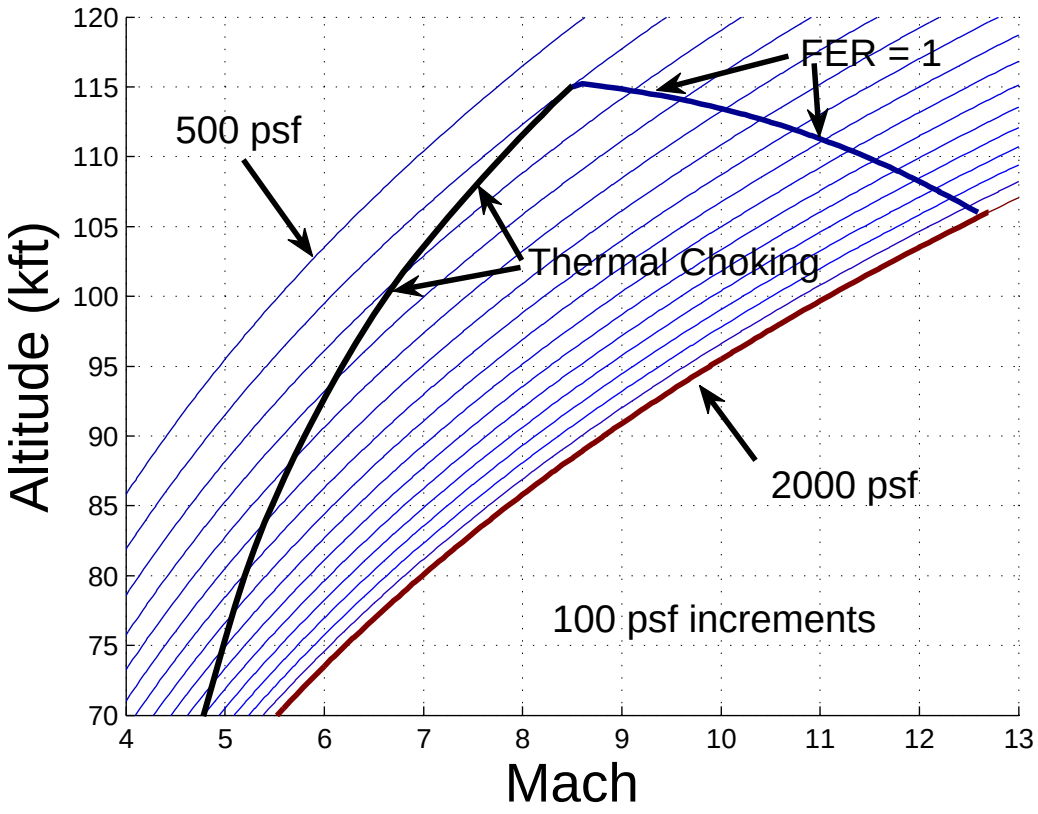

Figure 3.1: Air-Breathing Corridor Illustrating Constant Dynamic Pressure (Altitude vs Mach) Profiles, Thermal Choking Constraint, and FER Constraint; Notes: (1) Hypersonic vehicle considered in this paper cannot be trimmed above the thermal choking line; (2) An FER ≤ 1 constraint is enforced to stay within validity of model; (3) Constraints in figure were obtained using viscous-unsteady model for level flight [1–10]

Figure 3.1 shows the constant dynamic pressure "trajectories" (or profiles) of altitude versus Mach. (It should be noted that the term trajectory is used loosely here since time is not shown in the fig-

ure.) With that said, Figure 3.1 demonstrates the permissible "air-breathing flight corridor" or "flight envelope" for air-breathing hypersonic vehicles. In addition to the dynamic pressure constraints discussed above, the figure also indicates a constraint associated with thermal choking and one due to unity stoichiometrically normalized fuel equivalency ratio (FER=1). Additional air-breathing corridor constraints are discussed within [105].

Aero-Propulsion Coupling. In contrast to sub- and supersonic vehicles, hypersonic vehicles are uniquely characterized by *unprecedented aero-propulsion coupling*; i.e. the components providing lift, propulsion, and volume are strongly coupled [23, pp. 11-12]. More specifically, *aero performance cannot be decoupled from engine performance* because external forebody and nozzle surfaces are part of the engine flowpath [106]. For this reason, the integrated airframe-engine is sometimes referred to as an "engineframe." More specifically, vehicle aerodynamic properties impact the bow shock - detached for blunt leading edges, attached for sharp leading edges. This influences the engine inlet conditions which, in turn, influences thrust, lift, drag, external nozzle conditions, and pitching moment. More specifically, while forebody compression results in lift and a nose-up pitching moment aftbody expansion results in lift and a nose-down pitching moment. With the engine thrust situated below the c.g., this produces a nose-up pitching moment that must be countered by some control effector. Finally, it must be noted that scramjet air mass capture area, spillage, engine performance, as well as overall vehicle stability and control properties depend upon Mach, angle-of-attack (AOA), side-slip-angle (SSA), and engine power setting.

Hypersonic Flow Phenomena. Hypersonic flow is characterized by certain physical variables becoming progressively important as Mach is increased [23, 29, 31]. The boundary layer (BL), for example, grows as $\frac{M_\infty^2}{\sqrt{Re_{local}}}$. This causes the body to appear thicker than it really is. Viscous interactions refers to BL mixing with the inviscid far field. This impacts pressure distribution, lift, drag, stability, skin friction, and heat transfer. Shock layer variability is observed to start at around Mach 3 [23, page 13].

Aero-Thermo-Elastic-Propulsion. Hypersonic vehicles are generally unstable (long forebody, rearward engine, cg aft of cp) [3, 87]. As such, such vehicles generally require a *minimum control bandwidth (BW) for stabilization* [3, 107, 108]. The achievable BW, however, can be limited

by flexible (structural) dynamics, actuator dynamics, right half plane zeros, other high frequency uncertain dynamics, and variable limits (e.g. control saturation level) [108]. High Mach numbers can induce significant heating and flexing (reduction of flexible mode frequencies) [39, 43, 109]. Carbon-Carbon leading edge temperatures on the X-43A Mach 10 flight, for example, reached nearly $2000^\circ F$ [19]. During the Pegasus boost (100 sec), surface temperatures reached nearly $1500\,^\circ F$ [19].

Heat induced forebody flexing can result in bow shock wave and engine inlet oscillations. This can impact the available thrust, stability, and achievable performance – a major control issue if the vehicle is too flexible (light) and open loop unstable. A thermal protection system (TPS) is important to reduce heat-induced flexing; i.e. *prevent lowering of structural mode frequencies* [5, 9, 60, 66]. Designers must generally tradeoff vehicle lightness (permissible payload size) for increased thermal protection and vice versa. Type IV shock-shock interactions (e.g. bow shock interaction with cowl shock, results in supersonic jet impinging on cowl) - can cause excessive heating [23, page 226] that leads to structural damage. Within [60], relevant cutting-edge structural strength/thermal protection issues are addressed; e.g. high specific strength (strength/density) that ceramic matrix composites (CMCs) offer for air-breathing hypersonic vehicles experiencing $2000^\circ - 3000^\circ F$ temperatures. Materials for leading edges, aeroshells, and control surfaces are also discussed.

Non-minimum Phase Dynamics. Tail controlled vehicles are characterized by a non-minimum phase (right half plane, RHP) zero which is associated with the elevator to flight path angle (FPA) map [10]. This *RHP zero limits the achievable elevator-FPA BW* [107, 108, 110]. This report illustrates how FER can be used to address this issue. It is argued, however, that FER constraints may require that a *canard is needed to achieve a high BW FPA control response* [10]. This illustrates how controls can significantly influence the vehicle design process.

High Temperature Gas Effects. Relevant high temperature gas effects include [23]:

1. Caloric imperfection (temperature dependent specific heats and specific heat ratio $\gamma \triangleq \frac{c_p}{c_v}$) begins at about 800K or about Mach 3.5 [23, pp. 18-19].

2. Vibrational excitation is observed around Mach 3 and fully excited around Mach 7.5 [23, pp. 460-461].

3. O_2 dissociation occurs at around 2000K and is observed at about Mach 7.5-8.5. It is complete at around 4000K or about Mach 15-17 [23, pp. 460-461].

For the scramjet Mach ranges under consideration ($\sim$5-15), the following phenomena will not be relevant:

- N_2 dissociation, plasma/ionization, radiation, rarefied gas effects [21, 23].

It should be noted that onset temperatures for molecular vibrational excitation, dissociation, and ionization decrease when pressure is increased.

The above hypersonic phenomena are accurately modeled by suitable partial differential equations (PDEs); e.g. Navier-Stokes, Euler, Euler-Bernoulli, Timoshenko, and heat transfer PDEs. This, together with the above interactions and associated uncertainty [1, 3, 5, 17–24, 26–34], highlights the relevant modeling and control challenges.

Chapter 4

DESCRIPTION OF NONLINEAR MODEL

This report considers a first principles nonlinear 3-DOF dynamical model for the longitudinal dynamics of a generic scramjet-powered hypersonic vehicle [1–9, 35, 36, 38]. The controls include: elevator, stoichiometrically normalized fuel equivalency ratio (FER), and a canard (not considered in this work). The vehicle may be visualized as shown in Figure 4.1 [1].

4.1 Modeling Approach Summary

The following summarizes the modeling approach that has been used.

- *Aerodynamics.* Pressure distributions are computed using inviscid compressible oblique-shock and Prandtl-Meyer expansion theory [23, 29, 38, 88]. Air is assumed to be calorically perfect; i.e. constant specific heats and specific heat ratio $\gamma \triangleq \frac{c_p}{c_v} = 1.4$ [23, 88]. A standard atmosphere is used.

  Viscous drag effects (i.e. an analytical skin friction model) are captured using EckertŠs temperature reference method [1, 23]. This relies on using the incompressible turbulent skin friction coefficient formula for a flat plate at a reference temperature.

  Unsteady effects (e.g. due to rotation and flexing) are captured using linear piston theory [1, 111]. The idea here is that flow velocities induce pressures just as the pressure exerted by a piston on a fluid induces a velocity.

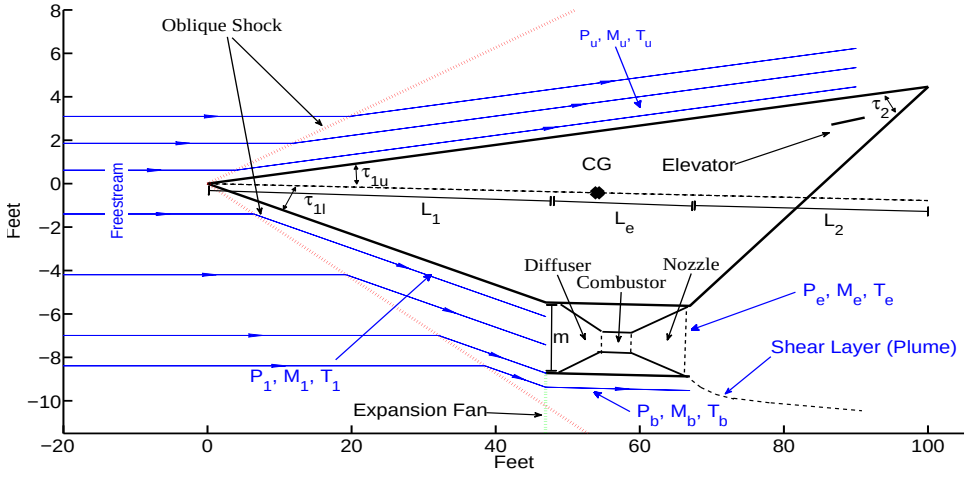

Figure 4.1: Schematic of Hypersonic Scramjet Vehicle

- *Propulsion.* The scramjet is modeled as in [87] (see discussion on page 7). A single (long) forebody compression ramp provides conditions to the rear-shifted scramjet inlet. The inlet is a variable geometry inlet (variable geometry is not exploited in this work).

  The model assumes the presence of an (infinitely fast) cowl door which uses AOA to achieve shock-on-lip conditions (assuming no forebody flexing). Forebody flexing, however, results in air mass flow spillage [38]. At the design cruise condition, the bow shock impinges on the engine inlet (assuming no flexing). At speeds below the design-flight condition and/or larger flow turning angles, the cowl moves forward to capture the shock. At larger speeds and/or smaller flow turning angles, the bow shock is swallowed by the engine. In either case, there is a shock reflected from the cowl or within the inlet (i.e. a bow shock reflection). This reflected shock further slows down the flow and steers it into the engine. It should be noted that shock-shock interactions are not modeled. For example, at larger speeds and smaller flow turning angles there is a shock off of the inlet lip. This shock interacts with the bow shock. This interaction is not captured in the model.

  The model uses liquid hydrogen (LH2) as the fuel. It is assumed that fuel mass flow is negligible compared to the air mass flow. The model also captures linear fuel depletion. Thrust is linearly related to FER for all expected FER values. For large FER values, the thrust levels off. In practice, when FER > 1, the result is decreased thrust. This phenomena [38] is not captured in the model. As such, control designs based on this nonlinear model (or derived linear models) should try to maintain FER below unity.

  The model also captures thermal choking. In what follows, it will be shown how to compute the FER required to induce thermal choking as well as the so-called *thermal choking FER margin*. The above will lead to a useful FER margin definition - one that is useful for the design of control systems for scramjet-powered hypersonic vehicles.

- *Structural.* A single free-free Euler-Bernoulli beam partial differential equation (infinite dimensional pde) model is used to capture vehicle elasticity. As such, out-of-plane loading, torsion, and Timoshenko effects are neglected. The assumed modes method (based on a global basis) is used to obtain natural frequencies, mode shapes, and finite-dimensional approximants. This results in a model whereby the rigid body dynamics influences the flexible dynamics through generalized forces. This is in contrast to the model described within [38] which uses fore and aft cantilever beams (clamped at the center of gravity) and leads to the rigid body modes being inertially coupled to the flexible modes (i.e. rigid body modes di-

rectly excite flexible modes). Within the current model, forebody deflections influence the rigid body dynamics via the bow shock which influences engine inlet conditions, thrust, lift, drag, and moment [9]. Aftbody deflections influence the AOA seen by the elevator. As such, flexible modes influence the rigid body dynamics.

- *Actuator Dynamics.* Simple first order actuator models (contained within the original model) were used in each of the control channels: elevator - $\frac{20}{s+20}$, FER - $\frac{10}{s+10}$, canard - $\frac{20}{s+20}$ (Note: canard not used in this study). These dynamics did not prove to be critical in this study. While no saturation level was used for the elevator, a (state dependent) saturation level - associated with FER (e.g. thermal choking and unity FER) - was directly addressed and is discussed below.

Generally speaking, the vehicle exhibits unstable non-minimum phase dynamics with nonlinear aero-elastic-propulsion coupling and critical (state dependent) FER constraints. The model contains 11 states: 5 rigid body states (speed, pitch, pitch rate, AOA, altitude) and 6 flexible states.

4.2 Detailed Modeling

Longitudinal Dynamics. The equations of motion for the 3DOF flexible vehicle are given as follows:

$$\dot{v} = \left[\frac{T\cos\alpha - D}{m}\right] - g\sin\gamma \tag{4.1}$$

$$\dot{\gamma} = \left[\frac{L + T\sin\alpha}{mv}\right] - \left[\frac{g}{v} - \frac{v}{R_E + h}\right]\cos\gamma \tag{4.2}$$

$$\dot{q} = \frac{\mathcal{M}}{I_{yy}} \tag{4.3}$$

$$\dot{h} = v\sin\gamma \tag{4.4}$$

$$\dot{\theta} = q \tag{4.5}$$

$$\ddot{\eta}_i = -2\zeta\omega_i\dot{\eta}_i - \omega_i^2\eta_i + N_i \qquad i = 1,2,3 \tag{4.6}$$

$$\alpha \triangleq \theta - \gamma \tag{4.7}$$

$$g = g_0\left[\frac{R_E}{R_E + h}\right]^2 \tag{4.8}$$

where L denotes lift, T denotes engine thrust, D denotes drag, $\mathcal{M}$ is the pitching moment, N_i denotes generalized forces, ζ demotes flexible mode damping factor, ω_i denotes flexible mode undamped natural frequencies, m denotes mass, I_{yy} is the pitch moment of inertia, g is the acceleration due to gravity.

- *States.* Vehicle states include: velocity v, FPA γ, altitude h, pitch rate q, pitch angle θ, and the flexible body states $\eta_1, \dot{\eta_1}, \eta_2, \dot{\eta_2}, \eta_3, \dot{\eta_3}$. These eleven (11) states are summarized in Table 4.1.

♯	Symbol	Description	Units
1	v	speed	kft/sec
2	γ	flight path angle	deg
3	θ	pitch angle	deg
4	q	pitch rate	deg/sec
5	h	altitude	ft
6	η_1	1^{st} flex mode	-
7	$\dot{\eta_1}$	1^{st} flex mode rate	-
8	η_2	2^{nd} flex mode	-
9	$\dot{\eta_2}$	2^{nd} flex mode rate	-
10	η_3	3^{rd} flex mode	-
11	$\dot{\eta_3}$	3^{rd} flex mode rate	-

Table 4.1: States for Hypersonic Vehicle Model

- *Controls.* The vehicle has three (3) control inputs: a rearward situated elevator δ_e, a forward situated canard δ_c [1], and stoichiometrically normalized fuel equivalence ratio (FER). These control inputs are summarized in Table 4.2. This report only considers elevator and FER; i.e. the canard has been removed.

In the above model, note that the rigid body motion impacts the flexible dynamics through the generalized forces. As discussed earlier, the flexible dynamics impact the rigid body motion through thrust, lift, drag, and moment. Additional details about the model may be found within the following references [1–9, 36]

♯	Symbol	Description	Units
1	FER	stoichiometrically normalized fuel equivalence ratio	-
2	δ_e	elevator deflection	deg
3	δ_c	canard deflection	deg

Table 4.2: Controls for Hypersonic Vehicle Model

[1] In this report, the canard has been removed. Future work will examine the potential need for canard as well as its viability.

Sum of Forces. The equations for these forces and moments are given by

$$L = F_x \sin(\alpha) - F_z \cos(\alpha) + L_{viscous} \tag{4.9}$$

$$D = -(F_x \cos(\alpha) - F_z \sin(\alpha)) + D_{viscous} \tag{4.10}$$

$$T = \dot{m}_a \cdot (V_e - V_\infty) - (P_1 - P_\infty) \cdot hi \tag{4.11}$$

$$N_i = \int p(x,t)\Phi_i(x)dx + \Sigma_j F_j(t)\Phi_i(x_j) \tag{4.12}$$

The sum of the forces in the x and z directions are given as

$$F_x = F_{x_{forebody}} + F_{x_{aftbody}} + F_{x_{inlet}} + F_{x_{elevator}} + F_{x_{upperbody}} + F_{x_{unsteady}} \tag{4.13}$$

$$F_z = F_{z_{forebody}} + F_{z_{aftbody}} + F_{z_{inlet}} + F_{z_{elevator}} + F_{z_{bottom}} + F_{z_{upperbody}} + F_{z_{unsteady}} \tag{4.14}$$

$$M = M_{forebody} + M_{aftbody} + M_{inlet} + M_{elevator} + (L_1 \tan(\tau_{1l}) + \frac{hi}{2} - cg_z) \cdot T + M_{upperbody} + M_{bottom} + M_c + M_{unsteady} + M_{viscous} \tag{4.15}$$

(4.16)

Inviscid Flow Model. A oblique shock will occur provided that the flow deflection angle δ_s is positive; i.e.

$$\delta_s \triangleq \text{AOA} + \text{flexing angle} + \tau > 0^\circ \tag{4.17}$$

where τ is the geometric angle of the surface with respect to the body axis. (see Figure 4.2). If $\delta_s < 0$, a Prandtl-Meyer expansion will occur.

Properties Across Oblique Shock. Let (M_1, T_1, p_1) denote the up-stream Mach, temperature, and pressure. Let $\gamma \triangleq \frac{c_p}{c_v} = 1.4$ denote the specific heat ratio for air - assumed constant in the model; i.e. air is calorically perfect [23]. The shock wave angle $\theta_s = \theta_s(M_1, \delta_s, \gamma)$ can be found as the middle root (weak shock solution) of the following shock angle polynomial [38, 88]:

$$sin^6\theta_s + bsin^4\theta_s + csin^2\theta_s + d = 0 \tag{4.18}$$

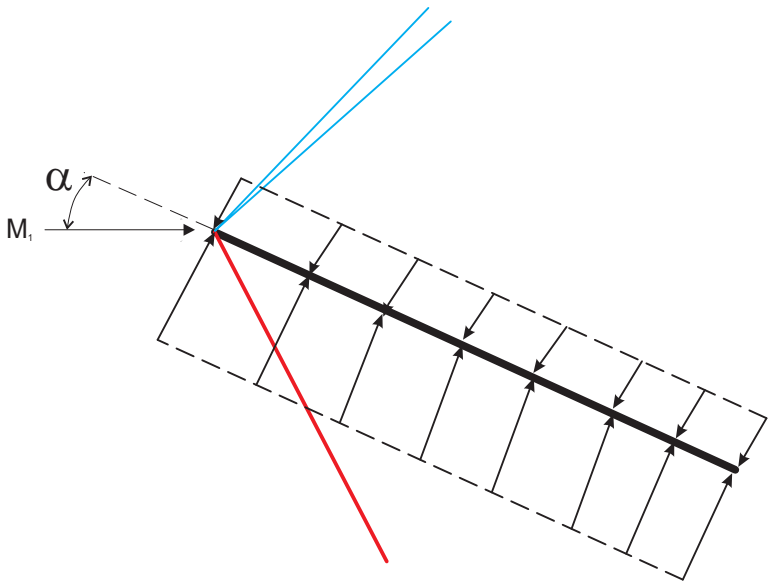

where

$$b = -\frac{M_1^2+2}{M_1^2} - \gamma sin^2\delta_s \tag{4.19}$$

$$c = \frac{2M_1^2+1}{M_1^4} + \left[\frac{(\gamma+1)^2}{4} + \frac{\gamma-1}{M_1^2}\right] sin^2\delta_s \tag{4.20}$$

$$d = -\frac{cos^2\delta_s}{M_1^4} \tag{4.21}$$

The above can be addressed by solving the associated cubic in $sin^2\theta_s$. A direct solution is possible if Emanuel's 2001 method is used [88, page 143]. After determining the shock wave angle θ_s, one can determine properties across the bow shock using classic relations from compressible flow [88, page 135]; i.e. M_s, T_s, p_s - functions of (M_1, δ_s, γ):

$$\frac{T_2}{T_1} = \frac{(2\gamma M_1^2 \sin^2\theta_s + 1 - \gamma)((\gamma-1)M_1^2\sin^2\theta_s + 2)}{(\gamma+1)^2 M_1^2 \sin^2\theta_s} \tag{4.22}$$

$$\frac{p_2}{p_1} = 1 + \frac{2\gamma}{\gamma+1}\left(M_1^2\sin^2\theta_s - 1\right) \tag{4.23}$$

$$M_2^2 sin^2(\theta_s - \delta_s) = \frac{M_1^2\sin^2\theta_s(\gamma-1)+2}{2\gamma M_1^2\sin^2\theta_s - (\gamma-1)} \tag{4.24}$$

It should be noted that for large M_1, the computed temperature T_2 across the shock will be larger than it should be because of the assumption that air is calorically perfect (i.e. constant specific heats) does not capture other forms of energy absorption; e.g. electronic excitation and chemical reactions [23].

Properties Across Prandtl-Meyer Expansion. Let (M_1, T_1, p_1) denote the up-stream Mach, temperature, and pressure. Let $\gamma \triangleq \frac{c_p}{c_v} = 1.4$ denote the specific heat ratio for air - assumed constant in

the model; i.e. air is calorically perfect The Mach number after an expansion is given by:

$$\nu(M_2) = \theta_e + \nu(M_1) \tag{4.25}$$

where θ_e is the expansion angle and $\nu(M)$ is given by:

$$\nu(M) = \sqrt{\frac{\gamma+1}{\gamma-1}}\tan^{-1}\sqrt{\frac{\gamma-1}{\gamma+1}(M^2-1)} - \tan^{-1}\sqrt{M^2-1} \tag{4.26}$$

and $\nu(M_2)$ is typically solved iteratively to the desired precision. The downstream temperature and pressure are given by:

$$T_2 = \frac{1+\frac{\gamma-1}{2}M_1^2}{1+\frac{\gamma-1}{2}M_2^2}T_1 \tag{4.27}$$

$$p_2 = \left[\frac{1+\frac{\gamma-1}{2}M_2^2}{1+\frac{\gamma-1}{2}M_1^2}\right]^{\frac{\gamma-1}{\gamma}} p_1 \tag{4.28}$$

Viscous Flow. The Viscous effects add a substantial amount of drag to the vehicle through the skin friction of the fluid moving around the vehicle. In this model Eckert's Reference Temperature Method is used to compute the viscous skin friction assuming a wall temperature of $2500\,^\circ R$.

$$T^* = T_e\left[1 + M_e^2 + 0.58\left(\frac{T_w}{T_e} - 1\right)\right] \tag{4.29}$$

$$\rho^* = \frac{p}{RT^*} \tag{4.30}$$

where p is the static pressure of the fluid. The viscosity at the reference temperature μ^* can then be computed using Sutherland's Forumula, which is known to be valid up to $3500\,^\circ R$.

$$\mu^* = 2.27 * 10^{-8}\frac{(T^*)^{3/2}}{T^* + 198.6} \tag{4.31}$$

$$Re^* = \frac{\rho^* V L}{\mu^*} \tag{4.32}$$

Once the Reynolds number is calculated at the reference temperature the skin friction coefficient for turbulent, supersonic flow over a flat plate can be computed.

$$c_f = \frac{0.0592}{(Re^*)^{1/5}} \tag{4.33}$$

now the shear stress at the wall τ_w can be computed by the following equation:

$$\tau_w = c_f((1/2)\rho_\infty V_\infty^2) \tag{4.34}$$

Unsteady Flow. Linear piston theory is utilized in order to integrate unsteady pressure distributions on the vehicle. This unsteady pressure distribution is a direct result of the interactions between the flow and the structure as well as the unsteady, rigid body motion of the vehicle. When the air flow is supersonic, the pressure acting on the face of a piston moving in a perfect gas is given by:

$$\frac{P}{P_i} = \left(1 + \frac{V_{n,i}}{5a_i}\right)^7 \tag{4.35}$$

where P_i is the local static pressure behind the bow shock, P is the pressure on the piston face, $V_{n,i}$ is the velocity of the surface normal to the flow, and a_i is the local speed of sound. By taking the first order binomial expansion of equation 4.35 we get the following:

$$\frac{P}{P_i} = 1 + \frac{7V_{n,i}}{5a_i} \tag{4.36}$$

$$P = P_i + \rho_i a_i V_{n,i} \tag{4.37}$$

The infitesimal force acting on the face of the piston is given as:

$$d\mathbf{F}_i = (PdA)\,\mathbf{n}_i \tag{4.38}$$

which becomes:

$$d\mathbf{F}_i = \left[-\left(P_i + \rho_i a_i V_{n,i}\right) dA\right] \mathbf{n}_i \tag{4.39}$$

Scramjet Model. The scramjet engine model is that used in [38, 87]. It consists of an inlet, an isentropic diffuser, a 1D Rayleigh flow combustor (frictionless duct with heat addition [88]), and an isentropic internal nozzle. A single (long) forebody compression ramp provides conditions to the rear-shifted scramjet inlet. Although the model supports a variable geometry inlet, it has not exploited in this work; i.e. diffuser area ratio $A_d = \frac{A_2}{A_1}$ will be fixed with $A_d = 1$, see Figure 4.2).

Translating Cowl Door. The model assumes the presence of an (infinitely fast) translating cowl door which uses AOA to achieve shock-on-lip conditions (assuming no forebody flexing). Forebody flexing, however, results in an oscillatory bow shock and air mass flow spillage [38]. A bow shock reflection (off of the cowl or inside the inlet) further slows down the flow and steers it into the engine. Shock-shock interactions are not modeled.

Inlet Properties. The bow reflection turns the flow parallel into the scramjet engine. The oblique shock relations are implemented again, using M_s as the free-stream input, $\delta_1 = \tau_{1l}$ as the flow deflection angle to obtain the shock angle $\theta_1 = \theta_1(M_s, \delta_1, \gamma)$ and the inlet (or diffuser entrance)

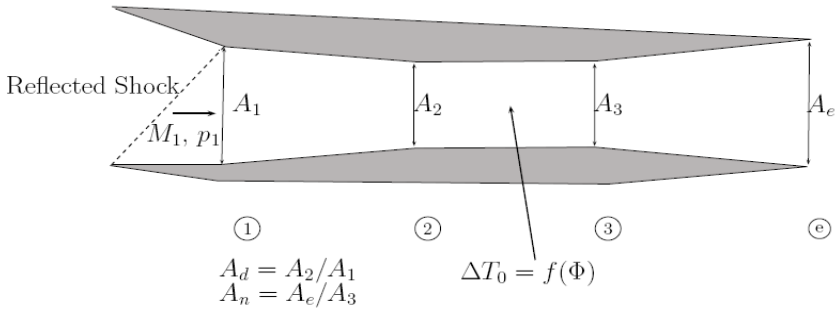

Figure 4.2: Schematic of Scramjet Engine

properties: M_1 , T_1 , p_1 - functions of (M_s , θ_1, γ).

Diffuser Exit-Combustor Entrance Properties. The diffuser is assumed to be isentropic. The combustor entrance properties are therefore found using the formulae in [38], [88, pp. 103-104] - $M_2 = M_2(M_1, A_d, \gamma)$, $T_2 = T_2(M_1, M_2, \gamma)$, $p_2 = p_2(M_1, M_2, \gamma)$:

$$\frac{\left[1+\frac{\gamma-1}{2}M_2^2\right]^{\frac{\gamma+1}{\gamma-1}}}{M_2^2} = A_d^2\,\frac{\left[1+\frac{\gamma-1}{2}M_1^2\right]^{\frac{\gamma+1}{\gamma-1}}}{M_1^2} \tag{4.40}$$

$$T_2 = T_1\left[\frac{1+\frac{1}{2}(\gamma-1)M_1^2}{1+\frac{1}{2}(\gamma-1)M_2^2}\right] \tag{4.41}$$

$$p_2 = p_1\left[\frac{1+\frac{1}{2}(\gamma-1)M_1^2}{1+\frac{1}{2}(\gamma-1)M_2^2}\right]^{\frac{\gamma}{\gamma-1}} \tag{4.42}$$

where $A_d \triangleq \frac{A_2}{A_1}$ is the diffuser area ratio. Also, one can determine the total temperature $T_{t_2} = T_{t_2}(T_2, M_2, \gamma)$ at the combustor entrance can be found using [88, page 80]:

$$T_{t2} = \left[1+\frac{\gamma-1}{2}M_2^2\right]T_2. \tag{4.43}$$

Since $A_d = 1$ in the model, it follows that $M_2 = M_1$, $T_2 = T_1$, $p_2 = p_1$, and $T_{t2} = \left[1+\frac{\gamma-1}{2}M_1^2\right]T_1 = T_{t_1}$.

Fuel Equivalence Ratio. The model uses liquid hydrogen (LH2) as the fuel. If f denotes fuel-to-air ratio and f_{st} denotes stoichiometric fuel-to-air ratio, then the stoichiometrically normalized fuel equivalency ratio is given by [21], [38]:

$$FER = \frac{f}{f_{st}} = \frac{\dot{m}_{H2}}{\dot{m}_{air}}\frac{1}{f_{st}} \tag{4.44}$$

. FER is the engine control. While FER is primarily associated with the vehicle velocity, its impact on FPA is significant (since engine is situated below vehicle cg). This coupling will receive further

examination in what follows.

Combustor Exit Properties. The model as a constant area combustor where the combustion process is captured via heat addition. To determine the combustor exit properties, one first determines the change in total temperature across the combustor [38]:

$$\Delta T_c = \Delta T_c(T_{t_2}, FER, H_f, \eta_c, c_p, f_{st}) = \left[\frac{f_{st}FER}{1+f_{st}FER}\right]\left(\frac{H_f\eta_c}{c_p} - T_{t_2}\right) \tag{4.45}$$

where $H_f = 51,500$ BTU/lbm is the heat of reaction for liquid hydrogen (LH2), $\eta_c = 0.9$ is the combustion efficiency, $c_p = 0.24\ BTU/lbm^\circ R$ is the specific heat of air at constant pressure, and $f_{st} = 0.0291$ is the stoichiometric fuel-to-air ratio for LH2 [21]. Given the above, the Mach M_3, temperature T_3, and pressure p_3 at the combustor exit are determined by the following classic 1D Rayleigh flow relationships [38], [88, pp. 103-104]:

$$\frac{M_3^2\left[1+\frac{1}{2}(\gamma-1)M_3^2\right]}{(\gamma M_3^2+1)^2} = \frac{M_2^2\left[1+\frac{1}{2}(\gamma-1)M_2^2\right]}{(\gamma M_2^2+1)^2} + \left[\frac{M_2^2}{(\gamma M_2^2+1)^2}\right]\frac{\Delta T_c}{T_2} \tag{4.46}$$

$$T_3 = T_2\left[\frac{1+\gamma M_2^2}{1+\gamma M_3^2}\right]^2\left(\frac{M_3}{M_2}\right)^2 \qquad p_3 = p_2\left[\frac{1+\gamma M_2^2}{1+\gamma M_3^2}\right] \tag{4.47}$$

Given the above, one can then try to solve equation (4.46) for $M_3 = M_3\left(M_2, \frac{\Delta T_c}{T_{2,}}, \gamma\right)$. This will have a solution provided that M_2 is not too small, ΔT_c is not too large (i.e. FER is not too large or T_2 is not too small. See discussion below.

Thermal Choking FER ($M_3 = 1$). Once the change in total temperature:

$$\Delta T_c = \Delta T_c(T_{t_2}, FER, H_f, \eta_c, c_p, f_{st}) \tag{4.48}$$

across the combustor has been computed, it can be substituted into equation (4.46) and one can "try" to solve for M_3. Since the left hand side of equation (4.46) lies between 0 (for $M_3 = 0$) and 0.2083 (for $M_3 = 1$), it follows that if the right hand side of equation (4.46) is above 0.2083 then no solution for M_3 exists. Since the first term on the right hand side of equation (4.46) also lies between 0 and 0.2083, it follows that this occurs when ΔT_c is too large; i.e. too much heat is added into the combustor or too high an FER. In short, a solution M_3 will exist provided that FER is not too large, T_2 is not too small (i.e. altitude not too high), and the combustor entrance Mach M_2 is not too small (i.e. FTA not too large). When $M_3 = 1$, a condition referred to as *thermal choking* [21, 88] is said to exist. The FER that produces this will be referred to as the *thermal choking FER* - denoted FER_{TC}. In general, FER_{TC} will be a function of the following: M_∞, T_∞, and FTA.

Physically, the addition of heat to a supersonic flow causes it to slow down. If the thermal choking FER (FER_{TC}) is applied, then $M_3 = 1$ (i.e. sonic combustor exit). When thermal choking occurs, it is not possible to increase the air mass flow through the engine. Propulsion engineers want to operate near thermal choking for engine efficiency reasons [21]. However, if additional heat is added, the upstream conditions can be altered and it is possible that this may lead to engine unstart. This is highly undesirable. For this reason, operating near thermal choking has been described by some propulsion engineers as "operating near the edge of a cliff." In general, thermal choking will occur if FER is too high, M_∞ is too low, altitude is too high (T_∞ too low), FTA is too high.

Internal Nozzle. The exit properties $M_e = M_e(M_3, A_n, \gamma)$, $T_e = T_e(M_3, M_e, \gamma)$, and $p_e = p_e(M_3, M_e, \gamma)$ of the scramjet's isentropic internal nozzle are founds as follows:

$$\frac{\left[1 + \frac{\gamma-1}{2} M_e^2\right]^{\frac{\gamma+1}{\gamma-1}}}{M_e^2} = A_n^2 \, \frac{\left[1 + \frac{\gamma-1}{2} M_3^2\right]^{\frac{\gamma+1}{\gamma-1}}}{M_3^2} \tag{4.49}$$

$$T_e = T_3 \left[\frac{1 + \frac{1}{2}(\gamma-1)M_3^2}{1 + \frac{1}{2}(\gamma-1)M_e^2}\right] \qquad p_e = p_3 \left[\frac{1 + \frac{1}{2}(\gamma-1)M_3^2}{1 + \frac{1}{2}(\gamma-1)M_e^2}\right]^{\frac{\gamma}{\gamma-1}} \tag{4.50}$$

where $A_n = \frac{A_e}{A_3}$ is the internal nozzle area ratio (see Figure 4.2). $A_n = 6.35$ is used in the model.

Thrust. The internal thrust produced by the scramjet is given by

$$T = \dot{m}_a \cdot (V_e - V_\infty) - (P_1 - P_\infty) \cdot hi \tag{4.51}$$

(4.52)

where $\dot{m}_a$ is the air mass flow through the engine, v_e is the exit flow velocity, v_∞ is the free-stream flow velocity. p_e is the pressure at the engine exit plane, A_1 is the engine inlet area, A_e is the engine exit area, $v_e = M_e sos_e$, $v_\infty = M_\infty sos_\infty$, $sos_e = \sqrt{\gamma R T_e}$, $sos_\infty = \sqrt{\gamma R T_\infty}$, and R is the gas constant for air. If the bow shock angle $\theta_s \neq 0$, then

$$\dot{m}_a = p_\infty M_\infty \sqrt{\frac{\gamma}{R T_\infty}} \, h_i \cos\tau_{1_l} \left[\frac{\sin\theta_s}{\sin(\theta_s - AOA - \tau_{1_l})}\right]. \tag{4.53}$$

If $\theta_s = 0$, then $AOA = -\tau_{1l}$ and the above yields

$$\dot{m}_a = p_\infty M_\infty \sqrt{\frac{\gamma}{R T_\infty}} \, h_i \cos\tau_{1_l} \tag{4.54}$$

where h_i is the height of the engine.

Backpressure. Calculating the backpressure (or aftbody pressure) is an open problem within the aerospace community. To reduce the computation complexity of the plume calculation, the authors of [87] made the following assumptions:

1. The pressure at the aft most tip of the vehicle will be equal to the freestream pressure (p_∞)
2. The aftbody pressure decreases along its length in an exponential fashion.
3. The aftbody pressure does not change with respect to change in angle of attack.

Based on these three assumptions, the following equation is used to calculate the pressure along the aftbody of the vehicle:

$$P_a(x) \approx \frac{P_e}{1 + \left(\frac{x}{L_2}\right)\left(\frac{P_e}{P_\infty} - 1\right)} \tag{4.55}$$

where

- P_a - Aftbody pressure
- x - Location along the aftbody where pressure is computed ($x \in 0, L_2$)
- P_∞ - Free stream pressure
- P_e - Pressure at the internal nozzle exit
- L_2 - Length of the aftbody.

One benefit to equation 4.55 is that it can be quickly computed and does not require discretization of the aftbody into segments. It must be noted, however, that the assumptions it is based on are not true in general. Additionally, we have the pressure at the end of the aftbody must equal the freestream pressure (from equation (4.55)) i.e. it is assumed that the external nozzle suffers from neither under-expanded nor over-expanded.

4.3 Unmodeled Phenomena/Effects.

All models possess limitations. They can either be fundamental libations related to the choice of modeling methodology, or implementation limitation related to the way the modeling methodology

is applied. Realizing limitations is crucial in order to avoid model misuse. Given this, a (somewhat lengthy) list of both fundamental phenomena/effects that are not captured within the model and implementation limitations has been provided.

Fundamental Limitations. Fundamental limitations result from a particular modeling method's inability to accurately capture physical effects that occur in real world situations. Sometimes these limitations are by choice, e.g. choosing an engineering methods vs computational fluid dynamics to reduce computational complexity, and sometimes they result from simplifications being made to describe a phenomena, e.g. turbulence. All modeling methods should be thought of as an approximation to the real world, and therefore are inherently uncertain. Gaining an understanding the associated magnitude of these uncertainties is key to control-relevant vehicle design. Below is a partial list of the fundamental limitations associated with the model.

- *Dynamics.* The above model does not capture longitudinal-lateral coupling and dynamics [112] and the associated 6 DOF effects.

- *Aerodynamics.* Aerodynamic phenomena/effects not captured in the model include the following: boundary layer growth, displacement thickness, viscous interaction, entropy and vorticity effects, laminar versus turbulent flow, flow separation, high temperature and real gas effects (e.g. caloric imperfection, electronic excitation, thermal imperfection, chemical reactions such as 0_2 dissociation) [23], non-standard atmosphere (e.g. troposphere, stratosphere), unsteady atmospheric effects [22], 3D effects, aerodynamic load limits.

- *Propulsion.* Propulsion phenomena/effects not captured in the model include the following: cowl door dynamics, multiple forebody compression ramps (e.g. three on X-43A [113, 114]), forebody boundary layer transition and turbulent flow to inlet [113, 114], diffuser losses, shock interactions, internal shock effects, diffuser-combustor interactions, fuel injection and mixing, flame holding, engine ignition via pyrophoric silane [19] (requires finite-rate chemistry; cannot be predicted via equilibrium methods [100], finite-rate chemistry and the associated thrust-AOA-Mach-FER sensitivity effects [115], internal and external nozzle losses, thermal choking induced phenomena (2D and 3D) and unstart, exhaust plume characteristics, cowl door dynamics, combined cycle issues [21].

  Within [115], a higher fidelity propulsion model is presented which addresses internal shock effects, diffuser-combustor interaction, finite-rate chemistry and the associated thrust-AOA-Mach-FER sensitivity effects. While the nominal Rayleigh-based model (considered here)

exhibits increasing thrust-AOA sensitivity with increasing AOA, the more complex model in [115] exhibits reduced thrust-AOA sensitivity with increasing AOA - a behavior attributed to finite-chemistry effects.

- *Structures.* Structural phenomena/effects not captured in the model include the following: out of plane and torsional effects, internal structural layout, unsteady thermo-elastic heating effects, aerodynamic heating due to shock impingement, distinct material properties [60], and aero-servo-elasticity [116, 117].

It should be emphasized that the above list is only a partial list. If one needs fidelity at high Mach numbers, then many other phenomena become important; e.g. N_2 dissociation [23]. Finally, it should be noted that Bolender and Doman have addressed various effects in their publications. For example, within [5, 9] the authors address the impact of heating on structural mode frequencies and mode shapes. Within [5], the authors consider a sustained two hour straight and level cruise at Mach 8, 85 kft with a constant $15 \frac{BTU}{ft^2 sec}$ heat rate. It is assumed that no fuel is consumed (to focus on impact of heat addition) and that the titanium beam is insulated from the cryogenic fuel. The paper assumes the presence of a thermal protection system consisting of a PM2000 honeycomb outer skin followed by a layer of silicon dioxide insulation. It was concluded that structural frequencies did not change appreciably ($< 1\%$) as a result of the accompanying $200\,^\circ R$ temperature increase in the titanium beam (initially at $559.67^\circ R = 100^\circ F$).

Implementation Limitations. Implementation limitations exist due the way that the modeling tool has been coded software. This is not to be confused with implementation issues that exist when trying to implement a control law within a hardware loop. Rather, this refers to the limitations resulting from the fact that no piece of modeling software is 100 % modular and extensible to all situations. Below is a partial listing of some of the implementation issues associated with the model:

- *Engine Control* Fuel equivalence ratio is utilized within the model for engine control. This is an unrealistic scenario because as is seen from equation due to the fact that $\dot{m}_{air}$ is an unknown or estimated quantity at any given point in time.

- *Elevator.* The elevator within this model is implemented as an all moveable wing surface. This was likely due to the fact that the X-43 utilized this type of elevator surface. However, for large vehicles, this implementation is not practical. The elevator surface will likely be

Figure 4.3: F-18 Breaking Sound Barrier, Courtesy of NASA.gov

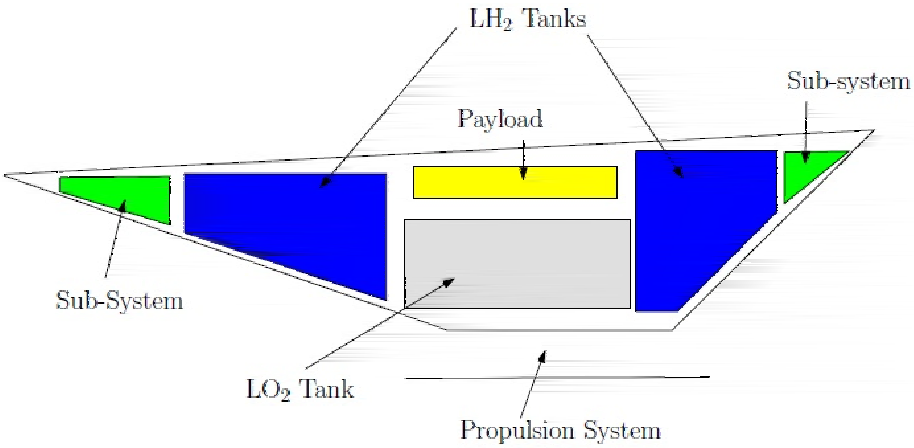

Figure 4.4: HSV Model: Internal Layout, courtesy of Williams et. al.

mounted a the rearward end of a fixed wing, similar to most conventional aircraft as well as the space shuttle. In addition, the freestream flow has been chosen as the upstream flow seen by the elevator. For a actual vehicle, an conical like shock system will form around the front nose of the vehicle, and extend reward. A similar concept is shown in Figure 4.3 , where a plane is shown as it breaks the sound barrier.

- *Fixed Internal Layout.* Within [9] the authors described the internal layout for the model as shown in Figure 4.4. Each component of the internal layout is given a fixed mass and size. The components are utilized to determine the horizontal CG location. The vertical CG location is fixed to be in line with the nose. The component masses and locations are fixed, and do not scale with changing vehicle size and shape.

- *Linear Mass Depletion.* The model is capable of allowing for a linear fuel mass depletion over

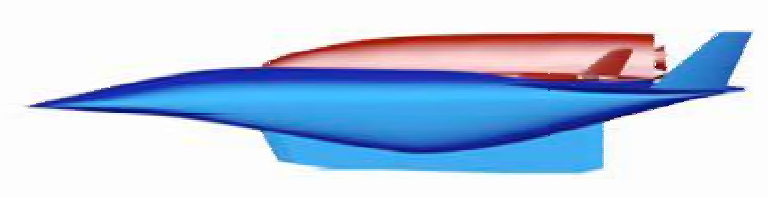

Figure 4.5: NASA Reference Vehicle Booster (Bottom) and Orbiter (Top), courtesy of Dr. Jeff Robinson

a fixed duration of time. This is unrealistic as the fuel mass being consumed is a function of flight condition, throttle setting, and fuel efficiency.

- *Flexible Coupling.* The flexible dynamics are coupled into the rigid body by adding the angular deflection to three different point on the vehicle (1) the nose of the vehicle utilizing the angular deflection at the nose (2) the canard deflection utilizing the angular defection at the nose, (3) the elevator deflection utilizing the angular deflection at the most rearward point. Both cases 2 and 3 will be increasingly inaccurate if the control surfaces are moved towards the center of the vehicle. In addition, the engine engine layout is unaffected by the flexing of the vehicle.

- *Instantaneous Cowl Door Translation.* The inlet dynamics are coded in a way to assume a shock on lip condition (modulo flexible effects) for all flight conditions. This essentially assumes that there is a cowl door capable of infinitely fast horizontal translation. This is not a feasible physical implementation, and as a result the model will over-predict the mass flow entering the engine.

- *Fixed Physical Constants.* The model assumes a constant specific heat ratio $\gamma = 1.4$ and a constant wall temperature $T_w = 2500R$ across the vehicle.

4.4 Modeling Modifications.

In order to more accurately model the NASA reference booster vehicle shown in Figures 1.1 & 4.5, numerous changes needed to be made to the existing model. These changes were necessary to address some of the fundamental and implementation limitations described within Section 4.3. Below is an in-depth description of the modifications made to the model.

Outer Mold Line. Figure 4.6 show the dimensions of the outer mold line for the original HSV model. The outer model line is completely defined by the 5 vertices listed in the figures, with vertex 0 being fixed as the origin, and vertex 5 is the location of the elevator hinge. An additional vertex

point would be necessary if the canard was included on the vehicle. All vertices have 2 degrees of freedom (X & Z) except for 0 which is completely fixed, 3 which is fixed in the X-direction, and 4 which is fixed in the Z-direction. This gives a total of 8 degrees of freedom when designing the outer mold line of the vehicle. This was generally felt to be inadequate in terms of modeling the NASA reference booster vehicle shown in Figure 4.5.

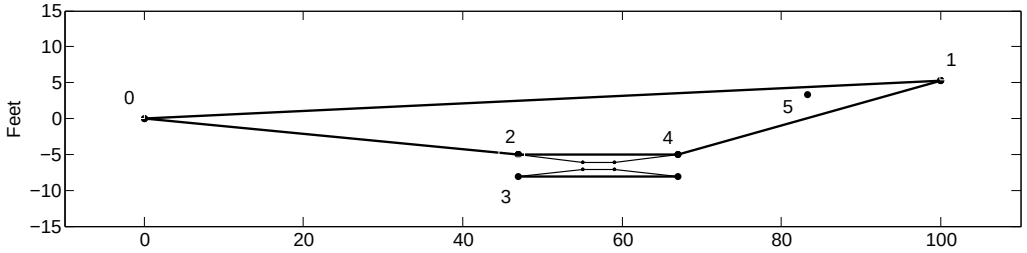

Figure 4.6: Original HSV Outer Mold Line

Figure 4.7 shows the modeling modification made to the outer mold geometry. The geometry is now defined completely defined by 9 vertices, of which only 5 and 6 are fixed in the x-direction. This gives a total of 16 degrees of freedom, which allows for a much closer approximation to the booster vehicle. Vertices 8 and 9 define a wing surface and it is assumed the elevon hinge is located at vertex 9 (further discussed below).

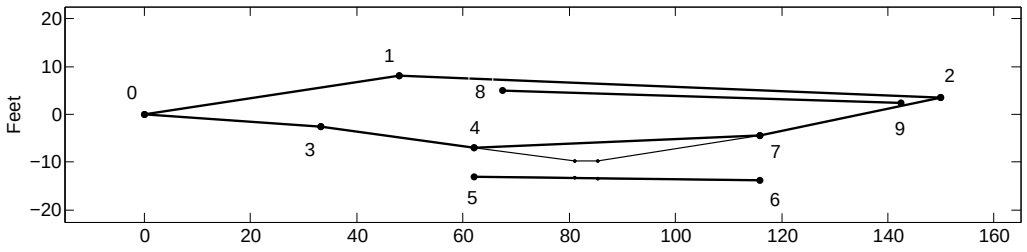

Figure 4.7: Modified HSV Outer Mold Line

Wing-Elevon Surface. The original model contained an elevator surface implemented as an all moveable flat plat. The design variables associated with it were the mounting location $[x_e,\ z_e]$ and the length L_e. The code has been modifed to allow a nonsymmetric wedge shaped wing with a rearward mounted elevator. The associated design variables are location of the hinge $[x_h,\ z_h]$, elevator length L_e, wing length L_w, wing mounting angle θ_w, and the wing wedge angles τ_{wu} & τ_{wl}.

Wing-Elevon Upstream Flow. The original model utilizes the free stream flow as the upstream

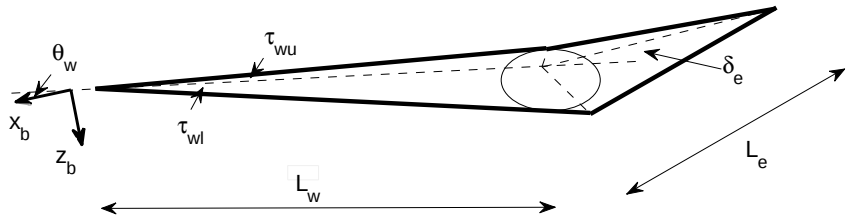

Figure 4.8: Modified Wing-Elevon Surface

conditions that process the flow over the elevator surface. This is unrealistic due to the 3-dimensional nature of the shock wave created in front of the vehicle. While there are 3-dimension methods for calculating the flow over conic shape, only CFD methods can give accurate results for nonuniform shapes. In order to approximate the flow, the following method is proposed:

1. An arbitrary oblique shock wave is created utilizing a wedge angle τ_s, see top down vehicle view in Figure 4.9

2. The shock wave processes the free stream condition $M_\infty,\ T_\infty,\ p_\infty$ to create $M_s,\ T_s,\ p_s$.

3. $M_s,\ T_s,\ p_s$ are used as the upstream condition for the flow processed on the upper and lower wing surfaces. The flow vector is assumed to have the same X,Z directional components as the free-stream flow, e.g. only the Y direction was processed by the θ_s shock wave.

4. τ_s can be varied to create uncertainty bounds for the wing-elevon pressures. One might vary the angle between zero degrees and the actual nose spatulation angle of the vehicle.

Engine Parameters and Base. The original model assumed that the base of the engine was flat and parallel to the body x-axis (as seen in Figure 4.6.) However, this limits the diffuser area ratio and internal nozzle ratio to an inverse relations:

$$A_d = \frac{1}{A_n} \tag{4.56}$$

This relationship was not strictly enforced within the model and numerous papers appeared in the literature with $A_d = 1$ and $A_n = 6.35$, [3], [5],[38], [37], [11] resulting in a geometrically inconsistent set of parameters. The additional degrees of freedom enable by the mold line changes no

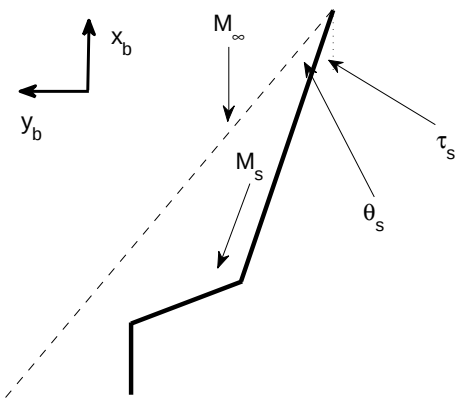

Figure 4.9: Wing-Elevon Flow Diagram

longer force this inverse relationship. The model now checks for geometric consistency between the engine base, inlet height, exhaust height, diffuser area ratio and internal nozzle ratio. Since the engine base no longer needs to be parallel to the body x-axis, the internal thrust is vectored along a line the bisects the inlet and exhaust heights, as seen in Figure

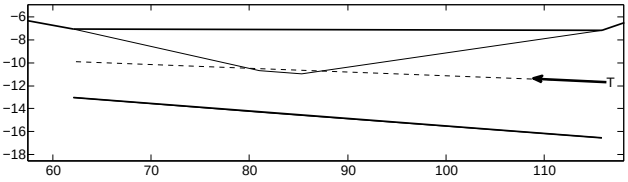

Figure 4.10: Internal Thrust Vectoring

Plume Modeling The original back pressure calculation was given by:

$$P_a(x) \approx \frac{P_e}{1 + \left(\frac{x}{L_2}\right)\left(\frac{P_e}{P_\infty} - 1\right)} \tag{4.57}$$

assuming the following three items:

1. The pressure at the aft most tip of the vehicle will be equal to the freestream pressure (p_∞)
2. The aftbody pressure decreases along its length in an exponential fashion.
3. The aftbody pressure does not change with respect to change in angle of attack.

Item number 1 need not be true, but is generally a good approximation to the real world. Item number 2 holds true, but item number 3 is not true, as is shown in Figure 4.11.

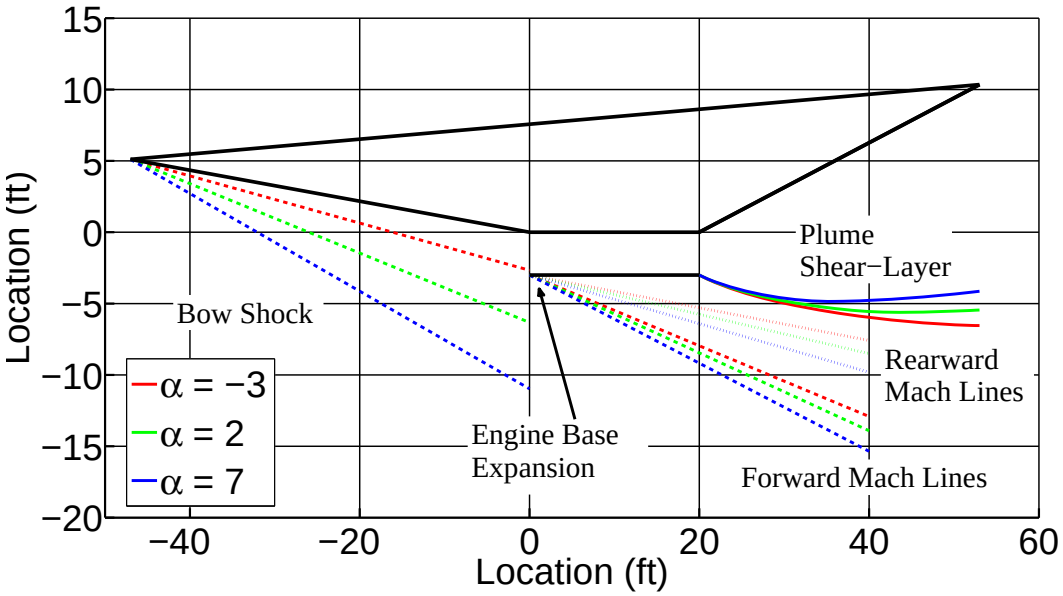

Figure 4.11: Plume Shape w.r.t. AOA

Within [118] the authors propose a numerical scheme for calculating the back pressure. The aftbody and shear-layer are discretized into N segment. The flow within each section (bounded by the aftbody and the 'linearized' segment of the shear layer) is modeled as an isentropic nozzle (Figure 4.12 illustrates one such segment).

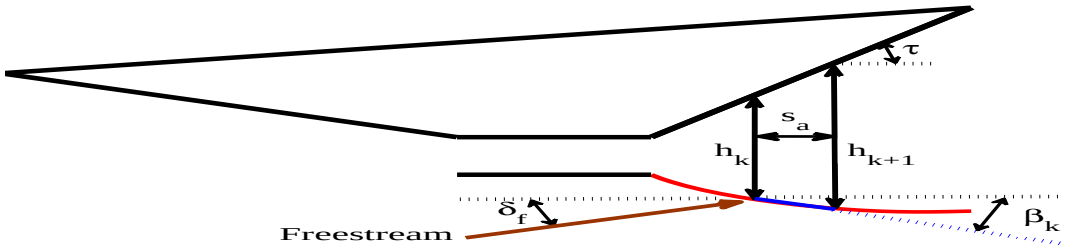

Figure 4.12: Segmentation of plume

The pressure in segment k ($k \in [0, \mathrm{N}]$) is obtained by solving the following equations numerically [118]:

$$h_{k+1} = h_k + s_a \tan(\tau) + s_a \tan(\beta_k) \tag{4.58a}$$

$$A_k = \frac{h_{k+1}}{h_k} \tag{4.58b}$$

$$f(M_k) = 1 + \frac{1}{2}(\gamma - 1) M_k^2 \tag{4.58c}$$

$$\frac{f(M_k)^{\frac{\gamma+1}{\gamma-1}}}{M_k^2} = A_k^2 \frac{f(M_{k-1})^{\frac{\gamma+1}{\gamma-1}}}{M_{k-1}^2} \tag{4.58d}$$

$$P_k = P_{k-1}\left[\frac{f(M_{k-1})}{f(M_k)}\right]^{\frac{\gamma}{\gamma-1}} \tag{4.58e}$$

$$\overline{P_k} = \overline{\rho_e}\overline{V_e}^2 \sin^2(\beta_k - \delta_f) + \overline{P_e} \tag{4.58f}$$

subject to the following constraints:

$$0 \leq \beta_k < \frac{\pi}{2} \tag{4.59}$$

where

- A_k - Nozzle area ratio of segment k of aftbody
- M_k - Nozzle Mach at segment k of aftbody
- P_k - Nozzle pressure in segment k of the aftbody
- $\overline{M_k}$ - External stream Mach at segment k of aftbody
- $\overline{P_k}$ - External stream pressure in segment k of the aftbody
- $\overline{P_e}$ - Pressure of stream under the shear layer
- $\overline{\rho_e}$ - Density of stream under the shear layer
- $\overline{V_e}$ - Velocity of stream under the shear layer
- τ - Inclination of aftbody to the body axis
- β_k - Inclination of kth segment of the shear layer to the body axis
- δ_f - Inclination of external flow to body axis
- γ - Ratio of specific heats (=1.4)
- s_a - Width of each segment of the aftbody
- h_k - Height of segment k of aftbody nozzle
- M_0, P_0 - conditions at internal nozzle exit
- h_0 - exit height of engine

By substituting equation (4.58c) into (4.58d) we obtain the equation relating the Mach in an isentropic nozzle with an area ratio of A_k. Similarly, equation (4.58e) is the equation for the

pressure across an isentropic nozzle. Furthermore, the freestream impacts the shear layer at an angle of β - δ_f, and this is modeled using Newtonian impact theory (i.e. equation (4.58f)).

Equations (4.58a) – (4.58e) provide an iterative procedure to calculating the pressure across the entire plume. Central to this procedure is obtaining β_k such that P_k from equations (4.58e) matches $\overline{P_k}$ from equation (4.58f). The solution for each segment of the aftbody must be found through numeric iteration. Also, each segment must be calculated sequentially (since it depends on the conditions from the segment prior to it), and therefore the algorithm cannot be well parallelized. In practice, bounds on β_k can be used to speed up its estimation (we know that $\{\beta_i, i \in \{0, 1, 2, \ldots, N\}\}$ is a monotonically decreasing sequence), but the computation time is still significant.

It is clear that there exists a solution to system of equations (4.58), (4.59) so long as the pressure within the plume is greater than the pressure of the stream under the shear layer (i.e. the plume is under-expanded). In case this is not true, there does not exist a positive β solution, and equation (4.58f) can no longer be used (however, equations (4.58a) - (4.58e) are still valid as long as $\beta \leq -\tau$). In case the plume is over-expanded, we replace the Newtonian impact equation (4.58f) by a Prandtl-Meyer expansion relation:

$$\nu\left(\overline{M}\right) = \sqrt{\frac{\gamma+1}{\gamma-1}}\arctan\left(\sqrt{\frac{\gamma-1}{\gamma+1}(\overline{M}^2-1)}\right) - \sqrt{\overline{M}^2-1} \tag{4.60a}$$

$$\nu\left(\overline{M_{k+1}}\right) = \nu\left(\overline{M_k}\right) + \delta_{f,k} - \beta_k \tag{4.60b}$$

$$\overline{P_k} = \overline{P_{k-1}}\left[\frac{f(\overline{M_{k-1}})}{f(\overline{M_k})}\right]^{\frac{\gamma}{\gamma-1}} \tag{4.60c}$$

where

- $\overline{P}$, $\overline{M}$ are conditions of external stream
- $\delta_{f,k}$ is external flow orientation to body axis before segment k.

Since an expansion fan turns the flow parallel to the surface, we assume $\delta_{f,k} = \beta_{k-1}$. The initial conditions are approximated using the last segment where the pressure inside the plume is greater than the pressure beneath the shear layer.

As in the over-expanded case, we use an iterative procedure wherein each β_k is calculated such that $\overline{P_k}$ (from equation (4.60c)) equals P_k (from equation (4.58e)).

Figure 4.11 shows the plume shear-layer for several different angles of attack at Mach 8, 85,000 ft. It is important to note that:

- α = 2 represents the trim value for this flight condition
- The plume shear layer will interact with the pressure due to the flow expansion that occurs at the engine base for most flight scenarios. Only for large negative angles of attack will part of the plume shear-layer interact with the free stream flow. This situation would not occur for trimming of the vehicle, or typical control maneuvers.

Due to the computation time required for the previous method (see Table 4.3), an approximation to this method is useful. The approximation method developed by S. Sridharan is in M.S. thesis has been employed within the model. The approximation method outlined below that will attempt to exploit the following from equation (4.58d):

$$\frac{(M_k)^2}{(M_{k-1})^2} \rightarrow 1 \; as \; (A_k)^2 = \frac{(h_{k+1})^2}{(h_k)^2} \rightarrow 1 \tag{4.61}$$

This allows for equation (4.58e) to be approximated as:

$$\hat{P_k} = P_{k-1} A_k^{\frac{-2\gamma}{\gamma+1}} \tag{4.62}$$

$$= P_{k-1} \left[\left(1 + \frac{s_a \tan(\tau)}{h_k} \right) + \frac{s_a}{h_k} \tan(\beta_k) \right]^{\frac{-2\gamma}{\gamma+1}} \tag{4.63}$$

where

- $\hat{P_k}$ is an approximation to P_k of equation (4.58e).

Since s_a in equation (4.58a) is an adjustable parameter that can be made arbitrarily small, and $\beta_k \leq 90°$, A_k (equivalently $\frac{M_k}{M_{k-1}}$) can be made arbitrarily close to 1. However, the number of iterations increases linearly with the decreasing of s_a. Hence there is a computational tradeoff between accuracy and computation time. The error between the approximated pressure ($\hat{P_k}$) and the original pressure (P_k) is calculated by subtraction equation (4.58e) from equation (4.63):

$$|\hat{P_k} - P_k| = \left| P_{k-1} A_k^{\frac{-2\gamma}{\gamma+1}} \right| \left| 1 - \left(\frac{M_k}{M_{k-1}} \right)^{\frac{-2\gamma}{\gamma+1}} \right| \tag{4.64}$$

$$\leq P_{k-1} \left| 1 - \left(\frac{M_k}{M_{k-1}} \right)^{\frac{-2\gamma}{\gamma+1}} \right| \tag{4.65}$$

Equation (4.65) shows us that $|\hat{P}_k - P_k| \to 0$ as $s_a \downarrow 0$. Thus we can achieve accurate approximations to the pressure in equation (4.58e). This approximation is further simplified to improve the computational speed. Consider the following Maclaurin expansion to equation (4.63):

$$\tilde{P}_k = P_{k-1}[\left(\frac{c_1}{c_2}\right)^{\kappa} + \kappa\left(\frac{c_1}{c_2}\right)^{\kappa-1}\Delta_k + \frac{\kappa(\kappa-1)}{2!}\left(\frac{c_1}{c_2}\right)^{\kappa-2}\Delta_k^2 + \ldots \frac{\kappa(\kappa-1)\ldots(\kappa-n-1)}{n!}\left(\frac{c_1}{c_2}\right)^{\kappa-n}\Delta_k^n]c_2^{\kappa} \quad (4.66)$$

where

- $c_1 = \left(1 + \frac{s_a \tan(\tau)}{h_k}\right)$
- $c_2 = \frac{s_a}{h_k}$
- $\kappa = \frac{-2\gamma}{\gamma+1}$
- $\Delta_k = \tan(\beta_k)$

We can calculate the error between this polynomial approximation $\tilde{P}_k$ and the original approximation $\hat{P}_k$ by using the remainder term for a truncated Maclaurin series [119]:

$$|\hat{P}_k - \tilde{P}_k| = P_{k-1}\left|\left[\frac{\kappa(\kappa-1)\ldots(\kappa-n)}{(n+1)!}\left(\frac{c_1}{c_2} + t_k\right)^{\kappa-n-1}\Delta_k^{n+1}\right]c_2^{\kappa}\right| \quad (4.67)$$

where

- t_k is some number between 0 and Δ_k

In order to obtain bounds on the error between the original pressure (P_k, equation (4.58e)) and the pressure from the truncated MacLaurin series ($\tilde{P}_k$, equation (**??**)), we use the triangle inequality to combine equation (4.65) and equation (4.67) as follows:

$$|\tilde{P}_k - P_k| \leq P_{k-1}\left(\left|\left[\frac{\kappa(\kappa-1)\ldots(\kappa-n)}{(n+1)!}\left(\frac{c_1}{c_2} + t_k\right)^{\kappa-n-1}\Delta_k^{n+1}\right]c_2^{\kappa}\right| + \left|1 - \left(\frac{M_k}{M_{k-1}}\right)^{\frac{-2\gamma}{\gamma+1}}\right|\right) \quad (4.68)$$

From equation (4.68) we see that $|\tilde{P}_k - P_k|$ can be made arbitrarily close to zero (irrespective of t_k) by choosing s_a sufficiently small (since $\kappa < 0$, $\frac{c_1}{c_2} \geq 1$, and $c_2 \downarrow 0$ as $s_a \downarrow 0$). Specifically, if the order of the approximation is fixed for all segments of the plume, we observe the following:

- For a fixed order, $|\tilde{P}_k - \hat{P}_k| \downarrow 0$ (exponentially) as $s_a \downarrow 0$.

- For a fixed nozzle area ratio (A_k), $\frac{M_k}{M_{k-1}} \downarrow 1$ as M_{k-1} increases; for a fixed M_{k-1}, $\frac{M_k}{M_{k-1}} \downarrow 1$ as the nozzle area ratio (A_k) decreases.

Hence, when the order of the approximation is fixed, a fixed s_a can be chosen to bound $|\tilde{P}_k - P_k|$ irrespective of k: P_k (M_k) is bounded above (below) by the engine exhaust pressure (Mach), and Δ_k (equivalently A_k) is bounded above by the value of Δ_0 of the first step. A second order approximation was found to be sufficiently accurate.

Moreover, equation (4.58f) can also be expanded as a polynomial in $\tan(\beta_k)$, and we can equate the two polynomials. Since the restriction of the tangent function to the open interval (0, $\frac{\pi}{2}$) is bijective functions from its domain to the positive reals, we can obtain β_k by solving the polynomial expression and choosing the appropriate solution. For the case of an under-expanded plume, a similar polynomial expression for a function of β_k can be easily obtained by using an approximation to the Prandtl-Meyer expansion [120] and equations (4.60).

The objective of the method is find β_k s.t. $\hat{P}_k$ from equations (**??**) matches $\overline{P_k}$ from equation (4.58f) (or the equivalent under-expanded approximation, assuming the base pressure for P_e). While this method still require's an iterative solution to discretized of the aftbody segments, β_k is can now be written in as a polynomial equation (through a Maclaurin expansion) as opposed to a general nonlinear equation. This will result in a significant computation speedup as shown in Table 4.3. Using a lookup table for calculating the polynomial roots can result in further savings to the computation time.

Computation Times. Table 4.3 shows the computation time necessary to make a single call to the model and the time to calculate the trim inputs/states at a single flight condition. The simple approximation is approximately two order of magnitude faster than the numerical discretization. the high fidelity approximation is one order of magnitude faster than the numerical discretization.

Method	Computation Time (Single point)	Computation Time (Trim)
Numerical Discretization	1.4 s	510.3 s
Simple Approximation	0.010 s	3.4 s
High Fidelity Approximation	0.17 s	65.1 s

Table 4.3: Computational Time for Each Method on 2.66 GHz Processor

Computational Fluid Dynamics. With the assistance of Dr. Jorge Bardina at NASA Ames Re-

search Center, CFD work has begun to compare the previous methodologies to a “truth model" (the most high fidelity model available). The NASA developed OVERFLOW code is being used to obtain a pressure profile across the entire vehicle. The initial grid used to calculate the flow can be seen in Figure 4.13.

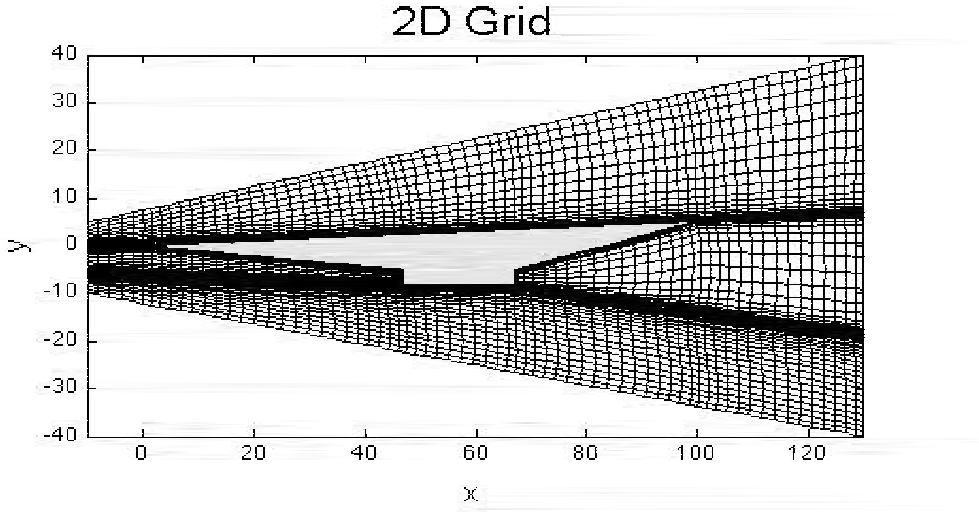

Figure 4.13: OVERFLOW CFD Grid

Pressure contours can be seen in Figures 4.14 & 4.15.

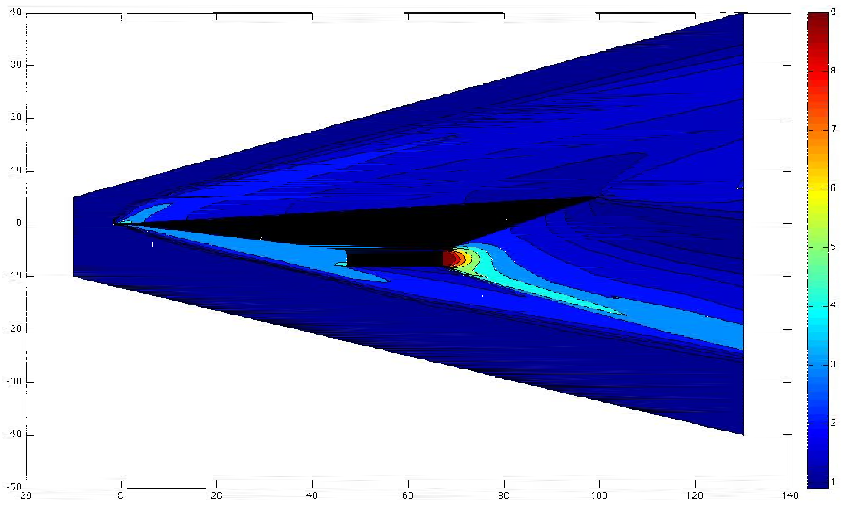

Figure 4.14: CFD Pressure Contours

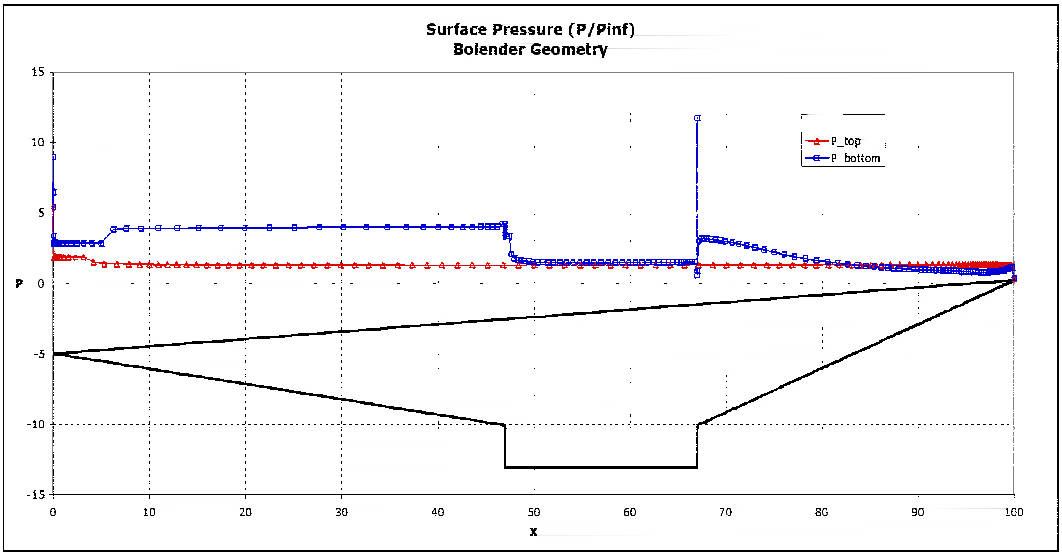

Figure 4.15: CFD Pressure Profile

Developing Bounds. Due to the large amount of uncertainty and time varying nature, a accurate "truth model" for the aftbody pressure may not be achievable. Formulating uncertainty bounds can be useful for both estimating static performance capabilities as well as developing robust controls laws. The following candidate uncertainty bounds can be categorized in order in decreasing conservativeness.

Conservative Bounds Conservative bounds can be formulated by assuming a constant pressure profile along the aftbody. An upper bound for the aftbody pressure is given by the exhaust pressure from the engine (p_e). A lower bound for the pressure is given by the freestream pressure of air (p_∞).

Non-conservative bounds Non-conservative bound can be formulated through piecewise linear segments as seen in Figure 4.16. The more aggressive the bound become, the more likely it is they are to violated through higher fidelity modeling methods. However, these aggressive bound can be useful for trim specifications and potential controller robustness.

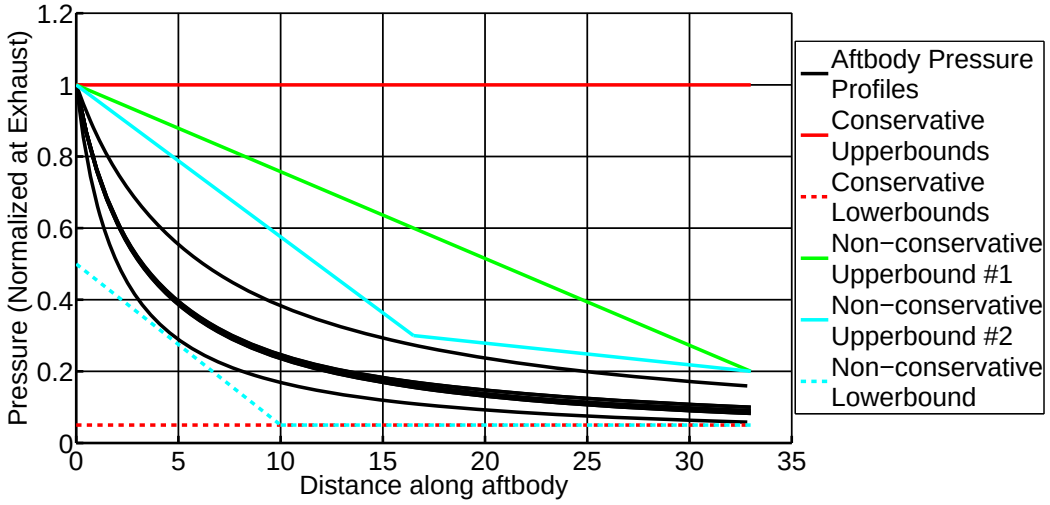

Figure 4.16: Aftbody Pressure Bounds

Static and Dynamic Comparisons

Static Properties: Mach 8, 85 kft. Table 4.4 shows the trim properties for the different modeling methodologies as well as the bounds.

From Table 4.4 the following observations can be made:

- For trim, all three methods yield similar properties at Mach 8, 85kft. This is not the case as the angle of attack starts to vary (shown in the next section).

	Elevator	FER	AOA	RHP Pole	RHP Zero
Conservative L.B.	10.67	0.26	2.54	2.80	7.44
Non-conservative L.B.	8.90	0.20	2.01	2.79	7.50
Numerical Discretization	6.58	0.14	1.83	2.20	7.60
Simple Approximation	6.84	0.15	1.83	2.98	7.57
High Fidelity Approx.	6.60	0.14	1.83	2.20	7.60
Non-conservative U.B. #2	-1.87	0.05	0.02	2.16	8.33
Non-conservative U.B. #1	-3.64	0.03	1.43	2.88	8.41
Conservative U.B.	-18.72	0.04	0.74	0.01	36.11

Table 4.4: Trim Properties

- The non-conservative lower bounds and upper bounds #2 do a good job of bounding the trim elevator and FER. Non-conservative upper bound #2 give a less conservative bound on the angle of attack than upper bound #1.
- The simple approximation model gives a dramatically more unstable linear model than the numerical and high fidelity approximation (34 %).
- The non-conservative lower bounds and upper bounds #2 do a good job of bounding the trim dynamic properties of the model.

Flexible Coupling. Within the original model the flexible dynamics are coupled into the rigid body by adding the angular deflection to the elevator deflection and the nose angle. The model has been modified so that every vertex of the geometry experiences the appropriate displacement given by the free-free beam model used to represent the structure of the vehicle. Figure 4.17 show the coupling of the flexible dynamics into the rigid body geometry (with a 10x amplification for illustrative purposes).

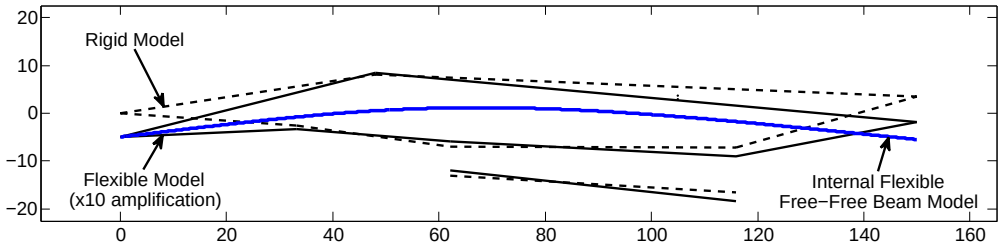

Figure 4.17: Modified Flexible Coupling

Dual Compression Ramp. The original model only allowed for a single state compression ramp before the engine inlet. Multistage compression ramps allow for more efficient propulsion efficiency due to a smaller loss of total pressure [88]. A two stage compression ramp has been implemented

as shown in Figure 4.18. The system is solved by iteratively adjusting the angle of the bottom most shock until the pressures on both sides of the slip line are equal [88, page 163].

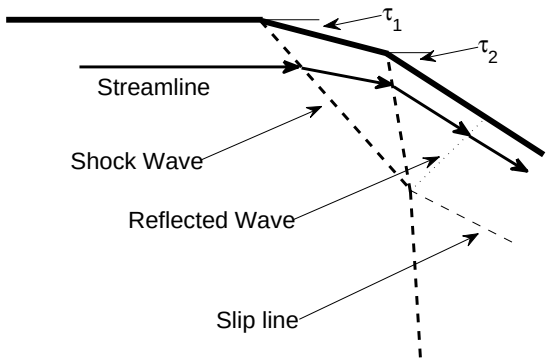

Figure 4.18: Dual Compression Ramp Shock System

Table 4.5 gives a comparison of equivalent single and dual compression ramp systems for a freestream Mach number of 8. As can be seen, the drop in total pressure is roughly 40 % less than with a single compression system.

Parameter	Single	Double
τ_1	8.1	4.3
τ_2	NA	9.1
Mach	6.17	6.17
p/p_0	3.99	4.69
p_t/p_{t0}	0.772	0.908
T/T_0	1.60	1.60

Table 4.5: Single vs Double Compression Ramp

Variable Specific Heat Ratio. The specific heat ratio can no be individually specified for different segments of the vehicle. The specific heat has been chosen as 1.4 everywhere in the vehicle with the exception of inside the engine combustor and internal nozzle. A value of 1.2 has been utilized in those locations due to the high temperatures [21].

Internal Layout. The original model had a static layout as show in Figure . The internal layout has been recoded as show in Figure 4.19. Fuels are now specified in terms of a percentage of the total volume within the vehicle, e.g. 50% liquid H_2, 25% liquid O_2, etc. The densities of each material are utilized to calculate the mass for each component based off the volume. Densities of of $4.42lbm/ft^3$ and $71.19lbm/ft^3$ have been used for liquid H_2 and liquid O_2 respectively. Table 4.6 gives the masses for the remaining components. The assumed width of the vehicle can be utilized as a design parameter, in this case, 33 ft. Furthermore, it is assumed that 90 % of the liquid O_2 will be utilized by the time the vehicle enters the hypersonic regime. The remaining 10% will be consumed after during the return portion of the mission after the vehicle has left the hypersonic regime.

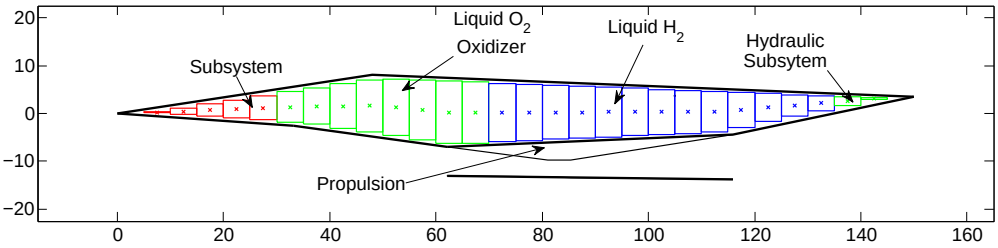

Figure 4.19: Modified Internal Layout

Parameter	Mass (lbm)
Structure	100,000
Engine	150,000
TPS	20,000
Hydraulics	1,000
Cargo	200,000
Misc	80,000
Liquid 0_2	40,000
Liquid H_2	108,840
Total	700,000

Table 4.6: Internal Layout: Nominal Masses

Mass Depletion. Mass depletion of liquid H_2 can now be handles in one of two ways. Mass depletion can be chosen as a fixed percent between 0 and 100. This mode of operation is utilized when trimming the vehicle. The percent can be varied across a trim trajectory to try to emulate mass depletion. The second mode of operation is to reduce the fuel mass at each instant of time during a nonlinear simulation. The mass is reduced as follows:

$$\Delta M = -\dot{m}_f W_v \Delta t \tag{4.69}$$

where $\dot{m}_f$ is the mass flow rate within the engine, W_v is the assumed width of the vehicle, and Δ_t is the simulation step size.

Chapter 5

Inlet and Plume Modeling

Both the inlet and plume modeling methodologies and assumptions have been altered from the original model. A more detailed account of each of these changes will be given in this chapter.

5.1 Dual Compression Ramp

Table 5.1 contains a comparison of various dual compression ramps for the lower forebody of the Bolender vehicle.

Assumptions for Dual Compression Ramp Study. For this study, the following assumptions have been made:

- Total lower forebody length: 47 ft
- Each compression ramp has an equal length: 23.5 ft
- The total height of both compression ramps must be 5.11 ft (original single compression ramp height)
- The second compression ramp angle (τ_2) must be greater than the first angle (τ_1). Both angles are assumed to be measured with respect to the horizontal body axis.

Parameter	$\tau_1 = 6.2°$	$\tau_1 = 5.5°$	$\tau_1 = 4.8°$	$\tau_1 = 4.1°$	$\tau_1 = 3.4°$	$\tau_1 = 2.7°$
τ_2	6.2	6.90	7.59	8.28	8.97	9.65
M_1	6.32	6.49	6.64	6.80	6.95	7.11
M_2	6.32	6.26	6.19	6.11	6.0	6.07
p_1/p_∞	3.61	3.25	2.91	2.60	2.32	2.06
p_2/p_∞	3.61	4.02	4.47	4.94	5.44	5.07
p_{t_1}/p_{t_∞}	0.81	0.851	0.886	0.916	0.942	0.963
p_{t_2}/p_{t_∞}	0.81	0.850	0.878	**0.890**	0.88	0.86
$\dot{m}_a$ (slugs/s)	2.104	2.101	2.099	2.095	2.091	2.086
Trim AOA (deg)	1.2	1.18	1.17	1.17	1.16	1.16
Trim FER	0.653	0.653	0.654	0.653	0.655	0.655
Trim H_2 rate	0.040	0.040	0.0396	0.0393	0.0397	0.0398
Trim Elev. (deg)	8.65	8.65	8.65	8.64	8.65	8.65

Table 5.1: Dual Compression Ramp Study

Conclusions

The typical efficiency measure for a compression system is total pressure drop (p_{t_2}/p_{t_∞}). It is maximized near a first compression angle of $\tau_1 = 4.1°$. The dual ramp compression system is less efficient if the first angle is too big or too small. The decrease in total pressure change is decreased from a 19% drop from the freestream for the nominal single compression ramp ($\tau_1 = \tau_2 = 6.2°$) to an 11% drop from the freestream for the optimized dual compression ramp ($\tau_1 = 4.1°$, $\tau_2 = 8.28°$). The impact of trim properties is nearly negligible.

5.2 Cowl Door and Inlet Modeling

The original model assumed a instantaneously translating cowl door that ensured a shock on lip condition for the rigid body dynamics. Flexing in the nose of the vehicle could cause the shock to move in front or behind the cowl lip. One major problem with this approach is the length requirement of the cowl door, even at relatively high Mach numbers. Figure 5.1 shows the 14 foot cowl door required to ensure shock on lip at Mach 7, 80 kft.This section compares the flow solutions for the SAMURI code with that of the original Bolender model. Criteria will be given for when the original Bolender model can be used to compute relatively accurate solutions and when it cannot be used.

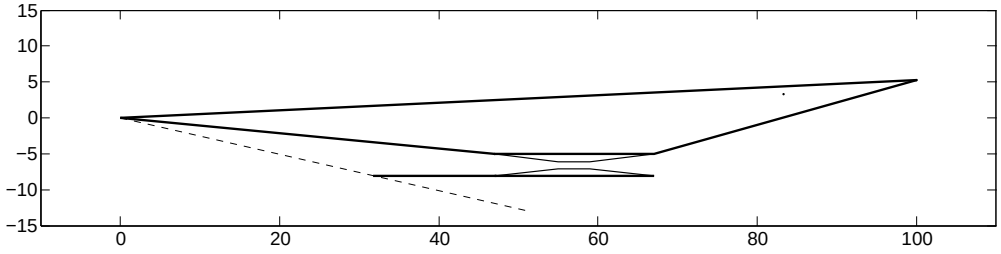

Figure 5.1: Original HSV with Cowl Door

Nominal Vision Vehicle Flow: Mach 8, 85kft, $0°$ *AOA*

Figure 5.2 shows the temperature of the flow for the vision vehicle geometry at Mach 8, 85kft, $0°$ AOA. The two shock system is being completely swallowed within the cowl lip. This causes an irregular flow pattern within the inlet, leading to increased heating at the bottom of the inlet.

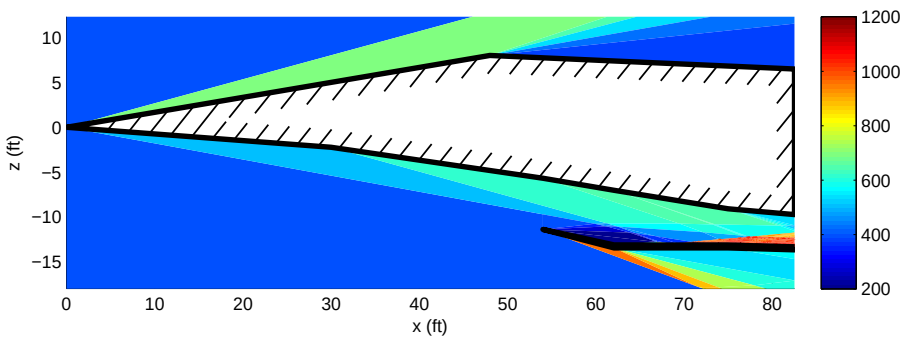

Figure 5.2: Vision Vehicle Flow: Temperature (R)

Figure 5.3 shows the temperature of the flow for a vertical slice at the cowl lip (roughly X = 54 ft in Figure 5.2).

- The Bolender method assumes that one single uniform shock is entering at the cowl lip.
- The SAMURI solution has shocks entering at the cowl lip.

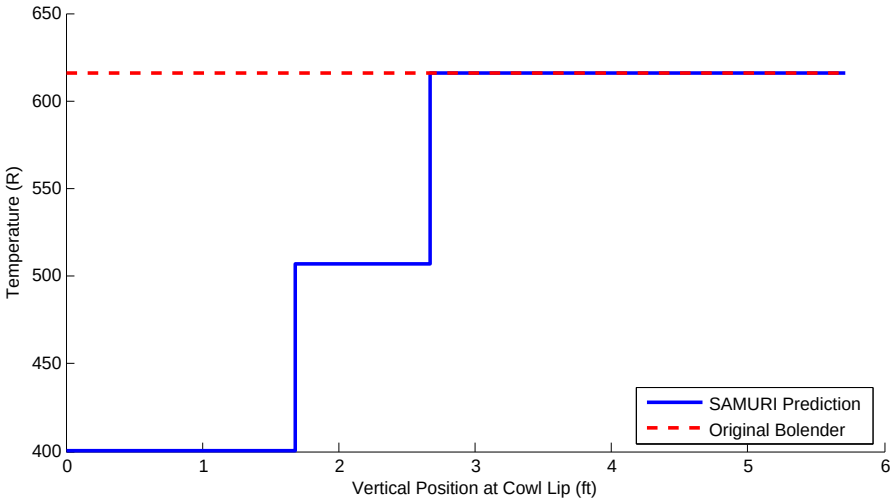

Figure 5.3: Vision Vehicle Flow at Cowl Lip: Temperature (R)

Figure 5.3 shows the temperature of the flow for a vertical slice at the inlet (roughly X = 83 ft in Figure 5.2). The Bolender method assumes that one single uniform shock is entering the inlet.

The SAMURI solution has many waves entering the inlet (approximately 100). This is due to the irregular flow condition shown in Figure 5.3. The Bolender solution may possibly be seen as a potential average to the SAMURI solution, but further study will show this was simply "dumb luck." Small changes in AOA or the flight condition will cause this to no longer hold true.

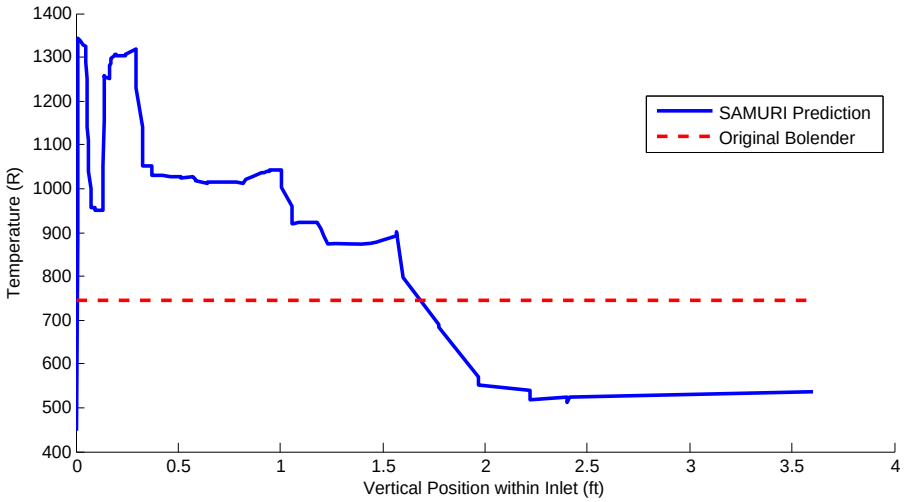

Figure 5.4: Vision Vehicle Flow at Inlet: Temperature (R)

5.3 Nominal Vision Vehicle Flow: Mach 8, 110kft, 0° AOA

Figure 5.5 shows the temperature of the flow for the vision vehicle geometry at Mach 8, 110kft, 0 ° AOA. This represents a flight condition that may be seen during a pull up maneuver.

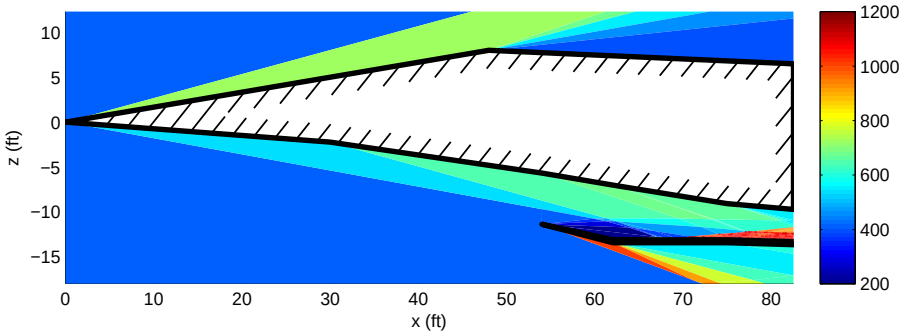

Figure 5.5: Vision Vehicle Flow: Temperature (R)

The shock system is being completely swallowed within the cowl lip. This causes an irregular flow pattern within the inlet, leading to increased heating at the bottom of the inlet. The flow patterns is identical to that shown in Figure 5.2. This is because the flow angles do not depend on altitude, only Mach. The state of the flow will be different as seen in Figures 5.6 and 5.7. Figure 5.6 shows the temperature of the flow for a vertical slice at the cowl lip (roughly X = 54 ft in Figure 5.5). The Bolender method assumes that one single uniform shock is entering at the cowl lip. The SAMURI solution has 3 shocks entering at the cowl lip. The temperature is higher than in Figure 5.3 because the temperature is increasing with altitude in the stratosphere. Figure 5.3 shows the temperature of the flow for a vertical slice at the inlet (roughly X = 83 ft in Figure 5.2). The SAMURI solution has many waves entering the inlet (approximately 100). This is due to the irregular flow condition shown in 5.3. The Bolender solution is no longer an accurate average to the SAMURI flow.

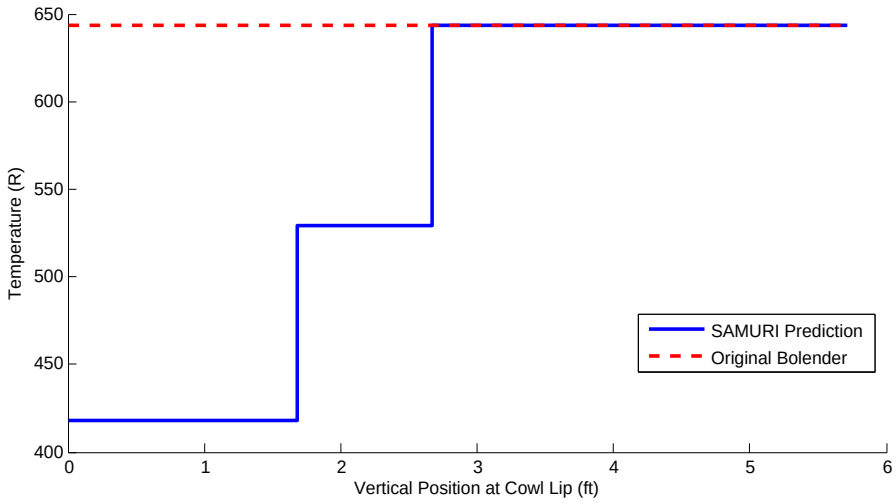

Figure 5.6: Vision Vehicle Flow at Cowl Lip: Temperature (R)

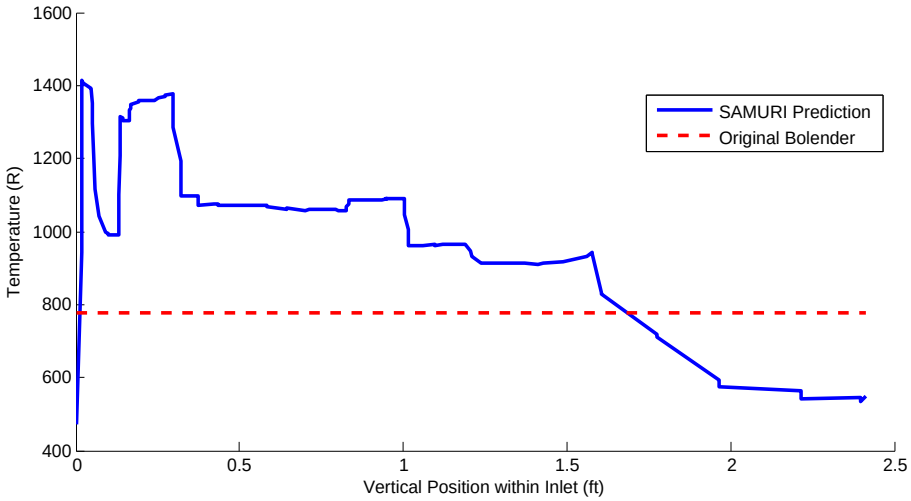

Figure 5.7: Vision Vehicle Flow at Inlet: Temperature (R)

5.4 Nominal Vision Vehicle Flow: Mach 5, 65kft, 0 AOA

Figure 5.8 shows the temperature of the flow for the Vision Vehicle geometry at Mach 6, 65kft, $0\,^{\circ}$ AOA. This represents a flight condition that may be seen near the beginning of scramjet flight.

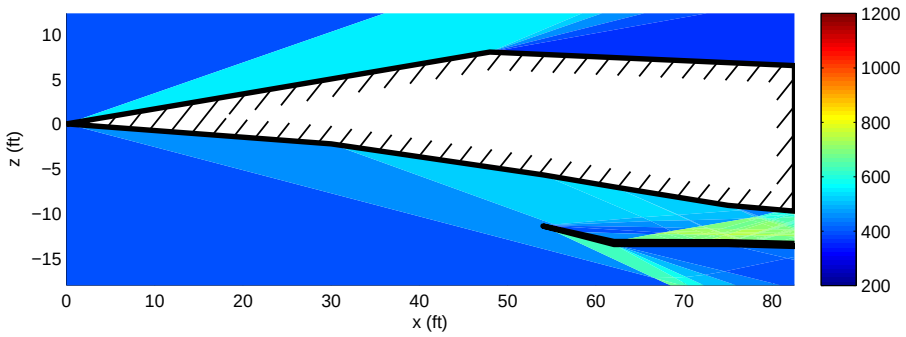

Figure 5.8: Vision Vehicle Flow: Temperature (R)

Only one of the two shocks is swallowed within the cowl lip. This causes an irregular flow pattern within the inlet. Heating is not nearly as severe as when both shocks are swallowed. Figure 5.6 shows the temperature of the flow for a vertical slice at the cowl lip (roughly X = 54 ft in Figure 5.8). The SAMURI solution has 2 shocks entering at the cowl lip. At this flight condition, the Bolender model does a better job of capturing the flow physics than in Figure 5.3. Figure 5.10 shows the temperature of the flow for a vertical slice at the inlet (roughly X = 83 ft in Figure 5.8). Again, the SAMURI solution has many waves entering the inlet (approximately 100). This is due to the irregular flow condition shown in Figure 5.8. The Bolender solution does a much better job of approximating the solution when multiple shocks are not being swallowed. However, we see that significant error still exists in some regions of the vertical slice.

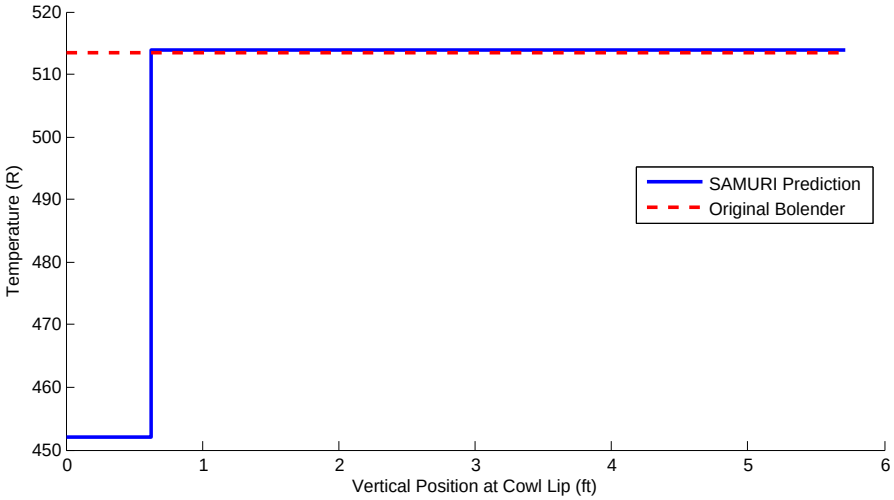

Figure 5.9: Vision Vehicle Flow: Temperature (R)

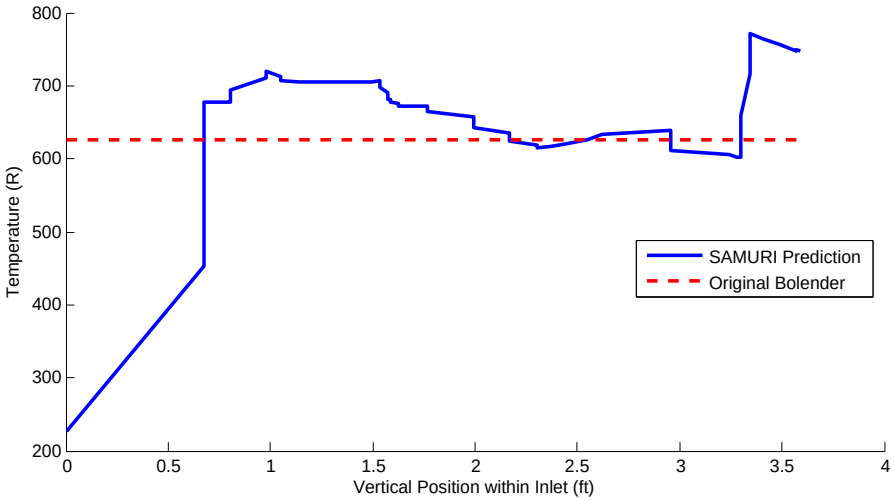

Figure 5.10: Vision Vehicle Flow: Temperature (R)

5.5 Optimized Lower Forebody Flow (no Cowl Rotation): Mach 8, 85kft, 0 AOA

Figure 5.11 shows the temperature of the flow for an optimized vehicle geometry at Mach 8, 85kft, 0° AOA. In this case, a non-rotating cowl door has been assumed.

Both shocks converge just in front of the cowl lip. Neither shock is swallowed within the cowl lip. This results in a uniform flow pattern within the inlet. Figure 5.12 shows the temperature of the flow for a vertical slice at the cowl lip (roughly X = 62 ft in Figure 5.11). Both methods show a

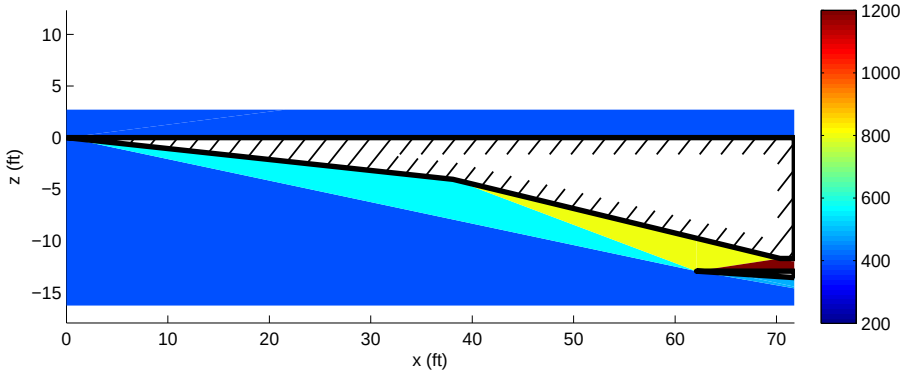

Figure 5.11: Optimized Vehicle Flow: Temperature (R)

singular shock condition at the cowl lip. Figure 5.13 shows the temperature of the flow for a vertical slice at the inlet (roughly X = 78 ft in Figure 5.11). The SAMURI solution has smaller number of shocks at the inlet compared to Figures 5.5 and 5.8. The different shocks have roughly the same state (temperature). The Bolender solution does an excellent job of determining the flow entering the inlet. It is off by roughly $8^\circ R$ (or 0.6%).

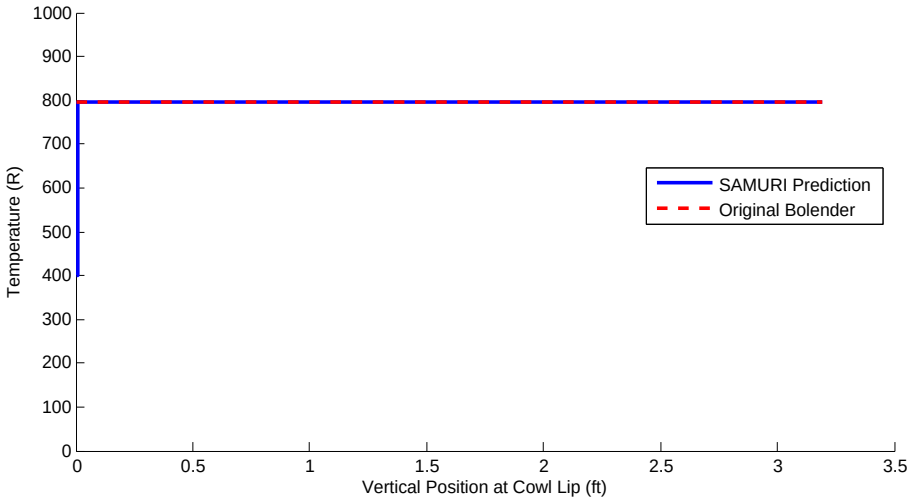

Figure 5.12: Optimized Vehicle Flow: Temperature (R)

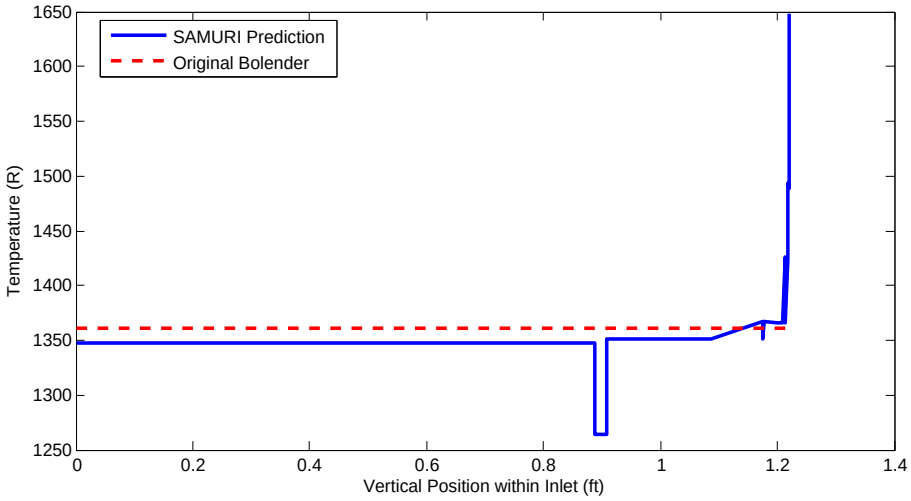

Figure 5.13: Optimized Vehicle Flow: Temperature (R)

5.6 Optimized Lower Forebody Flow (w/Rotated Cowl): Mach 8, 85kft, 0° AOA

Figure 5.14 shows the temperature of the flow for an optimized vehicle geometry at Mach 8, 85kft, 0° AOA. In this case a rotated cowl door has been assumed. This is a scenario the Bolender model was not explicitly coded to handle.

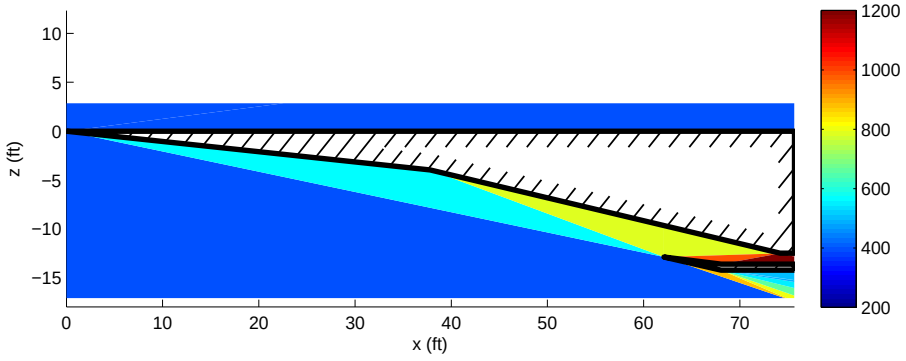

Figure 5.14: Optimized Vehicle Flow: Temperature (R)

Both shocks converge just in front of the cowl lip. Neither shock is swallowed within the cowl lip. This results in a uniform flow pattern within the inlet. Figure 5.15 shows the temperature

of the flow for a vertical slice at the cowl lip (roughly X = 63 ft in Figure 5.14). Figure 5.16 shows the temperature of the flow for a vertical slice at the inlet (roughly X = 78 ft in Figure 5.14). Similar to the no cowl case, the SAMURI solution has smaller number of shocks at the inlet. The different shocks have roughly the same state (temperature). The Bolender solution does a fair job of determining the flow entering the inlet. It is off by roughly $20\,^{\circ}R$ (or 1.5%).

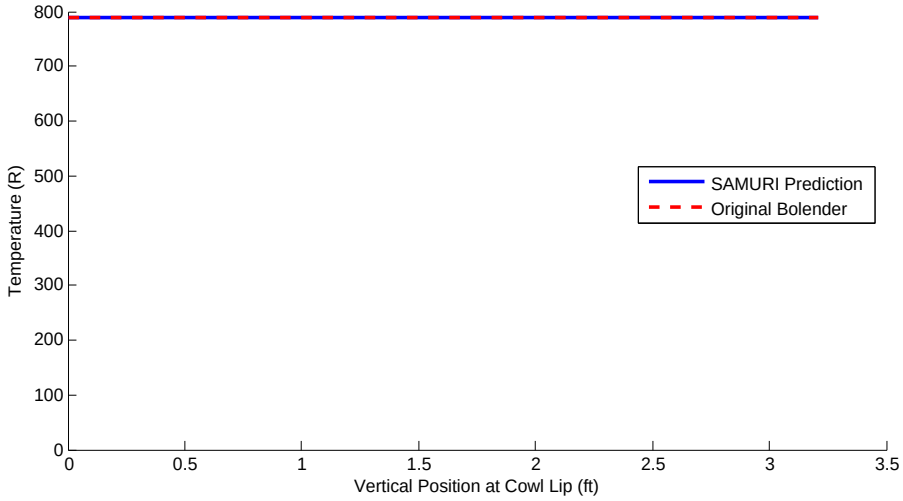

Figure 5.15: Optimized Vehicle Flow: Temperature (R)

- Both methods show a singular shock condition at the cowl lip.

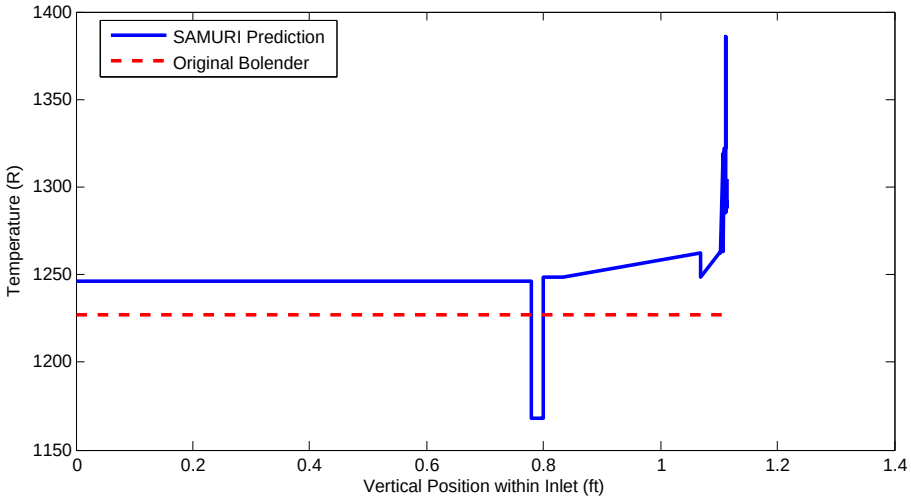

Figure 5.16: Optimized Vehicle Flow: Temperature (R)

Conclusions

The lower fidelity Bolender model accurately captures the physics of the higher fidelity SAMURI model when:

- No shocks are being swallowed within the cowl lip (easily calculated).
- No shocks are intersecting well in advance of the cowl lip (causing irregular flow patterns to be swallowed). Again, this is easily calculated for a small number of shocks (3 or less).

If either of these conditions is not met, the Bolender model cannot be used to accurately capture the static flow properties entering the engine.

5.7 Cowl Door Study

Within this subsection, we examine the results from a cowl door study for the Bolender model. The study examines the trimmable region (altitude in kft versus Mach) with and without the horizontally translating cowl door. It should be noted that horizontal cowl door extensions present very formidable, if not insurmountable, practical implementation issues. This motivates the the cowl-door-free study presented within this subsection.

Cowl Door Extension Required to Achieve Shock-on-Lip Condition

Figure 5.17 shows the cowl door extension (in feet) required to ensure a shock-on-lip condition over the trimmable region.

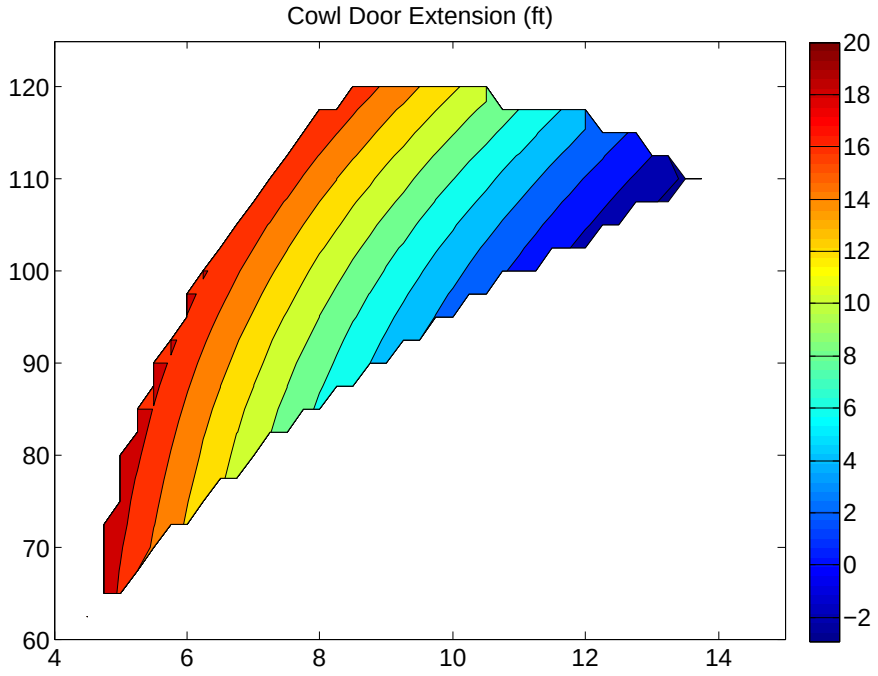

Figure 5.17: Cowl Door Extension (ft) Required to Ensure Shock-on-Lip Condition

Figure 5.17 shows that a cowl door extension occurs until around Mach 13.

At low Mach numbers, the required cowl door extension is observed to be prohibitively large.

Trim FER

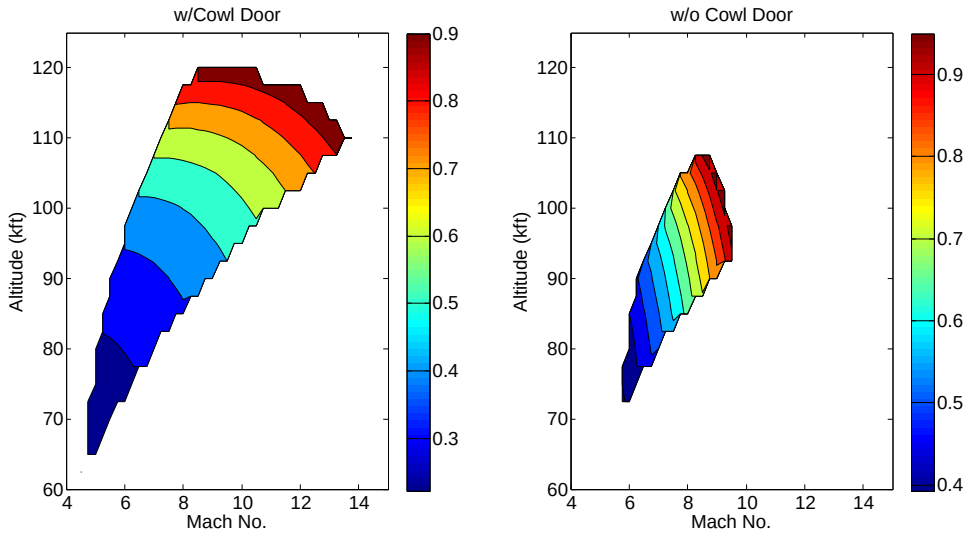

Figure 5.18: Trim FER Over Trimmable Region

- Size of trimmable region decreases significantly with no cowl door present
  - This is expected
  - Decreased air mass flow results in larger FER for same amount of H_2 fuel rate

Trim H_2 Fuel Rate

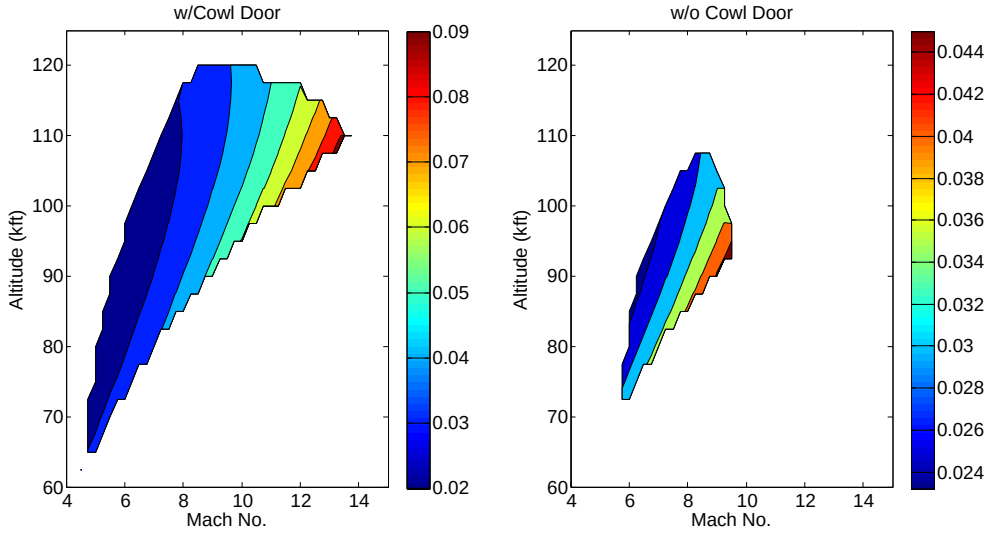

Figure 5.19: Trim H_2 Fuel Rate (slugs/s) Over Trimmable Region

- Size of trimmable region decreases significantly with no cowl door present
- At a given flight condition, more H_2 is required to achieve trim when no cowl door is present

Trim AOA

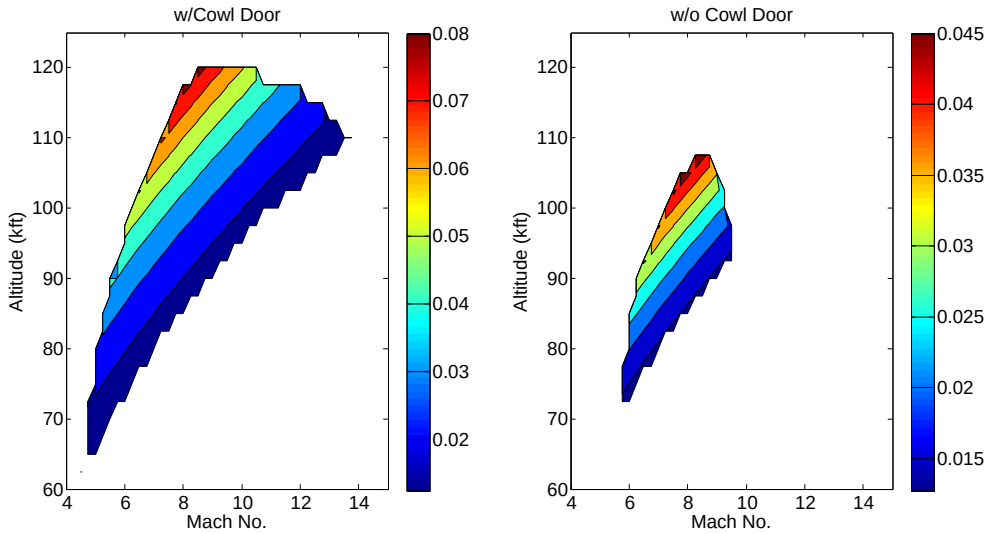

Figure 5.20: Trim Angle of Attack (deg) Over Trimmable Region

- Size of trimmable region decreases significantly with no cowl door present
- Trim AOA is relatively unaffected by cowl door removal in terms of overall trend.

Trim Elevator Deflection

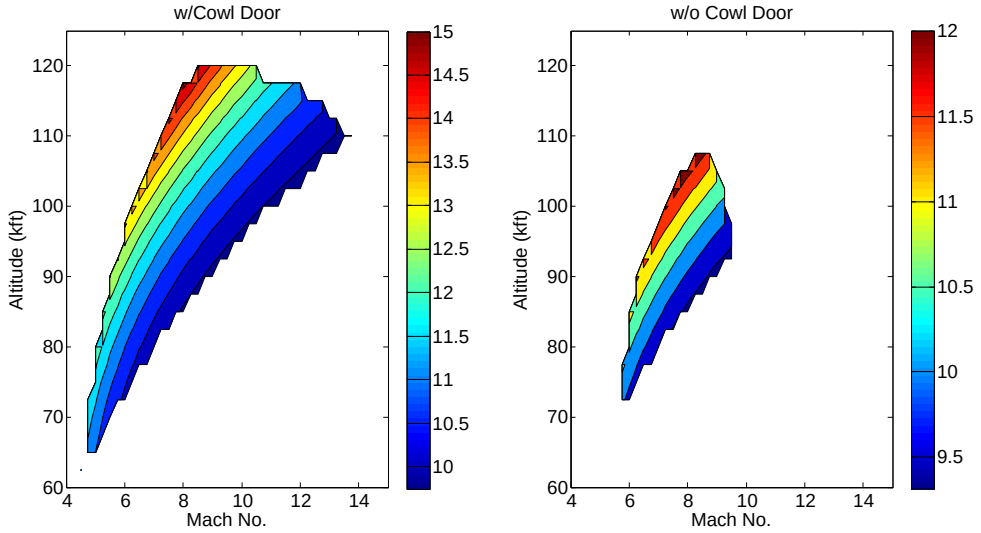

Figure 5.21: Trim Elevator Deflection (deg) Over Trimmable Region

- Trim elevator deflection is relatively unaffected by cowl door removal.

Vehicle Longitudinal Instability

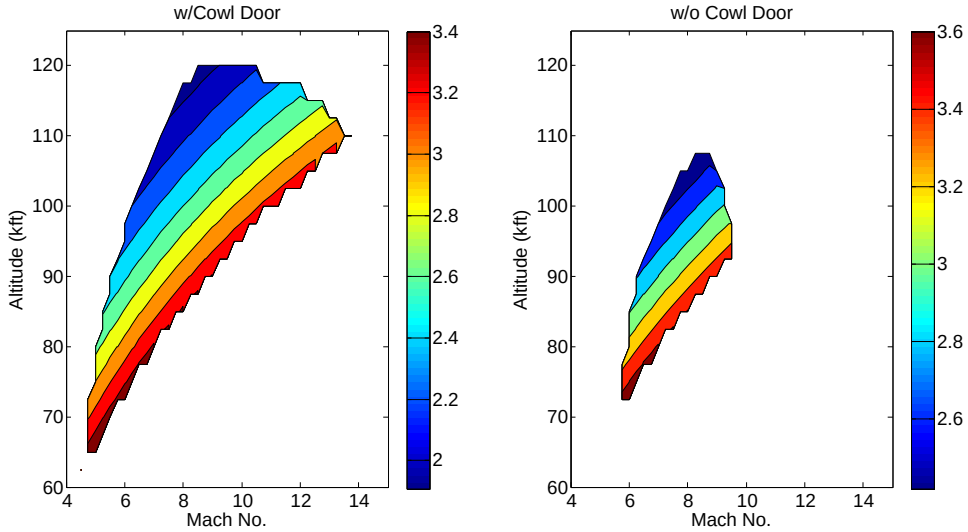

Figure 5.22: Right Half Plane Pole Over Trimmable Region

- Size of trimmable region decreases significantly with no cowl door present
- RHP pole is relatively unaffected by cowl door removal

Non-Minimum Phase Zero

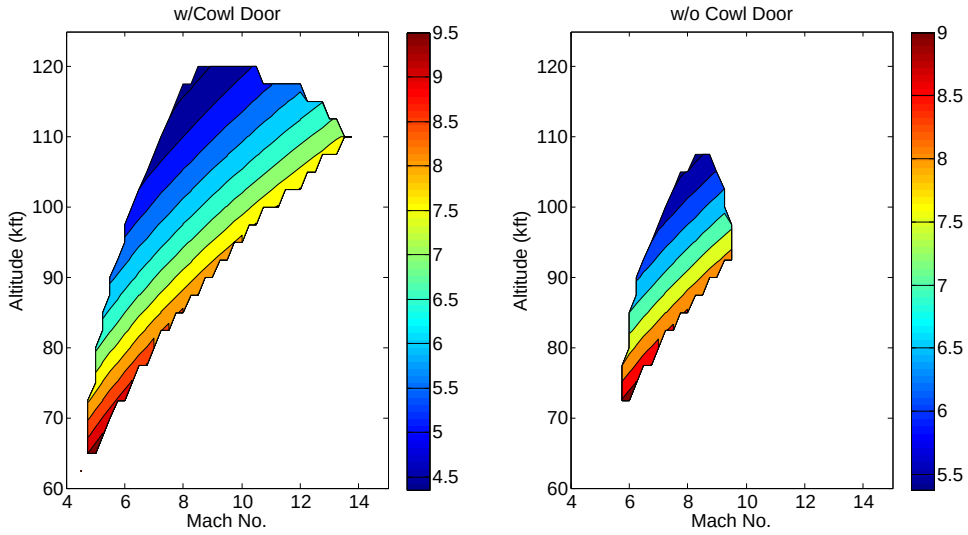

Figure 5.23: Right Half Plane Zero Over Trimmable Region

- Size of trimmable region decreases significantly with no cowl door present
- RHP zero is is relatively unaffected by cowl door removal

Chapter 6

TWO-STAGE TO ORBIT TRAJECTORY

This chapter will focus on a two-stage to orbit trajectory (TSTO) whereby a combined cycle rocket-scramjet booster vehicle is used to accelerate the two vehicle stack to a staging flight condition. At this point, the orbiter will separate from the booster and achieve LEO through rocket propulsion. The booster vehicle then returns to a base through a combination of a level cruise utilizing the scramjet, followed by an un-powered glide. The focus of this research begins at Mach 5, generally the velocity where scramjet technology becomes feasible [23]. A visualization of the trajectory can be seen in Figure 6.1.

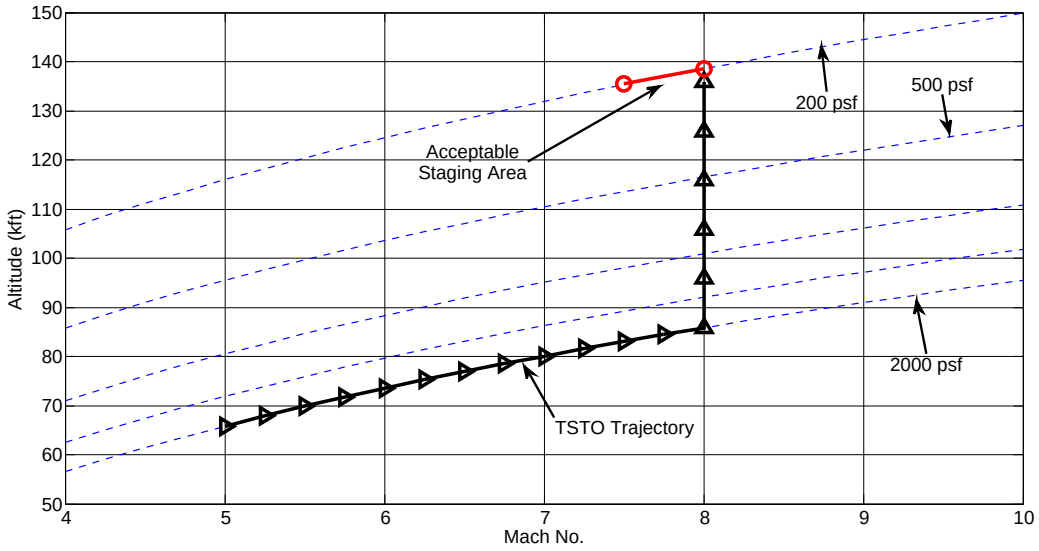

Figure 6.1: Two-Stage to Orbit Trajectory

The vehicle stack will fly at a constant dynamic pressure of 2000 pounds per square foot (psf) until Mach 8. At this point the stack initiates a constant Mach climb to a dynamic pressure of 200 psf. Due to the air-breathing nature of the scramjet engine, it may not be possible to maintain constant Mach at high altiudes/low dynamic pressures. Reaching a dynamic pressure of 200 psf between Mach 7.5 to Mach 8 will be considered an acceptable staging flight condition.

Chapter 7

OPEN-LOOP MODEL ANALYSIS

The chapter will focus on an open loop comparison between the Bolender model geometry and the NASA reference vehicle geometry (visualized in Figures 4.6and 4.7). The parameters for the Bolender and NASA reference vehicle are listed in Tables 7.1 and 7.2 respectively.

Parameter	Nominal	Parameter	Nominal
Total Length (L)	100 ft	Lower forebody angle (τ_{1L})	6.2^o(deg)
Forebody Length (L_1)	47 ft	Tail angle (τ_2)	14.342^o(deg)
Aftbody Length (L_2)	33 ft	Vehicle mass per unit width	6,154.1 lbs/ft
Engine Length	20 ft	Mean Elasticity Modulus	8.6482e+7 psi
Engine inlet height h_i	3.25 ft	Moment of Inertial I_{yy}	86,723 slugs ft^2/ft
Upper forebody angle (τ_{1U})	3^o(deg)	Center of gravity	(-55,0)ft
Elevator position	(-85,-3.5) ft	Elevator Area	17 ft^2
Diffuser area ratio	0.15	Nozzle exit/inlet area ratio	6.67

Table 7.1: Table of Parameters Values: Bolender Model

The paramters for the Bolender model are similar to what has been published within the literature [3], [5], [38] with the exception of the Diffuser ratio and the Internal Nozzle ratio, for reasons listed in Section 4.4. Section 7.1 will examine the static properties of vehicle, and Section 7.2 will focus on the dynamic properties of the vehicle.

Parameter	Nominal	Parameter	Nominal
Total Length (L)	150 ft	Upper Fore-angle 1 (τ_{1U})	9.6^o(deg)
Upper Fore-Length 1 (L_{U1})	48 ft	Upper Fore-angle 2 (τ_{2U})	-2.5^o(deg)
Upper Fore-Length 2 (L_{U1})	102 ft	Lower Fore-angle 1 (τ_{1L})	4.3^o(deg)
Lower Fore-Length 1 (L_{U1})	33.3 ft	Lower Fore-angle 2 (τ_{2L})	7.2^o(deg)
Lower Fore-Length 2 (L_{U2})	28.8 ft	Tail angle (τ_2)	14.342^o(deg)
Aftbody Length (L_{aft})	34.1 ft	Mass per Unit Width	21,212 lbs/ft
Engine Length	53.8 ft	Mean Elasticity Modulus	8.6482e+7 psi
Engine inlet height h_i	5 ft	Moment of Inertial I_{yy}	86,723 slugs ft^2/ft
Upper forebody angle (τ_{1U})	3^o(deg)	Center of gravity	(-90,0)ft
Elevator position (hinge)	(-120,-3.65) ft	Wing Area	26 ft^2
Wing position (centroid)	(-133,-3.31) ft	Elevator Area	13 ft^2
Diffuser Area Ratio	0.3	Nozzle Area Ratio	2.61

Table 7.2: Table of Parameters Values: NASA Reference Vehicle

7.1 Open Loop Analysis: Trim Properties

The following figures show the static trim properties for the Bolender model and NASA reference vehicle as they are trimmed along the trajectory in Figure 6.1. Not that the trajectory in Figure 6.1 end at an altitude of 138,500 ft, something neither model is able to accomplish in trim. This means that for either of these vehicles to reach staging, they will be in a state of deceleration in the

forward direction. An important point of note from 6.1 is the transition altitude of 85,000 between the constant dynamic pressure segment and the constant mach pull-up.

States and Controls

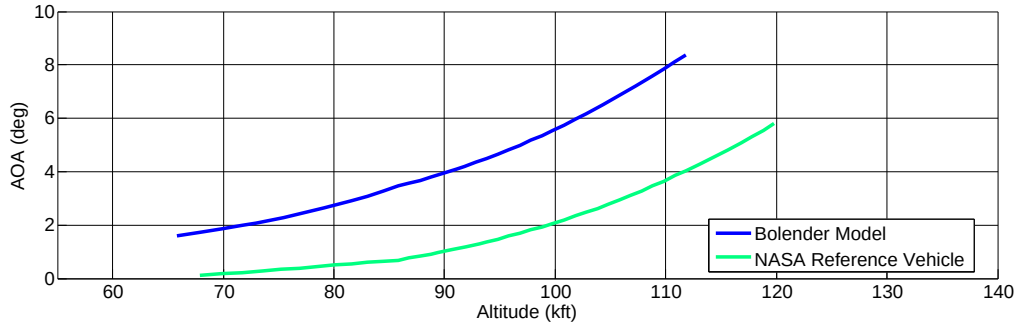

Figure 7.1: OL Comparisons: Trim Angle of Attack

- Both models increase in trim AOA slightly until the transition altitude, and then begin increase more rapidly
- Less AOA is needed by the reference vehicle due to the larger capture area of the inlet and the improved properties of the double compression ramp.

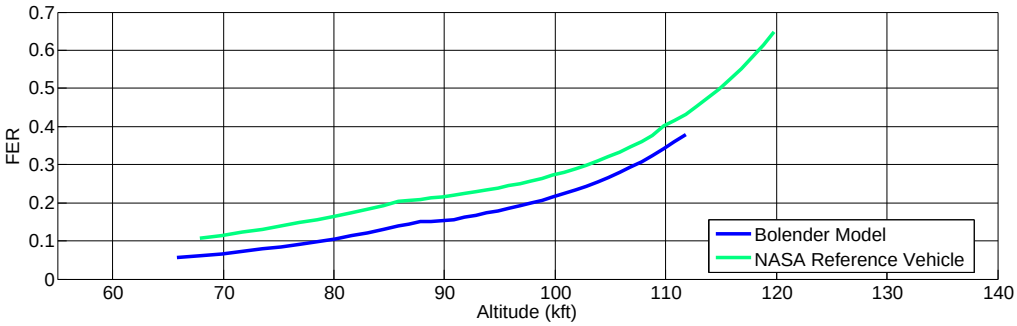

Figure 7.2: OL Comparisons: Trim Fuel Equivalence Ratio

- Both models increase in trim FER slightly until the transition altitude, and then begin increase more rapidly
- The reference vehicle requires more FER to trim due to it's larger whetted area. One might actually expect a larger difference, however the smaller trim AOA vs the Bolender model mitigates this effect.
- Both models increase in trim fuel rate until the transition point, then begin to decrease. This is due to the fact that the decrease dynamic pressure results in reduced drag. Eventually the fuel rate increases again due to the trim FER more rapidly increasing than the drag is decreasing.

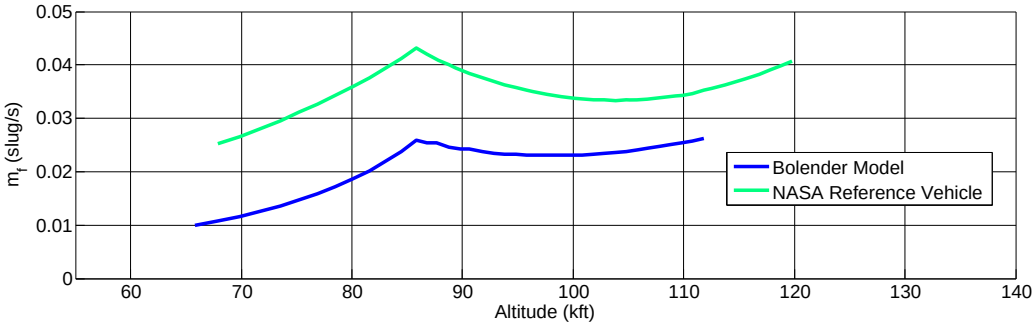

Figure 7.3: OL Comparisons: Trim Hydrogen Fuel Flow

- Again, the reference vehicle require a larger fuel rate due to the larger size.

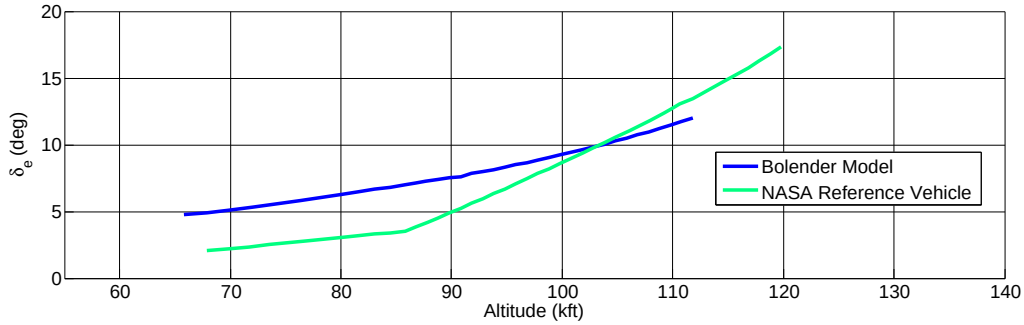

Figure 7.4: OL Comparisons: Trim Elevator Deflection

- The Bolender model has a total elevator area of 17 sqft, the vision vehicle has a 26 sqft wing with a 13 sqft elevator.
- Both vehicle require and increasing elevator deflection across the trajectory.
- At high dynamic pressure, the wing of the reference vehicle is able to provide lift, and less elevator deflection is needed. At higher altitudes, the smaller elevator area of the reference vehicle necessitates larger deflections.

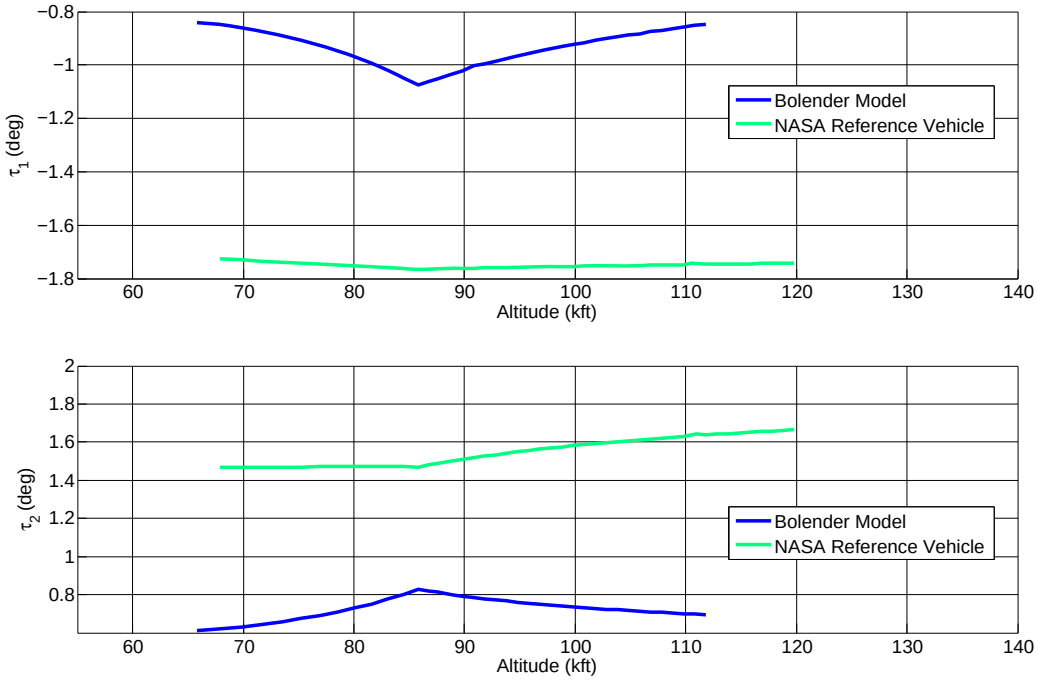

Figure 7.5: OL Comparisons: Trim Flexing Deflection Angle

- For both models, the flexing is worse at high dynamic pressure and high Mach No.
- The flexing of the reference vehicle is greater due to the increases length of the vehicle.

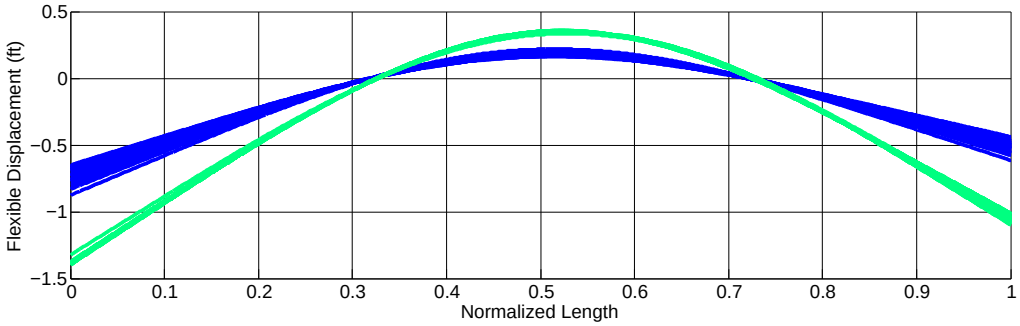

Figure 7.6: OL Comparisons: Trim Flexing Deflection

- This plot shows the vertical displacement of the structure due to the flexing.
- The x-axis has been normalized by the lengths of the vehicle for comparison purposes
- There are multiple lines per model: one for each trim point
  - There is more pronounced flexing for the reference vehicle, consistent with the previous plot
  - There is a greater spread of flexing for the Bolender model, likely due to its smaller mass vs the reference vehicle.

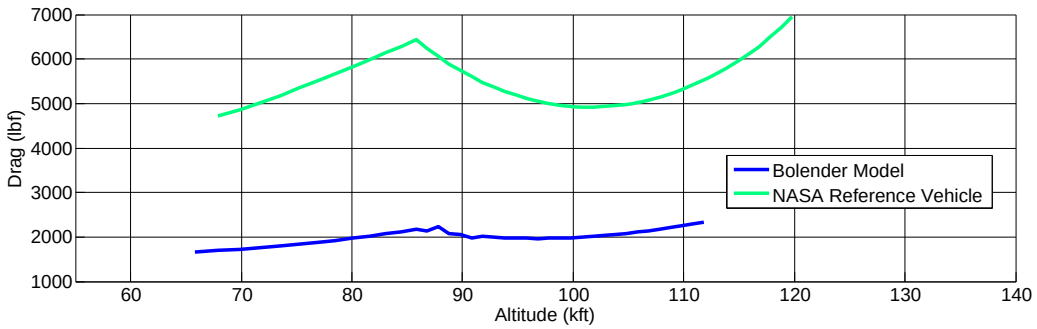

Figure 7.7: OL Comparisons: Trim Drag

- Similar to the fuel rate curves, the drag increases along constant dynamic pressure with increasing Mach. During the constant Mach pull-up, the drag begins to decrease due to the decreased dynamic pressure. Eventually the trim AOA and elevator deflection increase faster than the decrease in dynamic pressure, and the total drag begins to increase.

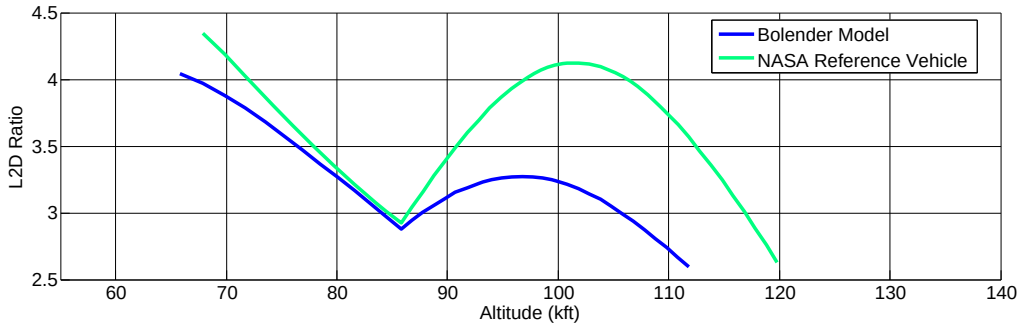

Figure 7.8: OL Comparisons: Trim Lift-to-Drag

- The lift-to-drag ratios are relatively similar for both vehicles. This is expected as they are fundamentally both wave-riders of somewhat similar design

- The lift for each vehicle is constant (equal to the weight), therefore the graph is just an inverse of the drag curve.

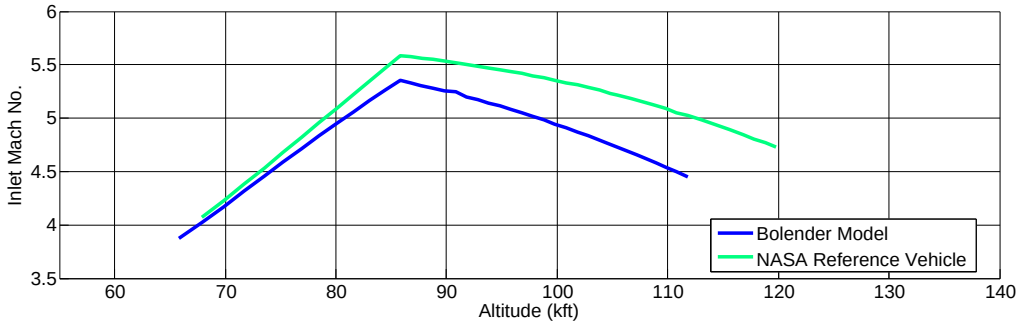

Figure 7.9: OL Comparisons: Trim Inlet Mach No.

- The reference vehicle has a greater inlet Mach despite the greater final ramp angle (7.2 deg vs 6.3 deg). This is due to the double compression ramp and smaller trim AOA.

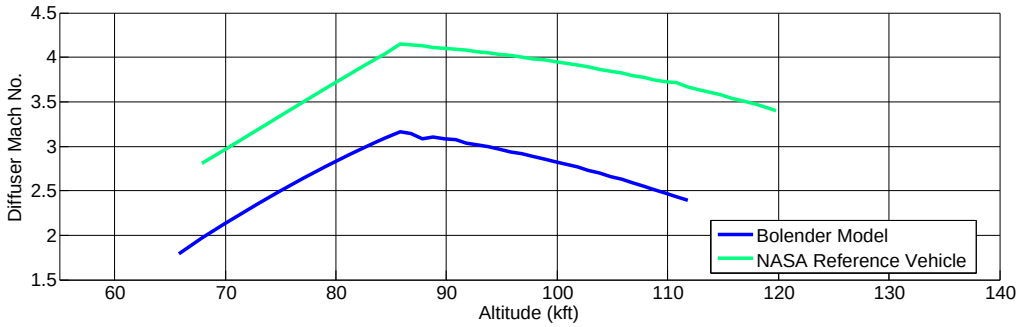

Figure 7.10: OL Comparisons: Trim Diffuser Mach No.

- The large diffuser contraction of the Bolender model (0.15 vs 0.3) causes the Mach to slow down significantly more than the reference vehicle. This will mean the Bolender model will thermally choke for smaller FER values than the reference vehicle.
- The combustor Mach is slower for the Bolender vehicle across all flight conditions
- As the combustor Mach approaches 1, the vehicle is no longer able to trim, hence the inability to reach the staging altitude of 138,500 ft in trim.
- The internal temperature of the combustor increases across the trajectory due to the increasing FER.
- The operational limit of the engine is 2500 ^{o} C (4900 R) [23]. Both engine would likely need to be enlarged to allow for greater air-mass to reduce the temperature within the combustor.

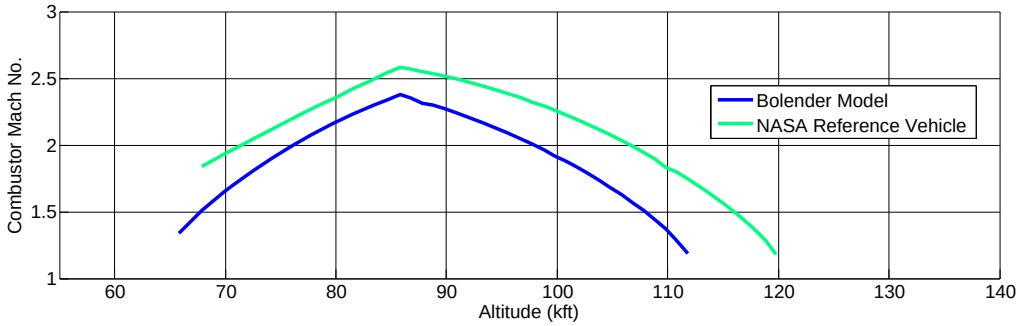

Figure 7.11: OL Comparisons: Trim Combustor Mach No.

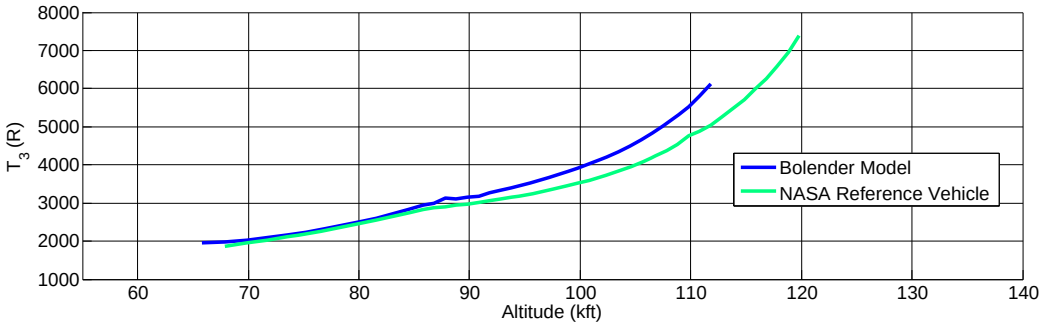

Figure 7.12: OL Comparisons: Combustor Temperature

Elevon-Wing Properties

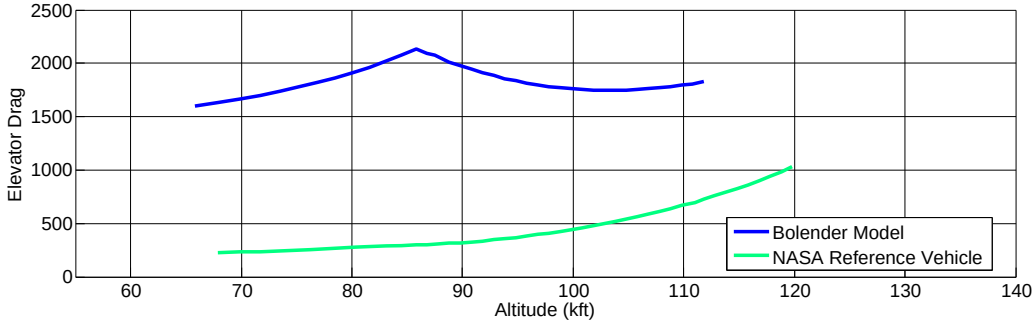

Figure 7.13: OL Comparisons: Trim Elevator Drag

- The trim elevator drag is much greater for the Bolender model vs the reference model.
  - The all movable wing necessitates a large deflection for trim
  - The large deflection combined with the larger elevator area results in a larger deflection

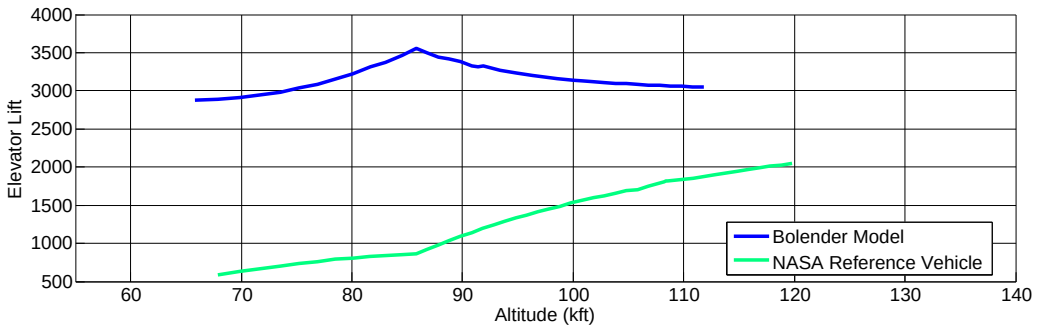

Figure 7.14: OL Comparisons: Trim Elevator Lift

- The elevator for the Bolender model is responsible for providing a much greater portion of the lift than the reference vehicle

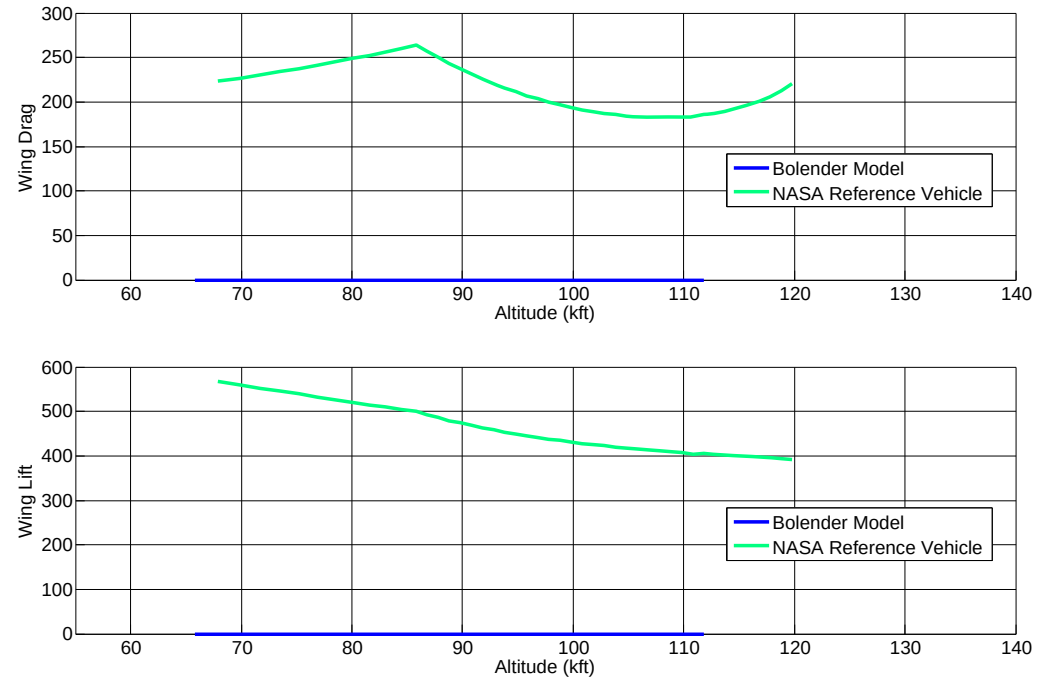

Figure 7.15: OL Comparisons: Trim Wing Drag & Lift

- The wing of the reference vehicle provides significantly amount of lift versus drag at all flight conditions.

7.2 Open Loop Analysis: Dynamic Properties

The following figures show the dynamic trim properties for the Bolender model and NASA reference vehicle as they are trimmed along the trajectory in Figure 6.1. Not that the trajectory in Figure 6.1 end at an altitude of 138,500 ft, something neither model is able to accomplish in trim. This means that for either of these vehicles to reach staging, they will be in a state of deceleration in the forward direction. An important point of note from 6.1 is the transition altitude of 85,000 between the constant dynamic pressure segment and the constant mach pull-up.

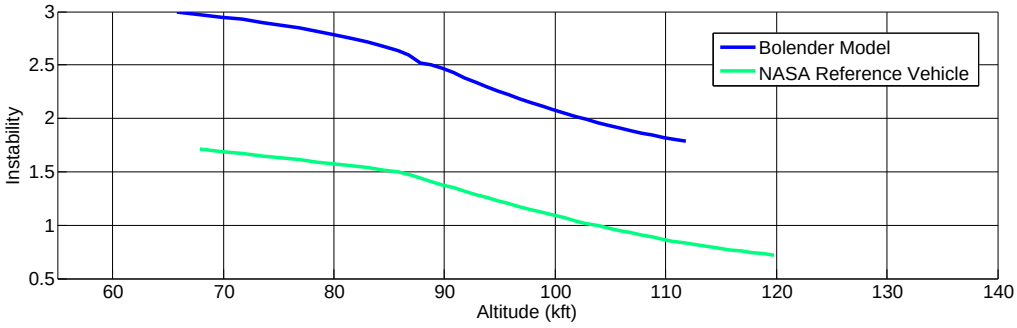

Figure 7.16: OL Comparisons: RHP Pole

- Both instabilities decrease along the trajectory
  - A single design at the largest instability may be sufficient for the entire trajectory (modulo mass change)
- The reference vehicle is significantly less unstable than the Bolender model
  - The overall larger wing and elevator surface combine to move the center of pressure more rearward than the all moveable wing of the Bolender model.

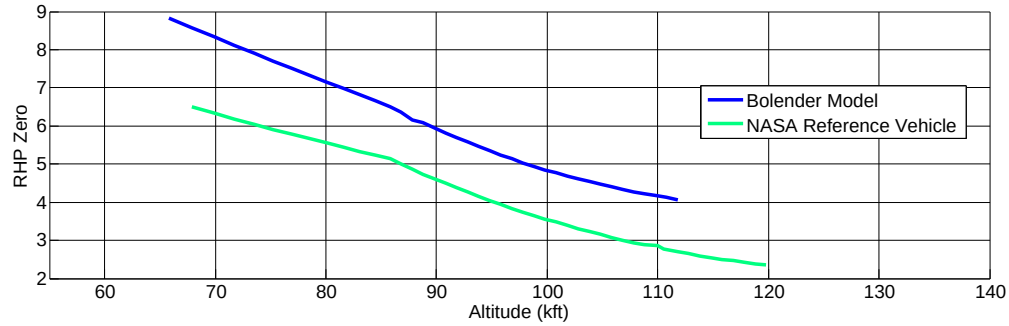

Figure 7.17: OL Comparisons: RHP Zero

- The RHP zero decreases along the trajectory for base designs
- The reference vehicle has a smaller RHP zero due to the larger forebody relative to Bolender model.

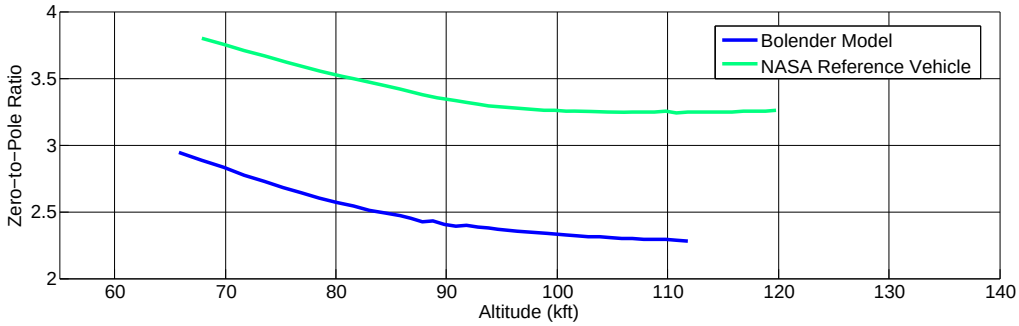

Figure 7.18: OL Comparisons: Zero-to-Pole Ratio

- The zero-to-pole ratio decreases for both cases
- The worst case scenario occurs at the end of the trajectory, indicating it may be the more difficult to design case
- The small ratio's for all cases indicate that output only feedback will not be feasible

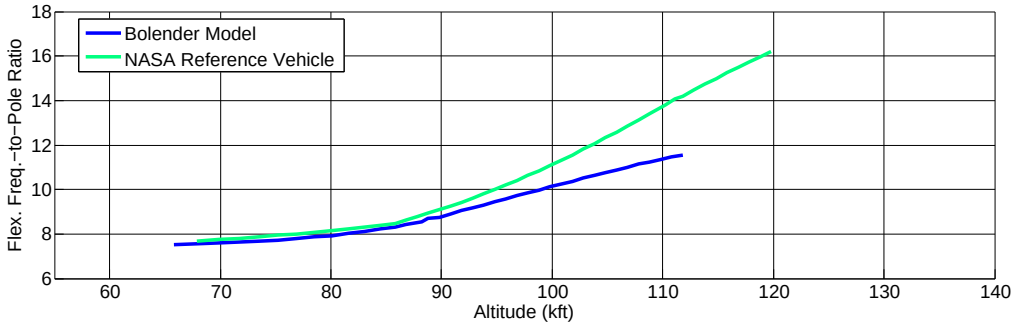

Figure 7.19: OL Comparisons: Flex. Mode Freq.-to-Pole Ratio

- The ratio of the first flexible mode frequency to the instability increases across the trajectories
- Small ratio's increase sensitivities at the elevator control

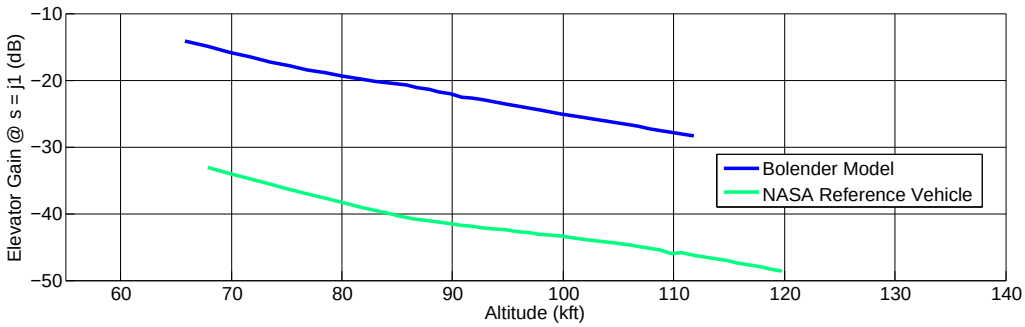

Figure 7.20: OL Comparisons: Elevator-to-FPA Gain @ $s = j1$ rad/s

- The elevator-to-FPA gain is decreasing across the trajectory
- Large transient responses will occur for commands at the end of the trajectory
  - It may be necessary to design the controller such that a small trim deflection occurs as the end of the trajectory
  - This might mean larger elevator and wing areas, large wing mounting angles, etc.

Chapter 8

VEHICLE DESIGN METHODOLOGY

The design methodology presented in this report can be broken down into two categories: (1) open loop design and (2) closed loop design. Closed loop analysis is inherently more expensive than open loop analysis, so where possible it is beneficial to attempt to predict the closed loop behavior utilizing open loop analysis/design methods. The following series of diagrams demonstrate the interactions of various components of the modeling, simulation and optimization framework. This framework will be utilized to generate a control-relevant vehicle design methodology. The following flow charts demonstrates the steps undertaken in doing an initial design. It may be necessary to iterate upon the procedure several times before satisfactory results are achieved.

8.1 Multidisciplinary Modeling, Analysis, Design and Optimization Framework

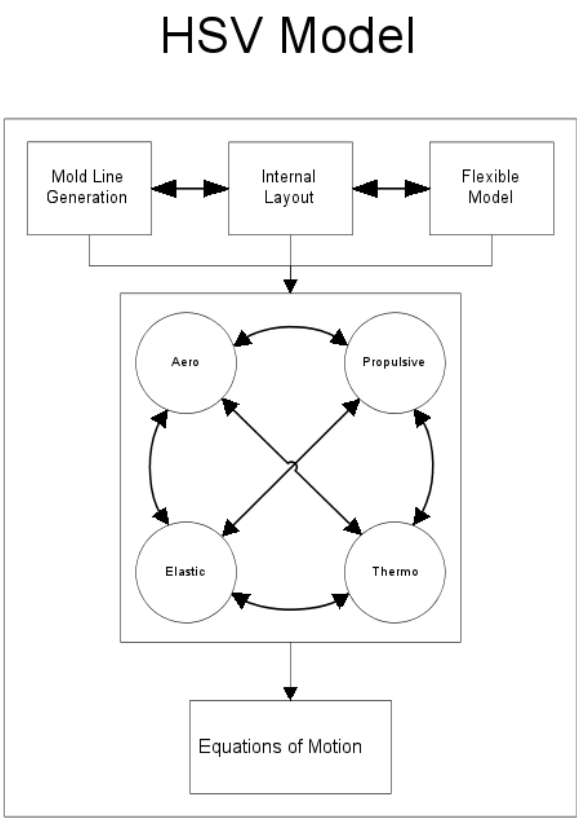

Figure 8.1: Aero-Thermo-Elastic-Propulsion Modeling Environment

Figure 8.1 demonstrates the basic components and interactions of the Aero-Servo-Thermo-Elastic-Propulsion Modeling (ASTEP) Environment. Three components of the components (mold line generation, internal layout, flexible model) are calculated offline (time and state independent) and fed

into the general modeling framework, which is responsible for generating the state derivatives from the equations of motion.

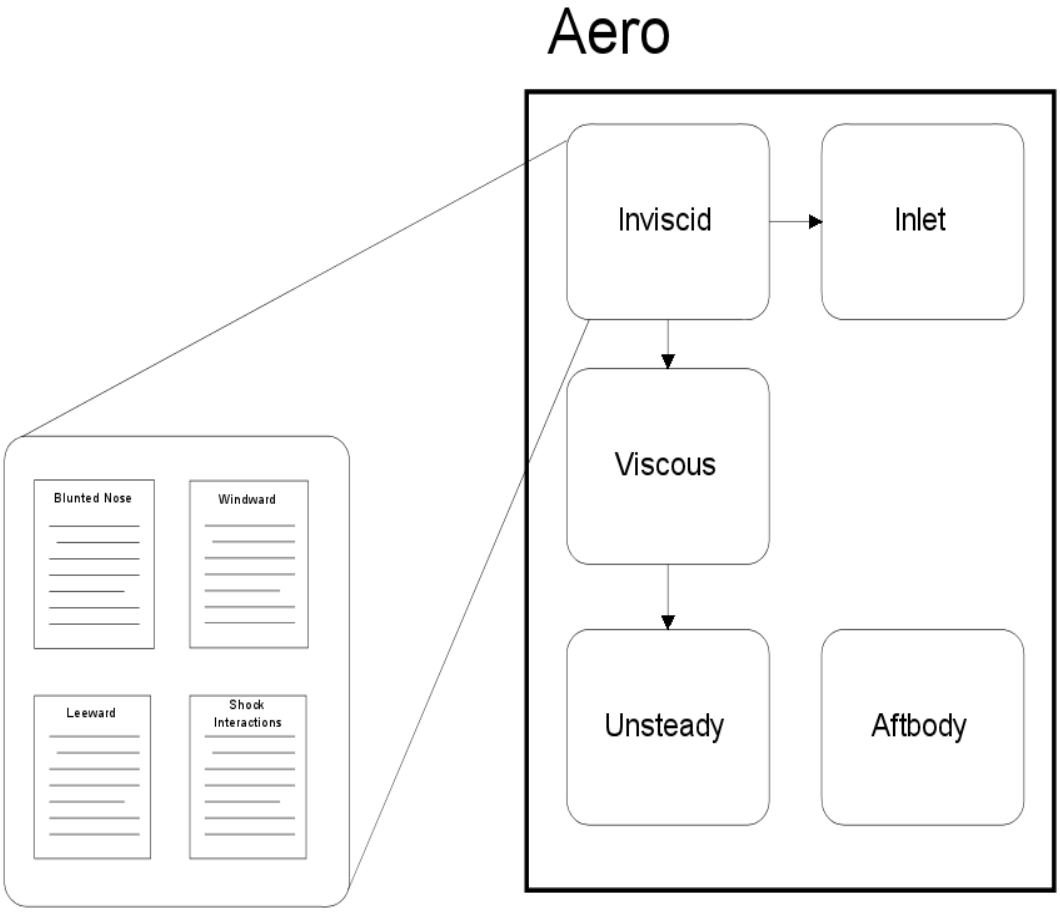

Figure 8.2: Abstraction Layers of the Aero-Thermo-Elastic-Propulsion Modeling Environment

Figure 8.2 notionally demonstrates the various layers of abstraction that go into each component of Figure 8.1. The model has been recoded such that it is simple to replace any one subcomponent with one of higher or lower fidelity depending upon the requirements of the task at hand.

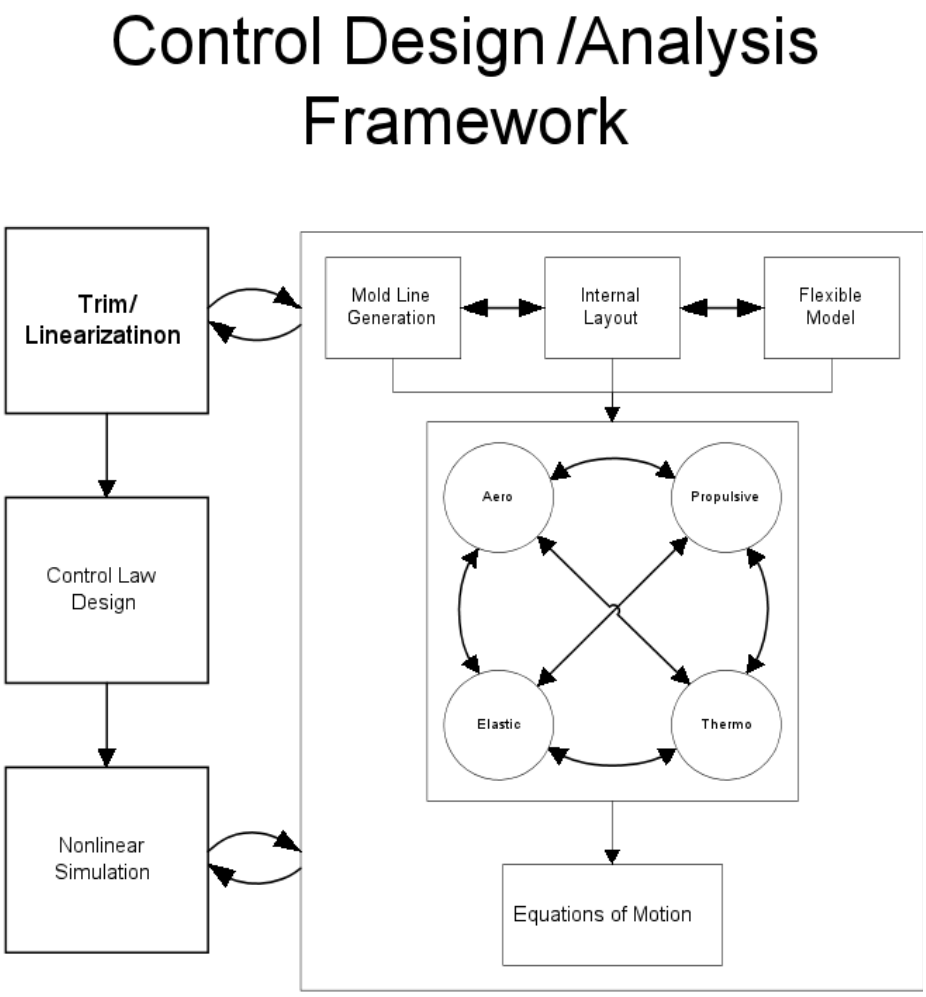

Figure 8.3: Control Design & Analysis Framework

Figure 8.3 shows the Control Design and Analysis Framework that is utilized with the ASTEP Model. The Trim/Linearization routine interacts with the ASTEP Model to determine trimmed states and control as well as to generate linear models for a particular flight condition. These results are fed into the Control Law Design routine to generate the control law for a particular flight condition. This control law as well as the trim data is then fed into the Nonlinear Simulation routine, which makes numerous calls to the ASTEP Model.

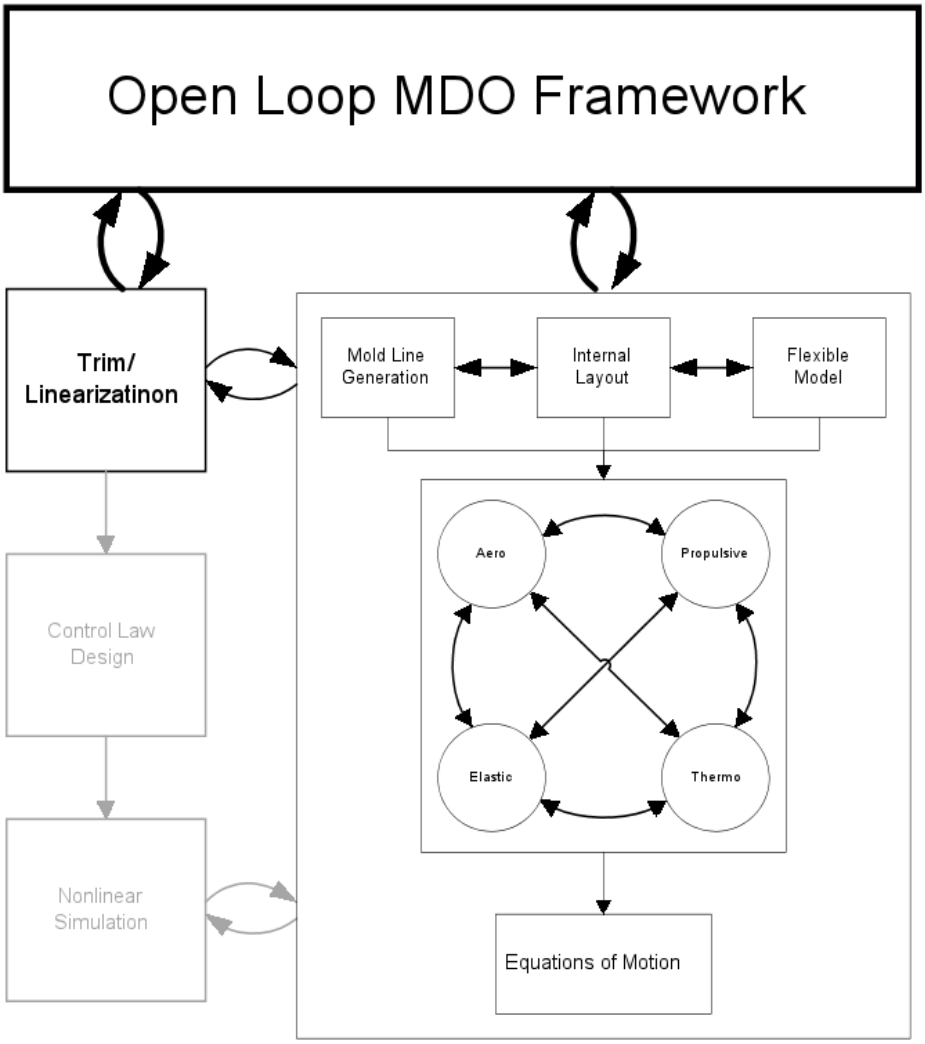

Figure 8.4: Open Loop MDO Framework

Figure 8.4 shows the addition of the Open Loop Multidisciplinary Design and Optimization Framework to the previous routine. This framework is responsible for generating static trade studies (trimmed and untrimmed) and optimization to the ASTEP Model. The Control Law Design and Nonlinear Simulation components are grayed in this diagram because they are not utilized by the open loop routine. More details of this routine can be seen in Section 8.2.

Figure 8.5 shows the addition of the Closed Loop Multidisciplinary Design and Optimization Framework to the previous routine. This framework is responsible for generating dynamic trade studies and optimizations to the ASTEP Model. More details of this routine can be seen in Section 8.2 .

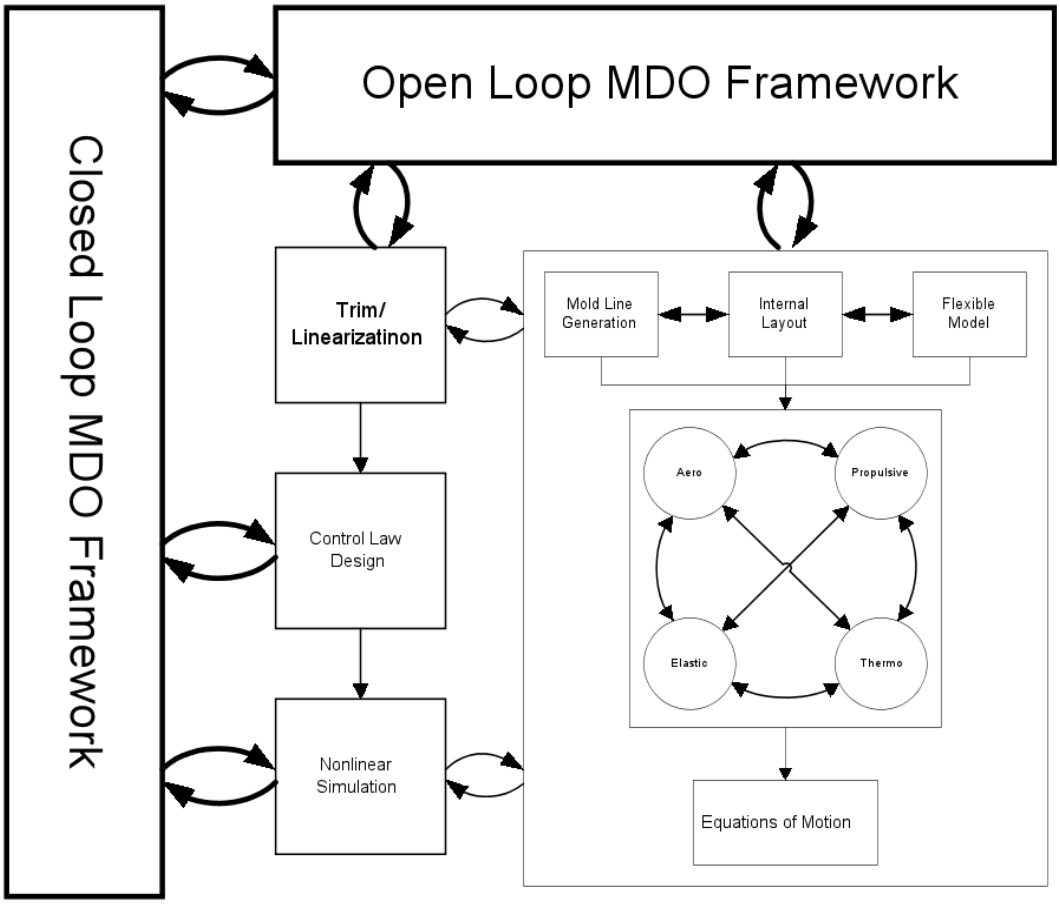

Figure 8.5: Closed Loop MDO Framework

8.2 Multidisciplinary Modeling, Analysis, Design and Optimization Methodology

The design methodology presented in this section can be broken down into two categories: (1) open loop design and (2) closed loop design. Closed loop analysis is inherently more expensive than open loop analysis, so where possible it is beneficial to attempt to predict the closed loop behavior utilizing open loop analysis/design methods. The following flow charts demonstrates the steps undertaken in doing an initial design.

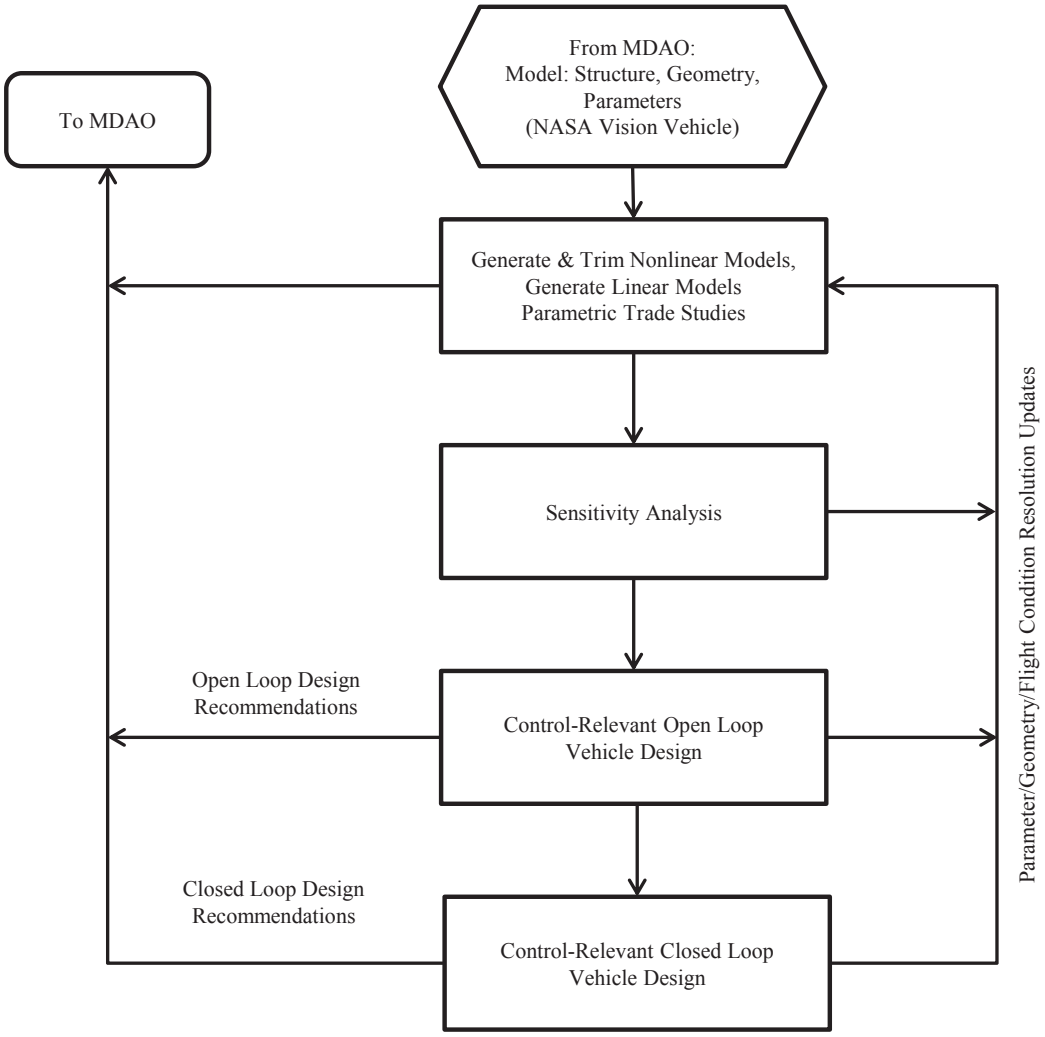

Figure 8.6: Design Methodology Overview

The flow diagram in Figure 8.6 gives a broad overview of the vehicle design process. In this case, an initial vehicle geometry is generated by the multi-disciplinary optimization group at NASA, and the redesigned vehicle will be returned to them.

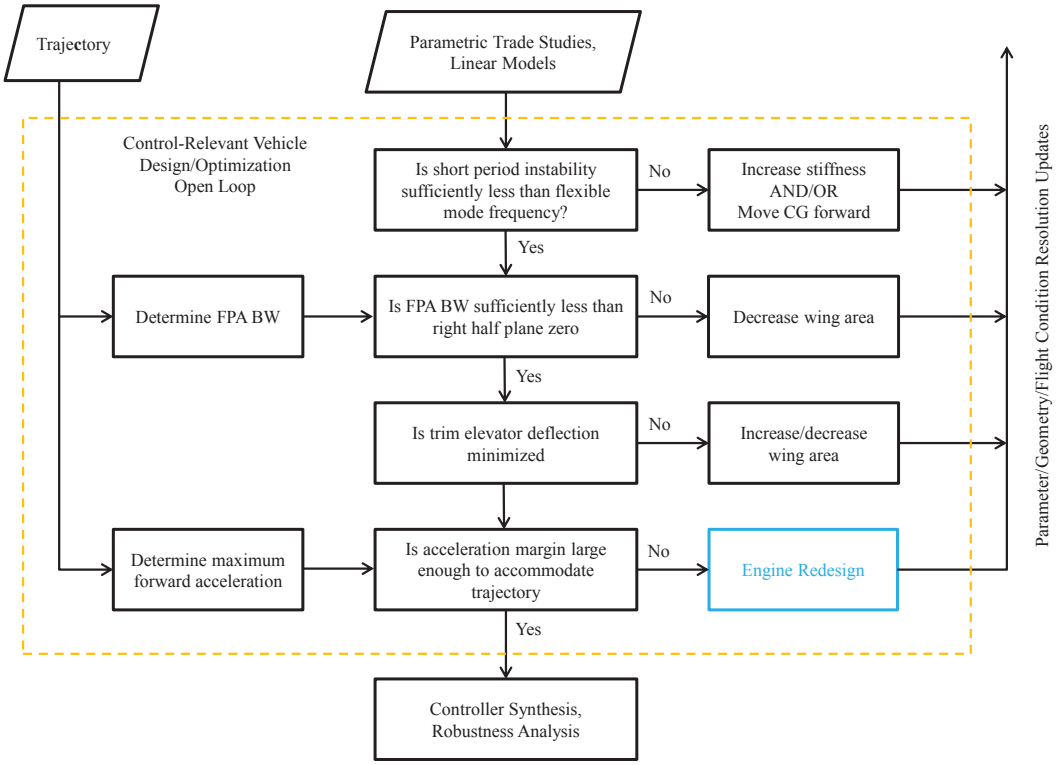

Figure 8.7: Open Loop Design Methodology

Figure 8.7 demonstrates methodology for the Control-Relevant Open Loop Vehicle Design block from Figure 8.6.

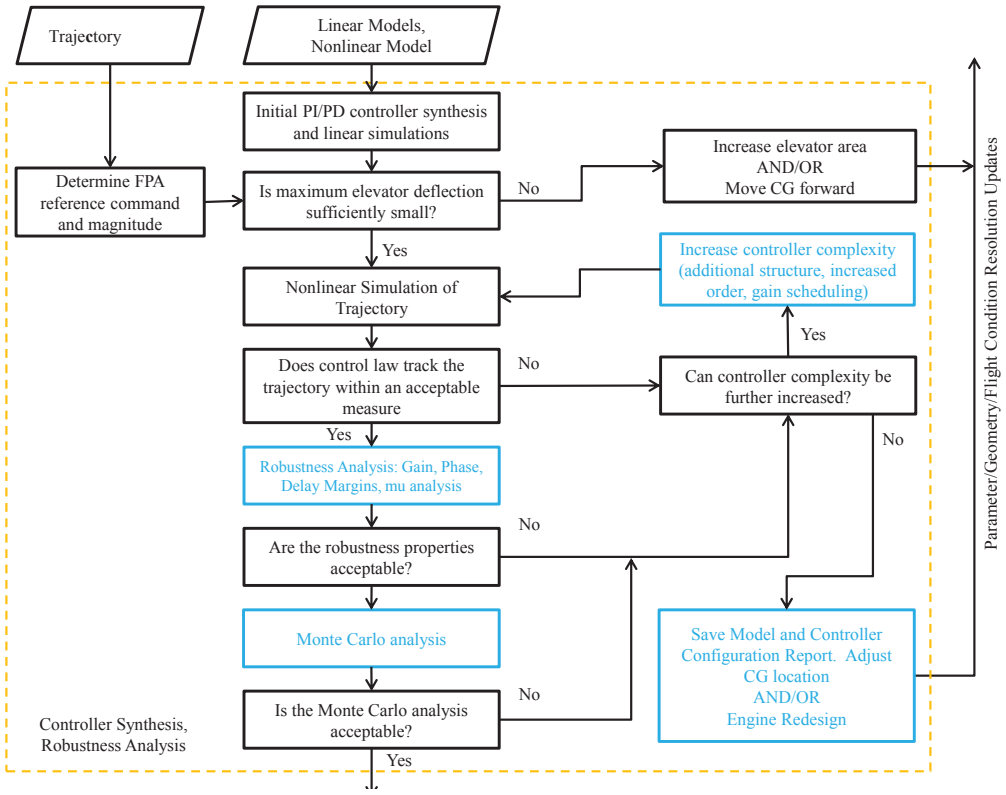

Figure 8.8: Closed Loop Design Methodology

Figure 8.8 demonstrates methodology for the Control-Relevant Closed Loop Vehicle Design block from Figure 8.6. Note that it may be necessary to iterate upon the procedures within Figures 8.7 & 8.8 several times before satisfactory results are achieved.

The primary aim of these flow diagrams is to enable a systematic means of parameter selection that will ensure vehicle closure. Closure refers to the ability of the vehicle to fly the desired trajectory, with the specified amount of fuel, subject to a set of constraints such as elevator deflection, heating, etc. This report will attempt to desire to the following closure case:

- Reaching the staging flight conditions ($\bar{q} = 200$ psf, Mach 7.5-8)
- 200,000 lbm of hydrogen fuel
- Elevator deflections less than 10 degrees in either direction
- Combustor temperatures less that 4500 rankine
- Sensitivities of less that 6 dB for all frequencies for all small signal design point

8.3 EI-CG Design

In order to have good closed loop sensitively properties, it is generally necessary to have the first flexible mode frequency time times greater than the instability (see 11.2, Rules of Thumb).

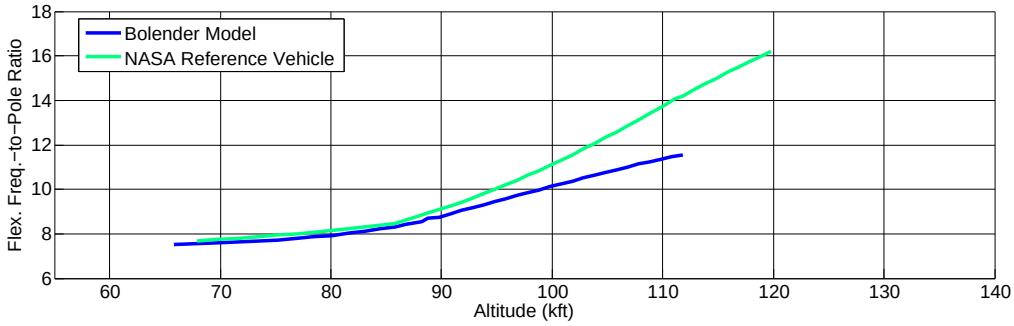

Figure 8.9: OL Comparisons: Flex. Mode Freq.-to-Pole Ratio

Figure is repeated here for convenience. It can be see that for low Mach numbers, the ratio is less than 10, closer to 8. From Figurefig:FlowOpenLoop, the first stage of the flow diagram shows that either an increase in stiffness or a forward movement of the CG will be necessary to remedy this problem.

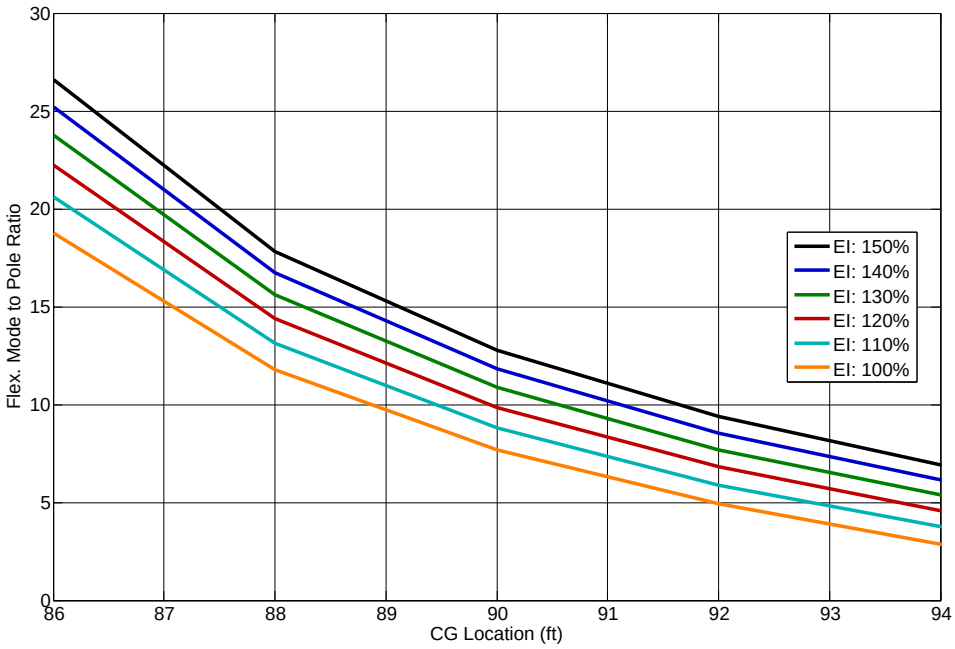

Figure 8.10: CG-EI Trade Study: Flex. Mode Freq.-to-Pole Ratio

Figure 8.10 show a trade study for CG and EI conducted at Mach 5.5, 70,000 ft. The nominal CG is located at 90 ft, and the EI value is 100 %. CG is measured in terms of feet from the nose of the vehicle, so a decrease in the value corresponds to a forward movement of the CG. We see that the trends of the trade study match what is recommended by the flow diagram.

While a small forward movement of the CG (roughly 1 foot) would satisfy our ratio of 10 criteria, lets assume that option is not available (only because EI results in a more interesting scenario). We can see that an increase in EI by 25 % would be enough to satisfy our rule of thumb. Since E (young's modulus) is a function of the material, lets attempt to modify I, the second moment of inertial in order to increase the stiffness. The equation for the moment of inertia for a beam is given by:

$$I_{xx} = \frac{1}{12} bh^1 2 \tag{8.1}$$

where b is the base of the beam and h is the height. For our 2D model, b = 1. For a 25 % increase in I_{xx}, we get the following equation:

$$\frac{b}{b_o} = \sqrt[3]{1.25} = 1.077 \tag{8.2}$$

Therefore a 7.7 % increase in the thickness of the titanium beam will yield the desired stiffness. From 4.6 we see that this will correspond 7,700 lbm increase to the structure of the vehicle and a 1.1 % increase to the 700,000 lb total mass of the vehicle.

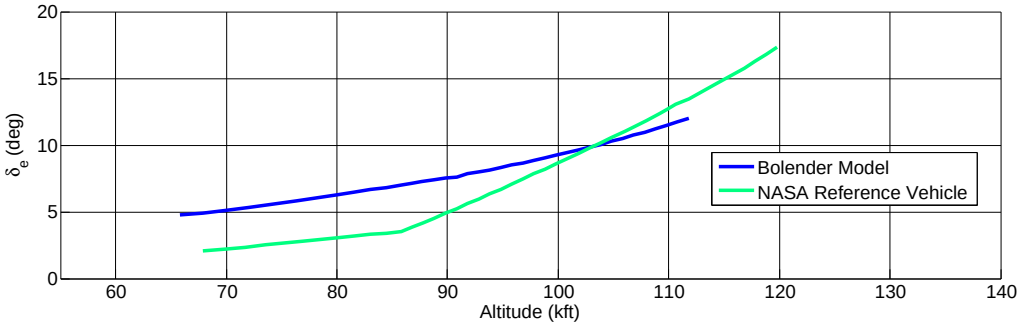

Figure 8.11: OL Comparisons: Trim Elevator Deflection

Figure 7.4 is repeated here for convenience. From this figure we can see the trim elevator deflection is roughly 17 degrees at 120,000 ft. This is too large to meet our closure requirements. Elevator deflection needs to be reduced by roughly 7 degrees. From Figurefig:FlowOpenLoop, the third stage of the flow diagram shows that either an increase in either wing area,wing mounting angle, or elevator area will be necessary.

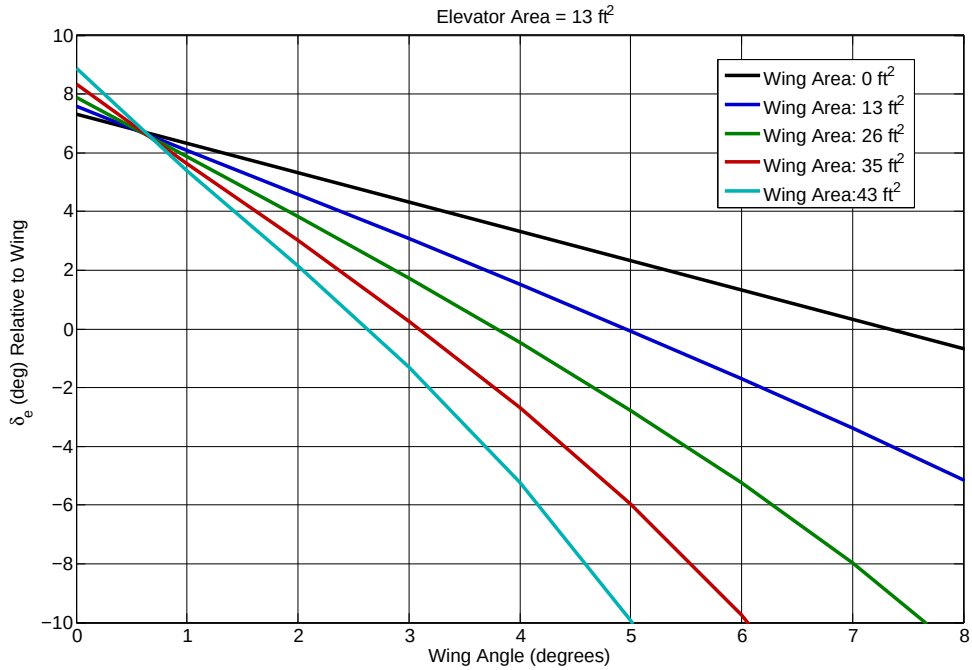

Figure 8.12: Wing Trade Study: Elevator Deflection

Figure 8.12 shows a wing design study conducted at Mach 8, 85 kft. The nominal parameters are a wing mounting angle of 2 degrees, and a wing area of 26 ft. This corresponds to roughly

a 4 degree trim elevator deflection. We would like to choose some combination of wing area and mounting angle that would yield a -3 degree trim elevator deflection. One combination that is apparent from this plot is a wing angle of 4 degrees, and area of 35 sqft. Lets examine what impact these choices have on other properties.

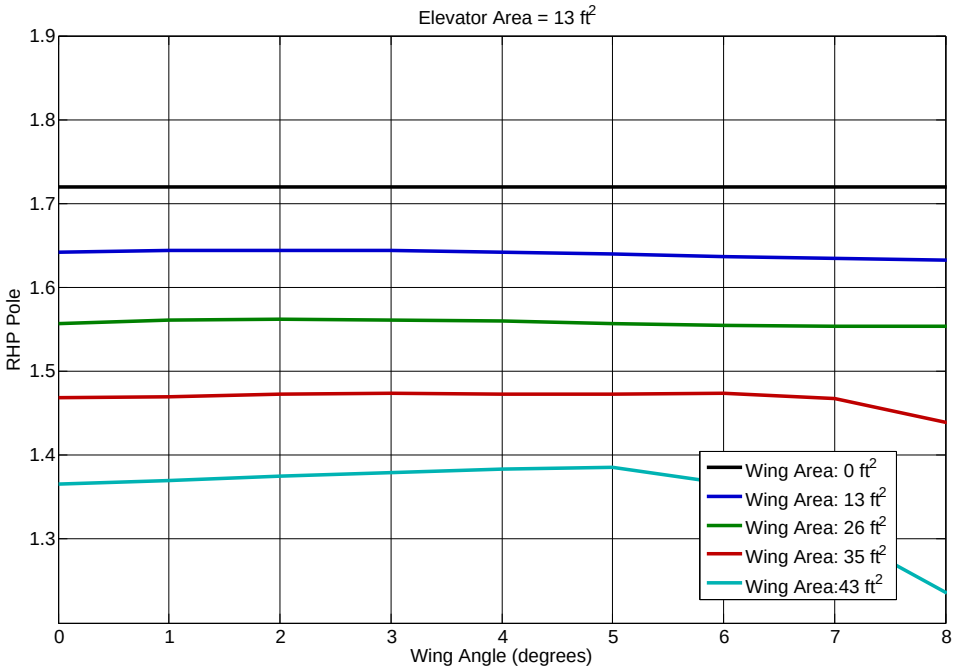

Figure 8.13: Wing Trade Study: Instability

From Figure8.13 we see that choosing a wing angle of 4 degrees, and area of 35 sqft (vs 2 degrees, and area of 25 sqft) decreases the instability from 1.53 to 1.48, a slight improvement.

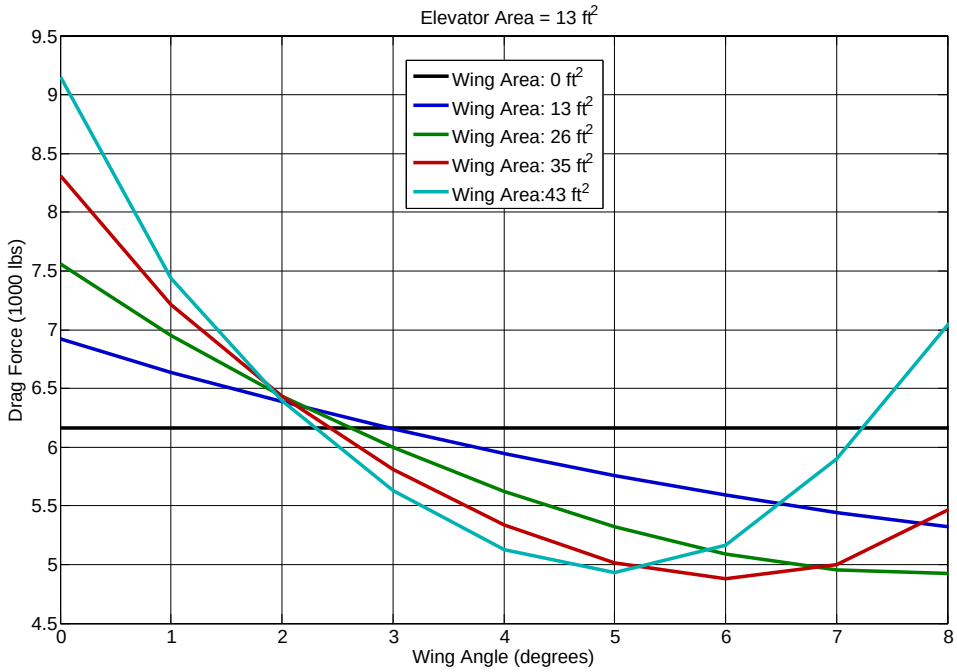

Figure 8.14: Wing Trade Study: Drag

From Figure8.14 we see that choosing a wing angle of 4 degrees, and area of 35 sqft (vs 2 degrees, and area of 25 sqft) decreases the trim drag from 6430 lbf to 5300 lbf a significant improvement. However, from this plot it is apparent that it should be possibly to further reduce the drag with a larger increase in wing angle. This may be worth examining on a second iteration. For now the chosen values will be maintained.

8.5 Engine Design

Choosing engine parameters is a somewhat complicated process. Rather than looking at a trimmed results, it becomes easier to examine the following scenario:

- Mach 8, 85kft
- Rigid Model
- AOA = FPA = 0
- H_2 Flow Rate = 73 lbm/s
- Vary the Inlet Height and the Diffuser Area Ratio
- Internal Nozzle is chosen based on the Diffuser Ratio (see 4.56)

The three items of primary importance are the net thrust (thrust-drag), the combustor temperature, and the combustor mach number. Ideally the engine parameters should maximize net thrust, maximize combustor mach number, and minimize combustor temperature. The following three figures will demonstrate the process

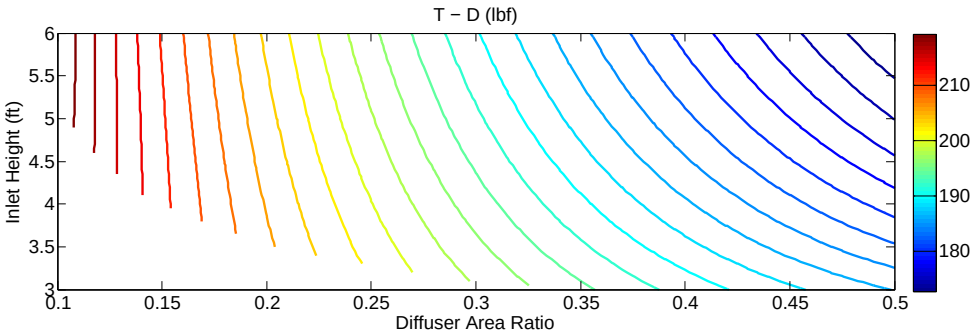

Figure 8.15: Engine Trade Study: Net Thrust

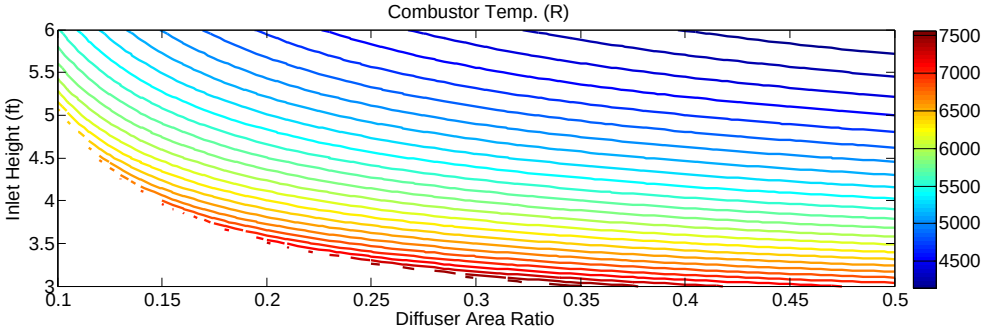

Figure 8.16: Engine Trade Study: Combustor Temperature

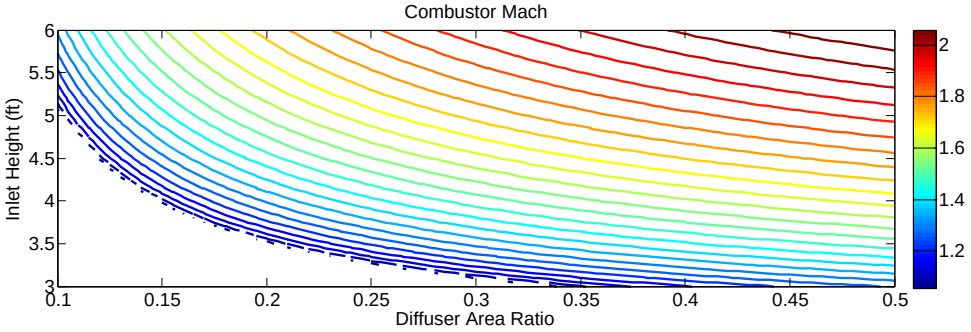

Figure 8.17: Engine Trade Study: Combustor Mach No.

Deriving results from these types of contour plots can sometimes be difficult, but in this case, it is relatively straightforward.

1. Being at Figure 8.15 at the very bottom right corner that [0.5, 3] and there is a teal contour associated with it
2. At this point, the combustor temperature is very large (6800 R), and the combustor mach number is very small (near 1.3
3. Now, follow the teal contour on Figure 8.15 up to the point [0.35, 6]. Keep in mind this was a constant net thrust contour line
4. At [0.35, 6], the combustor temperature is much lower (4500 R) and the combustor mach number is much larger (near 1.9)

Conclusion: In general, larger inlets with more diffuser contraction yield better engines than smaller inlets with less diffuser contraction, even though they both yield the same net thrust. Furthermore, more benefit is typically gained by increasing the inlet height than increasing the diffuser contraction. One limitation associated with this conclusion is that it did not take into account the increase in mass that would accompany a larger inlet

Based on Figure 7.11, the engine needs to be redesigned to lower the Mach number within the combustor. As a first pass attempt, we will change the engine inlet height from 5 ft to 6 ft.

Chapter 9

NONLINEAR SIMULATION

Finally the design methodology will be tested on the nonlinear model. An extensive explantation on the control law design can be found in 11.12.

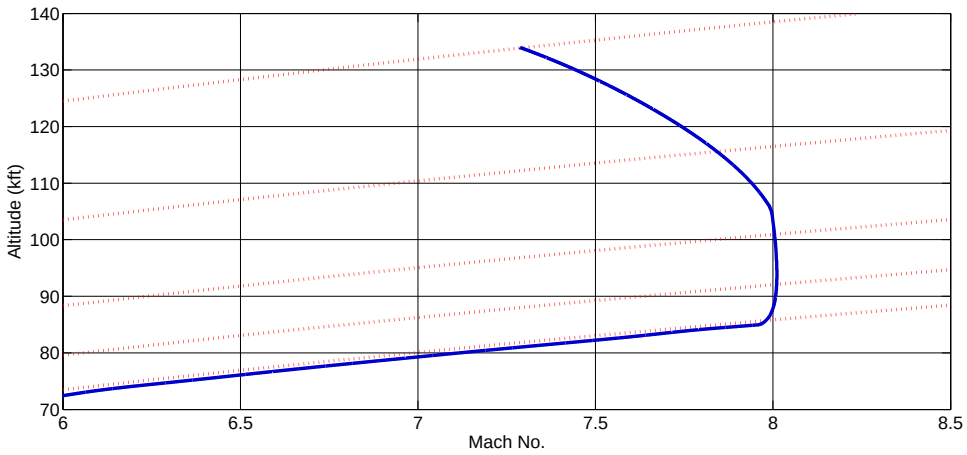

Figure 9.1: Nonlinear Sim: Trajectory

- The current design does not reach $\bar{q} = 200$ psf staging area of Mach 7.5-8.0
  - The design is relatively close at Mach 7.3
- The control law exhibits good command following for constant dynamic pressure.
- The control law exhibits good command following for constant Mach until 105 kft.

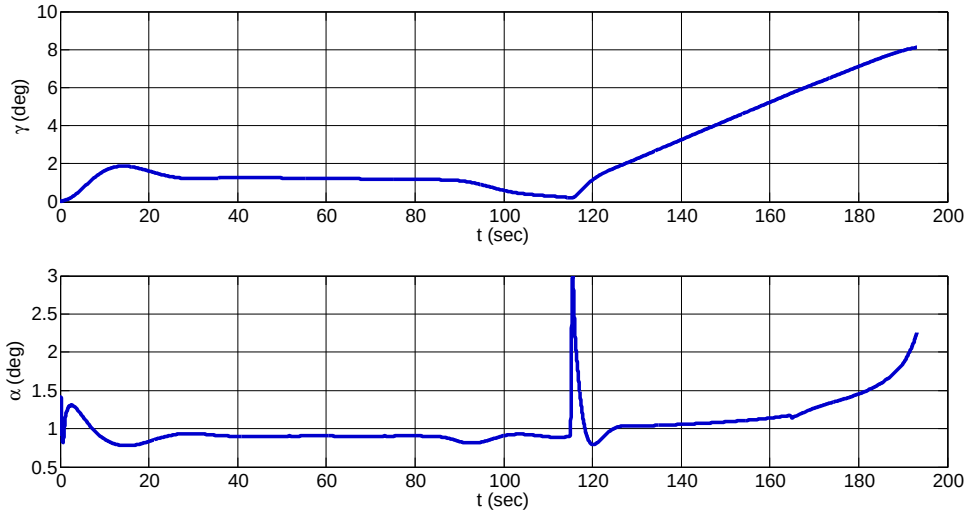

Figure 9.2: Nonlinear Sim: AOA & FPA

- Relatively low bandwidth FPA commands are necessary to follow this trajectory
  - Elevator to FPA control law bandwidth could potentially be lowered:
  - Lower BW control law could allow for a slightly more flexible model
  - Lower BW control law could allow for a smaller elevator (peak elevator deflection is inversely proportional to control BW)
- Small change in AOA vs trim prediction

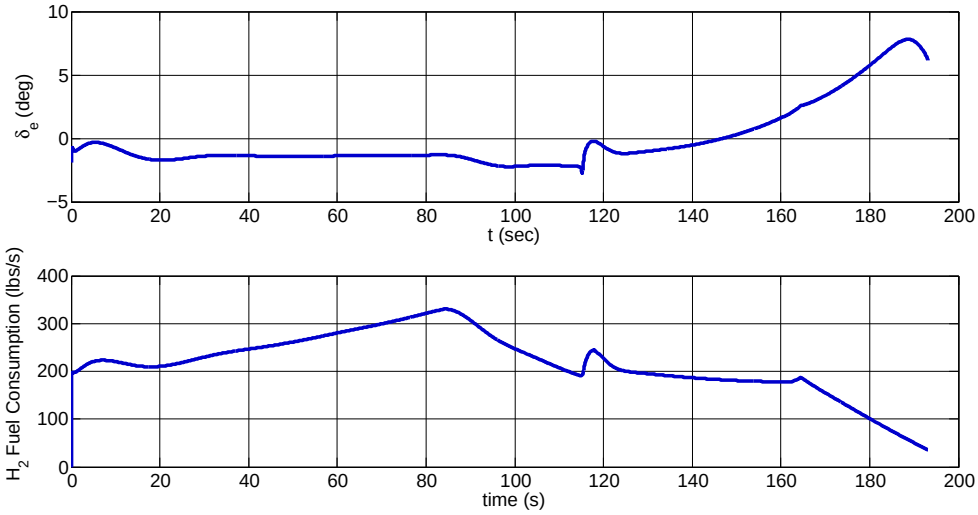

Figure 9.3: Nonlinear Sim: Elevator & Fuel Rate

- Elevator deflection is becoming large near the staging trajectory
  - May consider increasing wing area, mounting angle, or elevator area to reduce the deflection

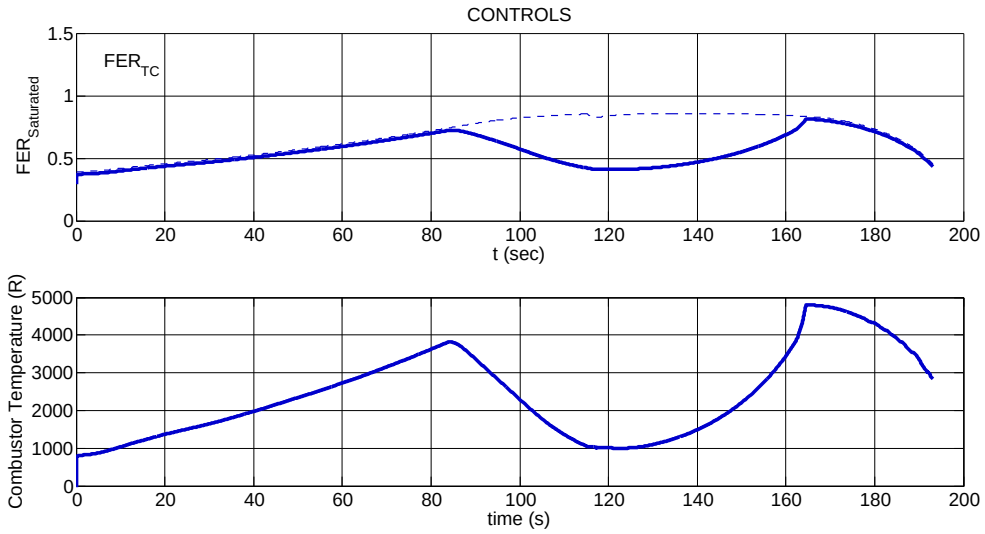

Figure 9.4: Nonlinear Sim: FER & Combustor Temperature

- Thermal choking is limiting engine performance early in the trajectory, and after 165 seconds (at an altitude of 105 kft).
- Temperature limitations of 4500 R is being exceeded slightly near the end of the trajectory.
- Both of the previous items point towards enlarging the engine inlet to increase performance and reduce temperature
  - Increasing engine size increases mass and total drag, therefore increasing fuel rate consumption.

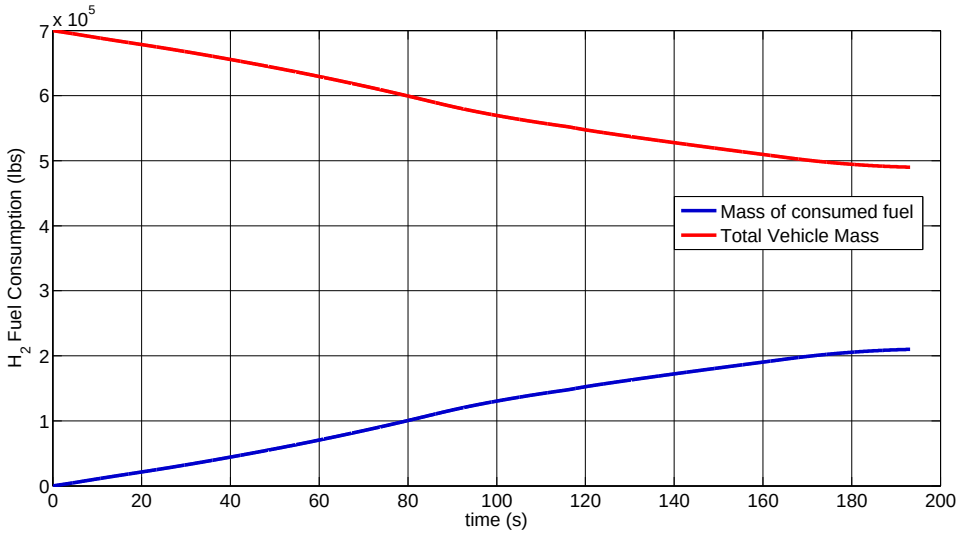

Figure 9.5: Nonlinear Sim: Fuel Consumption

- Slightly more fuel is consumed (5%) than was originally carried by the vehicle (200,000 lbs). This will necessitate an increase in the vehicle size to accommodate the additional volume.

Nonlinear Simulation Conclusions While the initial open loop design methodology did not yield a completely closed vehicle, it did yield a vehicle that was nearly closed. The vehicle needs a larger inlet to increase performance and reduce engine temperatures. This will necessitate more fuel, and therefore an increase in the vehicle size. Finally, an increase in elevator area would be appropriate to ensure sufficient elevator saturation margins.

Chapter 10

ANALYSIS OF 6DOF MODEL

In this section, the results from the 3DOF model will be compared to a newly developed 6DOF Hypersonic Vehicle model developed for NASA Ames Research Center. The Aerospace Vehicles Simulation and Analysis Program for Hypersonics (ASAP-HYP) developed by VSI Aerospace aims to provide rapid modeling and analysis capability for use in early stage vehicle design studies [93]. A brief over of the code will be provided below, followed by a comparison of trim results to the 3DOF model.

10.1 Model Description

The ASAP-HYP model (aeromesh pictured in Figure 10.1) is modeled using a modified Newtonial Impact method described below [93]:

$$M_L = \frac{M_\infty \cos\theta_L}{\left[1 + \left(\frac{\gamma-1}{2}\right) M_\infty^2 \sin^2\theta_L\right]^{\frac{1}{2}}} \tag{10.1}$$

where θ_L is the local panel inclination. The pressure coefficient for each panel is then calculated as follows:

$$C_{pL} \simeq 2\sin^2\theta_L \left[\sqrt{\left(\frac{\gamma+1}{4}\right)^2 + \left[(M_\infty^2 - 1)\sin^2\theta_L\right]^{-1}} + \frac{\gamma+1}{4}\right] \tag{10.2}$$

for positive inclination angles and

$$\theta_{exp} = \frac{2}{\gamma-1} - \left(\frac{1}{M_1} - \frac{1}{M_L}\right) \tag{10.3}$$

$$C_{pL} = \frac{2\theta_{exp}}{\gamma(M_1\theta_{exp})^2}\left(\left(1 - \frac{\gamma-1}{2}M_1\theta_{exp}\right)^{\frac{2\gamma}{\gamma-1}} - 1\right) \tag{10.4}$$

for negative angles, where M_1 can be either the local Mach number of the appropriate upstream panel, or M_∞. Many of the other modeling methods (including viscous effects, plume modeling) are similar to those utilized in the Bolender model. The structural model is highly integrated with the aerodynamic mesh as can be seen in Figure 10.2. The structural model is then passed to a NASTRAN routine to generate the eigenvalues and eigenvector used to represent structural deformations to the model.

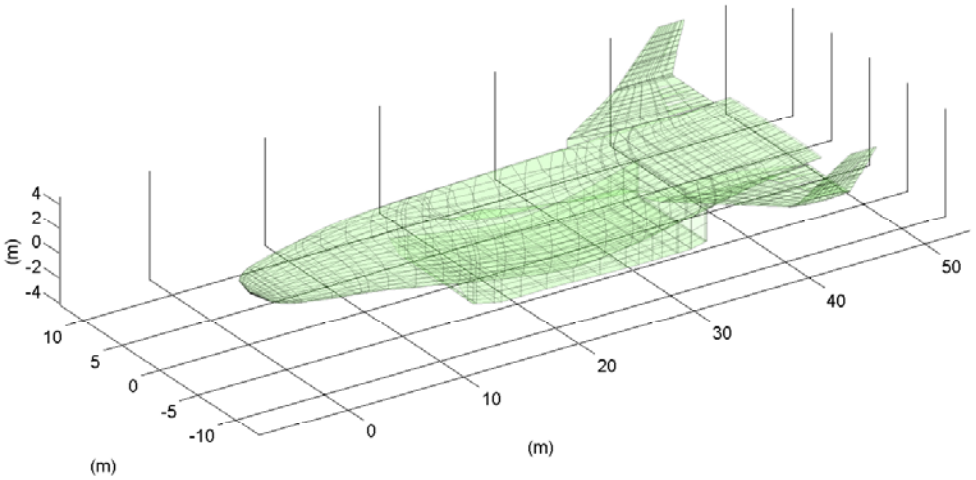

Figure 10.1: ASAP-Hyp AeroMesh

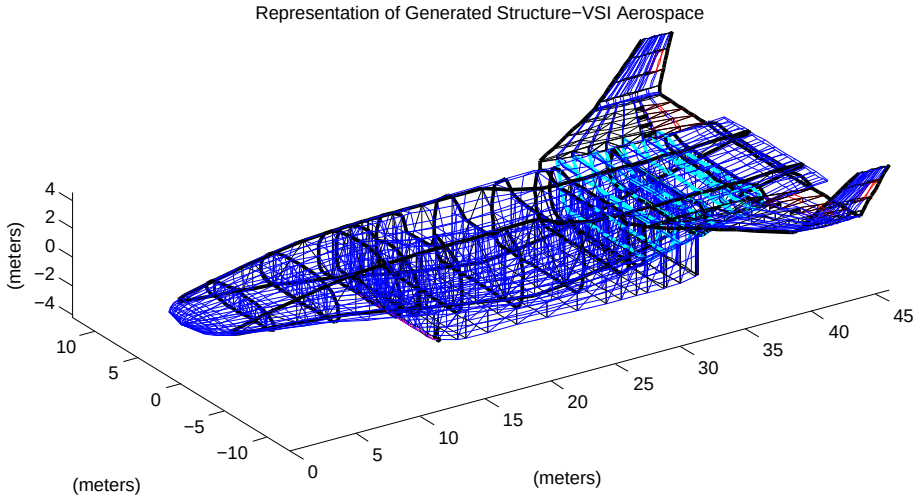

Figure 10.2: ASAP-Hyp Structural Modeling

10.2 ASAP-HYP Issues

Due to the recent release of the ASAP-HYP code to NASA, several issues have noted by author when attempting to utilize the toolsuite:

1. Numerous aspects of the GUI are not in a functional state. Some of these are documented within the user manual [93], some are not.
    - Engine modeling options including 1.5D modeling, chemistry effects, viscous effects, thermal effects.
    - Unsteady aerodynamic modeling
2. Generating a Mach/Altitude trajectory grid will only trim a small subset of the points chosen by the user
3. The trim routine is programmed with a large amount of logic to ensure trim when utilizing a nonlinear constrained optimization. However, the method routinely fail to find a trim point, and the code will default to a simplex method that not properly finding trim, but returning data indicating it is.
4. Due to the aerodynamic modeling methodology used, it is possible to have non-smooth aerodynamic data when attempting to linearize about an equilibrium conation. This can lead to invalid linear models being generated by the code.

10.3 Trim Analysis

This section will examine some basic trim/linearization results and compare them with previous 3DOF results.

Figures 10.3-10.8 demonstrate the static and dynamic properties across the swimmable region for the 6DOF Vision Vehicle model. Of particular note is the "jittery" nature of the trim results, particularly for the static properties. This is primarily due to how the model handles the flow turn within the inlet, as well as the aerodynamic modeling of small local inclination angles.

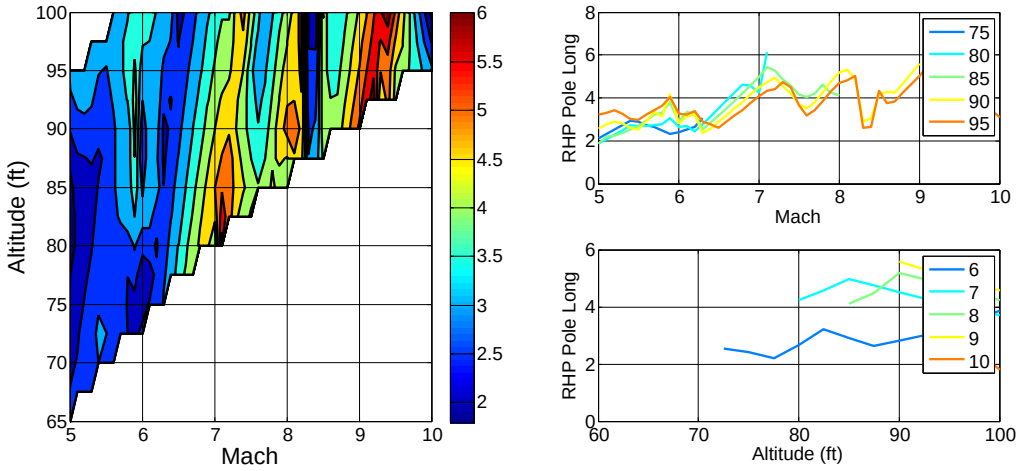

Figure 10.3: Trimmable Region: 6DOF Short Period Instability

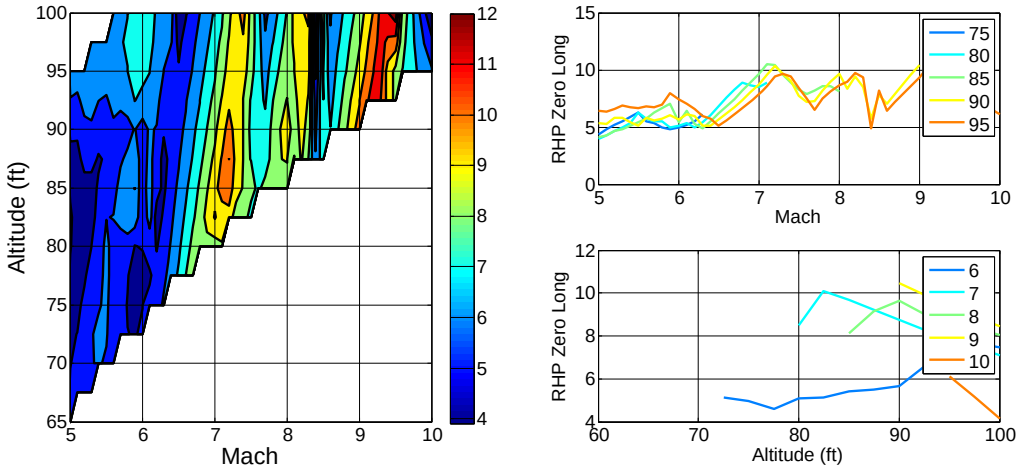

Figure 10.4: Trimmable Region: 6DOF Nonminimum Phase Zero

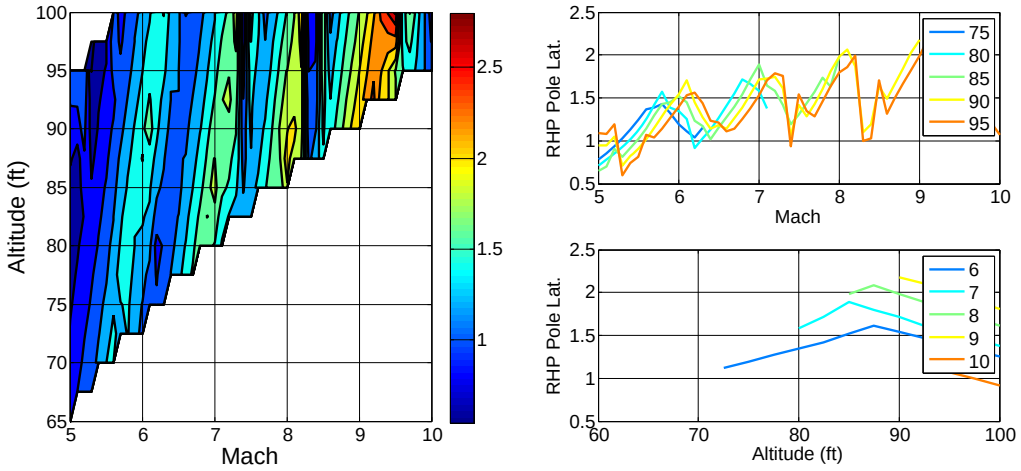

Figure 10.5: Trimmable Region: 6DOF Lateral Instability

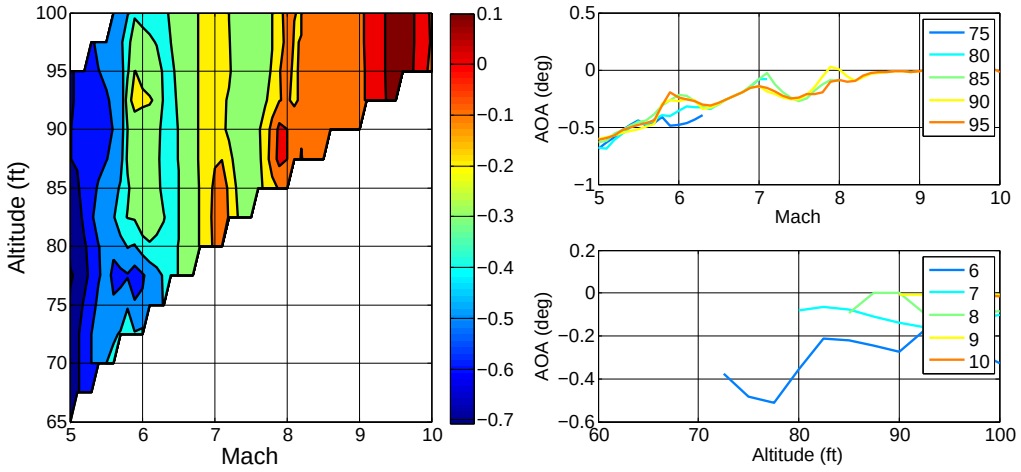

Figure 10.6: Trimmable Region: 6DOF AOA

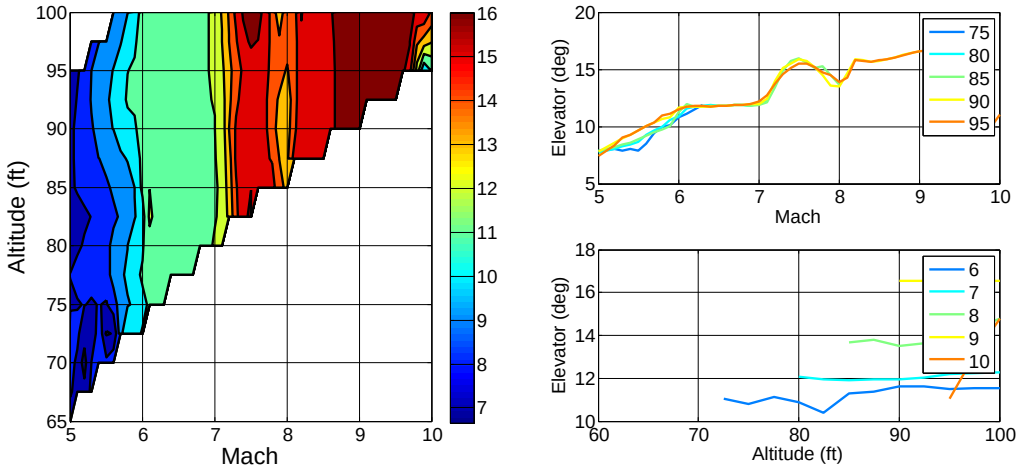

Figure 10.7: Trimmable Region: 6DOF Elevator Deflection

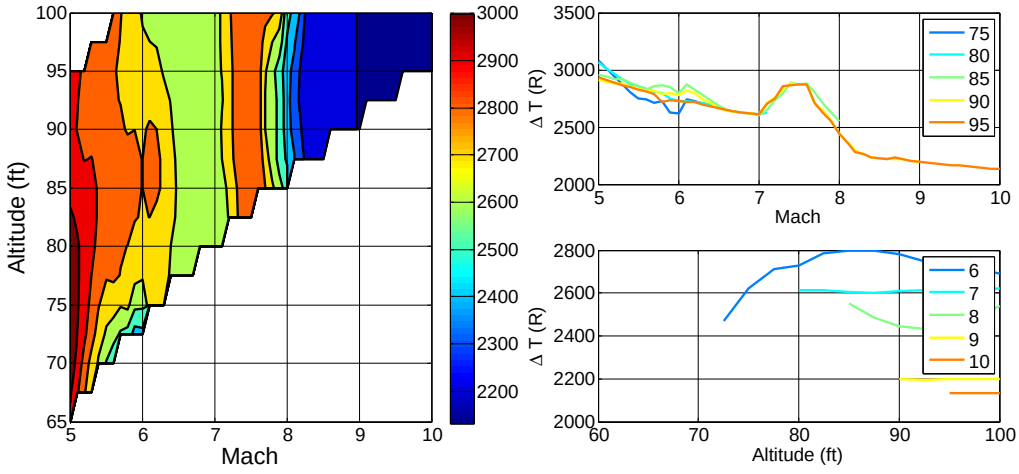

Figure 10.8: Trimmable Region: 6DOF Combustion Temp. Change

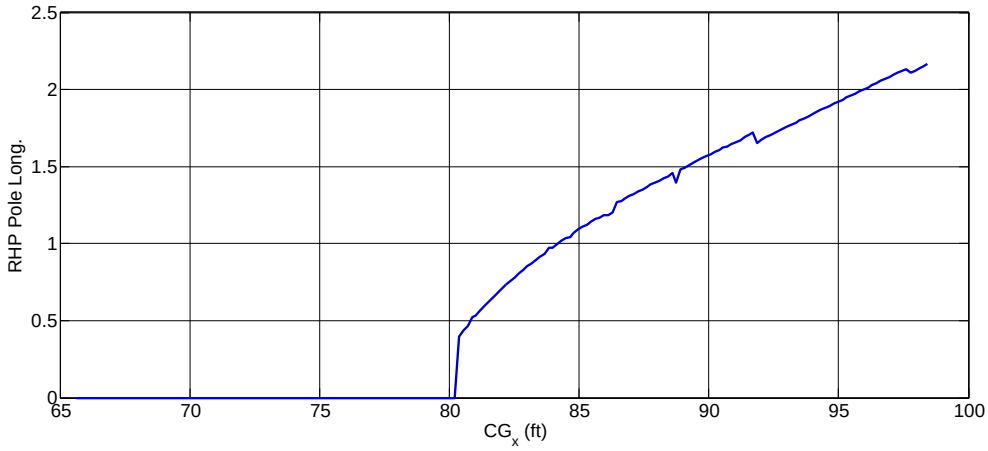

Figure 10.9: CG Trade Study: 6DOF Short Period Instability

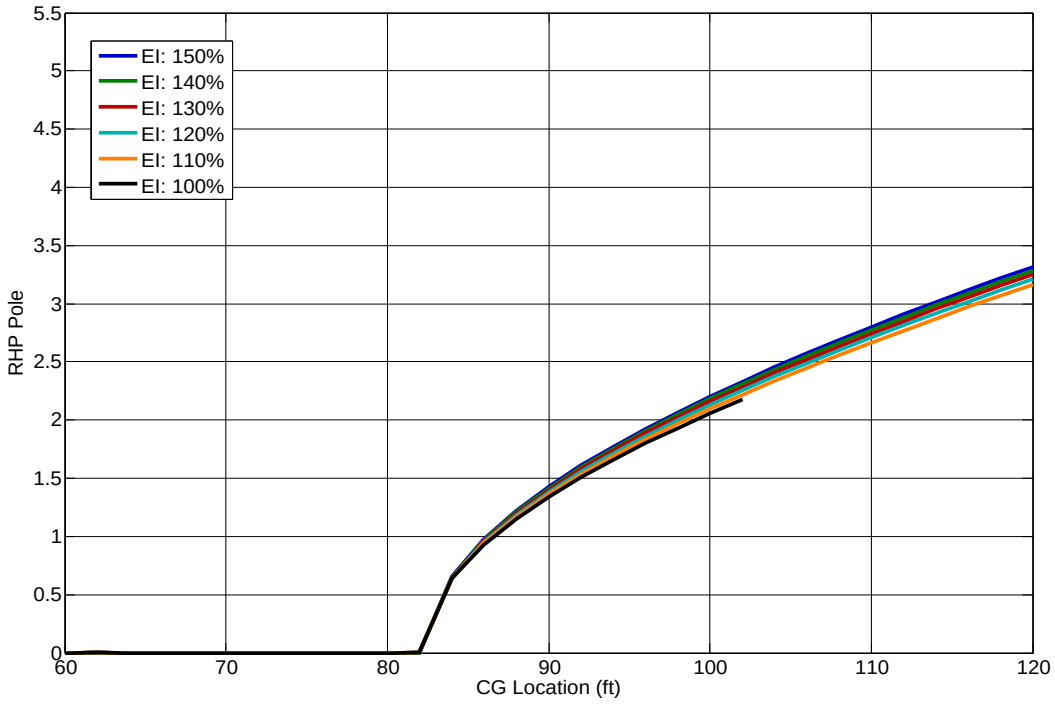

Figure 10.10: CG-EI Trade Study: 3DOF Short Period Instability

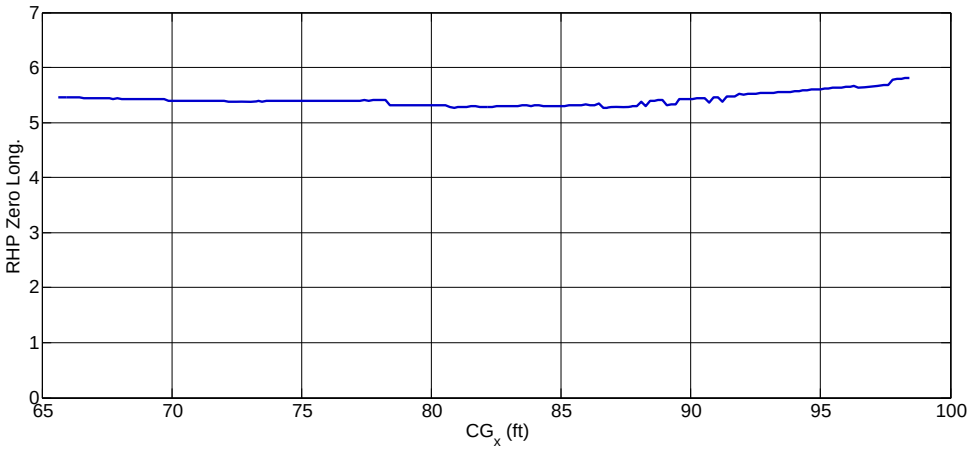

Figure 10.11: CG Trade Study: 6DOF Nonminimum Phase Zero

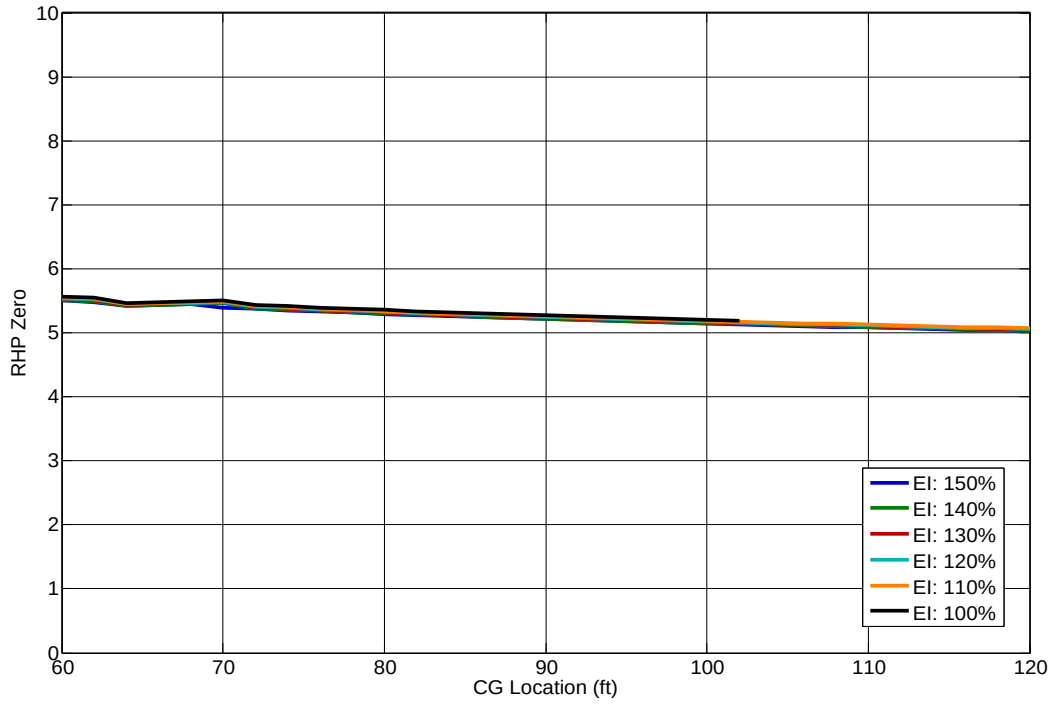

Figure 10.12: CG-EI Trade Study: 3DOF Nonminimum Phase Zero

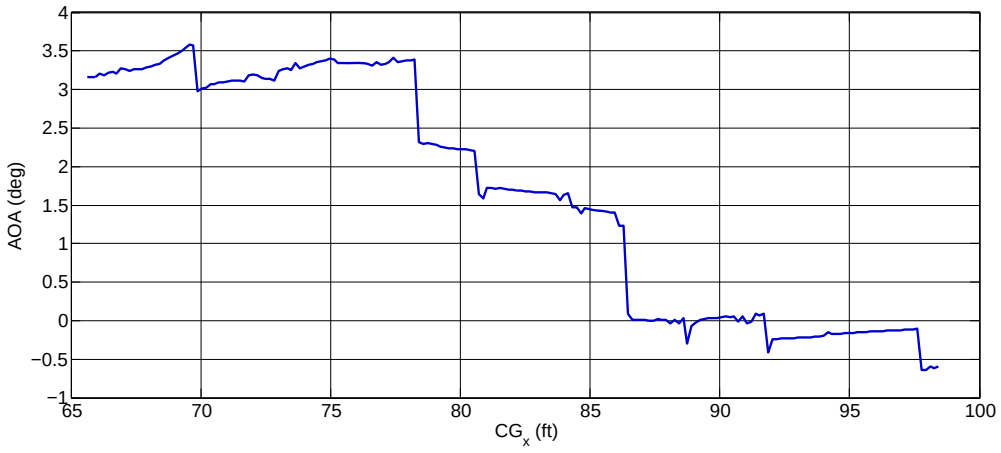

Figure 10.13: CG Trade Study: 6DOF AOA

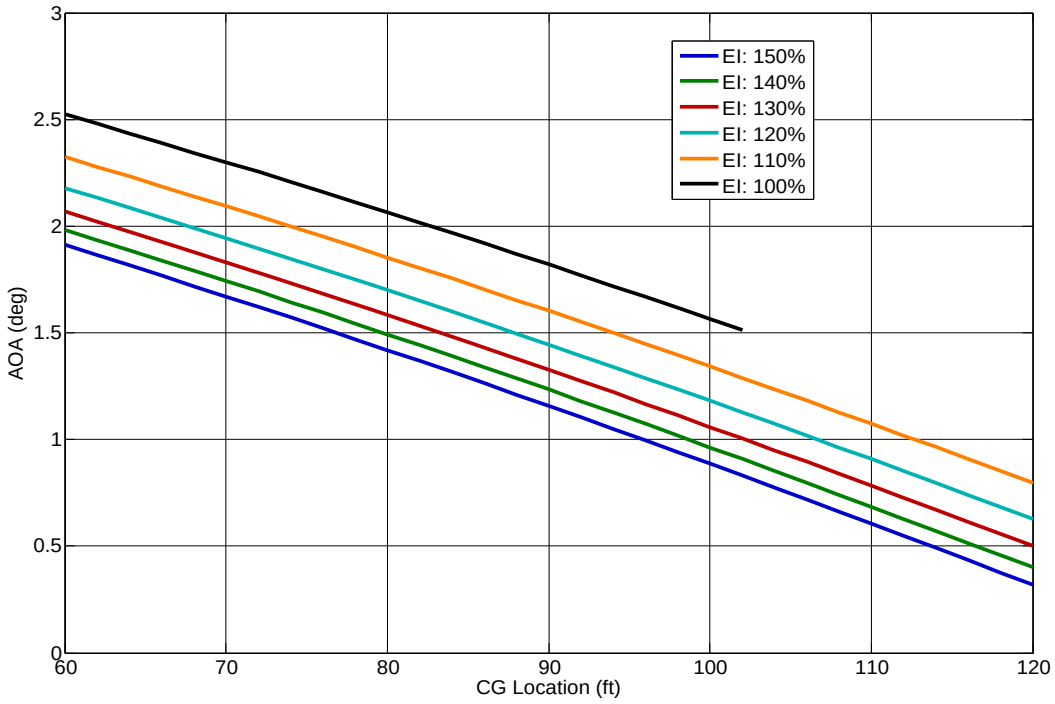

Figure 10.14: CG-EI Trade Study: 3DOF AOA

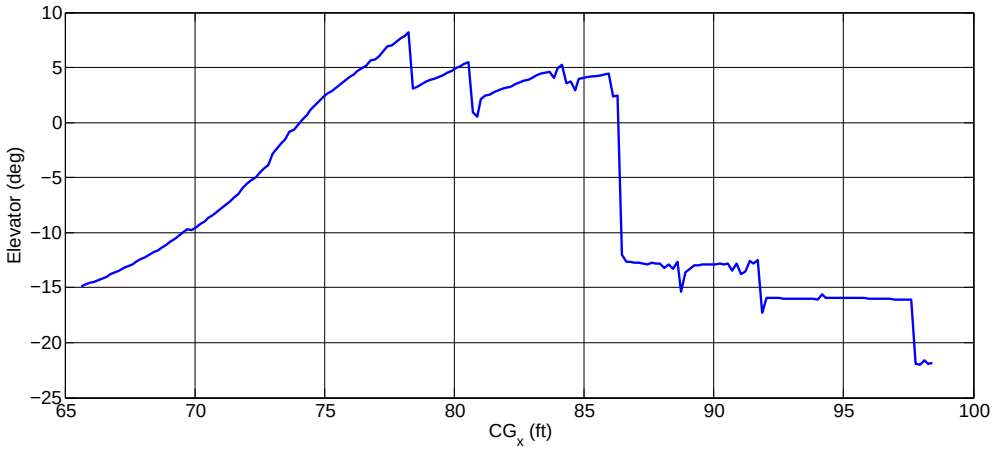

Figure 10.15: CG Trade Study: 6DOF Elevator Deflection

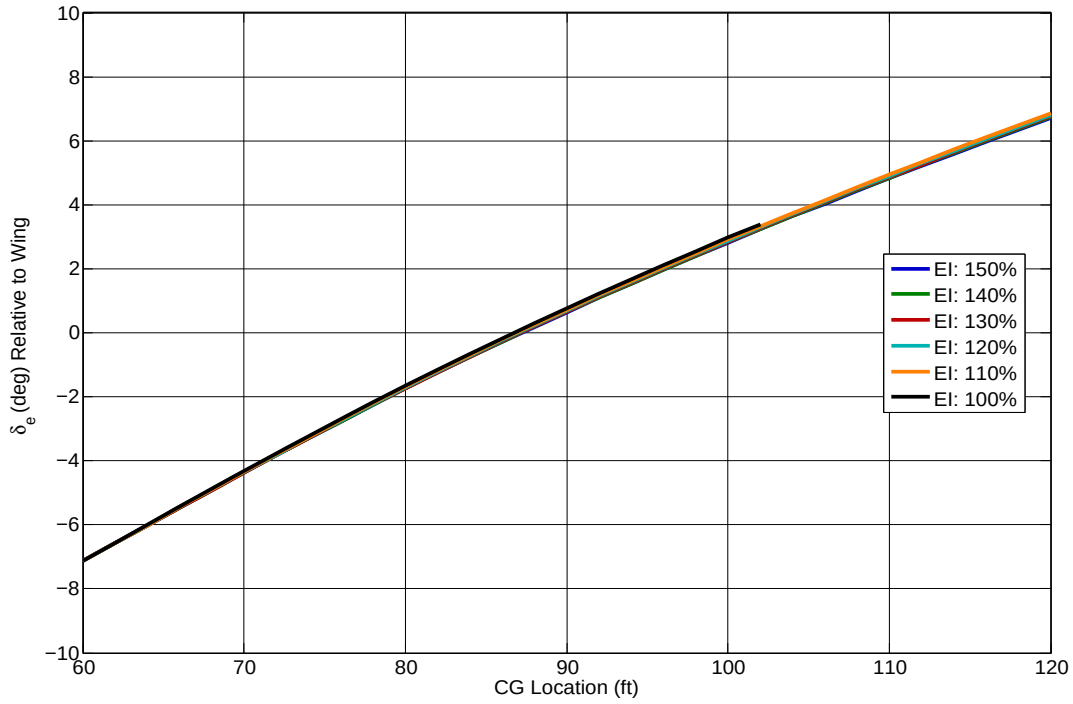

Figure 10.16: CG-EI Trade Study: 3DOF Elevator Deflection

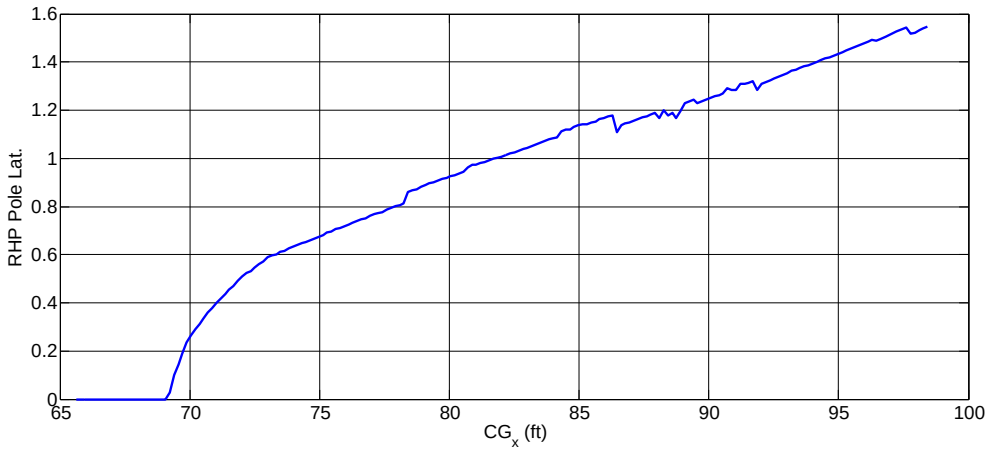

Figure 10.17: CG Trade Study: 6DOF Lateral Instability

Figures 10.9-10.16 demonstrated the impact of CG location on the static and dynamic properties of the vehicle. Figures 10.9-10.12 show excellent agreement between the dynamic properties for the two models. Figures 10.13-10.16 show that while the general trends for the static properties are the same, there are some large differences between the two models. This is primarily attributed to the different cowl door modeling techniques used between the two models (translating vs rotating cowl door), and the approximation each model makes to handle both spillage and flow turn within the inlet. Figure 10.17 has been included to show the impact of CG shift on the lateral instability. It is interesting to note that in longitudinal center of pressure is located at roughly 81 feet from the nose, while the lateral center of pressure is located at 69 feet from the nose. The lateral instability is be smaller than the longitudinal instability for all CG locations.

Chapter 11

SUMMARY AND FUTURE DIRECTIONS

11.1 Summary

Within this report an overview of scramjet-powered hypersonic vehicle research as well as modeling and control challenges. A generic nonlinear 3DOF longitudinal dynamical model has been analyzed over a range of two-state to orbit trajectory. Control system design issues and tradeoffs have been described. A vehicle design methodology has been proposed and tested on the nonlinear simulator.

11.2 Future Work

Due to the nature of the scramjet engine, direct measurements of key input and output variables (Mach, temperature) related to its operation will not be available. A flush-air-data systems (FADS) array of sensors will need to be utilized to derive estimates to important inviscid variables through potentially thick boundary layers. Modeling and control methodologies that are robust to this estimation uncertainly while maintaining a relatively safe operating margin for the engine need to be developed.

REFERENCES

[1] M. Bolender, M. Oppenheimer, and D. Doman, "Effects of Unsteady and Viscous Aerodynamics on the Dynamics of a Flexible Air-Breathing Hypersonic Vehicle," in *AIAA Atmospheric Flight Mechanics Conf, & Exhibit, Paper No. 2007-6397*.

[2] J. T. Parker, A. Serrani, S. Yurkovich, M. A. Bolender, and D. B. Doman, "Control-oriented modeling of an air-breathing hypersonic vehicle," *AIAA J. Guidance, Control, and Dynamics*, 2007.

[3] M. A. Bolender and D. B. Doman, "A Non-Linear Longitudinal Dynamical Model of an Air-Breathing Hypersonic Vehicle," *J. Spacecraft and Rockets*, vol. 44 no. 2, pp. 373 – 387, 2007.

[4] M. Oppenheimer, D. Doman, M. Bolender, and T. Skujins, "A Flexible Hypersonic Vehicle Model Developed with Piston Theory," in *AIAA Atmospheric Flight Mechanics Conference and Exhibit, Paper No. 2007-6396*, 2007.

[5] M. Bolender and D. Doman, "Modeling Unsteady Heating Effects on the Structural Dynamics of a Hypersonic Vehicle," in *AIAA Atmospheric Flight Mechanics Conf. and Exhibit, Paper No. 2006-6646*, 2006.

[6] D. Doman, M. Oppenheimer, and M. Bolender, "Progress in Guidance and Control Research for Space Access and Hypersonic Vehicles," Air Force Research Laboratory (AFRL), Wright Patterson Air Force Base, pp. 1 – 18, Tech. Rep., 2006.

[7] D. Sigthorsson, A. Serrani, S. Yurkovich, M. Bolender, and D. Doman, "Tracking Control for an Overactuated Hypersonic Air-Breathing Vehicle with Steady State Constraints," in *AIAA Guidance, Navigation and Control Conf., Paper No. 2006-6558*, 2006.

[8] T. Adami, J. Zhu, M. Bolender, D. Doman, and M. Oppenheimer, "Flight Control of Hypersonic Scramjet Vehicles Using a Differential Algebraic Approach," in *AIAA Guidance, Navigation and Control Conf., Paper No. 2006-6559*, 2006.

[9] T. Williams, M. A. Bolender, D. Doman, and O. Mortaya, "An Aerothermal Flexible Mode Analysis of a Hypersonic Vehicle," Airforce Research Laboratory (AFRL), Wright Patterson Air Force Base, pp. 1 – 25,, Tech. Rep., 2006.

[10] D. D. M. Bolender, "A non-linear model for the longitudinal dynamics of a hypersonic air-breathing vehicle," *AIAA Guidance, Navigation and Control Conference*, vol. 5, no. AIAA-2005-6255, pp. 3937–58, 2005.

[11] A. Rodriguez, J. Dickeson, O. Cifdaloz, R. McCullen, J. Benavides, S. Sridharan, A. Kelkar, J. Vogel, and D. Soloway, "Modeling and Control of Scramjet-Powered Hypersonic Vehicles: Challenges, Trends, & Tradeoffs," in *AIAA Conf. on Guidance, Navigation and Control, AIAA-2008-6793*, 2008.

[12] J. Dickeson, A. Rodriguez, S. Sridharan, D. Soloway, and J. Benavides, "Decentralized control of an airbreathing scramjet-powered hypersonic vehicle," in *AIAA Guidance, Navigation and Control Conf.*, AIAA-2009-6281.

[13] J. Dickeson, A. Rodriguez, S. Sridharan, D. Soloway, A. Korad, J. Khatri, J. Benavides, A. Kelkar, and J. Vogel, "Control-relevant modeling, analysis, and design for scramjet-powered hypersonic vehicles," in 16^{th} *AIAA/DLR/DGLR Inter. Space Planes and Hyperosnics Sys. and Tech. Conf.*, AIAA-2009-7287.

[14] J. Dickeson, A. Rodriguez, S. Sridharan, J. Benavides, D. Soloway, A. Kelkar, and J. Vogel, "Decentralized control of an airbreathing scramjet-powered hypersonic vehicle," in *AIAA Conf. on Guidance, Navigation and Control, AIAA-2009-6281*, 2009.

[15] J. J. Dickeson, A. A. Rodriguez, and S. Sridharan, "Elevator sizing, placement, and control-relevant tradeoffs for hypersonic vehicles," in *Submitted to the AIAA Guidance, Navigation, and Control Conference, 2010*, 2010.

[16] S. Sridharan, J. Dickeson, and A. Rodriguez, "Impact of plume modeling on the design and control for a class of air-breathing hypersonic ve," in *AIAA Guidance, Navigation and Control Conf.*, AIAA-2011.

[17] E. Baumann, C. Bahm, B. Strovers, R. Beck, and M. Richard, "The X-43A Six Degree of Freedom Monte Carlo Analysis," in 46^{th} *AIAA Aerospace Sciences Meeting and Exhibit, Paper No. 2008-203*, 2008.

[18] C. Peebles, *Road to Mach 10: Lessons Learned from the X-43A Flight Research Program*. AIAA, 2008.

[19] C. R. McClinton, "X-43 Scramjet Power Breaks the Hypersonic Barrier Dryden Lectureship in Research for 2006," 44^{th}*AIAA Aerospace Sciences Meeting and Exhibit, Paper No. 2006-1*, 2007.

[20] V. L. Rausch, C. R. McClinton, and J. L. Crawford, "Hyper-X Flight Validation of Hypersonic Airbreathing Technology," Technical Report, NASA Hyper-X Program Office, pp. 1 – 7, 1997.

[21] W. H. Heiser, D. T. Pratt, D. Daley, and U. Mehta, *Hypersonic Airbreathing Propulsion*. AIAA, 1994.

[22] M. Davis and J. White, "X-43A Flight-Test-Determined Aerodynamic Force and Moment Characteristics at Mach 7.0 ," *J. of Spacecraft and Rockets*, vol. 45, no. 3, pp. 472–484, 2008.

[23] J. Anderson, *Hypersonic and High-Temperature Gas Dynamics*. Second Edition. AIAA, 2006.

[24] E. A. Morelli, S. D. Derry, and M. S. Smith, "Aerodynamic Parameter Estimation for Flight 2 of the X-43A," *Joint Army Navy NASA Air Force JANNAF Conf.*, 2005.

[25] S. D. Holland, W. C. Woods, and W. C. Engelund, "Hyper-X Research Vehicle Experimental Aerodynamics Test Program Overview," *J. Spacecraft and Rockets*, vol. 38, no. 6, pp. 828–835, 2001.

[26] Q. Wang and R. F. Stengel, "Robust Nonlinear Control of a Hypersonic Vehicle," *J. Guidance, Control, and Dynamics*, pp. 577 – 585, 2000.

[27] B. Cobleigh, "Development of the X-33 Aerodynamic Uncertainty Model," NASA/TP-1998-206544, April 1998.

[28] H. Buschek and A. Calise, "Uncertainty Modeling and Fixed-Order Controller Design for a Hypersonic Vehicle Model," *J. Guidance, Control and Dynamics*, pp. 42 – 48, 1997.

[29] J. J. Bertin, *Hypersonic Aerothermodynamics*. AIAA Education Series, 1994.

[30] H. Buschek and A. J. Calise, "Robust Control of Hypersonic Vehicles Considering Propulsive and Aeroelastic Effects," *Paper No. AIAA-1993-3762*, pp. 1 – 11, 1993.

[31] J. Bertin, J. Periaux, and J. Ballmann, *Advances in Hypersonics: Defining the Hypersonic Environment, Volume 1*. Birkhauser Boston, 1992.

[32] J. Bertin, J. Periaux, and J. Ballman, *Advances in Hypersonics: Modeling Hypersonic Flows, Volume 2*. Birkhauser Boston, 1992.

[33] J. Bertin, J. Periaux, and J. Ballmann, *Advances in Hypersonics: Computing Hypersonic Flows, Volume 3*. Birkhauser Boston, 1992.

[34] J. Young and J. Underwood, "Development of Aerodynamic Uncertainties for the Space Shuttle Orbiter ," *J. of Spacecraft and Rockets*, vol. 20, no. 6, pp. 513–517, 1983.

[35] J. T. Parker, A. Serrani, S. Yurkovich, M. Bolender, and D. Doman, "Approximate feedback linearization of an air-breathing hypersonic vehicle," Air Force Research Laboratory (AFRL), Wright Patterson Air Force Base, pp. 1 – 20, Tech. Rep., 2005.

[36] K. Groves, D. Sigthorsson, A. Serrani, S. Yurkovich, M. Bolender, and D. Doman, "Reference Command Tracking for a Linearized Model of an Air-Breathing Hypersonic Vehicle," in *AIAA Guidance, Navigation and Control Conf. and Exhibit, Paper No. 2005-6144*, 2005.

[37] K. Groves, A. Serrani, S. Yurkovich, M. Bolender, and D. Doman, "Anti-Windup Control for an Air-Breathing Hypersonic Vehicle Model," in *AIAA Guidance, Navigation, and Control Conf. and Exhibit, Paper No. AIAA 2006-6557*, 2006.

[38] M. A. Bolender and D. B. Doman, "A Non-Linear Model for the Longitudinal Dynamics of a Hypersonic Air-Breathing Vehicle," in *Proceedings of the 2005 Guidance, Navigation and Control Conf., Paper No. 2005-6255*, 2005.

[39] J. Heeg, T. A. Zieler, A. S. Potozky, C. V. Spain, and W. C.Englend, "Aerothermoelastic Analysis of a NASP Demonstrator Model, Report No. NAS 1.15109007," NASA, Tech. Rep., 1993.

[40] D. Johnson, C. Hill, S. Brown, and G. Batts, "Natural Environment Application for NASP-X-30 design and mission planning ," in 31^{st} *Aerospace Sciences Meeting and Exhibit, Paper No. 1993-851*, 1993.

[41] D. Johnson, "Beyond the X-30 - Incorporating mission capability ," in 3^{rd} *Int. Aerospace Planes Conf., Paper No. 1991-5078*, 1991.

[42] J. D. Shaughnessy, S. Z. Pinckney, J. D. McMinn, C. I. Cruz, and M. L. Kelley, "Hypersonic Vehicle Simulation Model: Winged-Cone Configuration, No. 102610," NASA, Tech. Rep., 1990.

[43] J. J. McNamara and P. P. Friedmann, "Aeroelastic and Aerothermoelastic Analysis of Hypersonic Vehicles: Current Status and Future Trends," 48^{th} *AIAA/ASME/ASCE/AHS/ASC Structures, Structural Dynamics, and Materials Conference, Paper No. 2007-2013*, 2007.

[44] P. P. Friedmann, J. J. McNamara, B. Thuruthimattam, and I. Nydick, "Aeroelastic Analysis of Hypersonic Vehicles," *J. Fluids and Structures*, pp. 681 – 712, 2004.

[45] J. McNamara, P. Friedmann, K. Powell, B. Thuruthimattam, and R. Bartels, "Aeroelastic and Aerothermoelastic Vehicle Behavior in Hypersonic Flow ," in *AIAA/CIRA* 13^{th} *International Space Planes and Hypersonics Systems and Tech. Conf., Paper No. AIAA-2005-3305*, 2005.

[46] B. Pamadi, G. Brauckmann, M. Ruth, and H. Fuhrmann, "Aerodynamic Characteristics, Database Development, and Flight Simulation of the X-34 Vehicle," *J. of Spacecraft and Rockets*, vol. 38, pp. 334–344, 2001.

[47] C. Bahm, E. Baumann, J. Martin, D. Bose, R. E. Beck, and B. Strovers, "The X-43A Hyper-X Mach 7 Flight 2 Guidance, Navigation, and Control Overview and Flight Test Results," in *AIAA/CIRA International Space Planes and Hypersonic Systems and Technologies Conference*, 2005, pp. 682 – 704.

[48] J. Hank, J. Murphy, and R. Mutzman, "The X-51A Scramjet Engine Flight Demonstration Program ," in 15^{th} *AIAA International Space Planes and Hypersonic Systems and Technologies Conf, Paper No. AIAA-2008-2540*, 2008.

[49] S. Walker, M. Tang, S. Morris, and C. Mamplata, "Falcon HTV-3X - A Reusable Hypersonic Test Bed," in 15^{th} *AIAA International Space Planes and Hypersonic Systems and Tech. Conf., Paper No. AIAA-2008-2544*, 2008.

[50] S. Walker, J. Sherk, D. Shell, R. Schena, J. Bergmann, and J. Gladbach, "The DARPA/AF Falcon Program: The Hypersonic Technology Vehicle 2 (HTV-2) Flight Demonstration Phase," in 15^{th} *AIAA International Space Planes and Hypersonic Systems and Technologies Conf., Paper No. 2008-2539*, 2008.

[51] S. H. Walker and F. Rodgers, "Falcon Hypersonic Technology Overview," *AIAA/CIRA* 13^{th} *International Space Planes and Hypersonics Systems and Technologies, Paper No. 2005-3253*, 2005.

[52] "Blackswift Program Solicitation," Defense Advanced Research Projects Agency, Tech. Rep., February, 2008.

[53] B. Fidan, M. Mirmirani, and P. Ioannou, "Flight Dynamics and Control of Air-Breathing Hypersonic Vehicles: Review and New Directions," in 12^{th} *AIAA/AHI Space Planes and Hypersonic Systems and Technologies Conf. Paper No. 2003-7081*, 2003.

[54] R. T. Voland, L. D. Huebner, and C. R. McClinton, "X-43A Hypersonic Vehicle Technology Development," Technical Report, NASA Langley Research Center, Hampton, VA, Report No. IAC-05-D2.6.01, 2005.

[55] A. Kumar, J. P. Drummond, C. R. McClinton, and J. L. Hunt, "Research in Hypersonic Airbreathing Propulsion at the NASA Langley Research Center," National Aeronautics and Space Administration (NASA), Report No. ISABE-2001-4, Tech. Rep., 2001.

[56] J. Heeg, M. Gilbert, and A. Pototzky, "Active Control of Aerothermoelastic Effects for a Conceptual Hypersonic Aircraft," *J. of Aircraft*, pp. 453 – 458, 1993.

[57] M. G. Gilbert, J. Heeg, A. S. Potozky, C. V. Spain, D. L. Scistmann, and H. J. Dunn, "The Application of Active Controls Technology to a Generic Aircraft Configuration," National Aeronautics and Space Administration (NASA), Report No. NAS 1.15101689, Tech. Rep., 1990.

[58] J. Heeg, M. G. Gilbert, and A. S. Pototzky, "Active Control of Aerothermoelastic Effects for a Conceptual Hypersonic Vehicle," in *AIAA Guidance, Navigation and Control Conf., Paper No. AIAA-1990-3337, pp. 200 – 208*, 1990.

[59] A. S. Potozky, C. V. Spain, D. L. Spain, and T. E. Noll, "Application of Unsteady Aeroelastic Analysis Techniques on the National Aerospace Plane," NASA, Report No. NASA 1.15100648, Tech. Rep., 1988.

[60] D. Glass, "Ceramic Matrix Composite (CMC) Thermal Protection Systems (TPS) and Hot Structures for Hypersonic Vehicles ," in 15^{th} *AIAA International Space Planes and Hypersonic Systems and Technologies Conf/*, 2008.

[61] [Online]. Available: http://www.uq.edu.au/hypersonics/index.html?page=19501

[62] M. Smart, N. Hass, and A. Paull, "Flight Data Analysis of the HyShot 2 Scramjet Flight Experiment," *AIAA Journal*, vol. 44, Issue 10, pp. 2366–2375, 2006.

[63] S. Walker, F. Rodgers, A. Paull, and D. V. Wie, "HyCAUSE Flight Test Program," in 15^{th} *AIAA International Space Planes and Hypersonic Systems and Technologies Conf., Paper No. 2008-2580*, 2008.

[64] X-43A Mishap Investigation Board, "Report of Findings: X-43A Mishap," Technical Report, pp. 1 – 33, 2003.

[65] D. E. Reubush, L. T. Nguyen, and V. L. Rausch, "Review of X-43A Return to Flight Activities and Current Status," *12th AIAA International Space Planes and Hypersonic Systems and Technologies, Paper No. 2003-7085*, 2003.

[66] L. Marshall, G. Corpening, and R. Sherrill, "A Chief Engineer's View of the NASA X-43A Scramjet Flight Test," in *AIAA/CIRA* 13^{th} *International Space Planes and Hypersonics Systems and Tech. Conf., Paper No. AIAA-2005-3332* , 2005.

[67] C. Bahm, E. Baumann, J. Martin, D. Bose, R. Beck, and B. Strovers, "The X-43A Hyper-X Mach 7 Flight 2 Guidance, Navigation, and Control Overview and Flight Test Results," in *AIAA/CIRA* 13^{th} *International Space Planes and Hypersonics Systems and Technologies Conf., Paper No. AIAA-2005-3275*, 2005.

[68] S. M. Ferlemann, C. R. McClinton, K. E. Rock, and R. T. Voland, "Hyper-X Mach 7 Scramjet Design, Ground Test and Flight Results," Technical Report, NASA Langley Research Center, Hampton, VA, pp. 1 – 9, 2004.

[69] C. E. Cockrell, W. C. Englelund, R. D. Bittner, T. N. Jentink, A. D. Dilley, and A. Frendi, "Integrated Aeropropulsive Computational Fluid Dynamics Methodology for the Hyper-X Flight Experiment," *J. of Spacecraft and Rockets*, pp. 836 – 843, 2001.

[70] L. Marshall, C. Bahm, G. Corpening, and R. Sherril, "Overview With Results and Lessons Learned of the X-43A Mach 10 Flight," in *AIAA/CIRA* 13^{th} *International Space Planes and Hypersonics Systems and Technologies Conf., 2005-3336*.

[71] R. C. Rogers, A. T. Shih, and N. E. Hass, "Scramjet Engine Flowpath Development for the Hyper-X Mach 10 Flight Test," National Aeronautics and Space Administration (NASA), Report No. ISABE-2005-1025, Tech. Rep., 2005.

[72] J. Davidson, F. Lallman, J. D. McMinn, J. Martin, J. Pahle, M. Stephenson, and J. Selmon, "Flight Control Laws for NASA's Hyper-X Research Vehicle," *AIAA Guidance, Navigation, and Control Conference and Exhibit, 1999-4124*, 1999.

[73] E. Morelli, S. Derry, and M. Smith, "Aerodynamic Parameter Estimation for the X-43A (Hyper-X) from Flight Data," in *AIAA Atmospheric Flight Mechanics Conf. and Exhibit, Paper No. AIAA-2005-5921*, 2005.

[74] D. Dolvin, "Hypersonic International Flight Research and Experimentation (HIFiRE) Fundamental Science and Technology Development Strategy ," in 15^{th} *AIAA International Space Planes and Hypersonic Systems and Technologies Conf., Paper No. 2008-2582*, 2008.

[75] B. H. M. Tang and R. Chase, "The Quest for Hypersonic Flight with Air-Breathing Propulsion," in 15^{th} *AIAA International Space Planes and Hypersonic Systems and Technologies Conf., Paper No. 2008-2546*, 2008.

[76] M. D. Salas, "DIGITAL FLIGHT: the last CFD aeronautical grand challenge," *J. Scientific Computing*, pp. 1 – 63, 2004.

[77] J. J. McNamara, "Aeroelastic and Aerothermoelastic Behavior of Two and Three Dimensional Lifting Surfaces in Hypersonic Flow," Ph.D. dissertation, University of Michigan, 2005.

[78] M. Maughmer, L. Ozoroski, D. Straussfogel, and L. Long, "Validation of Engineering Methods for Predicting Hypersonic Vehicle Control Forces and Moments," *J. of Guidance, Control and Dynamics*, vol. 16, pp. 762–769, 1993.

[79] S. Keshmirir, "Nonlinear and Linear Longitudinal and Lateral-Directional Dynamical Model of Air-Breathing Hypersonic Vehicle," in 15^{th} *AIAA International Space Planes and Hypersonic Systems and Technologies Conf.*, 2008.

[80] S. Keshmiri, "Modeling and Simulation of a Generic Hypersonic Vehicle," Ph.D. dissertation, University of Kansas, 2007.

[81] S. Keshmiri, R. Colgren, and M. Mirmirani, "Modeling and Simulation of a Generic Hypersonic Vehicle using Merged Aerodynamic Models," in 14^{th} *AIAA/AHI Space Planes and Hypersonic Systems and Technologies Conf., 2006-8087*, 2006.

[82] ——, "Six-DOF Modeling and Simulation of a Generic Hypersonic Vehicle for Control and Navigation Purposes," in *AIAA Guidance, Navigation and Control Conf., Paper No. 2006-6694*, 2006.

[83] S. Keshmiri, R. Colgren, S. Farokhi, and M. Mirmirani, "Ramjet and Scramjet Engine Cycle Analysis for a Generic Hypersonic Vehicle," in 14^{th} *AIAA/AHI Space Planes and Hypersonic Systems and Technologies Conf., 2006-8158*, 2006.

[84] S. Keshmiri, R. Colgren, and M. Mirmirani, "Development of an Aerodynamic Database for a Generic Hypersonic Air Vehicle," in *AIAA Guidance, Navigation and Control Conf., Paper No. 2006-6257*, 2005.

[85] ——, "Six-DOF Modeling and Simulation of a Generic Hypersonic Vehicle for Conceptual Design Studies," in *AIAA Modeling and Simulation Technologies Conf., Paper No. 2004-4805*, 2004.

[86] P. Lohsoonthorn, E. Jonckheere, and S. Dalzell, "Eigenstructure vs Constrained $\mathcal{H}^{\infty}$ Design for Hypersonic Winged Cone," *J. Guidance, Control and Dynamics*, pp. 648 – 658, 2001.

[87] F. R. Chavez and D. K. Schmidt, "Analytical Aeropropulsive/Aeroelastic Hypersonic-Vehicle Model with Dynamic Analysis," *J. Guidance, Control and Dynamics*, pp. 1308 – 1319, 1994.

[88] J. D. Anderson, *Modern Compressible Flow, 3^{rd} Edition*. McGraw-Hill, 2002.

[89] K. Bowcutt, G. Kuruvila, T. Grandine, and E. Cramer, "Advancements in Multidisciplinary Design Optimization Applied to Hypersonic Vehicles to Achieve Performance Closure," in 15^{th} *AIAA International Space Planes and Hypersonic Systems and Technologies Conf, Paper No. AIAA-2008-2591*, 2008.

[90] A. Clark, C. Wu, M. Mirmirani, and S. Choi, "Development of an Airframe Integrated Generic Hypersonic Vehicle Model," in *AIAA Aerospace Conference and Exhibit,Paper No. 2006-6560*, 2006.

[91] A. Clark, M. Mirmirani, S.Choi, C. Wu, and K. Mathew, "An Aero-Propulsion Integrated Elastic Model of a Generic Airbreathing Hypersonic Vehicle," in *AIAA Guidance, Navigation, and Control Conf., Paper No. 2006-6560*, 2006.

[92] A. Kelkar, J. Vogel, A. Rodriguez, J. Dickeson, and R. McCullen, "Development of a First Principles 6DOF Model for a Scramjet-Powered Hypersonic Vehicle," in *to be submitted to 2008 American Control Conf.*, 2008.

[93] C. Whitmer, A. Kelkar, J. Vogel, D. Chausse, and C. Ford, "Control centric parametric trade studies for scramjet-powered hypersonic vehicle," in *AIAA Guidance, Navigation and Control Conf.*, 2010.

[94] A. Kelkar, J. Vogel, C. Whitmer, D. Chausse, and C. Ford, "Design tool for control-centric modeling, analysis and trade studies for hypersonic vehicles," in 17^{th} *AIAA Int. Space Planes and Hypersonics Systems and Tech. Conf.*, 2011.

[95] S. Frendries, S. Skujins, and C. Cesnick, "Six-degree-of-freedom simulation of hypersonic vehicles," in *AIAA Atmospheric Flight Mechanics Conf.*, 2009.

[96] R. Starkey and M. Lewis, "A Simple Analytical Model for Parametric Studies of Hypersonic Waveriders ," in 8^{th} *AIAA International Space Planes and Hypersonic Systems and Technologies Conf. Paper No. 1998-1616*, 1998.

[97] I. Blankson, "Airbreathing Hypersonic Cruise: Prospects for Mach 4-7 Waverider Aircraft," in *ASME Int. Gas Turbine and Aerospace Congress and Exposition, Paper No. 92-GT-437*, June 1992.

[98] D. Capriotti, K. Bowcutt, and J. Anderson, "Viscous Optimized Hypersonic Waveriders," in *AIAA* 25^{th} *Aerospace Sciences Meeting, Paper No. 1987-272*, 1987.

[99] T. Nonwiler, "Aerodynamic Problems of Manned Space Vehicles," *J. of the Royal Aeronautical Society*, vol. 63, pp. 521–528, 1959.

[100] R. Starkey, D. Liu, R. Chang, and P. Chem, "Rapid Conceptual Design and Analysis of a Hypersonic Air-Breathing Missile ," in 15^{th} *AIAA International Space Planes and Hypersonic Systems and Technologies Conf., 2008-2590*, 2008.

[101] P. Moses, K. Bouchard, R. Vause, S. Pinckney, S. Ferlemann, C. Leonard, L. Taylor, J. Robinson, J. Martin, D.H.Petley, and J. Hunt, "An Airbreathing Launch Vehicle Design with Turbine-Based Low-Speed Propulsion and Dual Mode Scramjet High-Speed Propulsion," in 21^{st} *International Space Planes and Hypersonic Systems and Technologies Conf.*, 1999.

[102] J. Robinson, J. Martin, J. Bowles, U. Mehta, and C. Snyder, "An Overview of the Role of Systems Analysis in NASA's Hypersonics Project," in 14^{th} *AIAA/AHI Space Planes and Hypersonic Systems and Technologies Conf., Paper No. AIAA-2006-8013*, 2006.

[103] J. Pittman and P. A. Bartolotta, "Fundamental Aeronautics Hypersonics Project Reference Document," National Aeronautics and Space Administration (NASA), Tech. Rep., 2006.

[104] C. McClinton, "High Speed Hypersonic Aircraft Propulsion Technology Development," NASA Hypersonics GNC Kickoff Workshop Presentation, NASA Glenn, 84 slides, April 2007.

[105] D. McRuer, "Design and Modeling Issues for Integrated Airframe/Propulsion Control of Hypersonic Flight Vehicles," in *American Control Conf., pp. 729 – 734*, 1991.

[106] J. C. E. Cockrell, A. H. Auslender, R. W. Guy, C. R. McClinton, and S. S. Welch, "Technology Roadmap for Dual-Mode Scramjet Propulsion to Support Space-Access Vision Vehicle Development," in *AIAA/AAAF International Space Planes and Hypersonic Systems and Technologies Conf., pp. 1 – 14*, 2002.

[107] G. Stein, "Respect the Unstable," IEEE Control Systems Magazine, August 2003, pp. 12 - 25.

[108] A. A. Rodriguez, *Analysis and Design of Multivariable Feedback Control Systems*. Control3D, LLC, 2004.

[109] R. Lind, "Linear Parameter-Varying Modeling and Control of Structural Dynamics with Aerothermoelastic Effects," *J. Guidance, Control, and Dynamics*, pp. 733 – 739, 2002.

[110] M. W. Oppenheimer and D. B. Doman, "Control of Unstable, Nonminimum Phase Hypersonic Vehicle," in *IEEE Aerospace Conf., pp. 5782 – 5787*, 2006.

[111] ——, "A Hypersonic Vehicle Model Developed with Piston Theory," in *AIAA 2006-6637*, 2006.

[112] C. Breitsamter, T. Cvrlje, B. Laschka, M. Heller, and G. Sachs, "Lateral–Directional Coupling and Unsteady Aerodynamic Effects of Hypersonic Vehicles," *J. Spacecraft and Rockets*, pp. 159 – 167, 2001.

[113] S. Berry, K. Daryabeigi, K. Wurster, and R. Bittner, "Boundary Layer Transition on X-43A ," in 38^{th} *Fluid Dynamics Conf. and Exhibit, Paper No. 2008-3736*, 2008.

[114] S. A. Berry, A. H. Auslender, A. D. Diller, and J. F. Calleja, "Hypersonic Boundary-Layer Trip Development for Hyper-X," *J. Spacecraft and Rockets*, pp. 853 – 864, 2001.

[115] S. Torrez, N. Scholten, J. Driscoll, M. Bolender, M. Oppenheimer, and D. D. Doman, "A Scramjet Engine Model Including Effects of Precomubstions Shocks and Dissociation," in 44^{th} *AIAA/ASME/SAE/ASEE Joint Propulsion Conference and Exhibit, Paper No. 2008-6386*, 2008.

[116] D. H. Baldelli, R. Lind, and M. Brenner, "Nonlinear Aeroelastic/Aeroservoelastic Modeling by Block-Oriented Identification," *J. Guidance, Control and Dynamics*, pp. 1056 – 1064, 2005.

[117] R. Lind and M. Brenner, *Robust Aeroservoelastic Stablity Analysis: Flight Test Applications*. Springer, 1999.

[118] F. R. Chavez and D. K. Schmidt, "An Integrated Analytical Aeropropulsive/Aeroelastic Model for the Dynamic Analysis of Hypersonic Vehicle, NASA ARC92-2," NASA, Tech. Rep., June 1992.

[119] M. Rosenlicht, *Introduction to Real Analysis*. Dover Publications Inc., 1986.

[120] I. M. Hull, "Inversion of the prandtl-meyer relation," *Aeronautical Journal*, vol. Vol. 79, Sept.1975, pp. pp. 417 – 418, 1975.

[121] R. Nelson, *Flight Stability and Automatic Control*. McGraw-Hill Science/Engineering/Math, 1997.

[122] D. J. Zhou, K. and K. Glover, *Robust and Optimal Control*. Prentice Hall, 1996.

[123] M. Chilali and P. Gahinet, "$\langle^{\infty}$ design with pole placement constrains: an lmi apprach," *IEEE Transactions on Automatic Control*, vol. Vol. 41, No. 3, pp. 358 – 367, 1996.

[124] D. W. Miles, "Lpv modeling and h-infinity control of a tiltwing rotorcraft," Master's thesis, Arizona State University, 2007.

APPENDIX A

Control Design Methodology

The nature of the vehicle design problem requires two separate control approaches. The first approach is a decoupled LQR design methodology for both the longitudinal and lateral dynamics with relatively straight forward tuning properties. This allows the control law design to be automated, and used within the vehicle design optimization loop. This control law will give some basic ideas about achievable closed loop properties. The second control methodology is an $\mathcal{H}^{\infty}$ LPV implementation to deal with the nonlinear model within an linear parameter varying framework. This is necessary to deal with the changing mass and dynamic pressures that occur along the trajectory. Finally, any control approach that is implemented on the nonlinear systems needs to have some sort of saturation method (e.g. anti-windup) to deal with the state-dependent saturation within the FER loop.

In this section, we provide an overview of the design methodology for the longitudinal control system. Emphasis is placed on the flight path angle (FPA) control system because it must address critical dynamics; e.g. instability, right half plane zero, flexible modes.

11.3 Decentralized PI-Outer, PD-Inner Loop Control Law Structure

The following assumptions have been made in order to develop a nominal control design procedure:

- The original 100 ft model linearized at Mach 8, 85kft. The same methodology will be applied to the larger vehicle
- Altitude state removed (to provide observability; included in all nonlinear simulations)
- Flexible mode states not directly measured; i.e. not available to control system.
- Simple (first order) elevator and FER actuator dynamics are assumed: $\frac{20}{s+20}$
- Small RHP zero[1] to RHP pole[2] ratio necessitates an Inner-Outer Loop feedback structure. The feedback system architecture can be visualized as shown below:

[1] Non-minimum phase zero associated with elevator to FPA map
[2] Instability associated with cg aft of cp

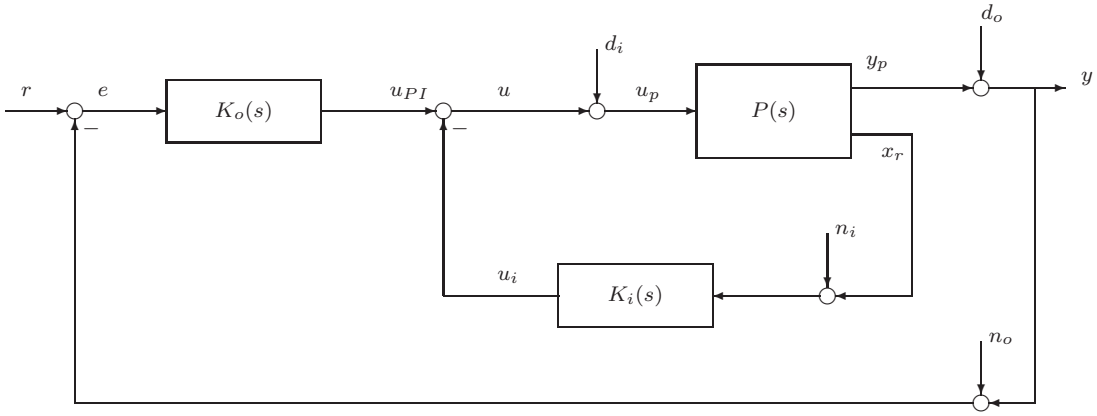

Figure 11.1: Inner Outer Feedback Loop

Output vector: $y = [\ y_1\ y_2\ ]^T = [\ v\ \gamma\ ]^T$

Control vector: $u = [\ u_1\ u_2\ ]^T = [\ FER\ \delta_e\ ]^T$

$x_r = [\ \theta\ q\ ]^T$

$x = [\ V\ \gamma\ \theta\ q\ \eta_1\ \dot{\eta_1}\ \eta_2\ \dot{\eta_2}\ \eta_3\ \dot{\eta_3}]^T$

11.4 Decentralized Plant Approximation

The nominal linear model (after altitude state removal) contains 10 states and is not suitable for performing the control design on. More specifically, the flexible dynamics need to be removed so that the control design methodology does not treat them as measured signals. Removal of the flexible dynamics necessitates a small amount of discussion. Consider the following general system:

$$\begin{bmatrix} \dot{X}_1 \\ \dot{X}_2 \end{bmatrix} = \begin{bmatrix} A_{11} & A_{12} \\ A_{21} & A_{22} \end{bmatrix} \begin{bmatrix} X_1 \\ X_2 \end{bmatrix} + \begin{bmatrix} B_1 \\ B_2 \end{bmatrix} U \tag{11.1}$$

The uppercase notation is used to show that all variables involved are either vectors or matrices. To extract the $A_{11}1$ dynamics, it is tempting to simply state:

$$\dot{X}_1 = A_{11}X_1 + B_1U \tag{11.2}$$

However, examination of the eigenvalues of $A_{11}1$ will show that they are not a subset of the eigenvalues of the larger system. In order to preserve this characteristic of the system, it is necessary to set $\dot{X}_2$ to zero, solve for X_2 in terms of X_1 and U, and then substitute that expression into the equation for $\dot{X}_1$ dot. The resulting system is:

$$\dot{X}_1 = \left[A_{11} - (A_{12}A_{22}^{-1}A_{21})\right] X_1 + \left[B_1 - (A_{12}A_{22}^{-1}B_2)\right] U \tag{11.3}$$

Note: If X2 consists entirely of integrators, then the eigenvalues of A11 will be a subset of the larger system and this method is not necessary (and in fact doesn't work due to divide by zero). Figure

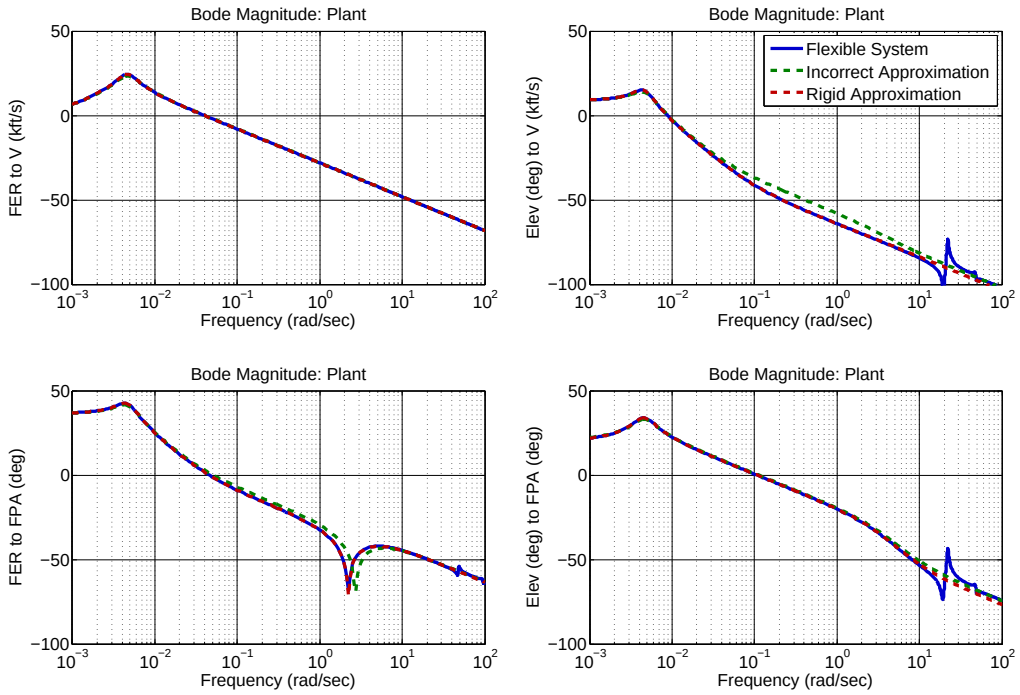

Figure 11.2: Approximation Comparisons: Bode Magnitude

11.5 Longitudinal Dynamics Approximation

The rigid portion of the ASTEP Model has the following form:

$$\begin{bmatrix} \dot{V}_t \\ \dot{\gamma} \\ \dot{\theta} \\ \dot{Q} \end{bmatrix} = \begin{bmatrix} a_{11} & a_{12} & a_{13} & a_{14} \\ a_{21} & a_{22} & a_{23} & a_{24} \\ 0 & 0 & 0 & 1 \\ a_{41} & a_{42} & a_{43} & a_{44} \end{bmatrix} \begin{bmatrix} V_t \\ \gamma \\ \theta \\ Q \end{bmatrix} + \begin{bmatrix} b_{11} & b_{12} \\ b_{21} & b_{22} \\ 0 & 0 \\ b_{41} & b_{42} \end{bmatrix} \begin{bmatrix} FER \\ \delta_e \end{bmatrix} \tag{11.4}$$

The system in equation 11.4 represents the typical coupled longitudinal dynamics associated with aircraft [121]. Several assumptions can be made about the model that will allows for significant simplification of the system.

- The Velocity mode is only affected by the FER. This places zeros in a_{12}, a_{13}, a_{14}, & b_{12}.
- Elevator-to-Flight Path Angle is decoupled from FER-to-Velocity, this places zeros in a_{21},a_{41},b_{21}, & b_{41}
- From the nonlinear Equations of Motion (equation 4.3) it should be apparent that Q does not directly impact $\dot{\gamma}$ or $\dot{Q}$. The only potential for this to change is from unsteady aerodynamic forces, but this cannot occur in trim, and therefore is not "seen" in the linear model. The a_{24} and a_{44} terms are epsilon terms due to the fact that trim means $\dot{x} - \epsilon < 0$. The a_{24} and a_{44} are set to zero.

In addition we take advantage of the fact that:

- $a_{22} = -a_{23}$

- $a_{42} = -a_{43}$

The rigid portion design system now has the following decentralized form:

$$\begin{bmatrix} \dot{V}_t \\ \dot{\gamma} \\ \dot{\theta} \\ \dot{Q} \end{bmatrix} = \begin{bmatrix} 0 & 0 & 0 & 0 \\ 0 & -a_{23} & a_{23} & 0 \\ 0 & 0 & 0 & 1 \\ 0 & -a_{43} & a_{43} & 0 \end{bmatrix} \begin{bmatrix} V_t \\ \gamma \\ \theta \\ Q \end{bmatrix} + \begin{bmatrix} b_{11} & 0 \\ 0 & b_{22} \\ 0 & 0 \\ 0 & b_{42} \end{bmatrix} \begin{bmatrix} FER \\ \delta_e \end{bmatrix} \tag{11.5}$$

The system in equation 11.5 is now a decoupled system consisting of one 1st order system expressing the relationship between Velocity and FER, and one 3rd order systems expressing the relationship between attitude dynamics and the elevator. The system can be rewritten as the following transfer functions:

$$\hat{P}_{\delta\gamma}(s) = \frac{g_\gamma(s-z)(s+z)}{s(s-p_1)(s+p_2)} \tag{11.6}$$

$$\hat{P}_{\phi V}(s) = \frac{g_V}{s} \tag{11.7}$$

where

$$g = b_{22} \tag{11.8}$$

$$z = \sqrt{a_{23}\frac{b_{42}}{b_{22}} - a_{43}} \tag{11.9}$$

$$p1 = -\frac{a_{23}}{2} + \frac{\sqrt{a_{23}^2 + 4a_{43}}}{2} \tag{11.10}$$

$$p2 = -\frac{a_{23}}{2} - \frac{\sqrt{a_{23}^2 + 4a_{43}}}{2} \tag{11.11}$$

$$g_V = b_{11} \tag{11.12}$$

11.6 Decentralized Approach Validation

One natural question to ask is "when is this decentralized control approach valid?" Consider the simplified 3 point mass systems shown in Figure 11.3 and the simplified equations of motions given in equations 4.1-4.3.

The forces can be linearly approximated by:

$$D_B = \bar{q}S_{ref}C_{D\alpha}\alpha + \bar{q}S_{ref}C_{Do} \tag{11.13}$$

$$L_B = \bar{q}S_{ref}C_{L\alpha}\alpha + \bar{q}S_{ref}C_{Lo} \tag{11.14}$$

$$N_e = \bar{q}S_eC_{D\delta}\delta \tag{11.15}$$

$$A_e = \bar{q}S_eC_{L\delta}\delta \tag{11.16}$$

$$\tag{11.17}$$

Assume that the drag and lift forces are given by

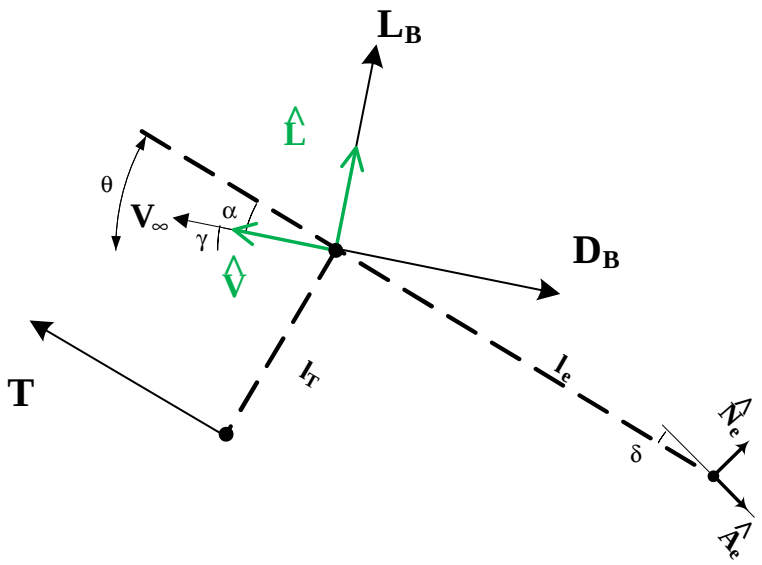

Figure 11.3: Nominal Sensitivity Tradeoffs

$$D = D_B + D_e \tag{11.18}$$
$$L = L_B + L_e \tag{11.19}$$

where D_e and L_e are the drag and lift forces associated with the elevator given by the following transformation to the wind axis:

$$\begin{bmatrix} L_e \\ D_e \end{bmatrix} = \begin{bmatrix} \cos(\alpha+\delta) & -\sin(\alpha+\delta) \\ -\sin(\alpha+\delta) & -\cos(\alpha+\delta) \end{bmatrix} \begin{bmatrix} N_e \\ A_e \end{bmatrix} \tag{11.20}$$

For the moment equation the normal and axial elevator forces must be translated into the body axis:

$$\begin{bmatrix} Z_e \\ X_e \end{bmatrix} = \begin{bmatrix} \cos(\delta) & -\sin(\delta) \\ -\sin(\delta) & -\cos(\delta) \end{bmatrix} \begin{bmatrix} N_e \\ A_e \end{bmatrix} \tag{11.21}$$

Utilizing the small angle assumption ($|\delta| + |\alpha| < 10^o$), then:

$$\cos(\alpha) = 1 \tag{11.22}$$
$$\sin(\alpha) = \alpha\frac{\pi}{180} \tag{11.23}$$
$$\cos(\delta) = 1 \tag{11.24}$$
$$\sin(\delta) = \delta\frac{\pi}{180} \tag{11.25}$$
$$\cos(\alpha+\delta) = 1 \tag{11.26}$$
$$\sin(\alpha+\delta) = (\alpha+\delta)\frac{\pi}{180} \tag{11.27}$$

Then we have

$$X_e \approx -N_e\frac{\pi}{180}\delta - A_e \tag{11.28}$$
$$Z_e \approx N_e - A_e\frac{\pi}{180}\delta \tag{11.29}$$
$$D_e \approx -N_e\frac{\pi}{180}(\alpha+\delta) - A_e \tag{11.30}$$
$$L_e \approx N_e - A_e\frac{\pi}{180}(\alpha+\delta) \tag{11.31}$$

While $N_e > A_e$, they are typically on the same order of magnitude, so the $\frac{\pi}{180}$ will tend to marginalize any terms it applies to, yielding:

$$X_e \approx -A_e \tag{11.32}$$
$$Z_e \approx N_e \tag{11.33}$$
$$D_e \approx -A_e \tag{11.34}$$
$$L_e \approx N_e \tag{11.35}$$

If equations 11.14-11.17 and 11.33 -11.35 along with the small angle approximation are applied to the equations of motion 4.1-4.3:

$$X_e \approx -A_e \tag{11.36}$$
$$Z_e \approx N_e \tag{11.37}$$
$$D_e \approx -A_e \tag{11.38}$$
$$L_e \approx N_e \tag{11.39}$$

$$\dot{V_T} = \left[\frac{T\cos\alpha - |\bar{q}S_{ref}C_{D\alpha}\alpha + \bar{q}S_eC_{D\delta} + \bar{q}S_{ref}\delta C_{Do}|}{m}\right] - g\sin\gamma \tag{11.40}$$
$$\dot{\gamma} = \left[\frac{|\bar{q}S_{ref}C_{L\alpha}\alpha + \bar{q}S_eC_{L\delta} + \bar{q}S_{ref}\delta C_{Lo}| + T\sin\alpha}{mV_T}\right] - \left(\frac{g}{V_T}\right)\cos\gamma \tag{11.41}$$
$$\dot{q} = \frac{\bar{q}S_{ref}C_{L\delta}l_e\delta - l_tT - M_B}{I_{yy}} \tag{11.42}$$

Where M_B is the unresolved moment associated with the body aerodynamics. If all of the derivatives are set to zero, then there is a system of 3 equations with 3 unknowns, and the equilibrium values of α_{eq}, δ_{eq} & T_{eq} can be solved for. It should be immediately obvious from equation that $\dot{V_T}$ is not controllable through δ alone because it is incapable of increasing $\dot{V_T}$, and hence the state V_T cannot be arbitrarily chosen. If we linearize equation 11.42, then we ge the following:

$$\Delta\dot{q} = \frac{\bar{q}S_{ref}C_{L\delta}l_e}{I_{yy}}\Delta\delta - \frac{l_t}{I_{yy}}\Delta T \tag{11.43}$$

If we scale the in inputs to equation 11.43 by their respective "maximum" values, then $\Delta\dot{q}$ can be controlled by δ as long as the following criteria for the elevator area holds true:

$$S_e > \frac{l_T}{l_e}\frac{T_{max}}{\delta_{max}}\frac{1}{\bar{q}C_{L\delta}} \tag{11.44}$$

11.7 Nominal Elevator-to-FPA Controller Structure

The elevator-to-FPA control law has the following structure:

$$K_i(s) = g_i(s + z_i) \qquad K_o(s) = \frac{g_o(s + z_o)}{s}\left[\frac{hf}{s + hf}\right]^3 \tag{11.45}$$

Four parameters associated with inner (PD)-outer (PI) loop FPA control system: (g_i, z_i, g_γ, z_γ). Here, h_f is a large value - typically 200. The modified plant (P_{mod}) is defined as the transfer function matrix from $u_{PI_2} \rightarrow y_{p_2}$. The structure of the elevator-to-FPA control law is such that the 4 relevant gains g_i,z_i,g_o,& z_o can be selected utilizing an LQR Servo design methodology.

11.8 Nominal Fuel Equivalence Ratio-to-Velocity Controller Structure

The FER-to-Velocity has the following single PI loop structure:

$$K_o(s) = \frac{g_V(s + z_V)}{s}\left[\frac{hf}{s + hf}\right]^3 \tag{11.46}$$

Two parameters associated with single PD loop velocity control system: (g_v , z_v). Here, h_f is a large value - typically (10 times largest relevant bandwidth, eg flexible dynamic bandwidth). Due to the simple nature of the FER-to-Velocity system (approximated as an integrator), simple 2nd order system ideas can be utilized to select g_V and z_V

11.9 Longitudinal Control System Design Methodology: Fundamental Results

This section will illustrate some of the fundamental tradeoffs and performance limitations associated with the inner/outer loop control architecture.

Error/Control Sensitivity Relationship

In this section, we consider the classic inner-outer loop control architecture shown below and derive a very important relationship between the sensitivity functions associated with the error $S_e \triangleq \frac{1}{1+L_e}$, the control $S_c \triangleq \frac{1}{1-L_c}$, and the inner loop $S_i \triangleq \frac{1}{1-L_i}$. The block diagram in Figure 11.1 is intended to depict two-input two-output (TITO) system for velocity and FPA. However, it is general and can also represent the single-input single-output (SISO) elevator-flight path angle (FPA) closed loop system. As such, the following is important to note:

- P_1 (elevator to pitch attitude map) is unstable and minimum phase
- P_2 (pitch attitude to FPA map) is stable but non-minimum phase

Moreover,

- K_i is typically a PD controller with an additional notch filter in order to deal with the vehicle's longitudinal flexible dynamics
- K_o is typically a PI controller with high frequency roll-off
- r_γ is typically a filtered reference command

Sensitivity at Error. Breaking the loop at the error e yields:

$$L_e = P_2\left(\frac{P_1}{1 - K_iP_1}\right)K_o = P_2P_{mod}K_o \tag{11.47}$$

where

$$P_{mod} = \frac{P_1}{1 - K_i P_1} \tag{11.48}$$

is referred to as the modified plant. It should be noted that we use a positive feedback sign convention for the inner loop and a negative feedback sign convention for the outer loop.

Inner Loop Sensitivity. The sensitivity associated with the inner loop is given by:

$$S_i = \frac{1}{1 - K_i P_1} \tag{11.49}$$

Sensitivity at Controls. Breaking the loop at the controls u_p yields:

$$L_c = [K_i - K_o P_2] P_1 \tag{11.50}$$

Fundamental Relationship Between S_c, S_e, S_i. Rewriting equation (11.48) in terms of K_i gives:

$$K_i = \frac{1 - P_1 P_{mod}^{-1}}{P_1} \tag{11.51}$$

Substituting equation (11.51) into (11.50) yields the following:

$$\begin{aligned}
L_c &= [1 - P_1 P_{mod}^{-1} - L_e P_{mod}^{-1} P_1] && (11.52)\\
&= [1 - (1 + L_e) P_{mod}^{-1} P_1] && (11.53)\\
&= [1 - S_e^{-1} P_{mod}^{-1} P_1] && (11.54)\\
1 - L_c &= S_e^{-1} P_{mod}^{-1} P_1 && (11.55)\\
S_c^{-1} &= S_e^{-1} P_{mod}^{-1} P_1 && (11.56)\\
S_c &= S_e P_{mod} P_1^{-1} && (11.57)\\
S_c &= S_e (1 - K_i P_1)^{-1} && (11.58)
\end{aligned}$$

This then yields the final relationship between S_c, S_e, and S_i:

$$S_c = S_e S_i \tag{11.59}$$

This relationship shows how S_e and S_i collectively shape S_c. More specifically, it can provide great insight into fundamental tradeoffs between properties at the error and at the controls. Generally speaking, the inner loop is (at least 5x) faster than the outer loop. This implies that at higher frequencies, $S_e \approx 1$ and $S_c \approx S_i$. This idea will be further examined as we move forwards. For our hypersonic vehicle application, getting a desirable S_e is generally easy while getting a desirable S_c can be challenging.

Weighted Sensitivity Integral Formula

For a plant with a single right-half plane zero z and right half plane pole p, the following holds (see page 168, "Multivariable Feedback Control: Analysis and Design," Skogestad and Postlethwaite):

$$\int_0^\infty \ln |S(j\omega)| \ \frac{2z}{z^2 + \omega^2} \ d\omega \ = \ \pi \ \ln \left| \frac{p + z}{p - z} \right| \tag{11.60}$$

Typical Sensitivity Function Bounds. If the sensitivity is assumed to be bounded from above by the following:

$$|S(j\omega)| \leq -\ln s_m \qquad 0 < \omega \leq \omega_1 \tag{11.61}$$
$$|S(j\omega)| \leq \ln s_p \qquad \omega_1 < \omega \leq \omega_p \tag{11.62}$$
$$\tag{11.63}$$

Here,

- $s_m > 1$ represents a sensitivity attenuation factor
- $s_p \geq 1$ represents the peak sensitivity
- ω_1 represents an effective bandwidth over which sensitivity attenuation is desired
- ω_p represents the available bandwidth (G. Stein "Respect the Unstable," vol. 23, no. 4, Aug. 2003, pp. 12 Ű 25)

Given the above, the following relationship can be derived:

$$\ln s_p = \frac{\frac{\pi}{2}\ln\left|\frac{p+z}{p-z}\right| + \ln s_m \tan^{-1}\left(\frac{\omega_1}{z}\right)}{\tan^{-1}\left(\frac{\omega_p}{z}\right) - \tan^{-1}\left(\frac{\omega_1}{z}\right)} \tag{11.64}$$

This relationship reveals fundamental performance limitations that must be considered by control system designers. Specifically, we observe the following:

1. As $\omega_p \to \infty$, $s_p \to \left|\frac{z+p}{z-p}\right|$
2. As $s_m \to \infty$, $s_p \to \infty$
3. As $\omega_1 \to \omega_p$, $s_p \to \infty$
4. As $p \to z$, $s_p \to \infty$
5. As $p \to 0$, $\ln s_p \to \frac{\ln s_m \tan^{-1}\left(\frac{\omega_1}{z}\right)}{\tan^{-1}\left(\frac{\omega_p}{z}\right) - \tan^{-1}\left(\frac{\omega_1}{z}\right)}$
6. As $p \to 0$, and $\omega_p \to \infty$, $\ln s_p \to \frac{\ln s_m \tan^{-1}\left(\frac{\omega_1}{z}\right)}{\frac{\pi}{2} - \tan^{-1}\left(\frac{\omega_1}{z}\right)}$
7. As $p \to 0$ and $\omega_1 \to 0$, $s_p \to 1$ (0 dB)

For our hypersonic application, the relationships in (5)-(7) hold for the sensitivity at the error when the inner loop plant has been stabilized by the inner loop feedback; i.e. the modified plant P_{mod} is stable.

Moreover, the above relationship can be used to guide system design; i.e. determining the relationship between the instability p and the non-minimum phase zero z. For example, given constraints on s_m, s_p, and z, what must p satisfy?

Weighted Sensitivity Integral Formula Results: Nominal Plant

Consider the following nominal parameters:

$$p_1 = p_2 = 3 \tag{11.65}$$
$$z = 9 \tag{11.66}$$
$$s_m = 10 \tag{11.67}$$

Note that $\frac{1}{s_m}$ represents the attenuation at low frequencies.

Consider a classic negative feedback system. For such an architecture, we observe the fundamental sensitivity tradeoffs depicted in the following figure.

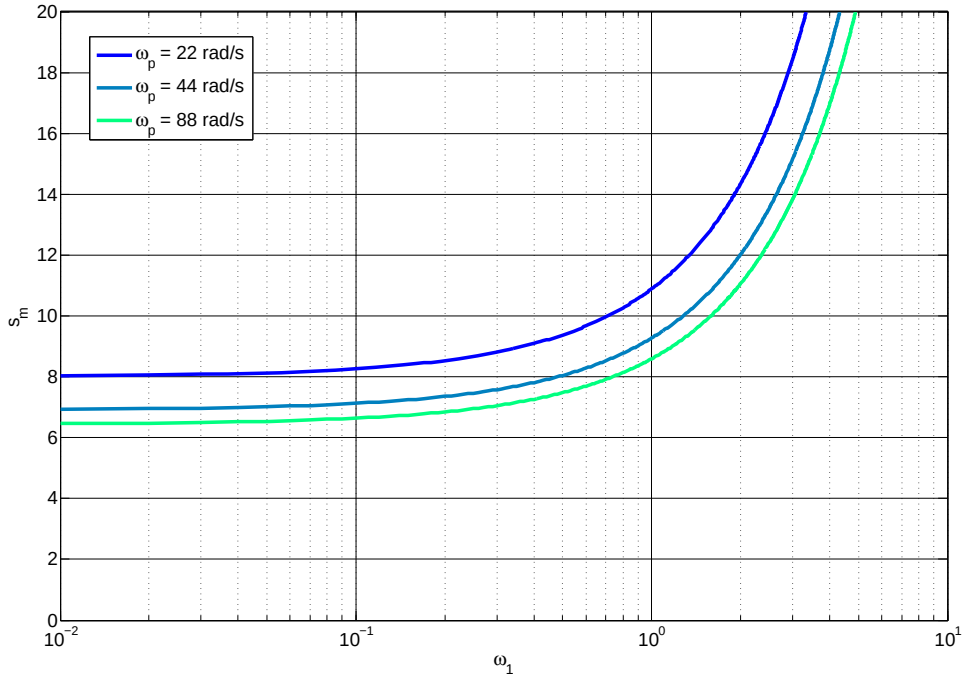

Figure 11.4: Nominal Sensitivity Tradeoffs

Figure 11.4 shows the tradeoff in peak sensitivity s_p (measured in dB) versus ω_1 and ω_p. It can be seen from the figure that as $\omega_p \to \infty$, we observe that the peak sensitivity $s_p \to 2$ or 6 dB (i.e. $s_p \to \frac{z+p}{z-p} = \frac{9+3}{9-3} = \frac{12}{6} = 2$ from the maximum modulus theorem and Blashke all-pass term analysis).

In practice, however, the available bandwidth ω_p will be fundamentally limited by any one or all of the following: flexible modes, actuator dynamics, sensor dynamics, unsteady aerodynamic effects, sampling rate, actuation rate, control update rate.

Weighted Sensitivity Integral Formula Results: Inner Loop Sensitivity

Application of the above weighted sensitivity integral ideas to our inner loop, yields the tradeoffs depicted in the following figure.

This figure shows that the peak sensitivity s_p associated with the inner loop will be undesirable for a bandwidth of about $\omega_1 = 3$ rad/sec (minimum bandwidth required to stabilize the unstable plant)

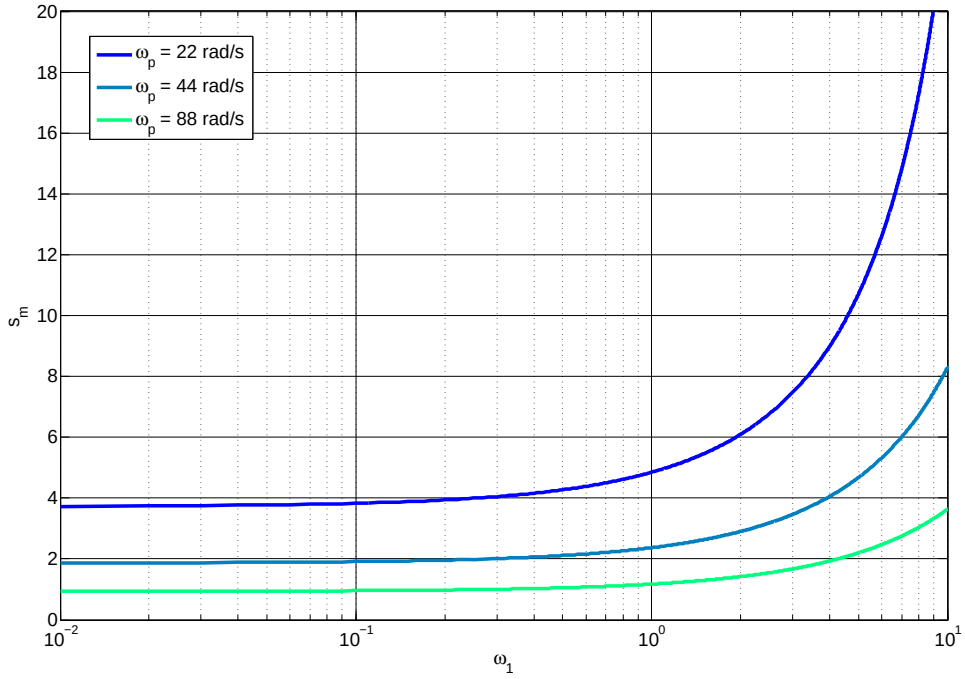

Figure 11.5: Fundamental Inner Loop Sensitivity Tradeoffs

if the available bandwidth ω_p is below say 30 rad/sec.

Sensitivity Integral Results: Sensitivity at Error

Lets suppose that the inner loop has stabilized our unstable plant P_1. When the above weighted sensitivity integral results are applied at the error signal for our hypersonic vehicle control application, we obtain the fundamental error sensitivity tradeoffs depicted in the following figure.

The above figure suggests that an acceptable peak error sensitivity will be achievable if the bandwidth ω_1 is sufficiently small relative to the achievable bandwidth ω_p.

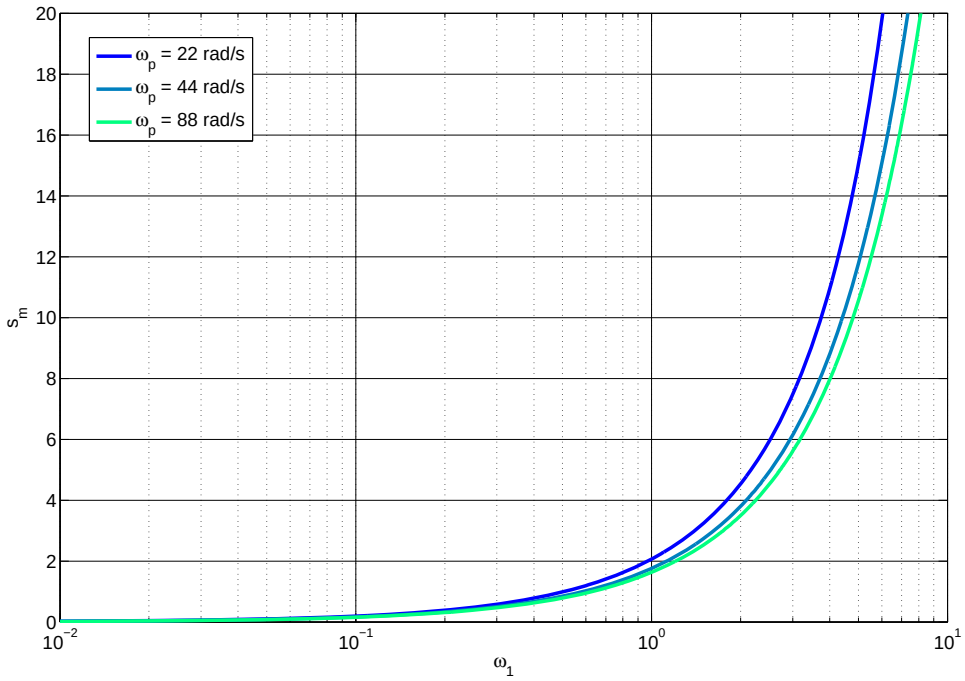

Figure 11.6: Fundamental Sensitivity Tradeoffs at Error

11.10 Summary of Modern Neo-Classical Stability Robustness Results

Given bounds on the sensitivity and complementary sensitivity, one can determine bounds on classical stability robustness margins; i.e. upward gain margin $\uparrow GM$, downward gain margin $\downarrow GM$, phase margin PM.

Bounds on Classic Stability Robustness Margins from Sensitivity Bounds
Let $\alpha, \beta \geq 1$ denote upper bounds on the sensitivity $S = \frac{1}{1+L}$ and complementary sensitivity $T = 1 - S = \frac{L}{1+L}$, respectively; i.e.

$$|S(j\omega)| < \alpha \quad |T(j\omega)| < \beta \tag{11.68}$$

for all frequencies $\omega \in [0, \infty)$. From this, one can use Nyquist and inverse Nyquist concepts in order to obtain the following bounds on $\uparrow GM$, $\downarrow GM$, and PM:

$$\uparrow GM > \max \{ \frac{\alpha}{\alpha - 1}, \frac{\beta + 1}{\beta} \} \tag{11.69}$$

$$\downarrow GM < \max \{ \frac{\alpha}{\alpha + 1}, \frac{\beta - 1}{\beta} \} \tag{11.70}$$

$$|PM| > 2 \max \{ \sin^{-1} \left(\frac{1}{2\alpha} \right), \sin^{-1} \left(\frac{1}{2\beta} \right) \} \tag{11.71}$$

It should be noted that

- $r_\alpha = \frac{1}{\alpha}$ denotes the distance to the critical -1 point within the Nyquist L plane
- $r_\beta = \frac{1}{\beta}$ denotes the distance to the critical -1 point within the inverse Nyquist L^{-1} plane

From the above, it follows that

- A design can exhibit great nominal classical stability robustness margins (i.e. $\uparrow GM$, $\downarrow GM$, and PM) and still have very poor sensitivity properties (i.e. large α, β or small r_α, r_β).
- It is therefore essential to closely examine nominal sensitivity properties - at the controls as well as at the error.
- Generally, we want
  - $|L|$ large at low frequencies for good low frequency command following, (output) disturbance attenuation, and stability robustness with respect to low frequency model uncertainty;
  - $|L|$ small at high frequencies for good high frequency sensor noise attenuation and stability robustness with respect to high frequency model uncertainty.

Classic Stability Robustness Margins - Dependence on α
From the above, we obtain the following:

$\alpha = 1$ (0 dB)	$\uparrow GM = \infty$	$\downarrow GM < \frac{1}{2}$	$\lvert PM \rvert > 60^\circ$
$\alpha = 2$ (6 dB)	$\uparrow GM > 2$	$\downarrow GM < \frac{2}{3}$	$\lvert PM \rvert > 28.89^\circ$
$\alpha = 3$ (9.54 dB)	$\uparrow GM > \frac{3}{2}$	$\downarrow GM < \frac{3}{4}$	$\lvert PM \rvert > 19.19^\circ$
$\alpha = 4$ (12.04 dB)	$\uparrow GM > \frac{4}{3}$	$\downarrow GM < \frac{4}{5}$	$\lvert PM \rvert > 14.36^\circ$
$\alpha = 5$ (13.98 dB)	$\uparrow GM > \frac{5}{4}$	$\downarrow GM < \frac{5}{6}$	$\lvert PM \rvert > 11.48^\circ$

Each row in the above table corresponds to a constant α. As such, the margin figures given on a row can be thought as being comparable - comparable in the sense that they result in the same α lower bound. This will be revisited below.

From the above, we see that

- As α or $\|S\|_{\mathcal{H}^\infty}$ approaches unity from above,
  - the lower bound for $\uparrow GM$ approaches ∞ from below
  - the upper bound for $\downarrow GM$ approaches $\frac{1}{2}$ from above
  - the lower bound for $|PM|$ approaches 60° from below

Classic Stability Robustness Margins - Dependence on β
From the above, we also obtain the following:

$\beta = 1$ (0 dB)	$\uparrow GM > 2$	$\downarrow GM = 0$	$\lvert PM \rvert > 60^\circ$
$\beta = 2$ (6 dB)	$\uparrow GM > \frac{3}{2}$	$\downarrow GM < \frac{1}{2}$	$\lvert PM \rvert > 28.89^\circ$
$\beta = 3$ (9.54 dB)	$\uparrow GM > \frac{4}{3}$	$\downarrow GM < \frac{2}{3}$	$\lvert PM \rvert > 19.19^\circ$
$\beta = 4$ (12.04 dB)	$\uparrow GM > \frac{5}{4}$	$\downarrow GM < \frac{3}{4}$	$\lvert PM \rvert > 14.36^\circ$
$\beta = 5$ (13.98 dB)	$\uparrow GM > \frac{6}{5}$	$\downarrow GM < \frac{4}{5}$	$\lvert PM \rvert > 11.48^\circ$

Each row in the above table corresponds to a constant β. As such, the margin figures given on a row can be thought as being comparable - comparable in the sense that they result in the same β lower bound. This will be revisited below.

From the above, we see that

- As β or $\|T\|_{\mathcal{H}^\infty}$ approaches unity from above,
  - the lower bound for $\uparrow GM$ approaches 2 from below
  - the upper bound for $\downarrow GM$ approaches 0 from above
  - the lower bound for $|PM|$ approaches 60° from below

Fundamental Performance - Sensitivity and Complementary Sensitivity - Limitations
From the above, it also follows that

- For systems with an open loop RHP zero, the upward gain margin is finite ($\uparrow GM < \infty$) and, hence, $\alpha > 1$; i.e. for non-minimum phase systems, the sensitivity must lie above unity.

  For our non-minimum phase hypersonic vehicles, inner loop feedback can assist with this at the elevator. Nothing can be done at the FPA error. From this, it follows that:

  The peak sensitivity at the FPA error must therefore lie above unity.

- For systems with an open loop RHP pole, the downward gain margin is finite ($\downarrow GM > 0$), and hence $\beta > 1$; i.e. for open loop unstable systems, the complementary sensitivity must lie above unity.

  For our open loop unstable hypersonic vehicles, inner loop feedback can assist with this at the FPA error. Nothing can be done about this at the elevator. From this, it follows that:

  The peak complementary sensitivity at the elevator must therefore lie above unity.

Sensitivity and Complementary Sensitivity Bounds from Classical Robustness Margins
From, the above, one can obtain the following sensitivity and complementary sensitivity bounds from the classical stability robustness margins:

$$\alpha \quad > \quad \max\left\{ \ \frac{\uparrow GM}{\uparrow GM - 1}, \ \frac{\downarrow GM}{1 - \downarrow GM}, \ \frac{1}{2\sin\left(\frac{|PM|}{2}\right)} \ \right\} \tag{11.72}$$

$$\beta \quad > \quad \max\left\{ \ \frac{1}{\uparrow GM - 1}, \ \frac{1}{1 - \downarrow GM}, \ \frac{1}{2\sin\left(\frac{|PM|}{2}\right)} \ \right\} \tag{11.73}$$

From the above, it follows that

- when the classical margins are too "small," they will significantly influence the lower bounds on α, β

Comparable α-Bound Classical Margins
The following are comparable classical margins in the sense that they result in the same lower bound for α.

- a lower bound of unity for α or $\|S\|_{\mathcal{H}^\infty}$ is produced by any of the following:

$$\uparrow GM = \infty \qquad \downarrow GM = \tfrac{1}{2} \qquad |PM| = 60^\circ$$

- a lower bound of 2 for α or $\|S\|_{\mathcal{H}^\infty}$ is produced by any of the following:

$$\uparrow GM = 2 \qquad \downarrow GM = \tfrac{2}{3} \qquad |PM| = 28.96^\circ$$

- a lower bound of 3 for α or $\|S\|_{\mathcal{H}^\infty}$ is produced by any of the following:

$$\uparrow GM = \tfrac{3}{2} \qquad \downarrow GM = \tfrac{3}{4} \qquad |PM| = 19.19^\circ$$

- a lower bound of 4 for α or $\|S\|_{\mathcal{H}^\infty}$ is produced by any of the following:

$$\uparrow GM = \tfrac{4}{3} \qquad \downarrow GM = \tfrac{4}{5} \qquad |PM| = 14.36^\circ$$

- a lower bound of 5 for α or $\|S\|_{\mathcal{H}^\infty}$ is produced by any of the following:

$$\uparrow GM = \tfrac{5}{4} \qquad \downarrow GM = \tfrac{5}{6} \qquad |PM| = 11.48^\circ$$

Comparable β-Bound Classical Margins
The following are comparable classical margins in the sense that they result in the same lower bound for β.

- a lower bound of unity for β or $\|T\|_{\mathcal{H}^\infty}$ is produced by any of the following:

$$\uparrow GM = 2 \qquad \downarrow GM = 0 \qquad |PM| = 60^\circ$$

- a lower bound of 2 for β or $\|T\|_{\mathcal{H}^\infty}$ is produced by any of the following:

$$\uparrow GM = \tfrac{3}{2} \qquad \downarrow GM = \tfrac{1}{2} \qquad |PM| = 28.96^\circ$$

- a lower bound of 3 for β or $\|T\|_{\mathcal{H}^\infty}$ is produced by any of the following:

$$\uparrow GM = \tfrac{4}{3} \qquad \downarrow GM = \tfrac{2}{3} \qquad |PM| = 19.19^\circ$$

- a lower bound of 4 for β or $\|T\|_{\mathcal{H}^\infty}$ is produced by any of the following:

$$\uparrow GM = \tfrac{5}{4} \qquad \downarrow GM = \tfrac{3}{4} \qquad |PM| = 14.36^\circ$$

- a lower bound of 5 for β or $\|T\|_{\mathcal{H}^\infty}$ is produced by any of the following:

$$\uparrow GM = \tfrac{6}{5} \qquad \downarrow GM = \tfrac{4}{5} \qquad |PM| = 11.48^\circ$$

11.11 Longitudinal Control System Design Methodology: Practical Results utilizing LQR

The PD Inner/PI Outer loop architecture described in the previous section can be more directly designed/generated/addressed via the LQ Servo design methodology. This methodology will be addressed within this section. Within the LQ Servo methodology, the plant is augmented at the output with an integrator. The integrator is then brought around the feedback loop to the error (classic controller location) in the actual implementation. By so doing, we preserve the LQ robustness properties at the plant input (e.g. gain and phase margins, peak sensitivity and complementary sensitivity).

For each of the following figures, a series of LQR controllers has been designed on the rigid plant without any actuator model. The controller is then tested against

(1) the design plant (i.e. rigid plant without actuator dynamics),
(2) the rigid plant with actuator dynamics,
(3) the flexible plant without actuator dynamics, and
(4) the flexible plant with actuator dynamics.

Design Families: Increasing Bandwidth at FPA Error

FPA Response to Unit Step FPA Reference Command

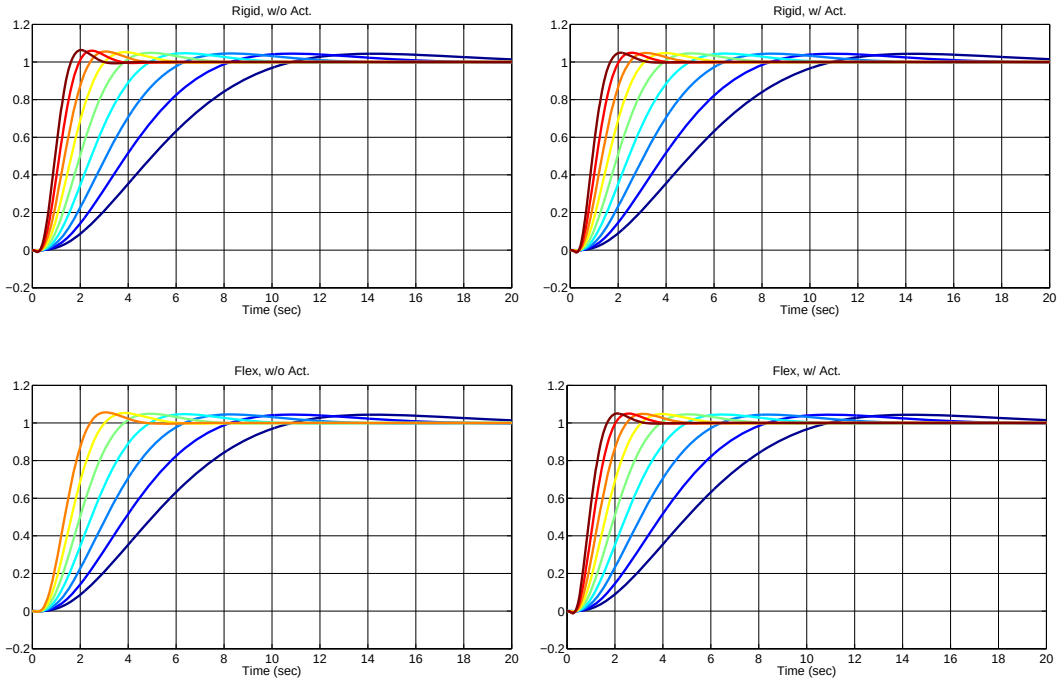

Figure 11.7: FPA Response to Unit Step FPA Reference Command

Observations

- Almost no discernable variation is observed in the output responses for the 4 different cases considered
- One exception to this is that the two highest BW designs are unstable for the flexible plant w/o actuator (not included within left subfigure of Figure 11.7).

- Addition of actuator dynamics helps overturn destabilizing effect of lightly damped flexible dynamics. See bottom right subfigure within Figure 11.7.
- Plots given below will show that even though all 4 cases appear to exhibit good performance, they possess vastly different stability robustness properties at the controls.

Elevator Response to Unit Step FPA Reference Command

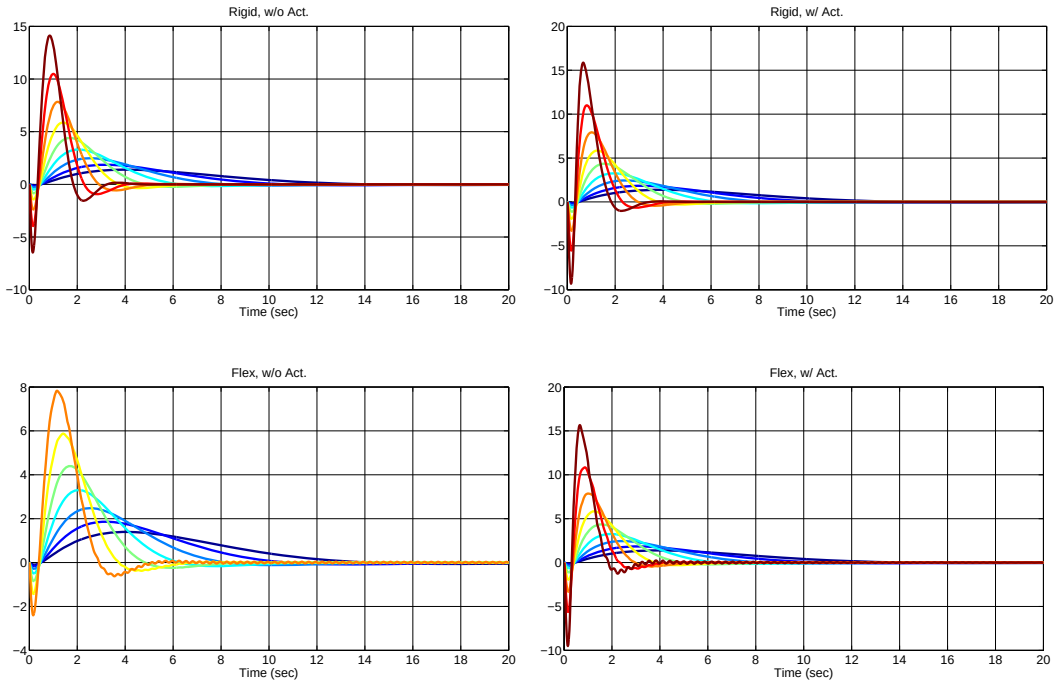

Figure 11.8: Elevator Response to Unit Step FPA Reference Command

Observations

- For comparable bandwidth designs, more elevator deflection is needed for the flexible case (compare responses rendered using the same color)
- For the flexible cases (bottom two subfigures of Figure 11.8), a 22 rad/sec ripple can be seen for the fast designs
- Again, the two highest BW designs are unstable for the flexible w/o actuator case (not shown in bottom left subfigure within Figure 11.8).

Sensitivity at FPA Error

- The sensitivity at the FPA error shows a significant increase in the high frequency design bump (orange) due to the addition of the actuator for the rigid plant. See bottom left subfigure within Figure 11.9.
- Peaking associated with lightly damped flexible mode dynamics dominates the response for faster bandwidth designs.
- The addition of actuator dynamics decreases the size of the flexible mode peaking. See bottom right subfigure within Figure 11.9.

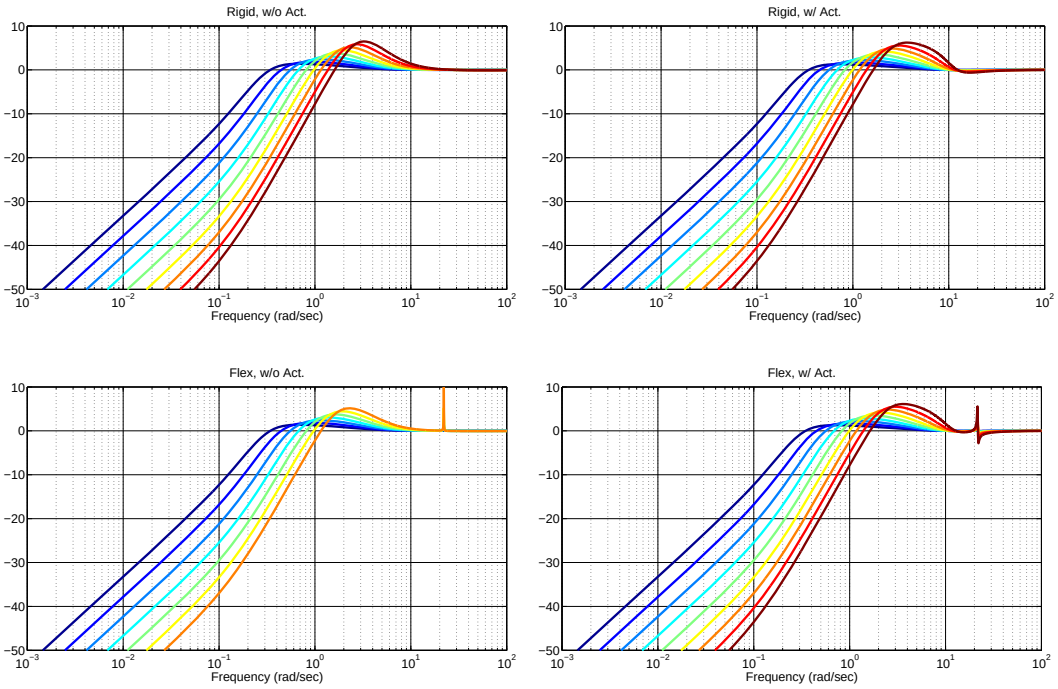

Figure 11.9: Sensitivity at FPA Error

- Again, the two highest BW designs are unstable for the flexible w/o actuator case (not shown in bottom left subfigure within Figure 11.9).

Nyquist Plots - Loop Broken at Elevator

Here, we examine Nyquist plots associated with breaking the loop at the elevator. This is useful for understanding the impact of the actuator and flexible mode dynamics on the closed loop stability robustness properties.

- Nyquist plots corresponding to rigid w/o actuator case (see upper left subfigure within Figure 11.10) all lie outside circle of (approximate) radius $r_\alpha = 0.85$ around -1 point. This implies good stability robustness properties. More specifically, $r_\alpha = \frac{1}{\alpha} = 0.85$ implies that $\alpha = \frac{100}{85} = 1.18$ which yields the following bounds:

$$\uparrow GM \quad > \quad \frac{\alpha}{\alpha - 1} = \frac{1.18}{0.18} = 6.56 \tag{11.74}$$

$$\downarrow GM \quad < \quad \frac{\alpha}{\alpha + 1} = \frac{1.18}{2.18} = 0.54 \tag{11.75}$$

$$|PM| \quad > \quad 2\sin^{-1}\left(\frac{1}{2\alpha}\right) = 2\sin^{-1}\left(\frac{1}{2(1.18)}\right) = 50.14^\circ \tag{11.76}$$

- Adding the actuator dynamics to the rigid model deteriorates the margins as illustrated in upper right subfigure within Figure 11.10.
- Flexible dynamics (without actuator dynamics) significantly deteriorates the margins as illustrated in lower left subfigure within Figure 11.10.
- Adding the actuator dynamics to the flexible model helps with the flexible dynamics. This is illustrated in lower right subfigure within Figure 11.10.

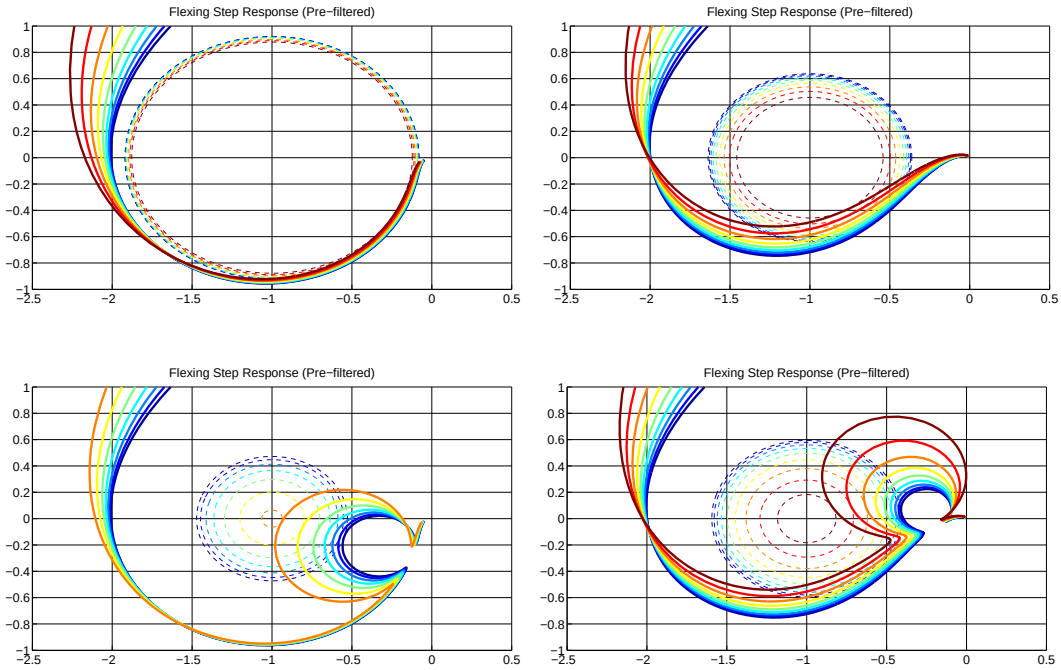

Figure 11.10: Nyquist Plots - Loop Broken at Elevator

The addition of the actuator dynamic improves the flexible case by shifting the flexible mode contribution from roughly -170° to -260°, improving the margins.

The following figures examine tradeoffs associated with settling time.

Settling Time vs State Weighting Q_{11}

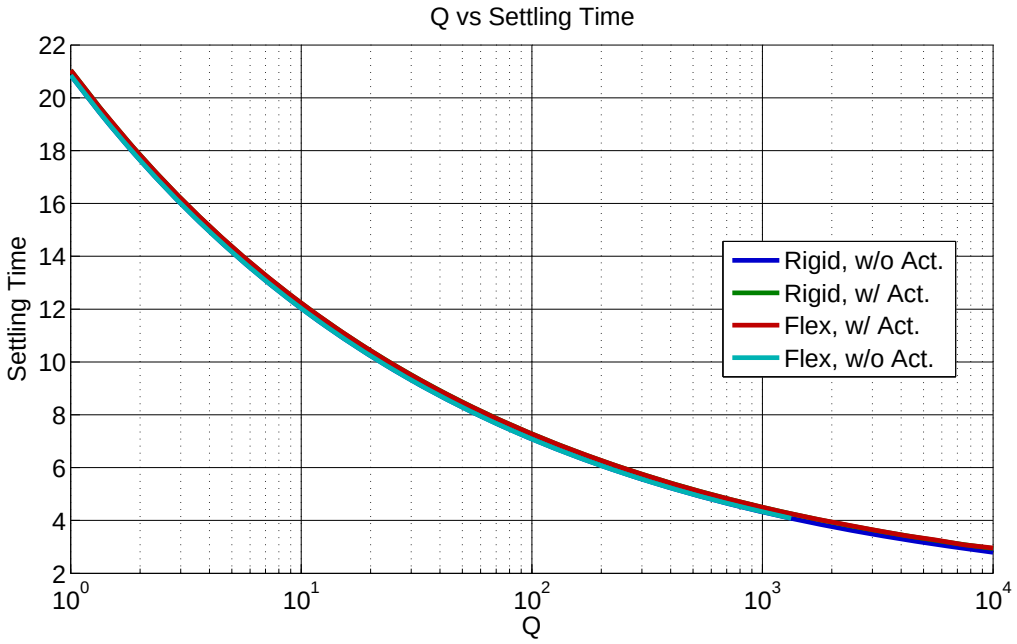

Figure 11.11: LQR Design: Settling Time vs State Weighting Q_{11}

- Figure 11.11 shows how settling time varies with the state weighting Q_{11}
- Settling time decreases as the state weighting Q_{11} is increased

Peak Elevator Deflection vs Settling Time (BW)

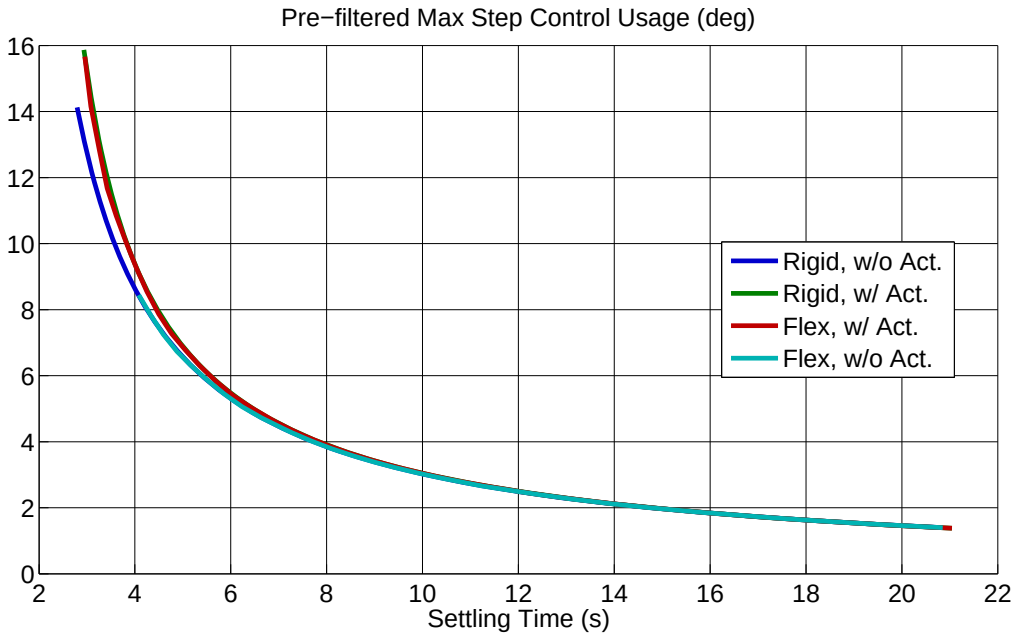

Figure 11.12: LQR Design: Peak Elevator Deflection (pre-filtered) vs Settling Time

- Figure 11.12 shows the tradeoff that exists between peak elevator deflection and settling time. No notch filter has been used here.
- Regardless of the system: as the peak elevator deflection is reduced, the settling time increases
- For small settling times (high BW designs), we see that the inclusion of the actuator dynamics results in slightly more peak elevator deflection
- The above plot is important for choosing control system BW (settling time) given elevator saturation constraints. It is probably the second most important plot. See Figure 11.14 on page 147.

FPA Percent Overshoot vs Settling Time (BW)

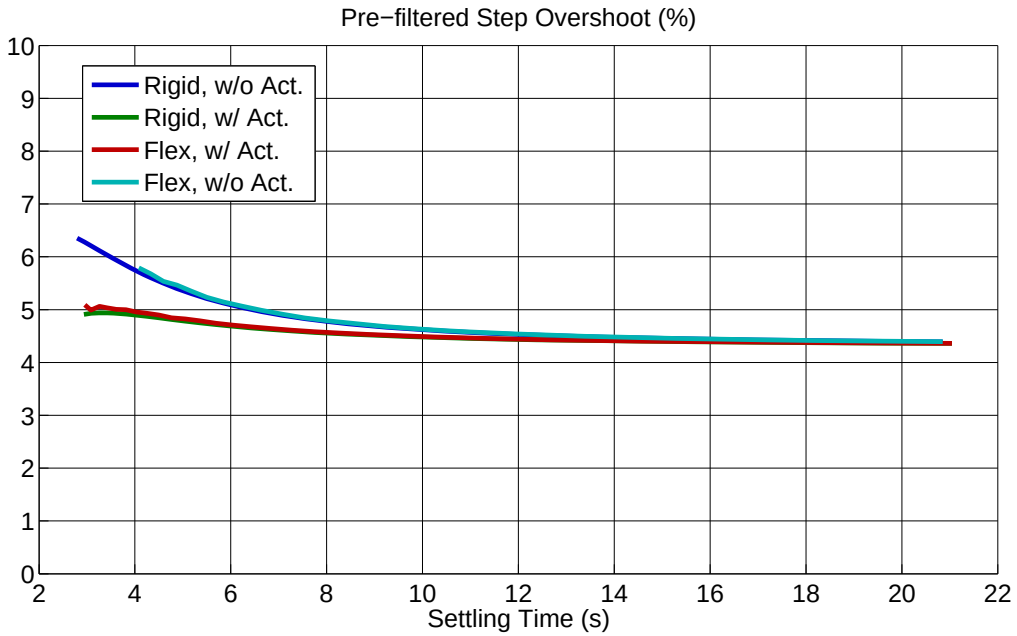

Figure 11.13: LQR Design: FPA Percent Overshoot (pre-filtered) vs Settling Time

- Figure 11.13 shows tradeoffs between FPA overshoot (for a pre-filtered reference command) vs settling time
- The variation in overshoot is small for all settlings times considered - less than 1.5 %

Peak FPA Error Sensitivity vs Settling Time (BW)

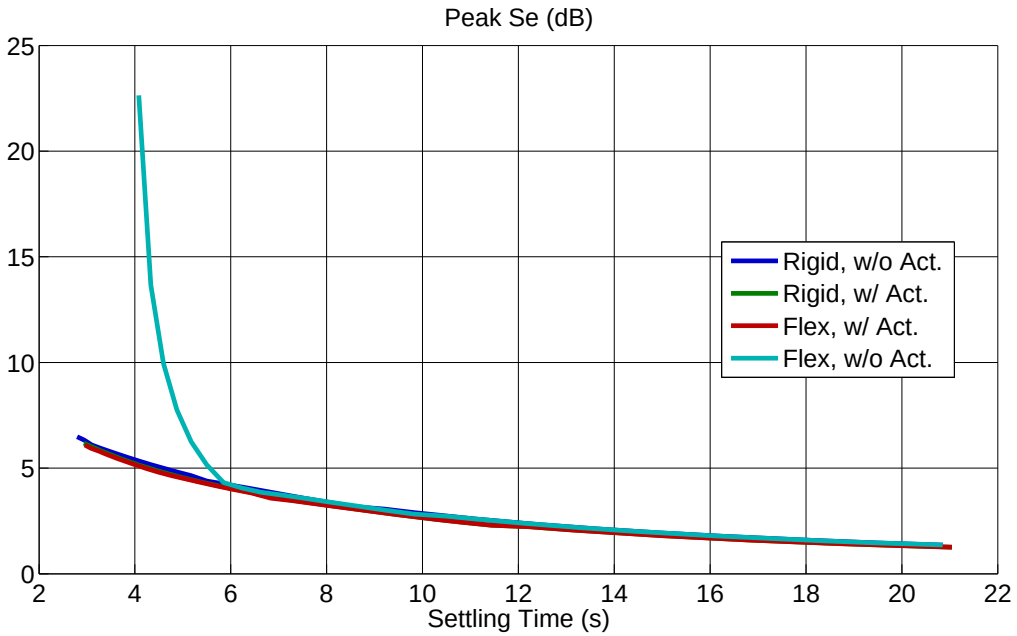

Figure 11.14: LQR Design: Peak FPA Error Sensitivity vs Settling Time

- Figure 11.14 shows tradeoffs between peak sensitivity at error and settling time
- Most of the systems show a fairly flat increase in peak sensitivity with decreasing settling time
- For small settling times, the flexible system w/o actuator is quickly becoming unstable - as evidenced by the spike in peak sensitivity; this might be anticipated from our Nyquist plot results

Peak Elevator Sensitivity vs Settling Time (BW)

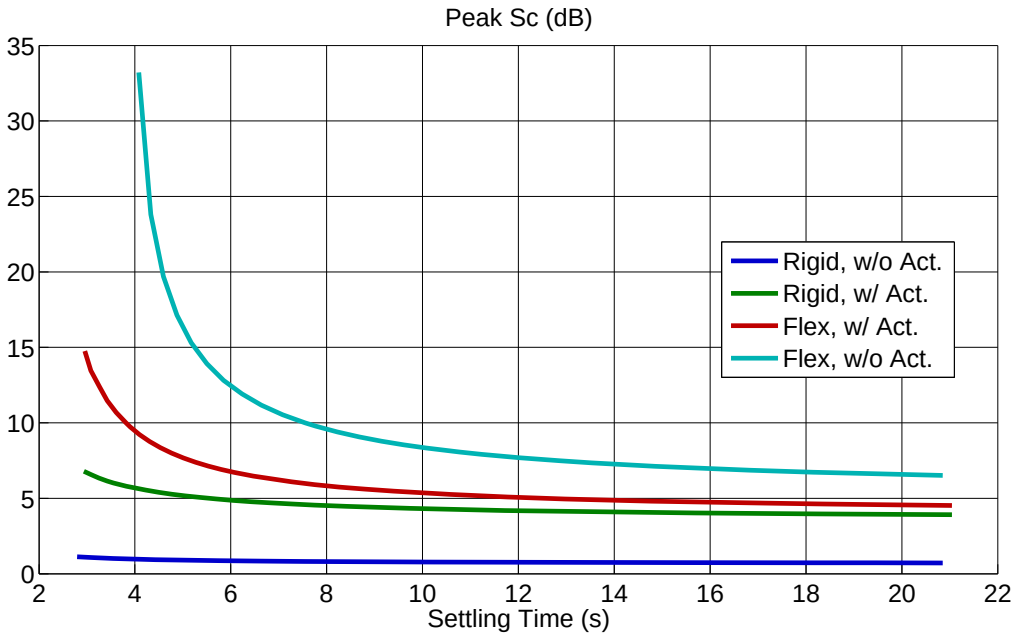

Figure 11.15: LQR Design: Peak Elevator (Control) Sensitivity vs Settling Time

- Figure 11.15 shows tradeoffs between peak sensitivity at the controls (elevator) and settling time. In general, all peak sensitivities increase with decreasing settling time (increasing BW).
- Peak sensitivity at elevator increase when (the unmodeled) actuator dynamics are added to rigid model (compare green and blue curves). NOTE: There is no way to recover this degradation in robustness without estimating the actuator state and using the state within the control system. This, however, would add significant structure (an increase in complexity) to the control system.
- Comparing the green and red curves shows how the flexible dynamics significantly increase peak sensitivity (deteriorate robustness). Any attempt to notch filter the flexible dynamics will attempt to recover the green performance (rigid with actuator) from the red system (flexible with actuator).
- Comparing the red and cyan curves shows how bad the sensitivity increase due to the flexible dynamics would be without the actuator. This demonstrates the fact that for the flexible system, the actuator helps to improve closed loop stability robustness; i.e. the actuator naturally rolls off the controller at frequencies near the flexible dynamics. Due to the potentially uncertain nature of the actuator dynamics, the tradeoff in robustness wrt the actuator frequency must be examined. See section 11.11.
- The above peak S_c vs settling time plot demonstrates the single most important tradeoffs between robustness and performance.

Peak Control vs Peak Error Sensitivities

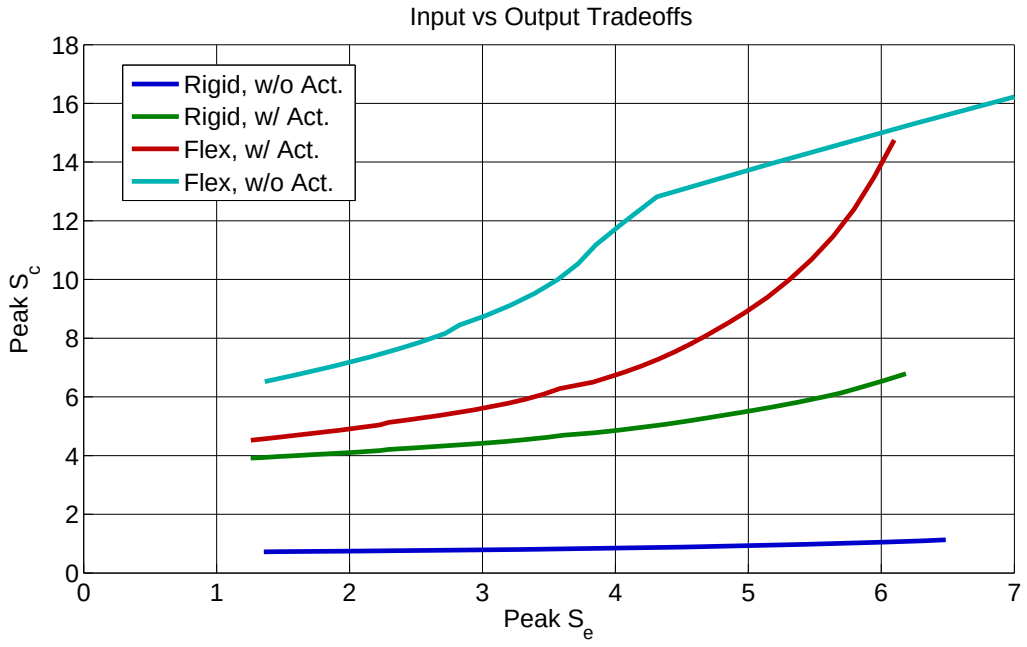

Figure 11.16: LQR Design: Peak Control vs Peak Error Sensitivities

- Figure 11.16 shows how peak S_c increases with increasing peak S_e
- For all cases, increasing the peak S_e also increases the peak S_c
- For the two most relevant cases - rigid with actuator (green) and flex with actuator (red) - the peak S_c is always greater than the peak S_e

Peak T_{d_iy} vs Settling Time (BW)

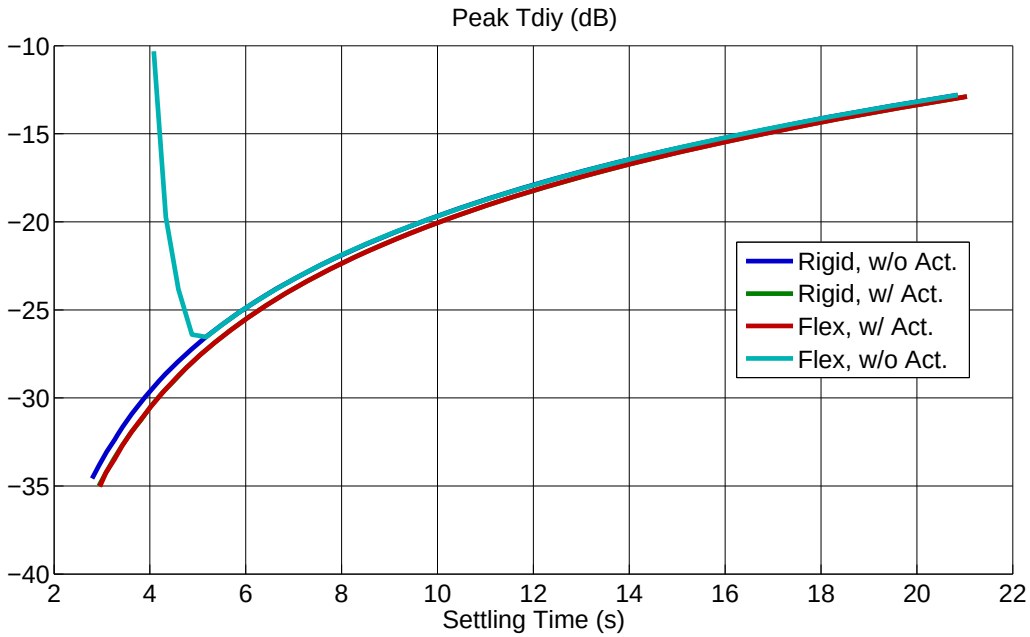

Figure 11.17: LQR Design: Peak T_{d_iy} vs Settling Time

- In general, all four cases show the same trend: Peak T_{diy} improves as settling time decreases; i.e. as BW increases. This is not terribly surprising as the amount of control action increases with decreasing settling time, allowing for input disturbances to be quickly attenuated.
- An exception occurs for small settling times - the flexible system w/o actuator is quickly becoming unstable, as evidenced by the spike in peak T_{diy}

Peak T_{ru} (no command pre-filter) vs Settling Time (BW)

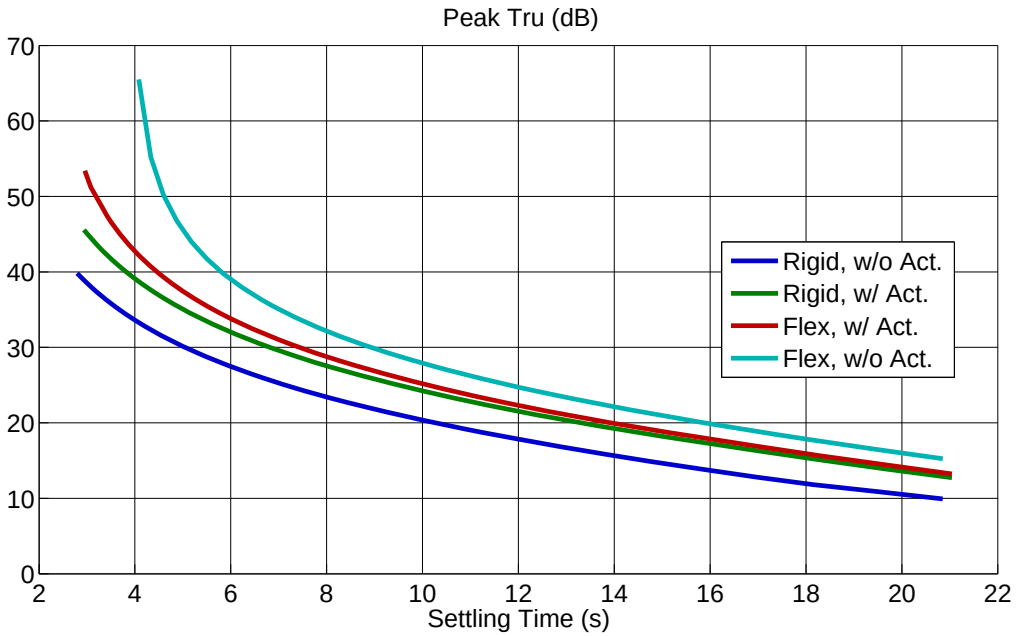

Figure 11.18: LQR Design: Peak T_{ru} (No Command Pre-filter) vs Settling Time

- Peak T_{ru} increases with decreasing settling time (increasing BW) for all four cases
- Addition of the actuator decreases the peak control for the flexible case (i.e. adds mid-frequency roll off)

Peak WT_{ru} (with command pre-filter) vs Settling Time (BW)

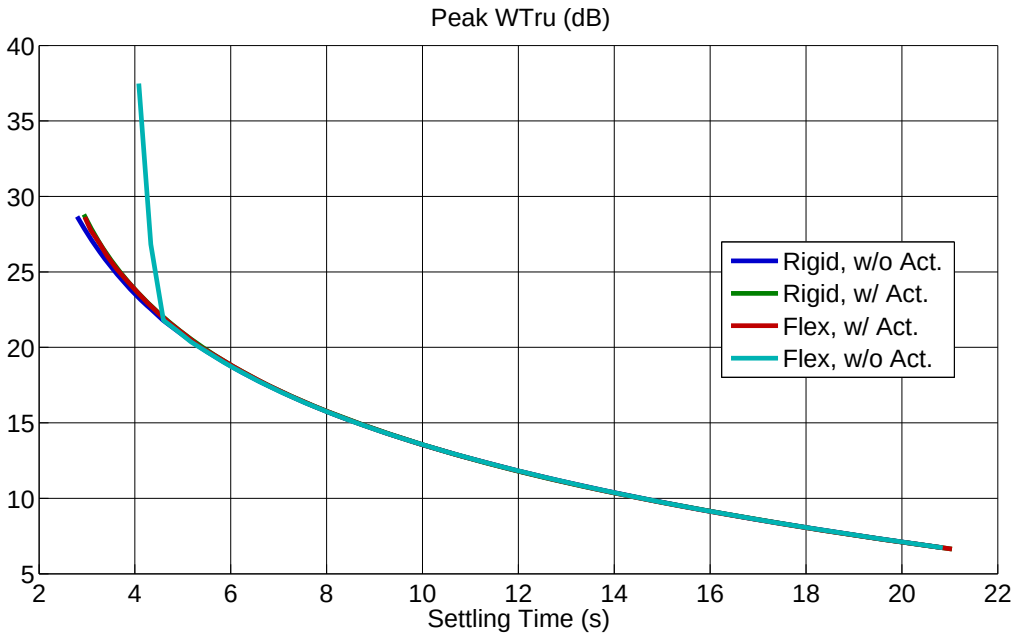

Figure 11.19: LQR Design: Peak WT_{ru} (With Command Pre-filter) vs Settling Time

- The peak WT_{ru} (with the command pre-filter) is significantly lower than that seen in Figure 11.18 on page 151.
- All four cases show nearly identical responses for most settling times. Deviation is seen for small settling times for flexible system without actuator (as expected.

Phase Margin at FPA Error vs Settling Time

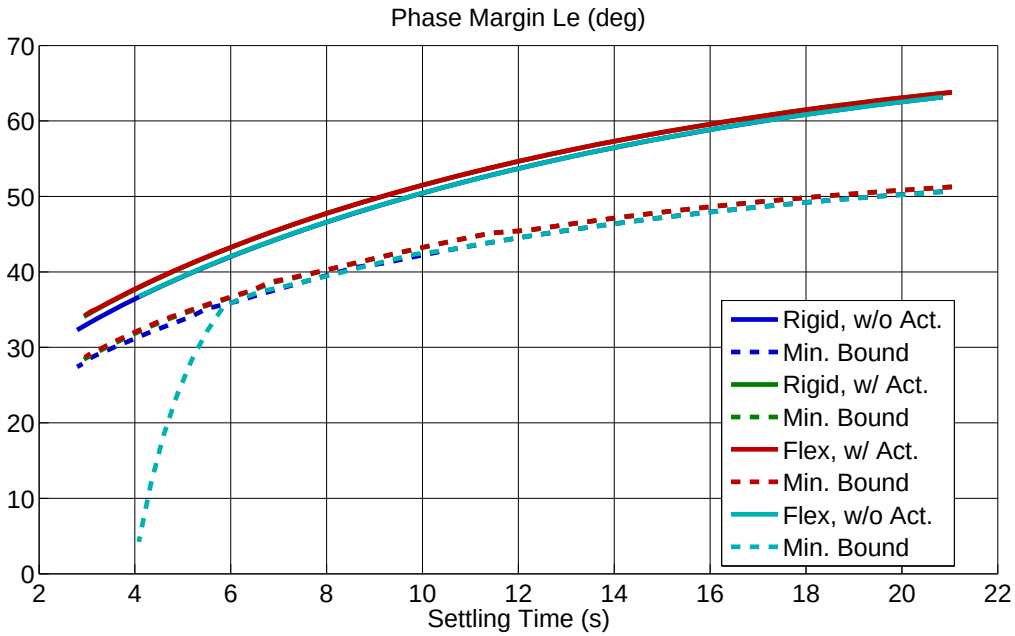

Figure 11.20: LQR Design: Phase Margin at FPA Error vs Settling Time

- Phase margin at FPA error (and the lower bound) decreases with decreasing settling time.
- Lower bound for PM is on average about 10° less than actual PM at FPA error.

Upward Gain Margin at FPA Error vs Settling Time (BW)

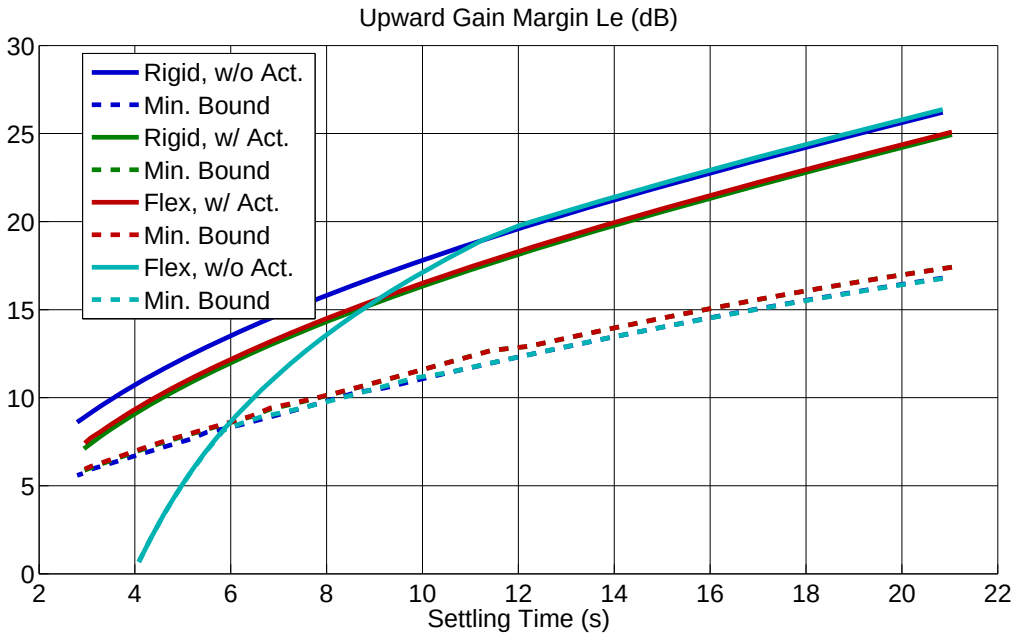

Figure 11.21: LQR Design: Upward Gain Margin at FPA Error vs Settling Time

- Upward gain margin (and lower bound) decreases with decreasing settling time.
- Lower bound is on average about 5 dB less than the actual gain margin at error.
- The downward gain margin at the error is 0 ($-\infty$ dB) and therefor not shown. This is because the inner PD θ attitude loop results in a modified FPA plant which is stable.

Phase Margin at Elevator vs Settling Time (BW)

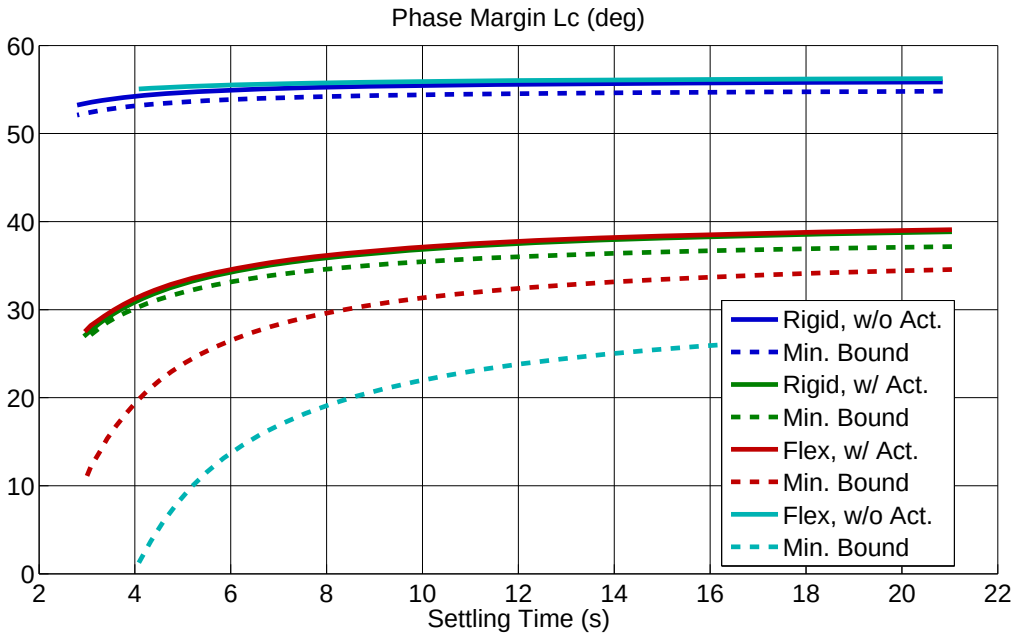

Figure 11.22: LQR Design: Phase Margin at Elevator vs Settling Time

- Figure 11.22 shows the Phase Margin and lower bound PM at the controls (elevator).
- The general trend for all cases is a slight decrease with decreasing settling time.
- Both rigid cases exhibit lower bounds that are very close to the actual phase margin.
- Both flexible cases show a considerable decrease in lower bound vs the actual phase margin. This demonstrates one of the perils of utilizing the standard gain margin as a design metric. The four second settling time flexible model without actuator shows a 55° phase margin, but the lower bound phase margin has approached zero. From other plots, it is clear that the system is approaching instability. This, however, is not reflected in the phase margin.

Downward Gain Margin at Elevator (Controls) vs vs Settling Time (BW)

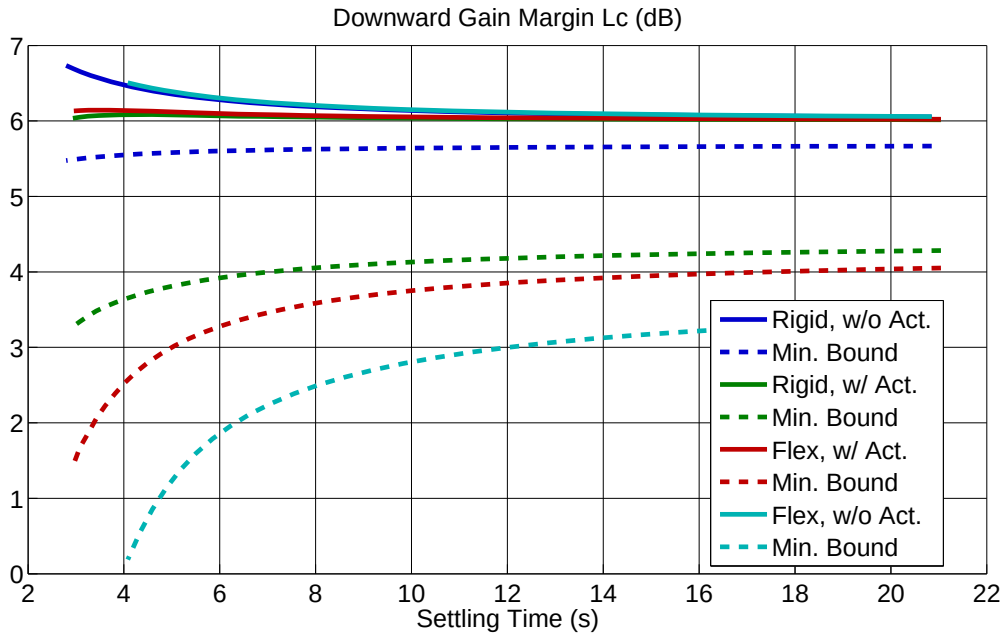

Figure 11.23: LQR Design: Downward Gain Margin at Elevator (Controls) vs Settling Time

- The downard gain margin (and lower bound) is roughly the same for all cases (6 dB), but the minimum bounds can be significantly worse.

Upward Gain Margin at Elevator (Controls) vs Settling Time (BW)

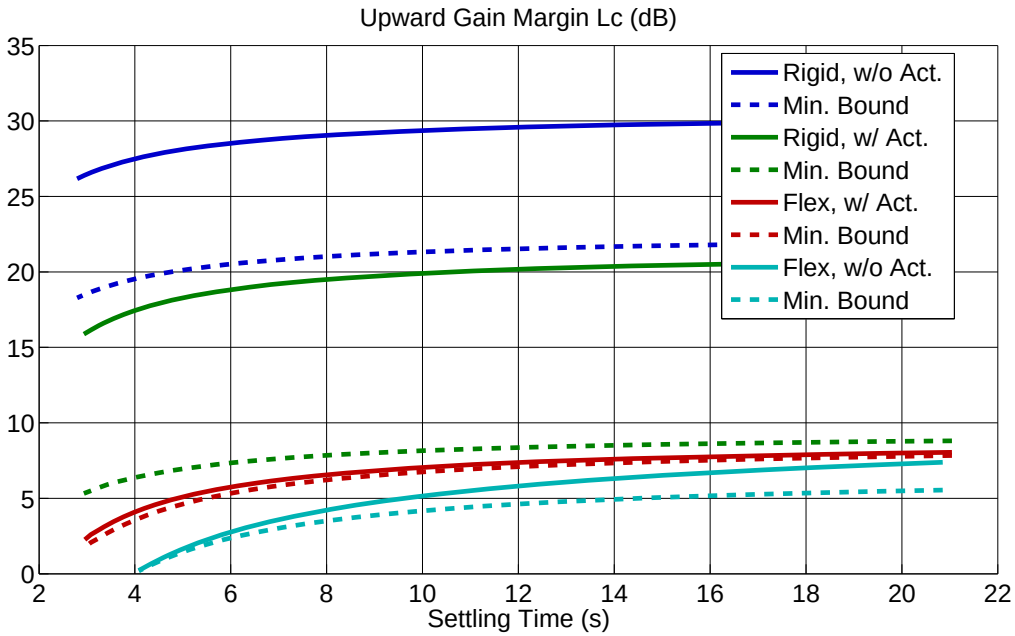

Figure 11.24: LQR Design: Upward Gain Margin at Elevator (Controls) vs Settling Time

- The upward gain margin for the two rigid cases is practically meaningless because they do not include any high order terms that would demonstrate some limit on the gain.
- The two flexible cases have decreasing upward gain margins as the settling time decreases (expected). Both cases show the minimum bounds is very close to the actual gain margin.

Conclusions

What can be seen is that error vs controls tradeoff increases severely when moving from the rigid w/actuator case to the flexible w/actuator case. Most studies after this will focus on attempting to recover the rigid w/actuator error vs controls tradeoff profile from the flexible w/actuator system.

Figure 11.25 demonstrates the robustness properties (at input and error) with respect to uncertainty in the actuator pole. For any given BW at the error, there exists an actuator pole that will minimize peak S_c, however it is not the same for all error BWs. In general the tradeoffs are more severe on the lower side of the minimums.

The nominal actuator poles used in the literature, $\frac{20}{s+20}$ is placed in a position that will maximize robustness at the controls for all but the fastest error BWs.

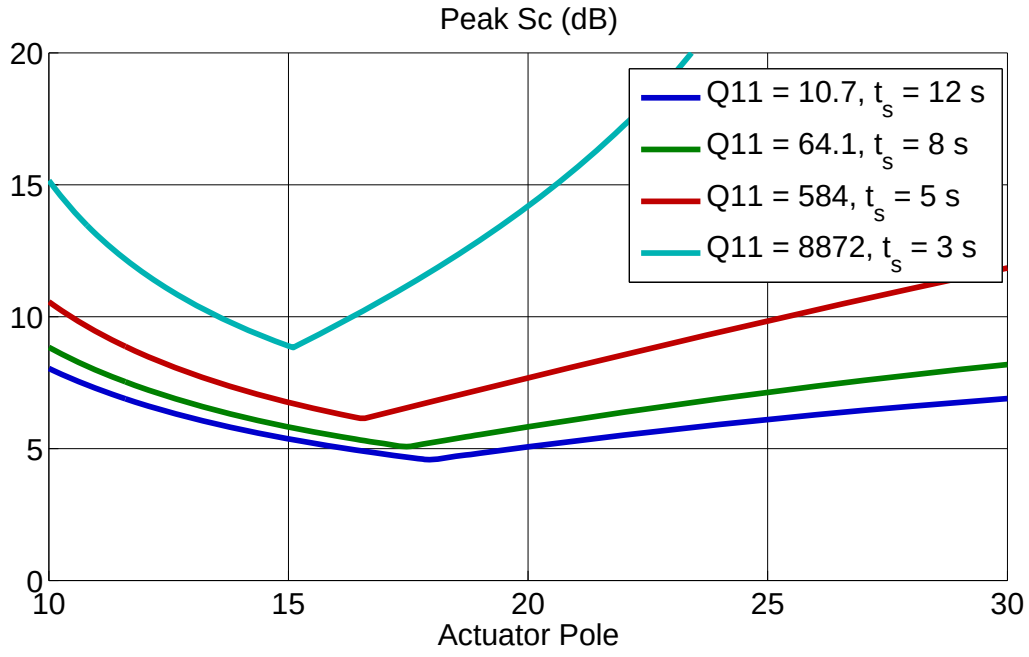

Figure 11.25: LQR Design: Peak S_c vs Actuator Pole

This study should be interpreted with great caution because the addition of a notch filter (to address flexible dynamics) can severely impact this tradeoff.

A fourth order Type II Chebyshev Notch filter will be designed to attempt to improve sensitivities; i.e. robustness with respect to the unmodelled flexible dynamics. Figure 11.26 demonstrates the shape of the notch filter as expressed by Equation (11.77).

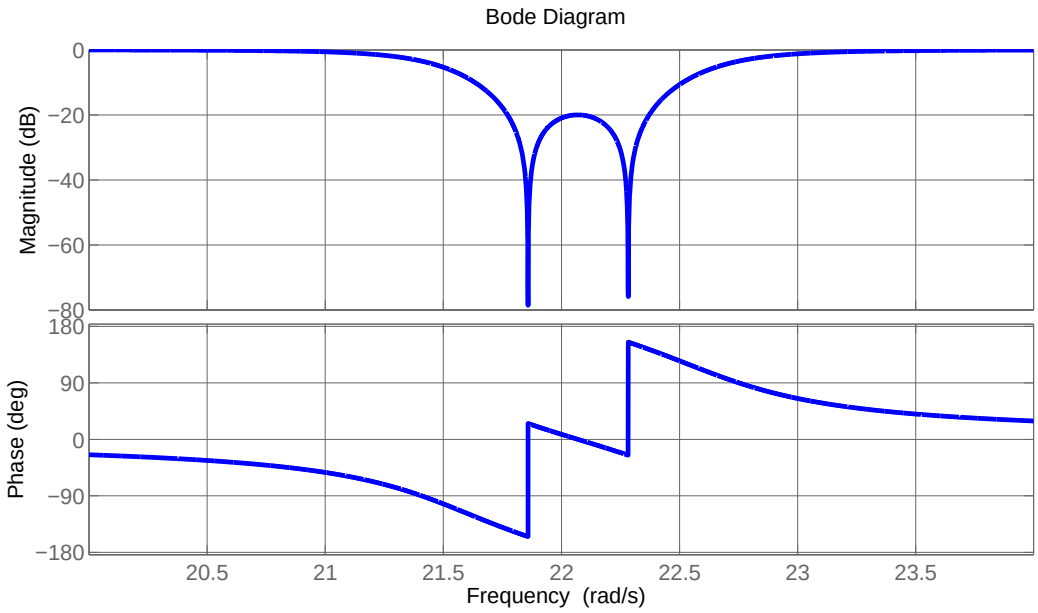

Figure 11.26: LQR Design: 4th Order Type II Chebyshev Notch Filter

$$N(s) = \left[\frac{s^2 + \omega_{z_1}^2}{s^2 + 2\zeta_1\omega_{p_1} + \omega_{p_1}^2}\right]\left[\frac{s^2 + \omega_{z_2}^2}{s^2 + 2\zeta_1\omega_{p_2} + \omega_{p_2}^2}\right] \tag{11.77}$$

Rather than study the 6 independent parameters (ζ_i, ω_{p_i}, ω_{z_i}; i=1, 2), MATLABs Filter Design toolboox allows them to be selected in terms of: (1) Notch Center, (2) Notch Attenuation (as measured from 0 dB to the center bump) (3) Notch Width as measured from the attenuated bump. The final notch selected is shown in Figure 11.26, with the following parameters: centered at 22.1 rad/s (location of the flexible mode), notch attenuation of 20 dB, notch width of 0.6 rad/s. The following subsection will demonstrate how these parameters were selected.

Notch Filter Width - Peak S_c and BW at Error

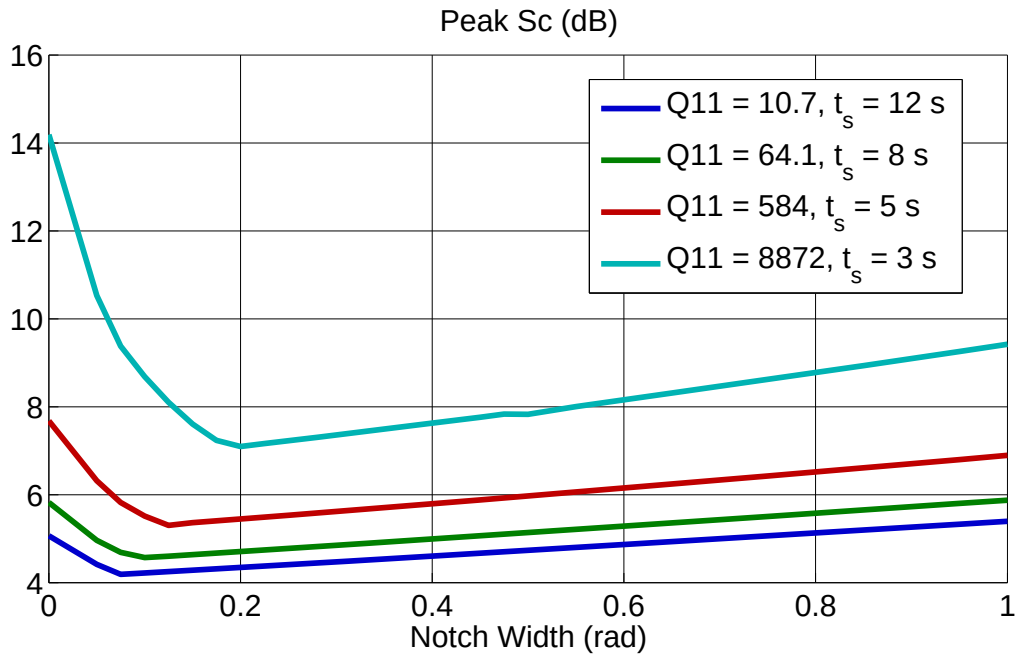

Figure 11.27: Notch Design: Peak S_c vs Notch Filter Width (rad/s)

Figure 11.27 demonstrates the improvement in properties (at input and error) with respect to notch width. The nominal notch parameters are as follows: notch center at first flexible mode frequency, notch attenuation of 20 dB. There is an optimal value for the notch width for each BW at the error.

Figure 11.27 shows that the tradeoff of making the notch width smaller than the minimizer is very severe. In contrast, making the notch width larger than the minimizer results in a very mild tradeoff. This observation suggests that one make the notch width bigger than the peak S_c notch width minimizer in order to avoid paying a high price for uncertainty as can be see in a subsequent study (see subsection 11.11).

Peak S_c vs Notch Filter Center and BW at Error

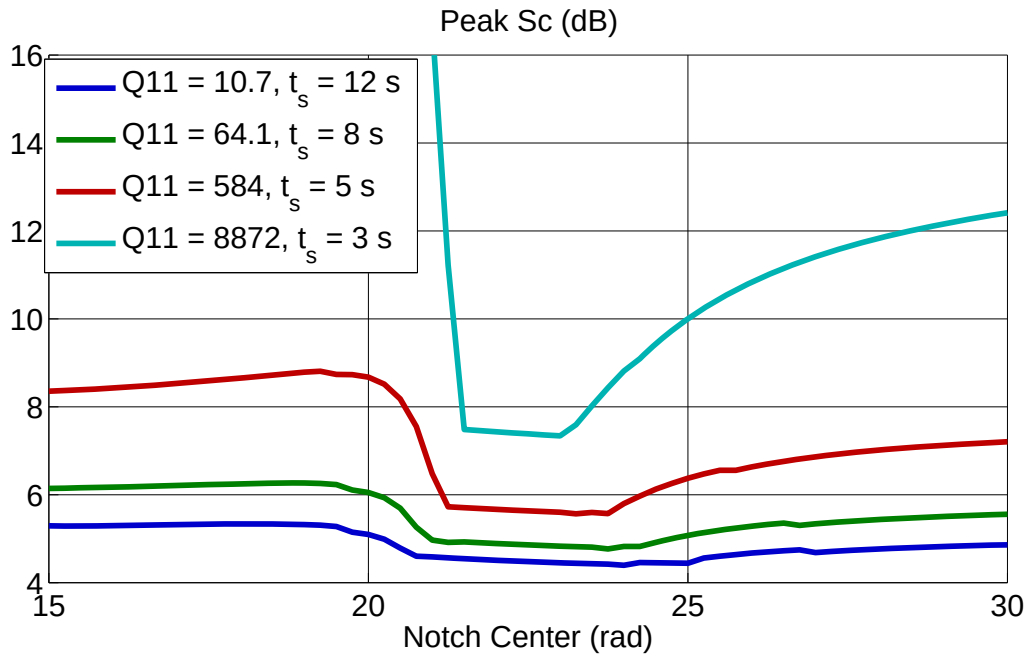

Figure 11.28: Notch Design: Notch Filter Center (rad/s)

Figure 11.28 demonstrates the robustness properties when the notch center is located off center of the flexible dynamics. For increasing error BW, there is a smaller and smaller region for which the robustness (measured by peak S_c) is very good. Outside this "good notch center" region, the robustness (peak S_c) becomes very bad.

It is necessary to evaluate the notch center vs notch width for the fast error BW in order to really understand how to select width given the small tolerance to variation in aligning the notch with the flexible mode.

Peak S_c Notch Width vs Notch Center

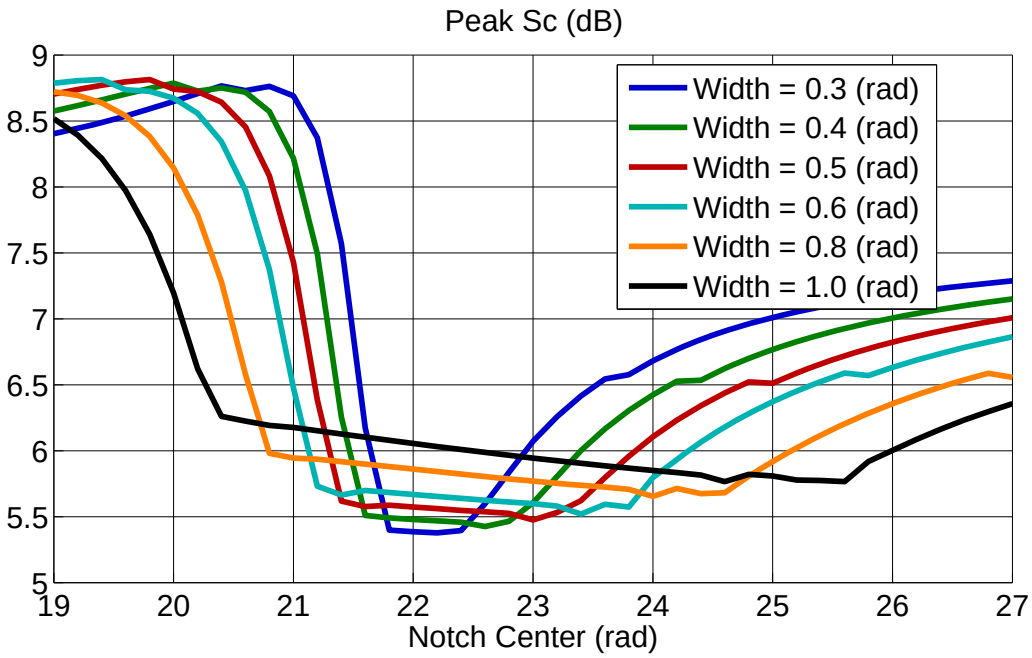

Figure 11.29: Notch Design: Peak S_c vs Notch Center (rad/s) and Notch Width (rad/s)

Figure 11.29 shows the tradeoffs in robustness for the notch width vs misalignment with the flexible mode for the 5 second settling time. The tradeoff associated with notch width is not too severe. This is in contrast to the tradeoff observed for misalignment with the flexible mode. This tradeoff can be very severe.

The robustness tradeoff can be improved with respect to misalignment in the notch location, at the expense of small amount of overall robustness. If there is a fair amount of uncertainty in the flexible mode frequency (such as due to long exposure to high temperatures), then the tradeoff is obviously favorable.

Nominal LQR Design with Notch: Peak Control Sensitivity vs Settling Time

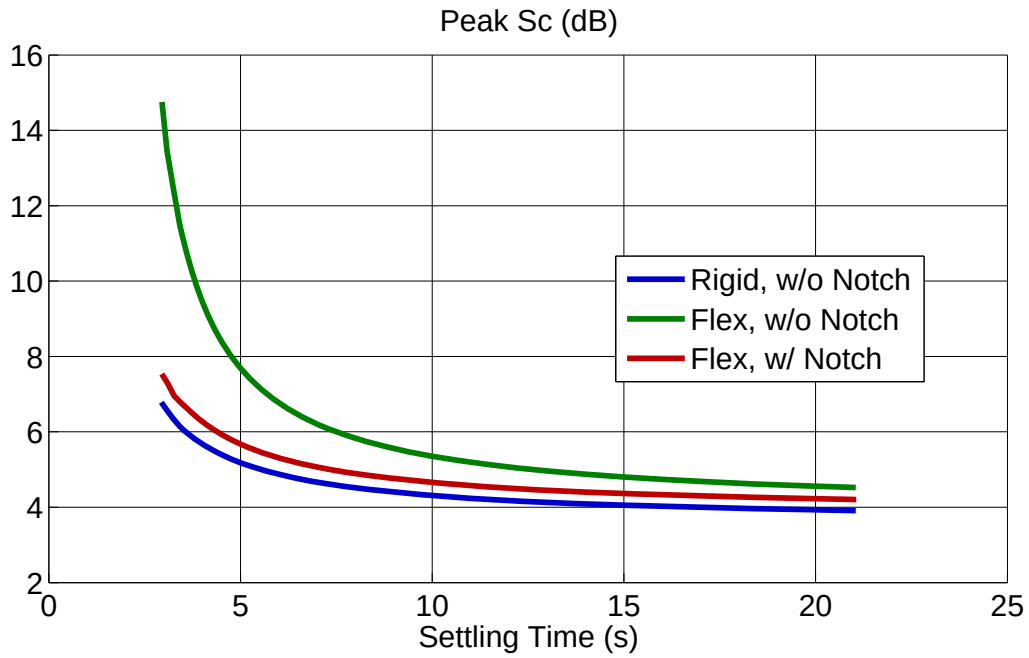

Figure 11.30: LQR Design with Notch: Peak Control Sensitivity vs Settling Time

Figure 11.30 shows the peak S_c as a function of the settling time when the notch filter is added. What is shown is that the notch filter is able to recover the rigid performance to within 0.5 dB for all settling times. This can turn a 5 second settling time design with questionable robustness properties (8 dB) into a design with acceptable properties (less than 6 dB).

This section presents LPV $\mathcal{H}^\infty$ control system designs for the conversion:

Weighted $\mathcal{H}^\infty$ Suboptimal Mixed Sensitivity Problem. The weighted $\mathcal{H}^\infty$ suboptimal mixed sensitivity problem is to find a real-rational (finite-dimensional) proper internally stabilizing controller K that satisfies

$$\|T_{wz}\|_{\mathcal{H}^\infty} = \left\| \begin{bmatrix} W_1 S \\ W_2 K S \\ W_3 T \end{bmatrix} \right\|_{\mathcal{H}^\infty} < \gamma. \tag{11.78}$$

where S and T are the sensitivity and complementary sensitivity transfer functions of the closed loop system respectively.

$\mathcal{H}^\infty$ Mixed-Sensitivity Weighting Functions. The selection of the weighting functions used in the $\mathcal{H}^\infty$ design process was kept consistent across the operating points. Using the same weighting function structure for each design keeps the order of the controllers the same and allows for interpolation of the weighting function parameters across the gain-scheduled conversion. In this case, it was sufficient to use one set of weightings for the entire conversion process. All the weight matrices are (diagonal) 2x2 matrices:

$$W_1^{i,j} = \begin{cases} \frac{s/\sqrt{M_{e_i}}+\omega_{e_i}}{s+\omega_{e_i}\sqrt{\epsilon_{e_i}}} & i=j \\ 0 & i \neq j \end{cases} \tag{11.79}$$

$$W_2^{i,j} = \begin{cases} \frac{s+\omega_{u_i}/\sqrt{M_{u_i}}}{\sqrt{\epsilon_{u_i}}s+\omega_{u_i}} & i=j \\ 0 & i \neq j \end{cases} \tag{11.80}$$

$$W_3^{i,j} = \begin{cases} \frac{s+\omega_{x_i}/\sqrt{M_{x_i}}}{\sqrt{\epsilon_{x_i}}s+\omega_{x_i}} & i=j \\ 0 & i \neq j \end{cases} \tag{11.81}$$

$$\tag{11.82}$$

Weighting function parameters are selected as given in Table 11.1.

Table 11.1: WEIGHTING and TRANSFORMATION FUNCTION PARAMETERS

	W_1		W_2		W_3	
	1	2	1	2	1	2
ϵ	10^{-5}	10^{-5}	10^{-5}	10^{-5}	10^{-5}	10^{-5}
M	1.6	4	4	4	10^6	10^6
ω	.0395	0.25	0.2	2	$20x10^3$	$20x10^3$

LPV $\mathcal{H}^\infty$ Controller Synthesis.

- Step 1. Augment model with integrators. We augment the plant with integrators on the output to ensure zero steady state error to a step reference input.
- Step 2. Choose weighting functions. Weighting functions W_1, W_2, and W_3 weight the sensitivity at the output S_o, the reference to control transfer function, KS_o, and the complimentary sensitivity at the output T_o.
- Step 3. Create generalized plant. The generalized plant incorporates the weighting functions and augmented plant. With the generalized plant we can seek to minimize *regulated signals*, which are our weighted mixed-sensitivities W_1, W_2, and W_3. The measurements to the controller are the (integrated) output errors, the pitch, and the pitch rate.

- Step 4. Generate LMI convex optimization constraints. The generalized plant is used to create several constraints to a convex optimization. Each constraint corresponds to a our LPV model evaluated for a parameter value and ensures that the regulated signals of the generalized plant have $\mathcal{H}^\infty$ norm less than some γ for that parameter value.
- Step 5. Solve LMI convex optimization problem. The convex optimization is solved with MATLAB's LMI Lab, specifically the *mincx* function.
- Step 6. Create controller from optimal solution. The convex optimization problem variables are for a transformed system. There are several steps to construct the controller from the optimal solution.
- Step 7. Augment controller with integrators. The integrators added to the plant are moved to the input (error channels) of the controller.

Linear Matrix Inequality Formulation. The state space block representation of generalized weighted plant [122]

$$\begin{pmatrix} \dot{x} \\ z \\ y \end{pmatrix} = \begin{pmatrix} A & B_1 & B_2 \\ C_1 & D_{11} & D_{12} \\ C_2 & D_{21} & D_{22} \end{pmatrix} \begin{pmatrix} x \\ w \\ u \end{pmatrix} \tag{11.83}$$

If we use an (output+state)-feedback controller $K : y \mapsto u$ with controller dynamics

$$\begin{pmatrix} \dot{x}_k \\ u \end{pmatrix} = \begin{pmatrix} A_k & B_k \\ C_k & D_k \end{pmatrix} \begin{pmatrix} x_k \\ y \end{pmatrix}$$

then combining the generalized plant with the output-feedback controller will result in the closed loop state space equations for $w \mapsto z$ (assuming a strictly proper plant, i.e., $D_{22} = 0$) [123]

$$\begin{pmatrix} \dot{x} \\ \dot{x}_k \\ \hline z \end{pmatrix} = \left(\begin{array}{cc|c} A + B_2 D_k C_2 & B_2 C_k & B_1 + B_2 D_k D_{21} \\ B_k C_2 & A_k & B_k D_{21} \\ \hline C_1 + D_{12} D_k C_2 & D_{12} C_k & D_{11} + D_{12} D_k D_{21} \end{array}\right) \times \begin{pmatrix} x \\ x_k \\ \hline w \end{pmatrix} \tag{11.84}$$

Our generalized plant is now used to create the constraints to a convex programming problem. We use a Linear Matrix Inequality to create constraints which guarantee a $\mathcal{H}^\infty$ norm less than some γ. If we create enough constraints and grid the parameters of our LPV plant finely enough, then a $\mathcal{H}^\infty$ controller can be sucessfully constructed from the solution to the convex programming problem [123]

We first use the result from [124] that a system has $\mathcal{H}^\infty$ norm less than γ if and only if there exist $R, S, \hat{A}_k, \hat{B}_k, \hat{C}_k, D_k$ such that

$$\begin{pmatrix} L_1 & L_3 \\ L_2 & L_4 \end{pmatrix} < 0, \tag{11.85}$$

$$L_1 = \begin{pmatrix} \left(RA + \hat{B}_k C_2\right) + \star & \star \\ \hat{A}_k^T + A + B_2 D_k C_2 & \left(AS + \hat{B}_2 \hat{C}_k\right) + \star \end{pmatrix}$$

$$L_2 = \begin{pmatrix} \left(RB_1 + \hat{B}_k D_{21}\right)^T & \left(B_1 + B_2 D_k D_{21}\right)^T \\ C_1 + D_{12} D_k C_2 & C_1 S + D_{12} \hat{C}_k \end{pmatrix}$$

$$L_3 = \begin{pmatrix} \star & \star \\ \star & \star \end{pmatrix} \quad L_4 = \begin{pmatrix} -\gamma I & \star \\ D_{11} + D_{12} D_k D_{21} & -\gamma I \end{pmatrix}$$

$$\begin{pmatrix} R & I \\ I & S \end{pmatrix} > 0.$$

where $\star$ denotes blocks that induce symmetry.

When our optimization algorithm has converged, we have a minimum γ as well as the final solutions $R, S, \hat{A}_k, \hat{B}_k, \hat{C}_k$ and $\hat{D}_k$. The procedure to recover the controller is as follows:

Find matrices M and N that satisfy

$$MN^T = I - RS$$

this can most easily be done by choosing $M = I$ and $N^T = I - RS$, or vice versa. Alternatively, using a singular value decomposition $USV^T = I - RS$, we could say that $M = US^{1/2}$ and $N^T = S^{1/2}V^T$. In general, any factorization will work just as well. Solve for A_k, B_k, C_k. Explicitly,

$$\begin{aligned} A_k = {} & M^{-1}\times \\ & \left(\hat{A}_k - \hat{B}_k C_2 S - R B_2 \hat{C}_k - R\left(A - B_2 D_k C_2\right) S - \dot{R}S - \dot{M}N^T\right) \\ & \times N^{-T} \end{aligned} \tag{11.86}$$

$$B_k = M^{-1}\left(\hat{B}_k - R B_2 D_k\right) \tag{11.87}$$

$$C_k = \left(\hat{C}_k - D_k C_2 S\right) N^{-T} \tag{11.88}$$

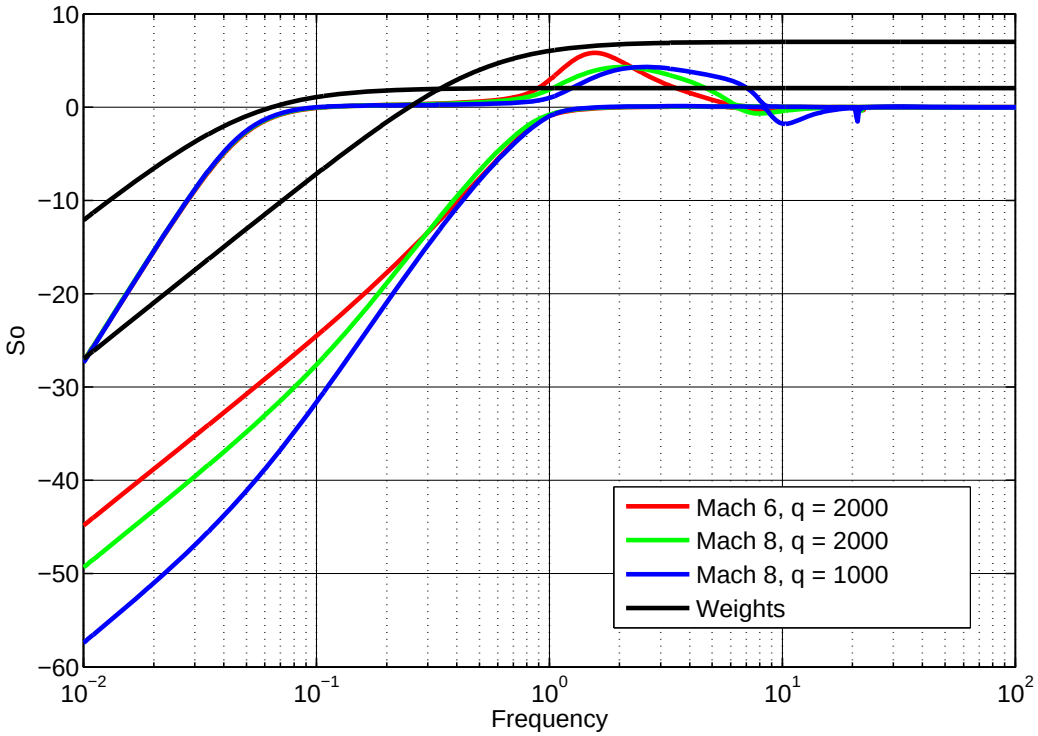

Figure 11.31: Sensitivity Singular Values at Plant Output

Closed-loop reference to output singular values are provided for several flight conditions along the trajectory. (Fig. 11.32 & 11.33). Output responses to step reference FPA commands are also provided (Fig. 11.34 & 11.35).

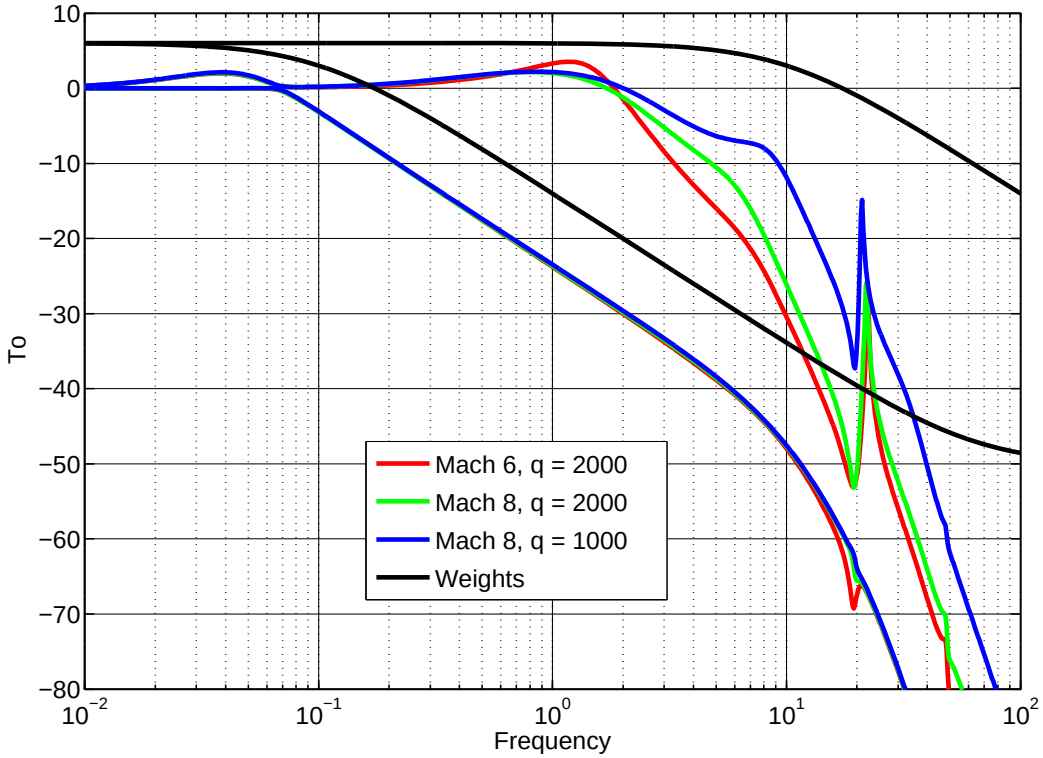

Figure 11.32: Complementary Sensitivity Singular Values

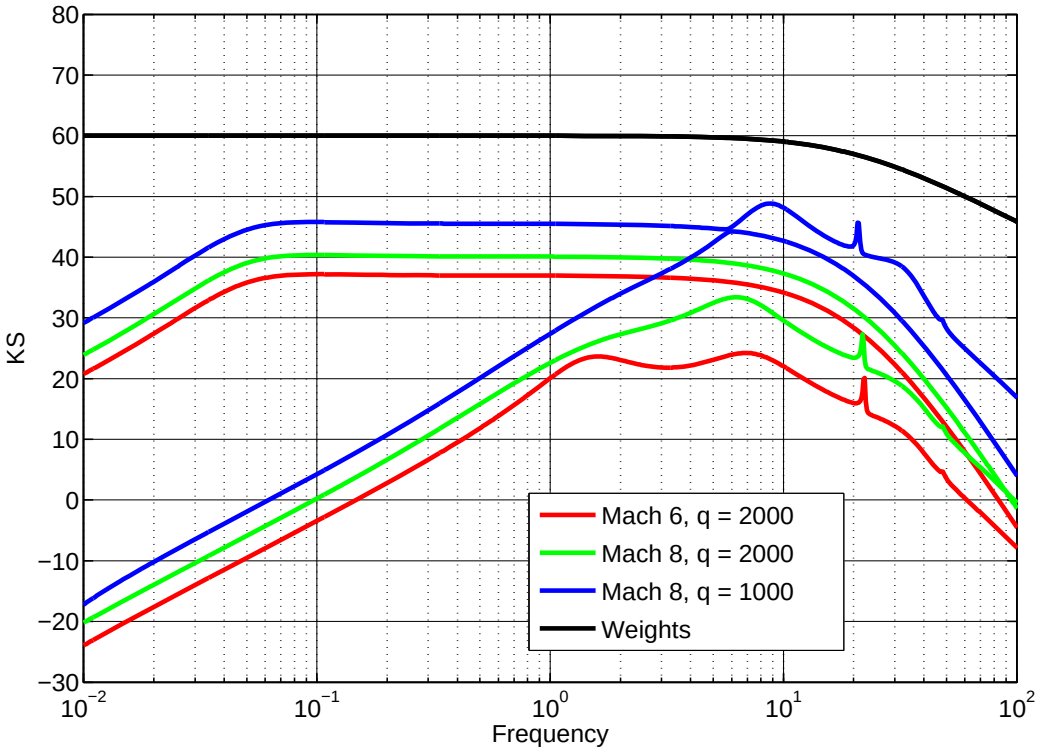

Figure 11.33: Reference to Control Singular Values

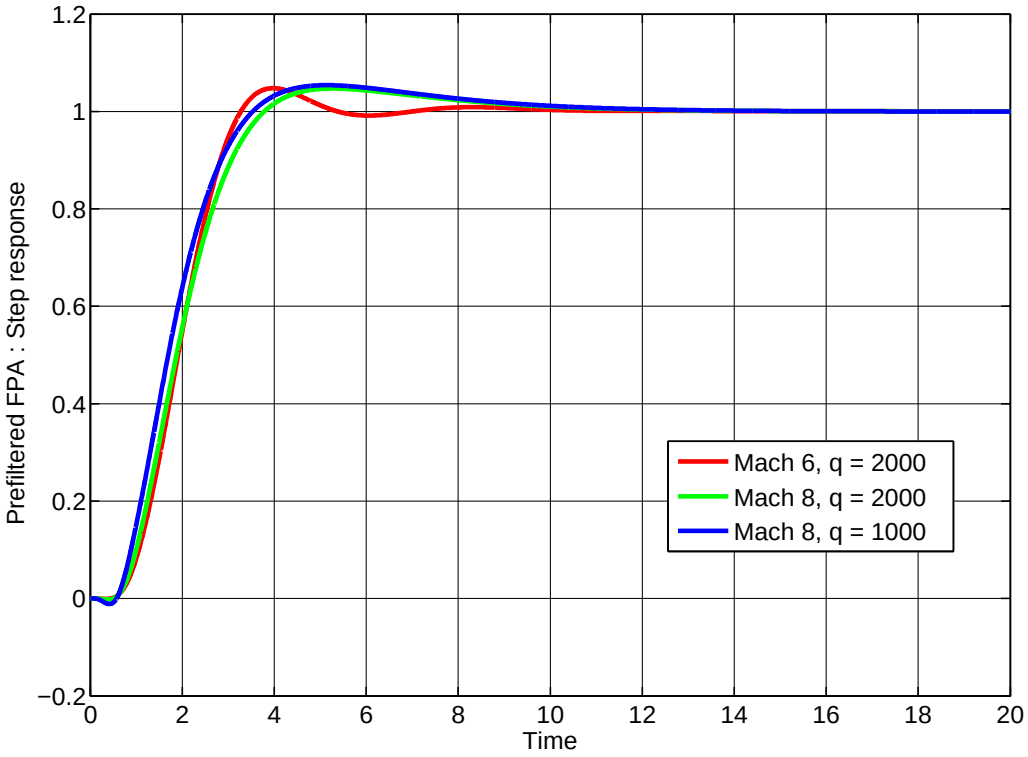

Figure 11.34: FPA Step Responses

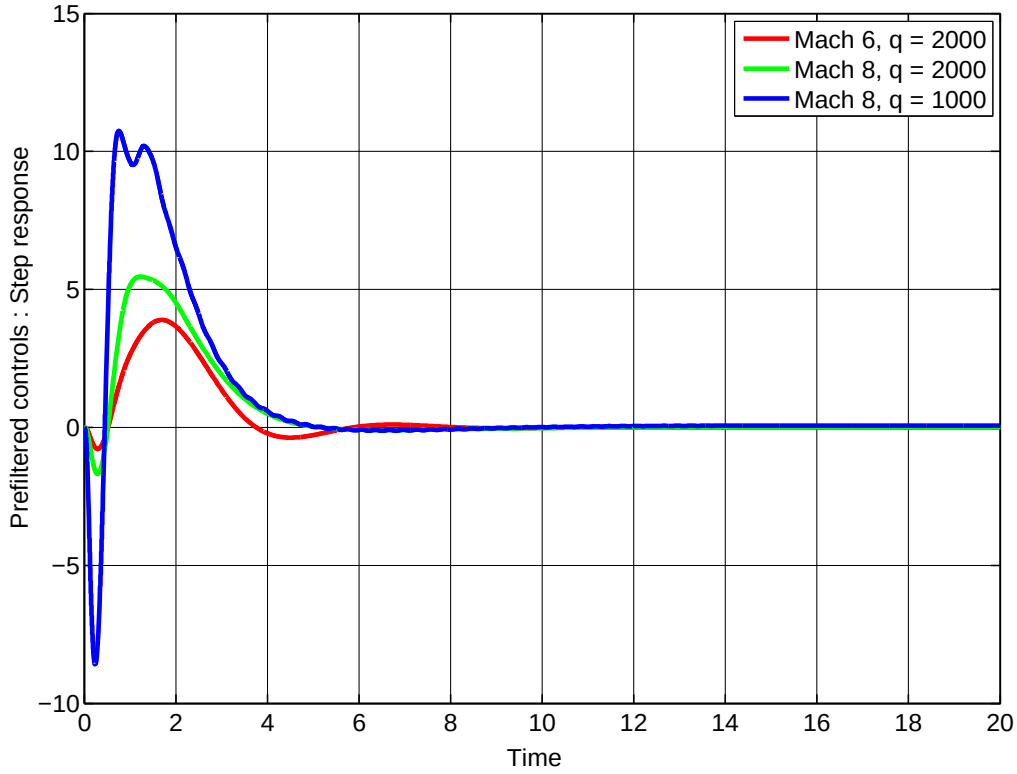

Figure 11.35: Elevator Step Responses

This LaTeX document was generated using the Graduate College Format Advising tool. Please turn a copy of this page in when you submit your document to Graduate College format advising. You may discard this page once you have printed your final document. DO NOT TURN THIS PAGE IN WITH YOUR FINAL DOCUMENT! font type: Arial font size: 10